N69-71273
The ch... (Accession No.)
for this Book is 37248

NASA-CR-98801

JPL Document No. 606-1

MARS SCIENTIFIC MODEL

Prepared by Members of the
Lunar and Planetary Sciences Section

LIBRARY COPY

JAN 15 1969

MANNED SPACECRAFT CENTER
HOUSTON, TEXAS

Approved: Robert J. Mackin Jr.
Robert J. Mackin, Jr., Manager
Lunar and Planetary Sciences
Section

JET PROPULSION LABORATORY
CALIFORNIA INSTITUTE OF TECHNOLOGY
PASADENA, CALIFORNIA

July 15, 1968

JPL Document No. 606-1
July 15, 1968

Copyright © 1968
Jet Propulsion Laboratory
California Institute of Technology
All Rights Reserved
Prepared Under Contract No. NAS 7-100
National Aeronautics & Space Administration

Photograph of Mars taken by R. B. Leighton of the California Institute of Technology on August 24, 1956, eighteen days before opposition. The planet was approximately 35.2 million miles from Earth at the time the photograph was obtained. Mare Cimmerium and Mare Tyrrhenum dominate the center of the disk, and Syrtis Major is at the far left. The season is late spring in the southern hemisphere (north is at the top). The Mt. Wilson 60-inch reflector was used and its aperture was cut to 21 inches with an off-axis diaphragm; exposure time was 20 seconds on Kodachrome Type A film. The positive, used in making the print, was composed by the Jet Propulsion Laboratory. (The repeated copying of this photograph in the reproduction processes has greatly decreased the clarity of surface detail and has caused the yellowish tones of the original positive to appear orange here.)

The charge out number (Accession No.) for this book is 37248

NASA MSC TECHNICAL LIBRARY

Call No: QB 641 C22 v.1 c.3

PREFACE

Our aim in this document is to present an up-to-date scientific model of the planet Mars, with data values, limitations and sources, and with a limited amount of interpretation where appropriate.

Material in this document has been reviewed extensively both by Jet Propulsion Laboratory scientists and by other reviewers. However, it is our intention to revise sections that contain errors in data or shortcomings in interpretation, and we will be grateful for comments, corrections, and criticisms from our readers. These should be directed to R. Newburn. Each page is dated to show the time of latest revision and will be updated as new information becomes available. At some future date we hope to add sections on such topics as atmospheric circulation, secular surface changes, atmospheric transmission, and detailed cloud behavior.

Preferred data values are presented first in each section, followed by more detailed analysis and discussion. The discussions were purposefully restricted in length to facilitate expedient use by the reader. For greater detail the reader is referred to source material. Data are thoroughly referenced, and bibliography lists are included for each section. Sections are extensively cross referenced.

We have attempted to hold speculative material to a minimum, but some "best guesses" have been included where data were absent and project planning was expected to require working hypotheses or estimates. We have been careful to identify speculations as such.

TECHNICAL LIBRARY BUILDING 45

NOV 12 1970

Manned Spacecraft Center Houston, Texas 77058

ACKNOWLEDGMENTS

Contributions from widely diversified scientific disciplines were necessary to compile this document. The cooperative spirit of the many individuals contacted both on and off the Laboratory is greatly appreciated.

The constructive criticism offered the earlier drafts of this document has enhanced its usefulness. We wish especially to acknowledge the comments of Drs. R. Sharp, R. Smoluchowski, M. Molloy, R. Carpenter, J. Conel, L. Kaplan, E. Haines, M. Neugebauer, A. Loomis, and J. Adams. Dr. H. T. U. Smith of the University of Massachusetts acted as a consultant in the field of Dust Transport. The section on Freeze-Thaw Phenomena is an extract of material prepared by consultant Dr. F. Alton Wade, Texas Technological College. Their contributions are much appreciated.

Thanks are expressed to C. Capen for his Martian observational data, photography, and Martian seasonal base maps which have not been previously published. G. de Vaucouleurs contributed the data for the albedo map of Section 3.2 before his own publication.

The cooperation of many elements of the Technical Documentation Section was essential to the preparation of the document. Mrs. Margaret Cannon is warmly commended for the untiring dedication given to the task of the final documentation editing.

Mrs. J. Negus de Wys made an especially great contribution both as an author and, in the early stages, as an editor of this document, putting in many months of intense, devoted work. Other authors were R. Choate, J. Conel, R. Lyttleton, R. Mackin, E. Miner, E. Monash, R. Newburn, and R. Norton.

TOPICAL SUMMARY

The Mars Scientific Model, which is intended to be a source of the most recent and accurate data for Mars spaceflight program needs, is organized to provide the user with the means for convenient and fast location of desired information and to facilitate updating. The following order of subject matter appears in each section (or sub-section) wherever possible or applicable: Data Summary, Discussion, Conclusions or Implications, Figures, Cross References, and Bibliography. Each section thus can be considered a separate entity but also can be used, with the aid of the cross references, in parallel with the remainder of the document. A topical summary of each section is given below and on page viii; for detailed contents, see the page(s) immediately following each of the six main-section dividers.

1. ORBITAL AND PHYSICAL DATA

Orbital values, season lengths, and ephemeris data for Mars. Orbital data for Phobos and Deimos. Physical data for Mars, Phobos, and Deimos. Calendars of Earth-Mars equivalent dates from 1963 to 1983.

2. INTERIOR

Geometric relationships and flattening. Dynamical, optical, and theoretical flattening. Interior models of Jeffreys, Ramsey, Lyttleton, Urey, Bullen, and Ringwood.

3. SURFACE

3.1 Thermal Properties. Surface temperatures. Brightness temperature characteristics. Thermal parameter. Temperature measurements and interpretations.

3.2 Ultraviolet, Visible, and Infrared Properties. Photometric function. Phase function. Radiance factor. Normal, geometric, and Bond albedo. Magnitude. Spectral reflectivity and distribution. Polarization.

3.3 Radar Properties. Techniques of radar astronomy. Target radar cross section, reflection coefficient, dielectric constant, directivity factor, gain, and microwave Bond albedo. Martian orbital and physical considerations. Observations, results, and implications: 1963-USSR, 1963-JPL, 1965-JPL, 1965-AIO, and 1967-JPL radar studies of Mars.

3.4 Chemical and Physical Properties. Chemical composition of terrestrial lavas and crustal rocks. Elemental and inferred oxide compositions at the Surveyor V, VI, and VII landing sites on the Moon. Stability of terrestrial iron oxides. Iron oxides and silicates on Mars. Water and carbon dioxide. Meteoritic and magnetic material. Size distribution of material. Bearing strength. Selected Surveyor pictures of the Moon.

3.5 Morphology and Processes. Relative elevation of dark and light areas through interpretation of thermal data, radar data, cloud formation movement, and seasonal observations. Grid system. Canals. Craters. Slope angle distribution. Possible surface processes including tectonic movement, meteorite impact, volcanic activity, thermal creep and fracture, freeze-thaw processes, and wind action. Possible surface features. Selected Lunar Orbiter photographs of the Moon. Selected Mariner IV pictures of Mars.

4. OBSERVATIONAL PHENOMENA

4.1 Clouds and Hazes. Violet layer, blue clouds, and blue clearing. White clouds. Yellow clouds. Green haze, gray clouds, and bright spots.

4.2 Seasonal Activity. Polar caps. Polar hoods. Dark fringe of the polar cap. Seasonal behavior of clouds. Wave of darkening. Seasonal behavior of surface features. Local seasonal activity. Global seasonal activity (color maps) including polar caps, white clouds, yellow clouds, wave of darkening, and possible frost phenomena.

5. ATMOSPHERE

5.1 Atmospheric Composition. Observed constituents: carbon dioxide, water vapor, carbon monoxide, and the unidentified Sinton band. Assumed constituents: argon, molecular nitrogen, atomic oxygen, molecular oxygen, and ozone. Possible constituents: oxides of nitrogen, methane and related compounds, ammonia, and carbonyl sulfide.

5.2 Surface Pressure. Spectroscopic results. Mariner IV occultation experiment results. Methods of surface pressure determination and their relative accuracy: spectroscopy, occultation, and photometry and polarimetry.

5.3 Lower Atmosphere. Layers of the lower atmosphere. Physics of the troposphere, stratosphere, and mesosphere. Convective, radiative, and convective-radiative models. Models I, II, and III.

5.4 Upper Atmosphere. Layers of the upper atmosphere. Physics of the photodissociation region. Physics of the ionosphere including ionization processes and thermal processes. Preliminary E-Model. F_1-Model. F_2-Model.

6. CIS-MARTIAN MEDIUM, RADIATION

Solar constant. Spectral distribution. Extreme ultraviolet radiation, x-rays, and radio waves. Absorption of solar electromagnetic radiation in the Martian atmosphere. Solar interplanetary magnetic field. Martian magnetic moment, magnetosphere, and surface field. Solar wind and its effects on the Martian atmosphere. Solar flares. Cosmic rays. Radiation level and dose at the Martian surface.

SECTION 1 CONTENTS

1. ORBITAL AND PHYSICAL DATA

Orbital Data Summary 3
Mars 3
Orbital Values 3
Length of Seasons 4
Ephemeris Data 4
Satellites 5
Physical Data Summary 6
Mars 6
Satellites 7
Earth-Mars Calendar 8
Equivalences 8
Basis of Zero Points 8
Mars Leap Years 8
Cross References 27
Bibliography 28

Figures
1. Earth orbit plane cut by Earth equatorial plane, Mars equatorial plane, Phobos orbit plane, and Deimos orbit plane 10
2. Orbits of the inner planets of the solar system drawn to scale 11
3. Orbits of the two moons of Mars drawn to scale 11
4. Table of opposition dates of Mars 12
5. Table of exceptionally close Mars approaches 12
6. Oppositions of Mars from 1877 to 1988 13
7. Apparent angular sizes of disk of Mars at oppositions from 1965 to 1980 13
8. Mars ephemeris for physical observations, January 1 to April 2, 1968 14
9. Mars ephemeris for physical observations, October 1, 1968, to January 1, 1969 15
10. Calendar of Earth-Mars equivalent dates for 1963 16
11. Calendar of Earth-Mars equivalent dates for 1964 and 1965 17
12. Calendar of Earth-Mars equivalent dates for 1966 and 1967 18
13. Calendar of Earth-Mars equivalent dates for 1968 and 1969 19
14. Calendar of Earth-Mars equivalent dates for 1970 and 1971 20
15. Calendar of Earth-Mars equivalent dates for 1972 and 1973 21
16. Calendar of Earth-Mars equivalent dates for 1974 and 1975 22
17. Calendar of Earth-Mars equivalent dates for 1976 and 1977 23
18. Calendar of Earth-Mars equivalent dates for 1978 and 1979 24
19. Calendar of Earth-Mars equivalent dates for 1980 and 1981 25
20. Calendar of Earth-Mars equivalent dates for 1982 and 1983 26

1. ORBITAL AND PHYSICAL DATA

ORBITAL DATA SUMMARY (Figs. 1 through 9)

Mars[1*]

Orbital Values

Mean elements of planetary orbit (Figs. 1 and 2):	March 16.0 E.T. J.D. 2439200.5 1966	April 20.0 E.T. J.D. 2439600.5 1967
Mean distance from Sun, a (semi-major orbital axis)	1.523691 A.U.[†]	1.523691 A.U.
Eccentricity, e	0.093374	0.093375
Inclination, i	1°.84989 var.=0	1°.84989 var.=0 (1°51')
Mean longitude of ascending node, Ω	49°.29686	49°.30530
100-day variation	0°.00211	0°.00211
Mean longitude of perihelion, ω	335°.43689	335°.45705
100-day variation	0°.00504	0°.00504
Sidereal period, P (revolution)	1.88089 tropical years or 686.9804 mean solar days	
Mean daily motion, n	0°.524033	0°.524033
Mean synodic period		779.94 mean solar days

Distance from Sun:	A.U.	km	mi
Mean (semi-major axis)	1.5236(91)	227,800,000	141,500,000
Perihelion	1.3815	206,500,000	128,300,000
Aphelion	1.6660	249,100,000	154,800,000

(American Ephemeris and Nautical Almanac)

*See page 27 for list of cross references.

†A.U. = Astronomical Unit = 149,597,891 ±6 km = 92.956 × 10^6 mi based on c = 299,792.5 km sec^{-1}, exactly 499.00478 ±0.00002 lt-sec (American Astronomical Society, 1966).

Distance from Earth (Figs. 4 through 7)	A.U.	km	mi
Mean opposition	0.5236	78,350,000	48,695,000
Minimum distance	0.3728	55,810,000	34,670,000
Maximum distance	2.6657	398,900,000	247,900,000

(Americal Ephemeris and Nautical Almanac)

Orbital velocity
($G = 6.668 \pm 0.005 \times 10^{-8}$ cgs;
Mass $\odot = 1.991 \pm 0.002 \times 10^{33}$ g.
Allen, 1963):

	km sec^{-1}	mi sec^{-1}
Mean	24.1	15.0
Perihelion	26.4	16.4
Aphelion	22.0	13.6

Length of Seasons

Northern hemisphere	Southern hemisphere	Martian seasons in Mars days	Terrestrial seasons in Earth days
Spring	Fall	194.2	92.9
Summer	Winter	176.8	93.6
Fall	Spring	141.8	89.7
Winter	Summer	155.8	89.1
		668.6	365.3

(Richardson and Bonestell, 1964)

Ephemeris Data (Figs. 8 and 9)

Ephemeris data symbols are defined as follows:

A_E Angular distance in the plane of the planetary equator from the ascending node of the orbit of the planet on its equator eastward to the great circle through the Earth and the celestial pole of the planet (planetocentric right ascension of the Earth).

D_E Planetocentric angular distance of the Earth from the equator of the planet (planetocentric declination of the Earth).

A_S-A_E Planetocentric right ascension of Sun minus planetocentric right ascension of Earth (phase angle measured along celestial equator; similar to true phase angle).

(American Ephemeris and Nautical Almanac)

D_S Planetocentric declination of the Sun.

L_S Planetocentric longitude of the Sun.

k Fraction of the disk illuminated.

i Inclination of orbit to ecliptic.

(American Ephemeris and Nautical Almanac)

Satellites* (Figs. 1 and 3)

Distance from center of Mars:	Phobos	Deimos
Mars radius = 1	2.743	6.891
Kilometers	9365	23,525
Miles	5820	14,615
Period:		
Sidereal	$0^d.31891$ or $7^h39^m13^s.85$	$1^d.26244$ or $1^d6^h17^m54^s.87$
Synodic	$0^d.319$	$1^d.265$
Inclination of orbit to equator of Mars	0°57'	1°18'
Orbital eccentricity	0.0210	0.0028
Rate of regression of nodes	158°.0 yr^{-1}	6°.374 yr^{-1}

(American Ephemeris and Nautical Almanac, Explanatory Supplement)

*Phobos and Deimos were discovered in 1877 by Asaph Hall.

PHYSICAL DATA SUMMARY

Mars[2]	Earth = 1 (Allen, 1963)	
Flattening:		
Dynamical	—	0.00525
Optical	—	0.012
Radius:		
Equatorial	0.5320	3393.4 km (±4.0) (Cain, 1967)
Polar (equatorial radius and dynamical flattening)	0.5310	3375.6 km
Area (calculated from radii)	0.283	1.4418×10^{8} km^2
Volume (calculated from radii)	0.150	1.6282×10^{11} km^3
Mass ($G = 6.668 \times 10^{-8}$ cgs)	0.1074	6.423×10^{26} g
Density (calculated from mass and volume)	0.715	3.945 g cm^{-3}
GM (gravitational constant × mass of Mars)	0.1074	4.28295×10^{4} (±0.00008) km^3 sec^{-2} (Cain, 1967)
Surface gravity at equator (calculated from Clairaut's equation and data of this section)	0.379	371 cm sec^{-2}
Velocity of escape at equator	0.449	5.024 km sec^{-1}

Inclination of equator to orbit (Fig. 1)	24°.936	(de Vaucouleurs, 1964b)
Position of north pole at beginning of year t	$\alpha_0 = 316°.55 + 0°.00675\ (t - 1905.0)$ $\delta_0 = 52°.85 + 0°.00346\ (t - 1905.0)$	(de Vaucouleurs, 1964b)

Magnitude at mean opposition	-2.01		(Harris, 1961)
Visual albedo (Bond)	0.159		
Mean color values	Color	Magnitudes	
	U-B	0.58	
	B-V	1.36 (therefore appears red)	
	V-R	1.12	
	R-I	0.38	
			(Harris, 1961)
Sidereal day (rotation)	$24^h39^m22^s.6689$		
Daily motion (rotation)	350°.891962		(1967 Ephemeris)
Mean solar day	$24^h39^m35^s$		
Zero point of longitudes	344°.41 on JD 2418322.0 = 1909 Jan 15.5 UT		
			(de Vaucouleurs, 1964a, 1964c)

Satellites

	Phobos	Deimos	
Apparent visual magnitude at mean opposition distance	11.6	12.8	(Harris, 1961)
Estimated diameter			
Kilometers	19	10	(Richardson and Bonestell, 1964)
Miles	12	6	
Color (magnitude), B-V	0.6	0.6 (therefore appears greenish)	
			(Harris, 1961)

EARTH-MARS CALENDAR (Figs. 10 through 20)

A Martian calendar is desirable to establish an equivalence of Earth and Mars dates and to simplify the presentation and interpretation of secular and seasonal changes on Mars.[3] Accordingly, the accompanying calendar was developed for use in appropriate sections of this document.

Equivalences

The basic units of time for a Mars calendar are the Mars tropical year and the Mars mean solar day. The variability of the length of Martian seasons, resulting from the eccentricity of the orbit, limits the usefulness of a seasonal calendar. However, seasons, referred to the northern hemisphere, have been included in the calendar as rough approximations beginning on the days listed below; no attempt has been made to define "months."

1) One mean Mars day = 1.02749133 mean Earth solar days.

2) One Mars tropical year = 668.592159 Mars solar days.

3) Mars spring begins on day 167.1.

4) Mars summer begins on day 361.3.

5) Mars fall begins on day 538.1.

6) Mars winter begins on day 11.3.

Basis of Zero Points

We have adopted the year 1000 as the year of the Mariner IV flyby. The start of this year has been defined such that the time of year was approximately 0.25 when Mars passed its vernal equinox prior to the Mariner IV flyby in July of 1965. This equinox occurred on September 12, 1964, Earth time. This day has therefore been designated as day number 167 of the Martian year 1000.

The start of each day on Mars is defined to be at midnight at 0° longitude; i.e., each day starts when the subsolar longitude is 180°.

Mars Leap Years

A Mars leap year is defined as follows:

1) If year is odd, it is a leap year (669 Mars solar days).

2) If year is even, it is not a leap year, except

   a) if year is divisible by 10, it is a leap year, except

   b) if year is divisible by 100, it is not a leap year, except

   c) if year is divisible by 500, it is a leap year.

At the conclusion of a Martian 500-year cycle, the cumulative error between the calendar date and the astronomical date based on the tropical year amounts to 0.08 Mars solar day (about two hours). This is slightly better than the present Earth calendar.

In the calendar, the column labeled 'Consecutive Mars day' gives a day number for Mars similar to the Julian day number for Earth. Consecutive Mars day number 1 was the first day of the Martian year 0 (which was a leap year). The calendar also contains a column of heliocentric ecliptic longitude equivalents for each day. Earth-Mars data for 1963 through 1983 are presented at this time. Further comments on the calendar are given on page 16.

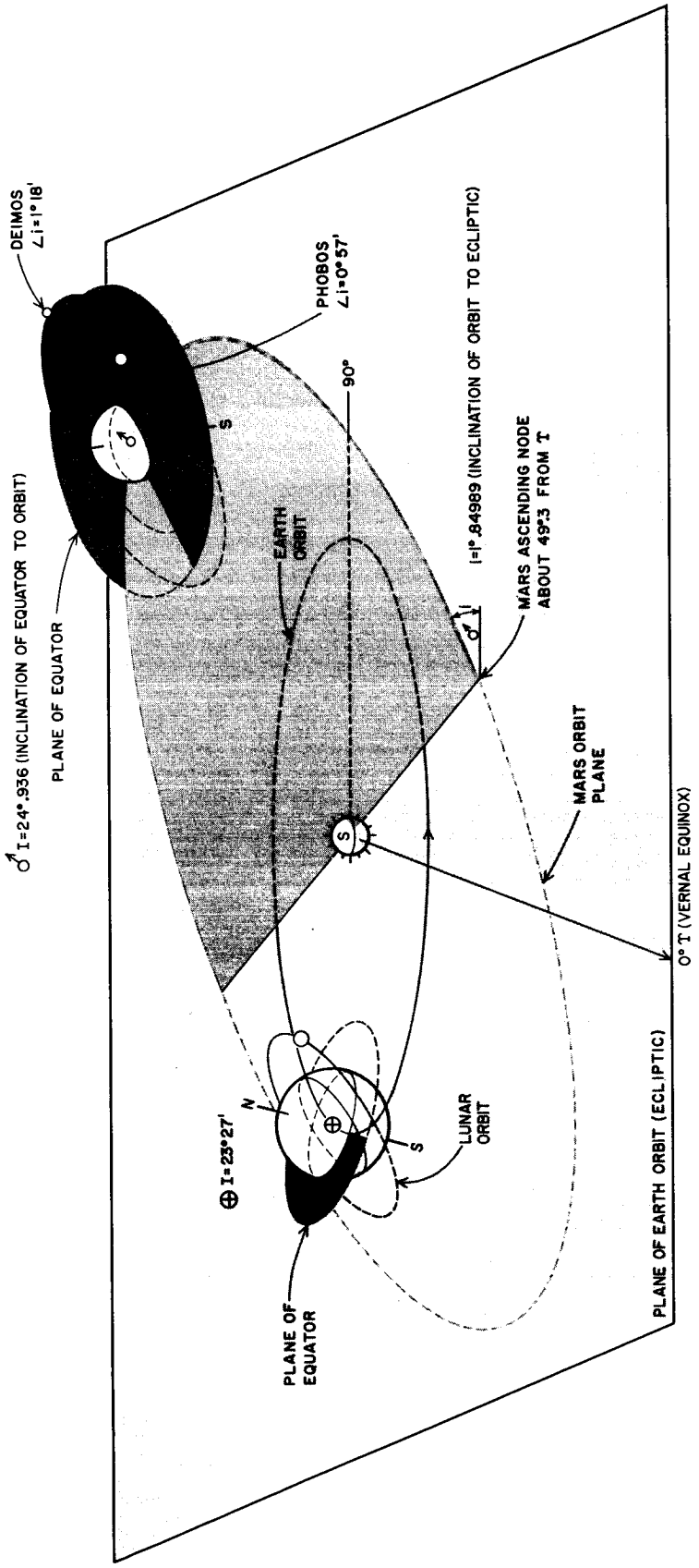

Fig. 1. Earth orbit plane cut by Earth equatorial plane, Mars equatorial plane, Phobos orbit plane, and Deimos orbit plane. Angular relationships are exaggerated. At perihelic opposition the south pole of Mars is tilted toward Earth; at aphelic opposition the north pole is tilted toward Earth. (de Wys, 1967)

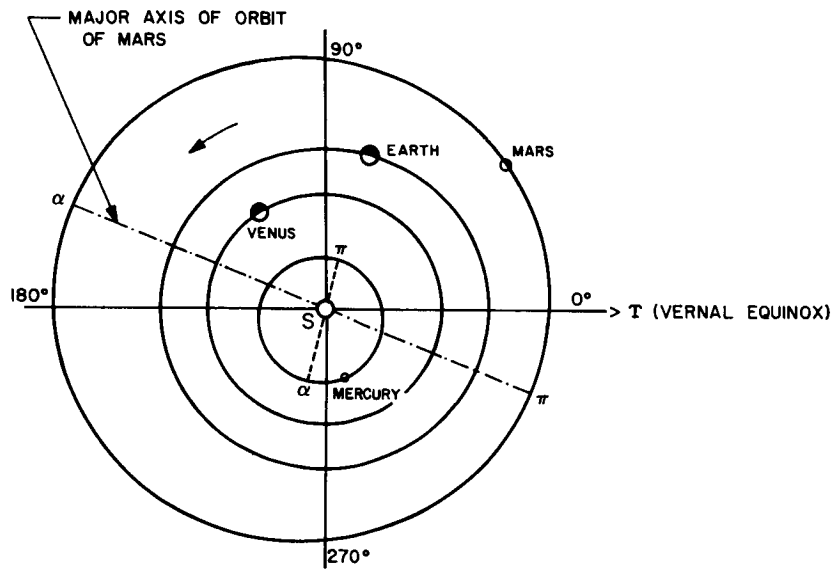

Fig. 2. Orbits of the inner planets of the solar system drawn to scale. Orbits of Venus and Earth are very nearly circular; orbits of Mercury and Mars show pronounced eccentricity. Perihelion points of Mercury and Mars are indicated by π, aphelion points by α. (Ley, Von Braun, and Bonestell, 1960)

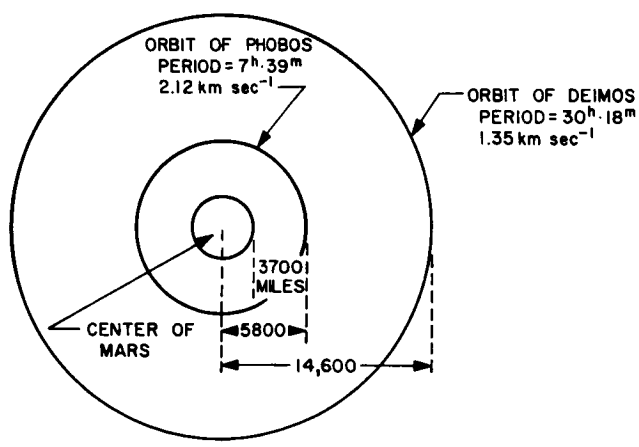

Fig. 3. Orbits of the two moons of Mars drawn to scale. (after Ley, Von Braun, and Bonestell, 1960)

Date of opposition	Interval, days	Distance from Earth[a]	
		Million miles	Million kilometers
1937 May 19		47.3	76.1
	795		
1939 Jul 23		36.1	58.0
	810		
1941 Oct 10		38.2	61.4
	786		
1943 Dec 5		50.1	80.7
	771		
1946 Jan 14		60.4	95.6
	764		
1948 Feb 17		63.0	101.4
	765		
1950 Mar 23		60.4	97.2
	770		
1952 May 1		51.9	83.5
	784		
1954 Jun 24		39.8	64.1
	806		
1956 Sep 11		35.2	56.6
	800		
1958 Nov 17		45.4	73.0
	775		
1960 Dec 30		56.3	90.6
	776		
1963 Feb 4		62.2	100.1
	763		
1965 Mar 9		62.0	99.8
	767		
1967 Apr 15		55.8	89.8
	777		
1969 May 31		44.5	71.7
	781		
1971 Aug 10		34.9	56.2
	807		
1973 Oct 25		40.4	65.0
	791		
1975 Dec 15		52.4	84.3
	771		
1978 Jan 22		60.8	97.8
	764		
1980 Feb 25		63.2	101.7

[a]At closest approach, which may be as much as 10 days before or after opposition.

Fig. 4. Table of opposition dates of Mars. (data from Slipher, 1962; American Ephemeris and Nautical Almanac, 1937-1969; Miner, 1967)

Date of opposition	Interval, years	Distance from Earth[a]	
		Million miles	Million kilometers
1877 Sep 5		34.8	56.0
	15.0		
1892 Aug 26		34.5	55.5
	17.1		
1909 Sep 18		36.2	58.3
	14.9		
1924 Aug 22		34.5	55.5
	14.9		
1939 Jul 23		36.1	58.0
	17.2		
1956 Sep 11		35.2	56.6
	14.9		
1971 Aug 10		34.9	56.2
	17.2		
1988 Sep 28		36.3	58.4

[a]At closest approach, which may be as much as 10 days before or after opposition.

Fig. 5. Table of exceptionally close Mars approaches.

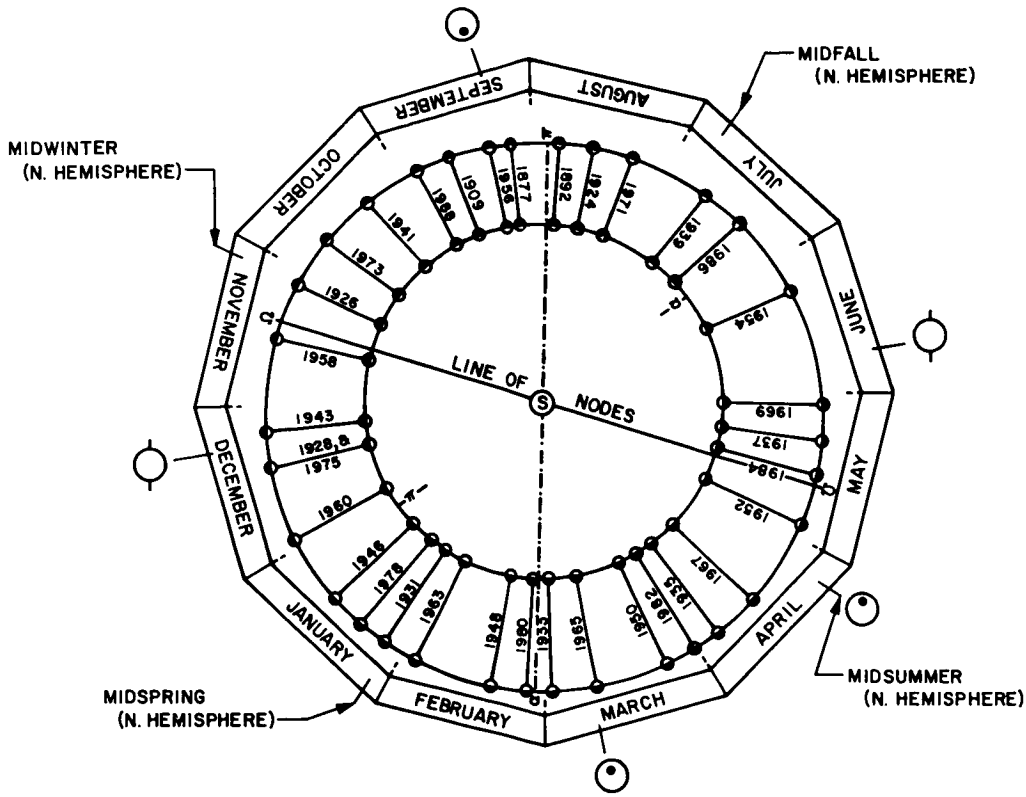

Fig. 6. Oppositions of Mars from 1877 to 1988. Surrounding calendar indicates time of occurrence. Broken line is major axis of Mars orbit connecting aphelion and perihelion. Aphelion and perihelion of Earth are indicated on Earth orbit. (after Ley, Von Braun, and Bonestell, 1960)

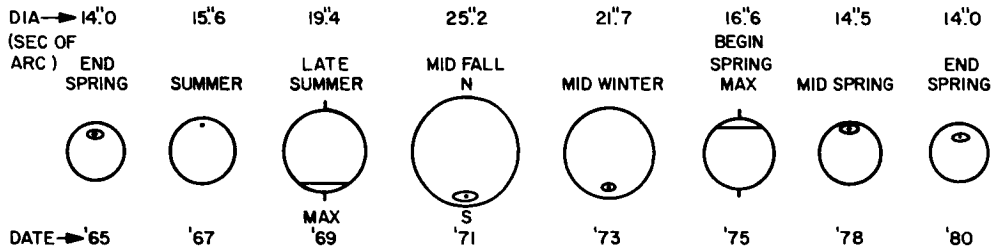

Fig. 7. Apparent angular sizes of disk of Mars at oppositions from 1965 to 1980. Seasons indicated are for northern hemisphere. North and south poles and approximate extent of polar caps are indicated. (Miner, de Wys, 1967)

Date	Light-time, m	Star magnitude	Diameter, sec	A_E+180°, deg	D_E, deg	A_S-A_E, deg	D_S, deg	L_S, deg	k	i, deg	Defect of illumination, sec	Position angle: Of defect, deg	Position angle: Of axis, deg	Central meridian: Of date, deg	Central meridian: Of following date, deg	Universal time of transit of zero meridian: Of date, hr min	Universal time of transit of zero meridian: Of following date, hr min
Jan. 1	15.95	+1.3	4.88	56.12	-21.71	+31.90	-24.75	268.21	0.936	29.41	0.31	71.86	354.07	152.57	142.63	14 13.3	14 54.1
3	16.03	1.3	4.86	57.76	22.08	31.65	24.76	269.46	.937	29.11	0.31	71.51	353.09	132.70	122.76	15 35.0	16 15.9
5	16.11	1.3	4.83	59.40	22.44	31.40	24.76	270.72	.938	28.80	0.30	71.17	352.10	112.82	102.88	16 56.8	17 37.7
7	16.19	1.3	4.81	61.05	22.77	31.13	24.75	271.98	.939	28.50	0.29	70.85	351.12	92.94	82.99	18 18.6	18 59.5
9	16.28	1.3	4.78	62.70	23.10	30.85	24.72	273.23	.941	28.19	0.28	70.54	350.14	73.04	63.09	19 40.5	20 21.4
11	16.36	+1.3	4.76	64.37	-23.40	+30.57	-24.68	274.48	0.942	27.89	0.28	70.25	349.17	53.14	43.19	21 02.3	21 43.3
13	16.44	1.3	4.73	66.04	23.69	30.27	24.63	275.74	.943	27.58	0.27	69.97	348.20	33.23	23.27	22 24.3	23 05.2
15	16.52	1.3	4.71	67.72	23.95	29.96	24.57	276.98	.944	27.27	0.26	69.71	347.24	13.32	3.36	23 46.2	.. .. .
17	16.61	1.3	4.69	69.40	24.20	29.65	24.49	278.23	.946	26.96	0.25	69.46	346.29	353.40	343.43	0 27.2	1 08.1
19	16.69	1.3	4.66	71.09	24.43	29.32	24.40	279.47	.947	26.65	0.25	69.22	345.34	333.47	323.51	1 49.1	2 30.1
21	16.77	+1.3	4.64	72.79	-24.64	+28.98	-24.30	280.72	0.948	26.33	0.24	69.00	344.40	313.54	303.57	3 11.1	3 52.1
23	16.85	1.4	4.62	74.49	24.83	28.64	24.19	281.96	.949	26.02	0.23	68.79	343.47	293.61	283.64	4 33.1	5 14.2
25	16.94	1.4	4.60	76.19	25.00	28.29	24.07	283.19	.951	25.70	0.23	68.60	342.55	273.67	263.69	5 55.2	6 36.2
27	17.02	1.4	4.57	77.90	25.15	27.92	23.93	284.43	.952	25.38	0.22	68.43	341.64	253.72	243.75	7 17.2	7 58.2
29	17.10	1.4	4.55	79.61	25.28	27.55	23.79	285.66	.953	25.06	0.21	68.26	340.74	233.78	223.80	8 39.3	9 20.3
31	17.18	+1.4	4.53	81.32	-25.39	+27.17	-23.63	286.89	0.954	24.74	0.21	68.12	339.85	213.83	203.86	10 01.3	10 42.4
Feb. 2	17.26	1.4	4.51	83.03	25.47	26.79	23.46	288.12	.955	24.42	0.20	67.98	338.98	193.88	183.91	11 23.4	12 04.4
4	17.34	1.4	4.49	84.74	25.54	26.39	23.28	289.34	.956	24.10	0.20	67.86	338.12	173.93	163.96	12 45.5	13 26.5
6	17.43	1.4	4.47	86.45	25.59	25.99	23.09	290.57	.958	23.78	0.19	67.76	337.27	153.99	144.01	14 07.5	14 48.6
8	17.51	1.4	4.45	88.17	25.62	25.59	22.89	291.78	.959	23.45	0.18	67.67	336.44	134.04	124.07	15 29.6	16 10.6
10	17.59	+1.4	4.43	89.87	-25.63	+25.18	-22.68	293.00	0.960	23.12	0.18	67.59	335.63	114.09	104.12	16 51.6	17 32.7
12	17.67	1.4	4.41	91.58	25.61	24.76	22.46	294.21	.961	22.80	0.17	67.53	334.83	94.15	84.18	18 13.7	18 54.7
14	17.75	1.4	4.39	93.28	25.58	24.34	22.23	295.42	.962	22.47	0.17	67.48	334.05	74.21	64.24	19 35.7	20 16.7
16	17.83	1.4	4.37	94.98	25.53	23.92	21.99	296.63	.963	22.14	0.16	67.45	333.28	54.28	44.31	20 57.7	21 38.7
18	17.91	1.5	4.35	96.68	25.45	23.49	21.74	297.83	.964	21.81	0.16	67.43	332.54	34.35	24.38	22 19.7	23 00.7
20	17.99	+1.5	4.33	98.37	-25.36	+23.06	-21.48	299.03	0.965	21.48	0.15	67.42	331.82	14.42	4.46	23 41.7	.. .. .
22	18.07	1.5	4.31	100.06	25.25	22.63	21.22	300.23	.966	21.15	0.15	67.43	331.11	354.50	344.54	0 22.6	1 03.6
24	18.15	1.5	4.29	101.74	25.12	22.20	20.94	301.42	.967	20.82	0.14	67.45	330.43	334.58	324.63	1 44.6	2 25.5
26	18.23	1.5	4.27	103.41	24.97	21.76	20.66	302.61	.968	20.49	0.14	67.48	329.77	314.68	304.72	3 06.5	3 47.4
28	18.31	1.5	4.25	105.07	24.80	21.32	20.37	303.80	.969	20.15	0.13	67.53	329.13	294.77	284.83	4 28.3	5 09.2
Mar. 1	18.39	+1.5	4.23	106.73	-24.61	+20.88	-20.07	304.98	0.970	19.82	0.13	67.59	328.52	274.88	264.94	5 50.1	6 31.0
3	18.47	1.5	4.22	108.38	24.41	20.45	19.77	306.16	.971	19.48	0.12	67.66	327.93	255.00	245.06	7 11.9	7 52.8
5	18.55	1.5	4.20	110.02	24.18	20.01	19.45	307.34	.972	19.14	0.12	67.75	327.36	235.12	225.18	8 33.7	9 14.6
7	18.62	1.5	4.18	111.66	23.94	19.57	19.13	308.51	.973	18.81	0.11	67.85	326.81	215.25	205.32	9 55.4	10 36.3
9	18.70	1.5	4.16	113.28	23.69	19.13	18.81	309.68	.974	18.47	0.11	67.96	326.30	195.39	185.47	11 17.1	11 57.9
11	18.78	+1.5	4.15	114.89	-23.41	+18.70	-18.47	310.84	0.975	18.13	0.10	68.08	325.80	175.55	165.63	12 38.7	13 19.5
13	18.85	1.5	4.13	116.49	23.12	18.27	18.13	312.00	.976	17.79	0.10	68.22	325.33	155.71	145.79	14 00.3	14 41.1
15	18.93	1.5	4.11	118.09	22.82	17.84	17.79	313.16	.977	17.45	0.09	68.37	324.89	135.88	125.97	15 21.8	16 02.6
17	19.00	1.5	4.10	119.67	22.50	17.41	17.44	314.32	.978	17.11	0.09	68.53	324.48	116.07	106.16	16 43.3	17 24.1
19	19.08	1.6	4.08	121.24	22.16	16.98	17.08	315.47	.979	16.77	0.09	68.70	324.09	96.26	86.36	18 04.8	18 45.5
21	19.15	+1.6	4.06	122.80	-21.81	+16.56	-16.72	316.61	0.980	16.43	0.08	68.89	323.73	76.47	66.57	19 26.2	20 06.9
23	19.22	1.6	4.05	124.35	21.45	16.14	16.36	317.76	.980	16.08	0.08	69.08	323.39	56.68	46.80	20 47.5	21 28.2
25	19.30	1.6	4.03	125.89	21.07	15.72	15.98	318.90	.981	15.74	0.08	69.29	323.08	36.91	27.03	22 08.8	22 49.5
27	19.37	1.6	4.02	127.41	20.68	15.31	15.61	320.03	.982	15.39	0.07	69.51	322.80	17.15	7.28	23 30.1	.. .. .
29	19.44	1.6	4.00	128.93	20.28	14.90	15.23	321.16	.983	15.05	0.07	69.73	322.55	357.40	347.53	0 10.7	0 51.3
31	19.51	+1.6	3.99	130.43	-19.86	+14.49	-14.84	322.29	0.984	14.70	0.07	69.97	322.32	337.66	327.80	1 31.9	2 12.4
Apr. 2	19.58	+1.6	3.98	131.93	-19.43	+14.09	-14.46	323.41	.984	14.36	0.06	70.22	322.13	317.94	308.08	2 53.0	3 33.5

Fig. 8. Mars ephemeris for physical observations, January 1 to April 2, 1968. For 0^h Universal Time. See page 4 for definitions of symbols. (The American Ephemeris and Nautical Almanac)

Date	Light-time, deg	Star magnitude	Diameter, sec	A_E+180°, deg	D_E, deg	A_S-A_E, deg	D_S, deg	L_S, deg	k	i, deg	Defect of illumination, sec	Position angle: Of defect, deg	Position angle: Of axis, deg	Central meridian: Of date, deg	Central meridian: Of following date, deg	Universal time of transit of zero meridian: Of date, hr min	Universal time of transit of zero meridian: Of following date, hr min
Oct. 1	20.11	+2.0	3.87	249.30	+23.85	-19.58	+19.39	52.41	0.974	18.73	0.10	293.68	13.67	342.78	333.00	1 10.8	1 51.0
3	20.02	2.0	3.89	250.65	24.01	20.04	19.62	53.29	.972	19.10	0.11	293.82	14.43	323.23	313.45	2 31.2	3 11.4
5	19.94	2.0	3.90	252.01	24.16	20.49	19.85	54.18	.971	19.46	0.11	293.95	15.19	303.68	293.90	3 51.6	4 31.8
7	19.85	2.0	3.92	253.36	24.30	20.94	20.08	55.06	.970	19.83	0.12	294.07	15.93	284.12	274.35	5 12.0	5 52.2
9	19.76	2.0	3.94	254.72	24.42	21.40	20.30	55.94	.969	20.19	0.12	294.18	16.68	264.57	254.79	6 32.4	7 12.6
11	19.67	+2.0	3.96	256.08	+24.53	-21.85	+20.52	56.81	0.968	20.55	0.13	294.29	17.41	245.02	235.24	7 52.8	8 33.0
13	19.58	2.0	3.98	257.44	24.63	22.30	20.73	57.69	.967	20.92	0.13	294.38	18.14	225.46	215.69	9 13.2	9 53.4
15	19.48	2.0	4.00	258.80	24.71	22.75	20.94	58.57	.966	21.28	0.14	294.46	18.86	205.91	196.13	10 33.6	11 13.8
17	19.39	2.0	4.02	260.17	24.78	23.19	21.14	59.45	.965	21.64	0.14	294.54	19.57	186.36	176.58	11 54.0	12 34.2
19	19.29	2.0	4.04	261.53	24.84	23.64	21.34	60.32	.964	22.00	0.15	294.60	20.27	166.80	157.03	13 14.4	13 54.6
21	19.19	+2.0	4.06	262.89	+24.89	-24.08	+21.53	61.20	0.962	22.36	0.15	294.66	20.97	147.25	137.48	14 34.7	15 14.9
23	19.08	1.9	4.08	264.24	24.92	24.52	21.72	62.07	.961	22.71	0.16	294.71	21.65	127.70	117.93	15 55.1	16 35.3
25	18.98	1.9	4.10	265.60	24.94	24.96	21.90	62.95	.960	23.07	0.16	294.74	22.33	108.15	98.38	17 15.5	17 55.7
27	18.87	1.9	4.13	266.96	24.95	25.39	22.08	63.82	.959	23.42	0.17	294.77	22.99	88.61	78.84	18 35.9	19 16.0
29	18.76	1.9	4.15	268.31	24.95	25.82	22.25	64.70	.958	23.78	0.18	294.79	23.65	69.07	59.29	19 56.2	20 36.4
31	18.65	+1.9	4.17	269.66	+24.93	-26.24	+22.42	65.57	0.956	24.13	0.18	294.80	24.29	49.53	39.76	21 16.5	21 56.7
Nov. 2	18.53	1.9	4.20	271.01	24.90	26.66	22.58	66.44	.955	24.48	0.19	294.80	24.92	29.99	20.22	22 36.9	23 17.0
4	18.42	1.9	4.23	272.36	24.86	27.08	22.73	67.32	.954	24.83	0.20	294.80	25.54	10.45	0.69	23 57.2	.... .
6	18.30	1.9	4.25	273.70	24.80	27.49	22.88	68.19	.953	25.17	0.20	294.78	26.15	350.92	341.16	0 37.3	1 17.5
8	18.18	1.9	4.28	275.04	24.73	27.89	23.03	69.06	.951	25.52	0.21	294.75	26.75	331.40	321.63	1 57.6	2 37.7
10	18.06	+1.9	4.31	276.38	+24.65	-28.29	+23.17	69.94	0.950	25.86	0.22	294.72	27.33	311.87	302.11	3 17.9	3 58.0
12	17.94	1.9	4.34	277.71	24.56	28.68	23.30	70.81	.949	26.20	0.22	294.67	27.90	292.35	282.60	4 38.1	5 18.2
14	17.81	1.8	4.37	279.04	24.46	29.07	23.43	71.68	.947	26.54	0.23	294.62	28.46	272.84	263.09	5 58.3	6 38.5
16	17.69	1.8	4.40	280.36	24.34	29.45	23.55	72.55	.946	26.88	0.24	294.56	29.01	253.33	243.58	7 18.6	7 58.6
18	17.56	1.8	4.43	281.68	24.21	29.83	23.67	73.43	.945	27.22	0.25	294.48	29.54	233.83	224.08	8 38.7	9 18.8
20	17.43	+1.8	4.47	282.99	+24.07	-30.19	+23.78	74.30	0.943	27.55	0.25	294.40	30.05	214.33	204.59	9 58.9	10 39.0
22	17.29	1.8	4.50	284.30	23.92	30.55	23.89	75.17	.942	27.88	0.26	294.32	30.55	194.84	185.10	11 19.0	11 59.1
24	17.16	1.8	4.54	285.60	23.76	30.91	23.99	76.05	.941	28.21	0.27	294.22	31.04	175.35	165.61	12 39.1	13 19.2
26	17.03	1.8	4.57	286.90	23.59	31.25	24.08	76.92	.939	28.53	0.28	294.11	31.51	155.88	146.14	13 59.2	14 39.2
28	16.89	1.8	4.61	288.19	23.41	31.59	24.17	77.79	.938	28.85	0.29	294.00	31.97	136.40	126.67	15 19.2	15 59.2
30	16.75	+1.8	4.65	289.47	+23.21	-31.92	+24.25	78.67	0.937	29.17	0.29	293.87	32.41	116.94	107.21	16 39.2	17 19.2
Dec. 2	16.61	1.7	4.69	290.75	23.01	32.23	24.32	79.54	.935	29.49	0.30	293.74	32.84	97.48	87.76	17 59.2	18 39.2
4	16.46	1.7	4.73	292.01	22.80	32.55	24.39	80.42	.934	29.80	0.31	293.60	33.25	78.03	68.31	19 19.2	19 59.1
6	16.32	1.7	4.77	293.28	22.57	32.85	24.46	81.29	.933	30.11	0.32	293.45	33.64	58.59	48.87	20 39.1	21 19.0
8	16.18	1.7	4.81	294.53	22.34	33.14	24.52	82.17	.931	30.42	0.33	293.29	34.02	39.15	29.44	21 59.0	22 38.9
10	16.03	+1.7	4.86	295.78	+22.10	-33.43	+24.57	83.05	0.930	30.72	0.34	293.13	34.38	19.73	10.02	23 18.8	23 58.7
12	15.88	1.7	4.90	297.02	21.84	33.70	24.61	83.92	.928	31.02	0.35	292.95	34.73	0.31	350.60	.... .	0 38.6
14	15.73	1.6	4.95	298.25	21.58	33.97	24.65	84.80	.927	31.32	0.36	292.77	35.06	340.90	331.19	1 18.5	1 58.4
16	15.58	1.6	5.00	299.47	21.31	34.23	24.69	85.68	.926	31.61	0.37	292.58	35.37	321.49	311.79	2 38.3	3 18.2
18	15.43	1.6	5.04	300.69	21.04	34.48	24.72	86.56	.925	31.90	0.38	292.38	35.67	302.10	292.40	3 58.0	4 37.9
20	15.28	+1.6	5.10	301.90	+20.75	-34.71	+24.74	87.44	0.923	32.18	0.39	292.18	35.95	282.71	273.02	5 17.7	5 57.5
22	15.12	1.6	5.15	303.09	20.46	34.94	24.75	88.32	.922	32.46	0.40	291.97	36.22	263.34	253.65	6 37.3	7 17.2
24	14.97	1.6	5.20	304.28	20.16	35.16	24.76	89.20	.921	32.73	0.41	291.74	36.46	243.97	234.29	7 57.0	8 36.7
26	14.81	1.5	5.26	305.46	19.85	35.37	24.76	90.08	.919	33.00	0.42	291.52	36.69	224.61	214.93	9 16.5	9 56.3
28	14.65	1.5	5.31	306.64	19.53	35.57	24.76	90.97	.918	33.26	0.44	291.28	36.91	205.26	195.59	10 36.0	11 15.8
30	14.49	+1.5	5.37	307.80	+19.21	-35.76	+24.75	91.85	0.917	33.52	0.45	291.04	37.10	185.92	176.26	11 55.5	12 35.3
32	14.33	1.5	5.43	308.95	+18.88	35.94	24.73	92.74	.916	33.77	0.46	290.79	37.29	166.59	156.93	13 15.0	13 54.7

Fig. 9. Mars ephemeris for physical observations, October 1, 1968, to January 1, 1969. For 0^h Universal Time. See page 4 for definitions of symbols. (The American Ephemeris and Nautical Almanac)

Comments on Earth-Mars Calendars

The Earth-Mars calendars (Figs. 10 through 20) are explained on page 8. An additional column has been included in each figure to give opposition dates and distances, spacecraft events, and other information which may be of interest. It is hoped that readers concerned with planning for present and future flight projects will find the calendars helpful. The calendars also can be used to correlate Martian seasons with past observations.

Certain observations of Mars which were conducted during the first five years given in the calendars (1963-1967) are discussed in various sections of this document. In general, the reader is referred to Sec. 3.2 for a discussion of polarimetric and reflectivity studies and to Sec. 3.3 for details of radar measurements. Observations undertaken to determine composition of the Martian atmosphere are given in Sec. 5.1. Seasonal activity maps and data—the results of many years of visual observations—appear in Sec. 4.2.

EARTH			MARS				NOTES
J.D. Julian day	Northern hemisphere season and date	Year	Year	Northern hemisphere season and year day	Consecutive Mars day	Heliocentric ecliptic longitude, deg	
	WINTER	1963	999 (leap year)	SPRING			
2438030.5	Jan 1			232.670	668155.66	119.52	
2438040.5	Jan 11			242.403	668165.40	124.04	
2438050.5	Jan 21			252.135	668175.13	128.52	
2438060.5	Jan 31			261.868	668184.87	132.97	
2438070.5	Feb 10			271.600	668194.59	137.39	FEB 4. APHELIC OPPOSITION
2438080.5	Feb 20			281.333	668204.33	141.79	Earth-Mars distance at closest approach:
2438090.5	Mar 2			291.065	668214.06	146.18	62.2 million mi (100.1 million km).
2438100.5	Mar 12			300.798	668223.80	150.55	Earth days until next opposition: 763.
	SPRING						
2438110.5	Mar 22			310.530	668233.52	154.92	
2438120.5	Apr 1			320.262	668243.26	159.29	
2438130.5	Apr 11			329.995	668252.99	163.66	
2438140.5	Apr 21			339.727	668262.73	168.04	
2438150.5	May 1			349.460	668272.45	172.44	
2438160.5	May 11			359.192	668282.19	176.85	
				SUMMER			
2438170.5	May 21			368.925	668291.92	181.30	
2438180.5	May 31			378.657	668301.66	185.77	
2438190.5	Jun 10			388.390	668311.38	190.27	
2438200.5	Jun 20			398.122	668321.12	194.82	
	SUMMER						
2438210.5	Jun 30			407.854	668330.85	199.42	
2438220.5	Jul 10			417.587	668340.59	204.06	
2438230.5	Jul 20			427.319	668350.31	208.77	
2438240.5	Jul 30			437.052	668360.05	213.53	
2438250.5	Aug 9			446.784	668369.78	218.36	
2438260.5	Aug 19			456.517	668379.52	223.27	
2438270.5	Aug 29			466.249	668389.24	228.25	
2438280.5	Sep 8			475.981	668398.98	233.31	
2438290.5	Sep 18			485.714	668408.71	238.45	
	FALL						
2438300.5	Sep 28			495.446	668418.45	243.69	
2438310.5	Oct 8			505.179	668428.17	249.01	
2438320.5	Oct 18			514.911	668437.91	254.43	
2438330.5	Oct 28			524.644	668447.64	259.94	
2438340.5	Nov 7			534.376	668457.38	265.55	
				FALL			
2438350.5	Nov 17			544.109	668467.10	271.25	Oct 3-Dec 31. Mars not clearly visible from Earth for physical observations.
2438360.5	Nov 27			553.841	668476.84	277.05	
2438370.5	Dec 7			563.573	668486.57	282.94	
2438380.5	Dec 17			573.306	668496.30	288.91	
	WINTER						
2438390.5	Dec 27			583.038	668506.03	294.97	

Fig. 10. Calendar of Earth-Mars equivalent dates for 1963. Earth dates are for 0^h GMT; Mars dates show day of year and fraction of day elapsed at 0° longitude on Mars.

EARTH			MARS				NOTES
J.D. Julian day	Northern hemisphere season and date	Year	Year	Northern hemisphere season and year day	Consecutive Mars day	Heliocentric ecliptic longitude, deg	
	WINTER	1964	999	FALL			
2438400.5	Jan 6	(leap		592.771	668515.77	301.10	
2438410.5	Jan 16	year)		602.503	668525.50	307.29	
2438420.5	Jan 26			612.236	668535.23	313.54	
2438430.5	Feb 5			621.968	668544.96	319.83	
2438440.5	Feb 15			631.701	668554.70	326.15	
2438450.5	Feb 25			641.433	668564.43	332.50	
2438460.5	Mar 6			651.165	668574.16	338.85	
2438470.5	Mar 16			660.898	668583.89	345.19	
	SPRING						
2438480.5	Mar 26		1000 (leap year)	1.630	668593.63	351.51	Jan 1-Jul 1. Mars not clearly visible from Earth for physical observations.
				WINTER			
2438490.5	Apr 5			11.363	668603.36	357.79	
2438500.5	Apr 15			21.095	668613.09	4.03	
2438510.5	Apr 25			30.828	668622.82	10.22	
2438520.5	May 5			40.560	668632.55	16.34	
2438530.5	May 15			50.293	668642.29	22.38	
2438540.5	May 25			60.025	668652.02	28.35	
2438550.5	Jun 4			69.757	668661.75	34.23	
2438560.5	Jun 14			79.490	668671.48	40.01	
	SUMMER						
2438570.5	Jun 24			89.222	668681.22	45.71	
2438580.5	Jul 4			98.955	668690.95	51.31	
2438590.5	Jul 14			108.687	668700.68	56.81	
2438600.5	Jul 24			118.420	668710.41	62.22	
2438610.5	Aug 3			128.152	668720.15	67.54	
2438620.5	Aug 13			137.885	668729.88	72.77	
2438630.5	Aug 23			147.617	668739.61	77.91	
2438640.5	Sep 2			157.349	668749.34	82.96	
				SPRING			
2438650.5	Sep 12			167.082	668759.08	87.94	Sep 12. Mars d167 y1000 = approx. 0.25 of Mars y1000 = Mars vernal equinox prior to Mariner IV flyby = basis of zero points of this calendar.
2438660.5	Sep 22			176.814	668768.81	92.84	
	FALL						
2438670.5	Oct 2			186.547	668778.54	97.67	
2438680.5	Oct 12			196.279	668788.27	102.43	
2438690.5	Oct 22			206.012	668798.01	107.13	
2438700.5	Nov 1			215.744	668807.74	111.77	Nov 5. Mariner III launched; unsuccessful mission.
2438710.5	Nov 11			225.477	668817.47	116.37	
2438720.5	Nov 21			235.209	668827.20	120.91	Nov 28. Mariner IV launched (Atlas-Agena vehicle).
2438730.5	Dec 1			244.941	668836.94	125.42	Nov 30. Zond 2 launched; unsuccessful mission.
2438740.5	Dec 11			254.674	668846.67	129.89	
	WINTER						
2438750.5	Dec 21			264.406	668856.41	134.33	
2438760.5	Dec 31			274.139	668866.13	138.75	
2438770.5	Jan 10	1965		283.871	668875.87	143.14	
2438780.5	Jan 20			293.604	668885.60	147.52	
2438790.5	Jan 30			303.336	668895.34	151.90	
2438800.5	Feb 9			313.068	668905.06	156.26	
2438810.5	Feb 19			322.801	668914.80	160.63	
2438820.5	Mar 1			332.533	668924.53	165.00	MAR 9. APHELIC OPPOSITION
2438830.5	Mar 11			342.266	668934.27	169.39	Earth-Mars distance at closest approach: 62.0 million mi (99.8 million km). Earth days until next opposition: 767.
	SPRING						
2438840.5	Mar 21			351.998	668943.99	173.79	
				SUMMER			
2438850.5	Mar 31			361.731	668953.73	178.21	
2438860.5	Apr 10			371.463	668963.46	182.66	
2438870.5	Apr 20			381.196	668973.20	187.14	
2438880.5	Apr 30			390.928	668982.92	191.66	
2438890.5	May 10			400.660	668992.66	196.22	
2438900.5	May 20			410.393	669002.39	200.83	
2438910.5	May 30			420.125	669012.13	205.50	
2438920.5	Jun 9			429.858	669021.85	210.22	
2438930.5	Jun 19			439.590	669031.59	215.00	
	SUMMER						
2438940.5	Jun 29			449.323	669041.32	219.86	
2438950.5	Jul 9			459.055	669051.05	224.78	Jul 15. Mariner IV Mars flyby. Television pictures taken above both hemispheres; occultation (ingress) occurred above southern hemisphere.
2438960.5	Jul 19			468.788	669060.78	229.79	
2438970.5	Jul 29			478.520	669070.52	234.87	
2438980.5	Aug 8			488.252	669080.25	240.05	
2438990.5	Aug 18			497.985	669089.98	245.31	
2439000.5	Aug 28			507.717	669099.71	250.66	
2439010.5	Sep 7			517.450	669109.45	256.11	
2439020.5	Sep 17			527.182	669119.18	261.65	
	FALL						
2439030.5	Sep 27			536.915	669128.91	267.29	
				FALL			
2439040.5	Oct 7			546.647	669138.64	273.03	
2439050.5	Oct 17			556.380	669148.38	278.86	
2439060.5	Oct 27			566.112	669158.11	284.77	
2439070.5	Nov 6			575.844	669167.84	290.77	
2439080.5	Nov 16			585.577	669177.57	296.85	
2439090.5	Nov 26			595.309	669187.30	303.00	
2439100.5	Dec 6			605.042	669197.04	309.22	
2439110.5	Dec 16			614.774	669206.77	315.48	
	WINTER						
2439120.5	Dec 26			624.507	669216.50	321.78	

Fig. 11. Calendar of Earth-Mars equivalent dates for 1964 and 1965. Earth dates are for 0^h GMT; Mars dates show day of year and fraction of day elapsed at 0° longitude on Mars.

EARTH			MARS				NOTES
J.D. Julian day	Northern hemisphere season and date	Year	Year	Northern hemisphere season and year day	Consecutive Mars day	Heliocentric ecliptic longitude, deg	
	WINTER	1966	1000 (leap year)	FALL			
2439130.5	Jan 5			634.239	669226.23	328.12	
2439140.5	Jan 15			643.972	669235.97	334.46	
2439150.5	Jan 25			653.704	669245.70	340.81	
2439160.5	Feb 4			663.436	669255.43	347.15	
2439170.5	Feb 14		1001 (leap year)	4.169	669265.16	353.46	
				WINTER			
2439180.5	Feb 24			13.901	669274.90	359.73	
2439190.5	Mar 6			23.634	669284.63	5.95	
2439200.5	Mar 16			33.366	669294.36	12.12	
	SPRING						
2439210.5	Mar 26			43.099	669304.09	18.22	
2439220.5	Apr 5			52.831	669313.83	24.24	
2439230.5	Apr 15			62.564	669323.56	30.17	
2439240.5	Apr 25			72.296	669333.29	36.02	
2439250.5	May 5			82.028	669343.02	41.78	Jan 2-Oct 1. Mars not clearly visible from Earth for physical observations.
2439260.5	May 15			91.761	669352.76	47.44	
2439270.5	May 25			101.493	669362.49	53.01	
2439280.5	Jun 4			111.226	669372.22	58.49	
2439290.5	Jun 14			120.958	669381.95	63.87	
	SUMMER						
2439300.5	Jun 24			130.691	669391.69	69.16	
2439310.5	Jul 4			140.423	669401.42	74.36	
2439320.5	Jul 14			150.155	669411.15	79.47	
2439330.5	Jul 24			159.888	669420.88	84.50	
				SPRING			
2439340.5	Aug 3			169.620	669430.62	89.45	
2439350.5	Aug 13			179.353	669440.35	94.33	
2439360.5	Aug 23			189.085	669450.08	99.14	
2439370.5	Sep 2			198.818	669459.81	103.88	
2439380.5	Sep 12			208.550	669469.55	108.56	
2439390.5	Sep 22			218.283	669479.28	113.19	
	FALL						
2439400.5	Oct 2			228.015	669489.01	117.77	
2439410.5	Oct 12			237.747	669498.74	122.31	
2439420.5	Oct 22			247.480	669508.48	126.80	
2439430.5	Nov 1			257.212	669518.21	131.26	
2439440.5	Nov 11			266.945	669527.94	135.70	
2439450.5	Nov 21			276.677	669537.67	140.11	
2439460.5	Dec 1			286.410	669547.41	144.50	
2439470.5	Dec 11			296.142	669557.14	148.87	
2439480.5	Dec 21			305.875	669566.87	153.24	
	WINTER						
2439490.5	Dec 31			315.607	669576.60	157.61	
2439500.5	Jan 10	1967		325.339	669586.34	161.98	
2439510.5	Jan 20			335.072	669596.07	166.35	
2439520.5	Jan 30			344.804	669605.80	170.74	
2439530.5	Feb 9			354.537	669615.53	175.15	
				SUMMER			
2439540.5	Feb 19			364.269	669625.27	179.58	
2439550.5	Mar 1			374.002	669635.00	184.04	
2439560.5	Mar 11			383.734	669644.73	188.53	
	SPRING						
2439570.5	Mar 21			393.467	669654.46	193.06	
2439580.5	Mar 31			403.199	669664.20	197.63	
2439590.5	Apr 10			412.931	669673.93	202.26	APR 15. OPPOSITION
2439600.5	Apr 20			422.664	669683.66	206.94	Earth-Mars distance at closest approach: 55.8 million mi (89.8 million km). Earth days until next opposition: 777.
2439610.5	Apr 30			432.396	669693.39	211.67	
2439620.5	May 10			442.129	669703.13	216.48	
2439630.5	May 20			451.861	669712.86	221.35	
2439640.5	May 30			461.594	669722.59	226.30	
2439650.5	Jun 9			471.326	669732.32	231.33	
2439660.5	Jun 19			481.059	669742.05	236.44	
	SUMMER						
2439670.5	Jun 29			490.791	669751.79	241.64	
2439680.5	Jul 9			500.523	669761.52	246.92	
2439690.5	Jul 19			510.256	669771.25	252.30	
2439700.5	Jul 29			519.988	669780.98	257.78	
2439710.5	Aug 8			529.721	669790.72	263.35	
				FALL			
2439720.5	Aug 18			539.453	669800.45	269.02	
2439730.5	Aug 28			549.186	669810.18	274.78	
2439740.5	Sep 7			558.918	669819.91	280.64	
2439750.5	Sep 17			568.650	669829.65	286.58	
	FALL						
2439760.5	Sep 27			578.383	669839.38	292.61	
2439770.5	Oct 7			588.115	669849.11	298.71	
2439780.5	Oct 17			597.848	669858.84	304.88	
2439790.5	Oct 27			607.580	669868.58	311.11	
2439800.5	Nov 6			617.313	669878.31	317.39	
2439810.5	Nov 16			627.045	669888.04	323.71	
2439820.5	Nov 26			636.778	669897.77	330.04	
2439830.5	Dec 6			646.510	669907.51	336.40	
2439840.5	Dec 16			656.242	669917.24	342.74	
	WINTER						
2439850.5	Dec 26			665.975	669926.97	349.08	

Fig. 12. Calendar of Earth-Mars equivalent dates for 1966 and 1967. Earth dates are for 0^h GMT; Mars dates show day of year and fraction of day elapsed at 0° longitude on Mars.

EARTH			MARS				NOTES
J.D. Julian day	Northern hemisphere season and date	Year	Year	Northern hemisphere season and year day	Consecutive Mars day	Heliocentric ecliptic longitude, deg	
	WINTER	1968 (leap year)	1002	FALL			
2439860.5	Jan 5			6.707	669936.70	355.38	
				WINTER			
2439870.5	Jan 15			16.440	669946.44	1.64	
2439880.5	Jan 25			26.172	669956.17	7.85	
2439890.5	Feb 4			35.905	669965.90	14.00	
2439900.5	Feb 14			45.637	669975.63	20.07	
2439910.5	Feb 24			55.370	669985.37	26.07	
2439920.5	Mar 5			65.102	669995.10	31.98	
2439930.5	Mar 15			74.834	670004.83	37.81	
	SPRING						
2439940.5	Mar 25			84.567	670014.56	43.54	
2439950.5	Apr 4			94.299	670024.30	49.18	
2439960.5	Apr 14			104.032	670034.03	54.72	
2439970.5	Apr 24			113.764	670043.76	60.16	
2439980.5	May 4			123.497	670053.49	65.52	
2439990.5	May 14			133.229	670063.23	70.78	
2440000.5	May 24			142.962	670072.96	75.95	
2440010.5	Jun 3			152.694	670082.69	81.04	
2440020.5	Jun 13			162.426	670092.42	86.04	
	SUMMER			SPRING			
2440030.5	Jun 23			172.159	670102.16	90.97	Apr 3-Sep 30. Mars not clearly visible from Earth for physical observations.
2440040.5	Jul 3			181.891	670111.89	95.83	
2440050.5	Jul 13			191.624	670121.62	100.61	
2440060.5	Jul 23			201.356	670131.35	105.34	
2440070.5	Aug 2			211.089	670141.09	110.00	
2440080.5	Aug 12			220.821	670150.82	114.62	
2440090.5	Aug 22			230.554	670160.55	119.18	
2440100.5	Sep 1			240.286	670170.28	123.70	
2440110.5	Sep 11			250.018	670180.02	128.19	
2440120.5	Sep 21			259.751	670189.75	132.64	
	FALL						
2440130.5	Oct 1			269.483	670199.48	137.06	
2440140.5	Oct 11			279.216	670209.21	141.47	
2440150.5	Oct 21			288.948	670218.95	145.85	
2440160.5	Oct 31			298.681	670228.68	150.23	
2440170.5	Nov 10			308.413	670238.41	154.60	
2440180.5	Nov 20			318.146	670248.14	158.96	
2440190.5	Nov 30			327.878	670257.88	163.33	
2440200.5	Dec 10			337.610	670267.61	167.71	
2440210.5	Dec 20			347.343	670277.34	172.11	
	WINTER						
2440220.5	Dec 30			357.075	670287.07	176.52	
2440230.5	Jan 9	1969		SUMMER			
2440240.5	Jan 19			366.808	670296.80	180.96	
2440250.5	Jan 29			376.540	670306.54	185.42	
2440260.5	Feb 8			386.273	670316.27	189.93	
2440270.5	Feb 18			396.005	670326.00	194.47	
2440280.5	Feb 28			405.737	670335.73	199.06	
2440290.5	Mar 10			415.470	670345.47	203.70	Feb 23-Apr 8. Mariner-'69 launch opportunity (Atlas-Centaur vehicle). Present plans allow for the launching of two spacecraft, one during the early and one during the late launch period within this opportunity.
	SPRING			425.202	670355.20	208.40	
2440300.5	Mar 20			434.935	670364.93	213.16	
2440310.5	Mar 30			444.667	670374.66	217.98	
2440320.5	Apr 9			454.400	670384.40	222.87	
2440330.5	Apr 19			464.132	670394.13	227.85	
2440340.5	Apr 29			473.865	670403.86	232.90	
2440350.5	May 9			483.597	670413.59	238.03	
2440360.5	May 19			493.329	670423.33	243.26	
2440370.5	May 29			503.062	670433.05	248.57	MAY 31. OPPOSITION
2440380.5	Jun 8			512.794	670442.79	253.98	Earth-Mars distance at closest approach: 44.5 million mi (71.7 million km). Earth days until next opposition: 781.
2440390.5	Jun 18			522.527	670452.52	259.48	
	SUMMER						
2440400.5	Jun 28			532.259	670462.26	265.08	
				FALL			
2440410.5	Jul 8			541.992	670471.98	270.78	
2440420.5	Jul 18			551.724	670481.72	276.56	
2440430.5	Jul 28			561.457	670491.45	282.44	Jul 29-Aug 15. Earliest-latest Mariner-'69 Mars flyby dates for Feb 23-Apr 8 launch opportunity. Present plans include a polar flyby for one spacecraft and an equatorial flyby for the other.
2440440.5	Aug 7			571.189	670501.19	288.41	
2440450.5	Aug 17			580.921	670510.91	294.46	
2440460.5	Aug 27			590.654	670520.65	300.58	
2440470.5	Sep 6			600.386	670530.38	306.77	
2440480.5	Sep 16			610.119	670540.12	313.01	
	FALL						
2440490.5	Sep 26			619.851	670549.84	319.30	
2440500.5	Oct 6			629.584	670559.58	325.63	
2440510.5	Oct 16			639.316	670569.31	331.97	
2440520.5	Oct 26			649.049	670579.05	338.32	
2440530.5	Nov 5			658.781	670588.77	344.66	
2440540.5	Nov 15		1003 (leap year)	0.513	670598.51	350.99	
2440550.5	Nov 25			10.246	670608.24	357.28	
				WINTER			
2440560.5	Dec 5			19.978	670617.98	3.53	
2440570.5	Dec 15			29.711	670627.70	9.72	
	WINTER						
2440580.5	Dec 25			39.443	670637.44	15.85	

Fig. 13. Calendar of Earth-Mars equivalent dates for 1968 and 1969. Earth dates are for 0^h GMT; Mars dates show day of year and fraction of day elapsed at 0° longitude on Mars.

EARTH			MARS				
J.D. Julian day	Northern hemisphere season and date	Year	Year	Northern hemisphere season and year day	Consecutive Mars day	Heliocentric ecliptic longitude, deg	NOTES
	WINTER	1970	1003 (leap year)	WINTER			Solar flare behavior varies according to the phase of the 11-year cycle. Thus the "solar maximum" behavior of 1959-1960 should be approximately repeated in 1970-1971.
2440590.5	Jan 4			49.176	670647.17	21.90	
2440600.5	Jan 14			58.908	670656.91	27.87	
2440610.5	Jan 24			68.641	670666.63	33.76	
2440620.5	Feb 3			78.373	670676.37	39.56	
2440630.5	Feb 13			88.105	670686.10	45.26	
2440640.5	Feb 23			97.838	670695.84	50.87	
2440650.5	Mar 5			107.570	670705.56	56.39	
2440660.5	Mar 15			117.303	670715.30	61.81	
	SPRING						
2440670.5	Mar 25			127.035	670725.03	67.13	
2440680.5	Apr 4			136.768	670734.77	72.37	
2440690.5	Apr 14			146.500	670744.50	77.52	
2440700.5	Apr 24			156.233	670754.23	82.58	
2440710.5	May 4			165.965	670763.96	87.56	
				SPRING			
2440720.5	May 14			175.697	670773.70	92.47	
2440730.5	May 24			185.430	670783.43	97.31	
2440740.5	Jun 3			195.162	670793.16	102.07	
2440750.5	Jun 13			204.895	670802.89	106.78	
	SUMMER						
2440760.5	Jun 23			214.627	670812.63	111.43	
2440770.5	Jul 3			224.360	670822.36	116.03	
2440780.5	Jul 13			234.092	670832.09	120.58	
2440790.5	Jul 23			243.824	670841.82	125.09	
2440800.5	Aug 2			253.557	670851.55	129.57	
2440810.5	Aug 12			263.289	670861.29	134.01	
2440820.5	Aug 22			273.022	670871.02	138.43	
2440830.5	Sep 1			282.754	670880.75	142.82	
2440840.5	Sep 11			292.487	670890.48	147.21	
2440850.5	Sep 21			302.219	670900.22	151.58	
	FALL						
2440860.5	Oct 1			311.952	670909.95	155.94	
2440870.5	Oct 11			321.684	670919.68	160.31	
2440880.5	Oct 21			331.416	670929.41	164.68	
2440890.5	Oct 31			341.149	670939.15	169.07	
2440900.5	Nov 10			350.881	670948.88	173.46	
2440910.5	Nov 20			360.614	670958.61	177.88	
				SUMMER			
2440920.5	Nov 30			370.346	670968.34	182.33	
2440930.5	Dec 10			380.079	670978.08	186.81	
2440940.5	Dec 20			389.811	670987.80	191.32	
	WINTER						
2440950.5	Dec 30			399.544	670997.54	195.88	
2440960.5	Jan 9	1971		409.276	671007.27	200.48	
2440970.5	Jan 19			419.008	671017.01	205.14	
2440980.5	Jan 29			428.741	671026.73	209.85	
2440990.5	Feb 8			438.473	671036.47	214.63	
2441000.5	Feb 18			448.206	671046.20	219.48	
2441010.5	Feb 28			457.938	671055.94	224.40	
2441020.5	Mar 10			467.671	671065.66	229.39	
2441030.5	Mar 20			477.403	671075.40	234.47	
	SPRING						
2441040.5	Mar 30			487.136	671085.13	239.63	
2441050.5	Apr 9			496.868	671094.87	244.88	
2441060.5	Apr 19			506.600	671104.59	250.23	
2441070.5	Apr 29			516.333	671114.33	255.66	
2441080.5	May 9			526.065	671124.06	261.20	
2441090.5	May 19			535.798	671133.80	266.83	
				FALL			
2441100.5	May 29			545.530	671143.52	272.55	
2441110.5	Jun 8			555.263	671153.26	278.37	
2441120.5	Jun 18			564.995	671162.99	284.27	
	SUMMER						
2441130.5	Jun 28			574.728	671172.73	290.26	
2441140.5	Jul 8			584.460	671182.45	296.34	
2441150.5	Jul 18			594.192	671192.19	302.48	
2441160.5	Jul 28			603.925	671201.92	308.68	
2441170.5	Aug 7			613.657	671211.66	314.94	AUG 10. PERIHELIC OPPOSITION
2441180.5	Aug 17			623.390	671221.38	321.24	Earth-Mars distance at closest approach: 34.9 million mi (56.2 million km)— exceptionally close approach.
2441190.5	Aug 27			633.122	671231.12	327.57	Earth days until next opposition: 807.
2441200.5	Sep 6			642.855	671240.85	333.92	Earth years until next exceptionally close approach: 17.2 (Sep 28, 1988).
2441210.5	Sep 16			652.587	671250.59	340.26	
	FALL						
2441220.5	Sep 26			662.320	671260.31	346.60	
2441230.5	Oct 6		1004	3.052	671270.05	352.92	
				WINTER			
2441240.5	Oct 16			12.784	671279.78	359.19	
2441250.5	Oct 26			22.517	671289.52	5.42	
2441260.5	Nov 5			32.249	671299.24	11.60	
2441270.5	Nov 15			41.982	671308.98	17.70	
2441280.5	Nov 25			51.714	671318.71	23.73	
2441290.5	Dec 5			61.447	671328.45	29.68	
2441300.5	Dec 15			71.179	671338.17	35.54	
	WINTER						
2441310.5	Dec 25			80.911	671347.91	41.31	

Fig. 14. Calendar of Earth-Mars equivalent dates for 1970 and 1971. Earth dates are for 0^h GMT; Mars dates show day of year and fraction of day elapsed at 0° longitude on Mars.

EARTH			MARS				
J.D. Julian day	Northern hemisphere season and date	Year	Year	Northern hemisphere season and year day	Consecutive Mars day	Heliocentric ecliptic longitude, deg	NOTES
	WINTER	1972 (leap year)	1004	WINTER			
2441320.5	Jan 4			90.644	671357.64	46.98	
2441330.5	Jan 14			100.376	671367.38	52.56	
2441340.5	Jan 24			110.109	671377.10	58.05	
2441350.5	Feb 3			119.841	671386.84	63.44	
2441360.5	Feb 13			129.574	671396.57	68.74	
2441370.5	Feb 23			139.306	671406.30	73.95	
2441380.5	Mar 4			149.039	671416.03	79.07	
2441390.5	Mar 14			158.771	671425.77	84.11	
	SPRING			SPRING			
2441400.5	Mar 24			168.503	671435.50	89.07	
2441410.5	Apr 3			178.236	671445.23	93.95	
2441420.5	Apr 13			187.968	671454.96	98.77	
2441430.5	Apr 23			197.701	671464.70	103.52	
2441440.5	May 3			207.433	671474.43	108.21	
2441450.5	May 13			217.166	671484.16	112.84	
2441460.5	May 23			226.898	671493.89	117.43	
2441470.5	Jun 2			236.631	671503.63	121.97	
2441480.5	Jun 12			246.363	671513.36	126.47	
	SUMMER						
2441490.5	Jun 22			256.095	671523.09	130.93	
2441500.5	Jul 2			265.828	671532.82	135.37	
2441510.5	Jul 12			275.560	671542.55	139.78	
2441520.5	Jul 22			285.293	671552.29	144.17	
2441530.5	Aug 1			295.025	671562.02	148.55	
2441540.5	Aug 11			304.758	671571.75	152.92	
2441550.5	Aug 21			314.490	671581.48	157.29	
2441560.5	Aug 31			324.223	671591.22	161.66	
2441570.5	Sep 10			333.955	671600.95	166.03	
2441580.5	Sep 20			343.687	671610.68	170.42	
	FALL						
2441590.5	Sep 30			353.420	671620.41	174.82	
				SUMMER			
2441600.5	Oct 10			363.152	671630.15	179.25	
2441610.5	Oct 20			372.885	671639.88	183.70	
2441620.5	Oct 30			382.617	671649.62	188.19	
2441630.5	Nov 9			392.350	671659.34	192.72	
2441640.5	Nov 19			402.082	671669.08	197.29	
2441650.5	Nov 29			411.815	671678.81	201.91	
2441660.5	Dec 9			421.547	671688.55	206.58	
2441670.5	Dec 19			431.279	671698.27	211.31	
	WINTER						
2441680.5	Dec 29			441.012	671708.01	216.11	
2441690.5	Jan 8	1973		450.744	671717.74	220.97	
2441700.5	Jan 18			460.477	671727.48	225.91	
2441710.5	Jan 28			470.209	671737.20	230.93	
2441720.5	Feb 7			479.942	671746.94	236.04	
2441730.5	Feb 17			489.674	671756.67	241.22	
2441740.5	Feb 27			499.407	671766.41	246.50	
2441750.5	Mar 9			509.139	671776.13	251.87	
2441760.5	Mar 19			518.871	671785.87	257.34	
	SPRING						
2441770.5	Mar 29			528.604	671795.60	262.90	
				FALL			
2441780.5	Apr 8			538.336	671805.34	268.56	
2441790.5	Apr 18			548.069	671815.06	274.31	
2441800.5	Apr 28			557.801	671824.80	280.16	
2441810.5	May 8			567.534	671834.53	286.09	
2441820.5	May 18			577.266	671844.27	292.11	
2441830.5	May 28			586.998	671853.99	298.20	
2441840.5	Jun 7			596.731	671863.73	304.37	
2441850.5	Jun 17			606.463	671873.46	310.59	
	SUMMER						
2441860.5	Jun 27			616.196	671883.20	316.86	
2441870.5	Jul 7			625.928	671892.92	323.18	
2441880.5	Jul 17			635.661	671902.66	329.51	
2441890.5	Jul 27			645.393	671912.39	335.86	
2441900.5	Aug 6			655.126	671922.13	342.21	
2441910.5	Aug 16			664.858	671931.85	348.54	
2441920.5	Aug 26		1005 (leap year)	6.590	671941.59	354.85	
				WINTER			
2441930.5	Sep 5			16.323	671951.32	1.11	
2441940.5	Sep 15			26.055	671961.05	7.33	
	FALL						
2441950.5	Sep 25			35.788	671970.78	13.48	
2441960.5	Oct 5			45.520	671980.52	19.56	
2441970.5	Oct 15			55.253	671990.25	25.57	
2441980.5	Oct 25			64.985	671999.98	31.49	OCT 25. OPPOSITION
2441990.5	Nov 4			74.718	672009.71	37.32	Earth-Mars distance at closest approach:
2442000.5	Nov 14			84.450	672019.45	43.06	40.4 million mi (65.0 million km).
2442010.5	Nov 24			94.182	672029.18	48.70	Earth days until next opposition: 791.
2442020.5	Dec 4			103.915	672038.91	54.25	
2442030.5	Dec 14			113.647	672048.64	59.71	
	WINTER						
2442040.5	Dec 24			123.380	672058.38	65.07	

Fig. 15. Calendar of Earth-Mars equivalent dates for 1972 and 1973. Earth dates are for 0^h GMT; Mars dates show day of year and fraction of day elapsed at 0° longitude on Mars.

EARTH			MARS				NOTES
J.D. Julian day	Northern hemisphere season and date	Year	Year	Northern hemisphere season and year day	Consecutive Mars day	Heliocentric ecliptic longitude, deg	
	WINTER	1974	1005 (leap year)	WINTER			
2442050.5	Jan 3			133.112	672068.11	70.34	
2442060.5	Jan 13			142.845	672077.84	75.53	
2442070.5	Jan 23			152.577	672087.57	80.62	
2442080.5	Feb 2			162.310	672097.30	85.64	
2442090.5	Feb 12			SPRING			
2442100.5	Feb 22			172.042	672107.04	90.57	
2442110.5	Mar 4			181.774	672116.77	95.44	
2442120.5	Mar 14			191.507	672126.50	100.23	
	SPRING			201.239	672136.23	104.96	
2442130.5	Mar 24			210.972	672145.97	109.64	
2442140.5	Apr 3			220.704	672155.70	114.25	
2442150.5	Apr 13			230.437	672165.43	118.83	
2442160.5	Apr 23			240.169	672175.16	123.35	
2442170.5	May 3			249.902	672184.90	127.84	
2442180.5	May 13			259.634	672194.63	132.30	
2442190.5	May 23			269.366	672204.36	136.72	
2442200.5	Jun 2			279.099	672214.09	141.13	
2442210.5	Jun 12			288.831	672223.83	145.52	
	SUMMER						
2442220.5	Jun 22			298.564	672233.56	149.89	
2442230.5	Jul 2			308.296	672243.29	154.26	
2442240.5	Jul 12			318.029	672253.02	158.63	
2442250.5	Jul 22			327.761	672262.76	163.00	
2442260.5	Aug 1			337.493	672272.49	167.38	
2442270.5	Aug 11			347.226	672282.22	171.77	
2442280.5	Aug 21			356.958	672291.95	176.18	
				SUMMER			
2442290.5	Aug 31			366.691	672301.69	180.62	
2442300.5	Sep 10			376.423	672311.42	185.08	
2442310.5	Sep 20			386.156	672321.15	189.58	
	FALL						
2442320.5	Sep 30			395.888	672330.88	194.12	
2442330.5	Oct 10			405.621	672340.62	198.71	
2442340.5	Oct 20			415.353	672350.35	203.34	
2442350.5	Oct 30			425.085	672360.08	208.03	
2442360.5	Nov 9			434.818	672369.81	212.79	
2442370.5	Nov 19			444.550	672379.55	217.60	
2442380.5	Nov 29			454.283	672389.28	222.49	
2442390.5	Dec 9			464.015	672399.01	227.45	
2442400.5	Dec 19			473.748	672408.74	232.50	
	WINTER						
2442410.5	Dec 29			483.480	672418.48	237.62	
2442420.5	Jan 8	1975		493.213	672428.21	242.84	
2442430.5	Jan 18			502.945	672437.94	248.15	
2442440.5	Jan 28			512.677	672447.67	253.54	
2442450.5	Feb 7			522.410	672457.41	259.04	
2442460.5	Feb 17			532.142	672467.14	264.63	
				FALL			
2442470.5	Feb 27			541.875	672476.87	270.31	
2442480.5	Mar 9			551.607	672486.60	276.09	
2442490.5	Mar 19			561.340	672496.34	281.96	
	SPRING						
2442500.5	Mar 29			571.072	672506.07	287.92	
2442510.5	Apr 8			580.805	672515.80	293.96	
2442520.5	Apr 18			590.537	672525.53	300.07	
2442530.5	Apr 28			600.269	672535.27	306.26	
2442540.5	May 8			610.002	672545.00	312.49	
2442550.5	May 18			619.734	672554.73	318.78	
2442560.5	May 28			629.467	672564.46	325.10	
2442570.5	Jun 7			639.199	672574.20	331.44	
2442580.5	Jun 17			648.932	672583.93	337.79	
	SUMMER						
2442590.5	Jun 27			658.664	672593.66	344.13	
2442600.5	Jul 7			668.397	672603.39	350.46	
2442610.5	Jul 17		1006	9.129	672613.13	356.76	
				WINTER			
2442620.5	Jul 27			18.861	672622.86	3.01	
2442630.5	Aug 6			28.594	672632.59	9.21	
2442640.5	Aug 16			38.326	672642.32	15.34	
2442650.5	Aug 26			48.059	672652.05	21.40	
2442660.5	Sep 5			57.791	672661.79	27.38	
2442670.5	Sep 15			67.524	672671.52	33.28	
	FALL						
2442680.5	Sep 25			77.256	672681.25	39.08	
2442690.5	Oct 5			86.989	672690.98	44.80	
2442700.5	Oct 15			96.721	672700.72	50.42	
2442710.5	Oct 25			106.453	672710.45	55.94	
2442720.5	Nov 4			116.186	672720.18	61.37	
2442730.5	Nov 14			125.918	672729.91	66.70	
2442740.5	Nov 24			135.651	672739.65	71.95	DEC 15. OPPOSITION
2442750.5	Dec 4			145.383	672749.38	77.10	Earth-Mars distance at closest approach: 52.4 million mi (84.3 million km).
2442760.5	Dec 14			155.116	672759.11	82.17	Earth days until next opposition: 771.
	WINTER						
2442770.5	Dec 24			164.848	672768.84	87.16	

Fig. 16. Calendar of Earth-Mars equivalent dates for 1974 and 1975. Earth dates are for 0^h GMT; Mars dates show day of year and fraction of day elapsed at 0° longitude on Mars.

EARTH			MARS				NOTES
J.D. Julian day	Northern hemisphere season and date	Year	Year	Northern hemisphere season and year day	Consecutive Mars day	Heliocentric ecliptic longitude, deg	
	WINTER	1976 (leap year)	1006	SPRING			
2442780.5	Jan 3			174.580	672778.58	92.08	
2442790.5	Jan 13			184.313	672788.31	96.92	
2442800.5	Jan 23			194.045	672798.04	101.70	
2442810.5	Feb 2			203.778	672807.77	106.41	
2442820.5	Feb 12			213.510	672817.51	111.06	
2442830.5	Feb 22			223.243	672827.24	115.67	
2442840.5	Mar 3			232.975	672836.97	120.22	
2442850.5	Mar 13			242.708	672846.70	124.74	
	SPRING						
2442860.5	Mar 23			252.440	672856.44	129.21	
2442870.5	Apr 2			262.172	672866.17	133.66	
2442880.5	Apr 12			271.905	672875.90	138.08	
2442890.5	Apr 22			281.637	672885.63	142.48	
2442900.5	May 2			291.370	672895.37	146.86	
2442910.5	May 12			301.102	672905.10	151.24	
2442920.5	May 22			310.835	672914.83	155.60	
2442930.5	Jun 1			320.567	672924.56	159.97	
2442940.5	Jun 11			330.300	672934.30	164.34	
	SUMMER						
2442950.5	Jun 21			340.032	672944.03	168.73	
2442960.5	Jul 1			349.764	672953.76	173.12	
2442970.5	Jul 11			359.497	672963.49	177.54	
				SUMMER			
2442980.5	Jul 21			369.229	672973.23	181.99	
2442990.5	Jul 31			378.962	672982.96	186.46	
2443000.5	Aug 10			388.694	672992.69	190.97	
2443010.5	Aug 20			398.427	673002.42	195.53	
2443020.5	Aug 30			408.159	673012.16	200.13	
2443030.5	Sep 9			417.892	673021.89	204.78	
2443040.5	Sep 19			427.624	673031.62	209.49	
	FALL						
2443050.5	Sep 29			437.356	673041.35	214.26	
2443060.5	Oct 9			447.089	673051.09	219.10	
2443070.5	Oct 19			456.821	673060.82	224.01	
2443080.5	Oct 29			466.554	673070.55	229.00	
2443090.5	Nov 8			476.286	673080.28	234.07	
2443100.5	Nov 18			486.019	673090.02	239.22	
2443110.5	Nov 28			495.751	673099.75	244.47	
2443120.5	Dec 8			505.484	673109.48	249.80	
2443130.5	Dec 18			515.216	673119.21	255.23	
	WINTER						
2443140.5	Dec 28			524.948	673128.95	260.76	
2443150.5	Jan 7	1977		534.681	673138.68	266.38	
				FALL			
2443160.5	Jan 17			544.413	673148.41	272.09	
2443170.5	Jan 27			554.146	673158.14	277.90	
2443180.5	Feb 6			563.878	673167.88	283.80	
2443190.5	Feb 16			573.611	673177.61	289.78	
2443200.5	Feb 26			583.343	673187.34	295.85	
2443210.5	Mar 8			593.076	673197.07	301.98	
2443220.5	Mar 18			602.808	673206.80	308.18	
	SPRING						
2443230.5	Mar 28			612.540	673216.54	314.44	
2443240.5	Apr 7			622.273	673226.27	320.73	
2443250.5	Apr 17			632.005	673236.00	327.06	
2443260.5	Apr 27			641.738	673245.73	333.40	
2443270.5	May 7			651.470	673255.47	339.75	
2443280.5	May 17			661.203	673265.20	346.09	
2443290.5	May 27		1007 (leap year)	2.935	673274.93	352.41	
				WINTER			
2443300.5	Jun 6			12.667	673284.66	358.69	
2443310.5	Jun 16			22.400	673294.40	4.92	
	SUMMER						
2443320.5	Jun 26			32.132	673304.13	11.10	
2443330.5	Jul 6			41.865	673313.86	17.21	
2443340.5	Jul 16			51.597	673323.59	23.25	
2443350.5	Jul 26			61.330	673333.33	29.20	
2443360.5	Aug 5			71.062	673343.05	35.07	
2443370.5	Aug 15			80.795	673352.79	40.85	
2443380.5	Aug 25			90.527	673362.52	46.53	
2443390.5	Sep 4			100.259	673372.26	52.12	
2443400.5	Sep 14			109.992	673381.98	57.61	
	FALL						
2443410.5	Sep 24			119.724	673391.72	63.01	
2443420.5	Oct 4			129.457	673401.45	68.32	
2443430.5	Oct 14			139.189	673411.19	73.54	
2443440.5	Oct 24			148.922	673420.91	78.67	
2443450.5	Nov 3			158.654	673430.65	83.71	
				SPRING			
2443460.5	Nov 13			168.387	673440.38	88.68	
2443470.5	Nov 23			178.119	673450.12	93.57	
2443480.5	Dec 3			187.851	673459.84	98.39	
2443490.5	Dec 13			197.584	673469.58	103.15	
	WINTER						
2443500.5	Dec 23			207.316	673479.31	107.85	

Fig. 17. Calendar of Earth-Mars equivalent dates for 1976 and 1977. Earth dates are for 0^h GMT; Mars dates show day of year and fraction of day elapsed at 0° longitude on Mars.

EARTH			MARS				NOTES
J.D. Julian day	Northern hemisphere season and date	Year	Year	Northern hemisphere season and year day	Consecutive Mars day	Heliocentric ecliptic longitude, deg	
	WINTER	1978	1007 (leap year)	SPRING			
2443510.5	Jan 2			217.049	673489.05	112.49	
2443520.5	Jan 12			226.781	673498.77	117.07	
2443530.5	Jan 22			236.514	673508.51	121.62	JAN 22. OPPOSITION
2443540.5	Feb 1			246.246	673518.24	126.12	
2443550.5	Feb 11			255.979	673527.98	130.59	Earth-Mars distance at closest approach:
2443560.5	Feb 21			265.711	673537.71	135.03	60.8 million mi (97.8 million km).
2443570.5	Mar 3			275.443	673547.44	139.44	Earth days until next opposition: 764.
2443580.5	Mar 13			285.176	673557.17	143.83	
	SPRING						
2443590.5	Mar 23			294.908	673566.91	148.21	
2443600.5	Apr 2			304.641	673576.64	152.58	
2443610.5	Apr 12			314.373	673586.37	156.95	
2443620.5	Apr 22			324.106	673596.10	161.32	
2443630.5	May 2			333.838	673605.84	165.69	
2443640.5	May 12			343.571	673615.57	170.07	
2443650.5	May 22			353.303	673625.30	174.48	
				SUMMER			
2443660.5	Jun 1			363.035	673635.03	178.90	
2443670.5	Jun 11			372.768	673644.77	183.35	
	SUMMER						
2443680.5	Jun 21			382.500	673654.50	187.84	
2443690.5	Jul 1			392.233	673664.23	192.36	
2443700.5	Jul 11			401.965	673673.96	196.93	
2443710.5	Jul 21			411.698	673683.70	201.54	
2443720.5	Jul 31			421.430	673693.43	206.21	
2443730.5	Aug 10			431.163	673703.16	210.93	
2443740.5	Aug 20			440.895	673712.89	215.73	
2443750.5	Aug 30			450.627	673722.63	220.58	
2443760.5	Sep 9			460.360	673732.36	225.52	
2443770.5	Sep 19			470.092	673742.09	230.53	
	FALL						
2443780.5	Sep 29			479.825	673751.82	235.62	
2443790.5	Oct 9			489.557	673761.55	240.80	
2443800.5	Oct 19			499.290	673771.29	246.08	
2443810.5	Oct 29			509.022	673781.02	251.44	
2443820.5	Nov 8			518.754	673790.75	256.90	
2443830.5	Nov 18			528.487	673800.48	262.45	
				FALL			
2443840.5	Nov 28			538.219	673810.22	268.10	
2443850.5	Dec 8			547.952	673819.95	273.84	
2443860.5	Dec 18			557.684	673829.68	279.68	
	WINTER						
2443870.5	Dec 28			567.417	673839.41	285.61	
2443880.5	Jan 7	1979		577.149	673849.15	291.62	
2443890.5	Jan 17			586.882	673858.88	297.71	
2443900.5	Jan 27			596.614	673868.61	303.86	
2443910.5	Feb 6			606.346	673878.34	310.08	
2443920.5	Feb 16			616.079	673888.08	316.35	
2443930.5	Feb 26			625.811	673897.80	322.66	
2443940.5	Mar 8			635.544	673907.54	329.00	
2443950.5	Mar 18			645.276	673917.27	335.35	
	SPRING						
2443960.5	Mar 28			655.009	673927.01	341.70	
2443970.5	Apr 7			664.741	673936.73	348.03	
2443980.5	Apr 17		1008	5.474	673946.47	354.34	
				WINTER			
2443990.5	Apr 27			15.206	673956.20	0.62	
2444000.5	May 7			24.938	673965.94	6.84	
2444010.5	May 17			34.671	673975.66	13.00	
2444020.5	May 27			44.403	673985.40	19.09	
2444030.5	Jun 6			54.136	673995.13	25.10	
2444040.5	Jun 16			63.868	674004.87	31.03	
	SUMMER						
2444050.5	Jun 26			73.601	674014.59	36.87	
2444060.5	Jul 6			83.333	674024.33	42.62	
2444070.5	Jul 16			93.066	674034.06	48.27	
2444080.5	Jul 26			102.798	674043.80	53.83	
2444090.5	Aug 5			112.530	674053.52	59.30	
2444100.5	Aug 15			122.263	674063.26	64.67	
2444110.5	Aug 25			131.995	674072.99	69.95	
2444120.5	Sep 4			141.728	674082.73	75.14	
2444130.5	Sep 14			151.460	674092.45	80.24	
	FALL						
2444140.5	Sep 24			161.193	674102.19	85.26	
				SPRING			
2444150.5	Oct 4			170.925	674111.92	90.21	
2444160.5	Oct 14			180.658	674121.66	95.08	
2444170.5	Oct 24			190.390	674131.38	99.88	
2444180.5	Nov 3			200.122	674141.12	104.61	
2444190.5	Nov 13			209.855	674150.85	109.29	
2444200.5	Nov 23			219.587	674160.59	113.91	
2444210.5	Dec 3			229.320	674170.31	118.49	
2444220.5	Dec 13			239.052	674180.05	123.02	
	WINTER						
2444230.5	Dec 23			248.785	674189.78	127.51	

Fig. 18. Calendar of Earth-Mars equivalent dates for 1978 and 1979. Earth dates are for 0^h GMT; Mars dates show day of year and fraction of day elapsed at 0° longitude on Mars.

EARTH			MARS				NOTES
J.D. Julian day	Northern hemisphere season and date	Year	Year	Northern hemisphere season and year day	Consecutive Mars day	Heliocentric ecliptic longitude, deg	
	WINTER	1980	1008	SPRING			
2444240.5	Jan 2	(leap		258.517	674199.52	131.97	
2444250.5	Jan 12	year)		268.250	674209.24	136.40	
2444260.5	Jan 22			277.982	674218.98	140.80	
2444270.5	Feb 1			287.714	674228.71	145.19	
2444280.5	Feb 11			297.447	674238.45	149.57	
2444290.5	Feb 21			307.179	674248.17	153.94	FEB 25. APHELIC OPPOSITION
2444300.5	Mar 2			316.912	674257.91	158.30	Earth-Mars distance at closest approach: 63.2 million mi (101.7 million km).
2444310.5	Mar 12			326.644	674267.64	162.67	
	SPRING						
2444320.5	Mar 22			336.377	674277.38	167.05	
2444330.5	Apr 1			346.109	674287.10	171.44	
2444340.5	Apr 11			355.841	674296.84	175.85	
				SUMMER			
2444350.5	Apr 21			365.574	674306.57	180.28	
2444360.5	May 1			375.306	674316.30	184.74	
2444370.5	May 11			385.039	674326.03	189.24	
2444380.5	May 21			394.771	674335.77	193.77	
2444390.5	May 31			404.504	674345.50	198.35	
2444400.5	Jun 10			414.236	674355.23	202.98	
2444410.5	Jun 20			423.969	674364.96	207.66	
	SUMMER						
2444420.5	Jun 30			433.701	674374.70	212.41	
2444430.5	Jul 10			443.433	674384.43	217.22	
2444440.5	Jul 20			453.166	674394.16	222.10	
2444450.5	Jul 30			462.898	674403.89	227.05	
2444460.5	Aug 9			472.631	674413.63	232.09	
2444470.5	Aug 19			482.363	674423.36	237.21	
2444480.5	Aug 29			492.096	674433.09	242.41	
2444490.5	Sep 8			501.828	674442.82	247.71	
2444500.5	Sep 18			511.561	674452.55	253.10	
	FALL						
2444510.5	Sep 28			521.293	674462.29	258.58	
2444520.5	Oct 8			531.025	674472.02	264.16	
				FALL			
2444530.5	Oct 18			540.758	674481.76	269.84	
2444540.5	Oct 28			550.490	674491.48	275.61	
2444550.5	Nov 7			560.223	674501.22	281.47	
2444560.5	Nov 17			569.955	674510.95	287.42	
2444570.5	Nov 27			579.688	674520.69	293.45	
2444580.5	Dec 7			589.420	674530.41	299.56	
2444590.5	Dec 17			599.153	674540.15	305.74	
	WINTER						
2444600.5	Dec 27			608.885	674549.88	311.98	
2444610.5	Jan 6	1981		618.617	674559.62	318.26	
2444620.5	Jan 16			628.350	674569.34	324.58	
2444630.5	Jan 26			638.082	674579.08	330.92	
2444640.5	Feb 5			647.815	674588.81	337.27	
2444650.5	Feb 15			657.547	674598.55	343.61	
2444660.5	Feb 25			667.280	674608.27	349.94	
2444670.5	Mar 7		1009	9.012	674618.01	356.24	
			(leap	WINTER			
2444680.5	Mar 17		year)	18.745	674627.74	2.50	
	SPRING						
2444690.5	Mar 27			28.477	674637.48	8.71	
2444700.5	Apr 6			38.209	674647.20	14.85	
2444710.5	Apr 16			47.942	674656.94	20.92	
2444720.5	Apr 26			57.674	674666.67	26.91	
2444730.5	May 6			67.407	674676.41	32.81	
2444740.5	May 16			77.139	674686.13	38.63	
2444750.5	May 26			86.872	674695.87	44.35	
2444760.5	Jun 5			96.604	674705.60	49.98	
2444770.5	Jun 15			106.336	674715.34	55.51	
	SUMMER						
2444780.5	Jun 25			116.069	674725.06	60.95	
2444790.5	Jul 5			125.801	674734.80	66.30	
2444800.5	Jul 15			135.534	674744.53	71.55	
2444810.5	Jul 25			145.266	674754.27	76.72	
2444820.5	Aug 4			154.999	674763.99	81.80	
2444830.5	Aug 14			164.731	674773.73	86.79	
				SPRING			
2444840.5	Aug 24			174.464	674783.46	91.72	
2444850.5	Sep 3			184.196	674793.20	96.57	
2444860.5	Sep 13			193.928	674802.92	101.35	
	FALL						
2444870.5	Sep 23			203.661	674812.66	106.07	
2444880.5	Oct 3			213.393	674822.39	110.73	
2444890.5	Oct 13			223.126	674832.13	115.33	
2444900.5	Oct 23			232.858	674841.85	119.90	
2444910.5	Nov 2			242.591	674851.59	124.41	
2444920.5	Nov 12			252.323	674861.32	128.89	
2444930.5	Nov 22			262.056	674871.05	133.34	
2444940.5	Dec 2			271.788	674880.78	137.77	
2444950.5	Dec 12			281.520	674890.52	142.17	
	WINTER						
2444960.5	Dec 22			291.253	674900.25	146.55	

Fig. 19. Calendar of Earth-Mars equivalent dates for 1980 and 1981. Earth dates are for 0^h GMT; Mars dates show day of year and fraction of day elapsed at 0° longitude on Mars.

EARTH			MARS				NOTES
J.D. Julian day	Northern hemisphere season and date	Year	Year	Northern hemisphere season and year day	Consecutive Mars day	Heliocentric ecliptic longitude, deg	
	WINTER	1982	1009 (leap year)	SPRING			
2444970.5	Jan 1			300.985	674909.98	150.92	
2444980.5	Jan 11			310.718	674919.71	155.29	
2444990.5	Jan 21			320.450	674929.45	159.66	
2445000.5	Jan 31			330.183	674939.18	164.03	
2445010.5	Feb 10			339.915	674948.91	168.41	
2445020.5	Feb 20			349.648	674958.64	172.80	
2445030.5	Mar 2			359.380	674968.38	177.22	
				SUMMER			
2445040.5	Mar 12			369.112	674978.11	181.66	
	SPRING						
2445050.5	Mar 22			378.845	674987.84	186.13	
2445060.5	Apr 1			388.577	674997.57	190.64	
2445070.5	Apr 11			398.310	675007.30	195.19	
2445080.5	Apr 21			408.042	675017.04	199.78	
2445090.5	May 1			417.775	675026.77	204.43	
2445100.5	May 11			427.507	675036.50	209.13	
2445110.5	May 21			437.240	675046.23	213.89	
2445120.5	May 31			446.972	675055.97	218.73	
2445130.5	Jun 10			456.704	675065.70	223.63	
2445140.5	Jun 20			466.437	675075.43	228.61	
	SUMMER						
2445150.5	Jun 30			476.169	675085.16	233.67	
2445160.5	Jul 10			485.902	675094.90	238.81	
2445170.5	Jul 20			495.634	675104.63	244.05	
2445180.5	Jul 30			505.367	675114.36	249.37	
2445190.5	Aug 9			515.099	675124.09	254.79	
2445200.5	Aug 19			524.832	675133.83	260.30	
2445210.5	Aug 29			534.564	675143.56	265.91	
				FALL			
2445220.5	Sep 8			544.296	675153.29	271.62	
2445230.5	Sep 18			554.029	675163.02	277.41	
	FALL						
2445240.5	Sep 28			563.761	675172.76	283.30	
2445250.5	Oct 8			573.494	675182.49	289.28	
2445260.5	Oct 18			583.226	675192.22	295.33	
2445270.5	Oct 28			592.959	675201.95	301.46	
2445280.5	Nov 7			602.691	675211.69	307.66	
2445290.5	Nov 17			612.423	675221.42	313.90	
2445300.5	Nov 27			622.156	675231.15	320.20	
2445310.5	Dec 7			631.888	675240.88	326.52	
2445320.5	Dec 17			641.621	675250.62	332.86	
	WINTER						
2445330.5	Dec 27			651.353	675260.35	339.21	
2445340.5	Jan 6	1983		661.086	675270.08	345.55	
2445350.5	Jan 16		1010 (leap year)	1.818	675279.81	351.87	
				WINTER			
2445360.5	Jan 26			11.551	675289.55	358.16	
2445370.5	Feb 5			21.283	675299.28	4.40	
2445380.5	Feb 15			31.014	675309.01	10.59	
2445390.5	Feb 25			40.747	675318.74	16.71	
2445400.5	Mar 7			50.479	675328.48	22.75	
2445410.5	Mar 17			60.212	675338.21	28.71	
	SPRING						
2445420.5	Mar 27			69.944	675347.94	34.59	
2445430.5	Apr 6			79.677	675357.67	40.38	
2445440.5	Apr 16			89.409	675367.41	46.07	
2445450.6	Apr 26			99.142	675377.14	51.67	
2445460.5	May 6			108.874	675386.87	57.18	
2445470.5	May 16			118.606	675396.60	62.59	
2445480.5	May 26			128.339	675406.34	67.90	
2445490.5	Jun 5			138.071	675416.07	73.13	
2445500.5	Jun 15			147.804	675425.80	78.27	
	SUMMER						
2445510.5	Jun 25			157.536	675435.53	83.33	
				SPRING			
2445520.5	Jul 5			167.269	675445.27	88.30	
2445530.5	Jul 15			177.001	675455.00	93.20	
2445540.5	Jul 25			186.734	675464.73	98.03	
2445550.5	Aug 4			196.466	675474.46	102.80	
2445560.5	Aug 14			206.198	675484.20	107.50	
2445570.5	Aug 24			215.931	675493.93	112.14	
2445580.5	Sep 3			225.663	675503.66	116.74	
2445590.5	Sep 13			235.396	675513.39	121.28	
	FALL						
2445600.5	Sep 23			245.128	675523.13	125.79	
2445610.5	Oct 3			254.861	675532.86	130.26	
2445620.5	Oct 13			264.593	675542.59	134.70	
2445630.5	Oct 23			274.326	675552.32	139.12	
2445640.5	Nov 2			284.058	675562.05	143.52	
2445650.5	Nov 12			293.790	675571.79	147.90	
2445660.5	Nov 22			303.523	675581.52	152.27	
2445670.5	Dec 2			313.255	675591.25	156.64	
2445680.5	Dec 12			322.988	675600.98	161.00	
	WINTER						
2445690.5	Dec 22			332.720	675610.72	165.38	

Fig. 20. Calendar of Earth-Mars equivalent dates for 1982 and 1983. Earth dates are for 0^h GMT; Mars dates show day of year and fraction of day elapsed at 0° longitude on Mars.

CROSS REFERENCES

The specific section number, subject, and page number to which the reader is referred is given below.

Cross Reference	Section and Subject
[1] Martian orbital data	3.3.....Radar return power (discussion), p.3. 6.....Solar electromagnetic radiation (discussion), p.5.
[2] Martian physical data	2.....Flattening (discussion), p.3. 3.2.....Albedo, magnitude, and color (discussion), p.4; Geometric albedo map (figure), p.7; Variation in color and brightness with rotation (figure), p.9; Photometric function (discussion), p.3. 3.3.....Radar return power (discussion), p.4.
[3] Seasonal changes	4.2.....Seasonal activity (discussion), p.2; Seasonal changes in specific areas (figures), p.11-17. Seasonal activity maps (figures), p.19-25.

BIBLIOGRAPHY

Allen, C. W., 1963, Astrophysical quantities, 2d Edition: U. of London, The Athalone Press.

American Astronomical Society, 1966, p. 97 in AAS meeting abstracts: Huntington Beach, Calif., July, in press.

The American ephemeris and nautical almanac, 1937, 1939, 1941, 1943, 1946, 1948, 1950, 1952, 1956, 1958, 1960, 1963, 1965, 1966, 1967, 1968, 1969: Wash., D.C., U.S. Government Printing Office.

Cain, D. L., 1967, The implications of a new Mars mass and radius, p. 7-9 in Supporting research and advanced development for the period December 1, 1966-January 31, 1967: Pasadena, Calif., Jet Propulsion Laboratory, Spa. Prog. Summ. 37-43, v. IV (unclassified).

de Vaucouleurs, G., 1954, Physics of the planet Mars: London, Faber and Faber.

_____, 1964a, Geometric and photometric parameters of the terrestrial planets: Wash., D.C., National Aeronautics and Space Administration, Memo. RM-4000-NASA.

_____, 1964b, The physical ephemeris of Mars: Icarus, v. 3, n. 3, p. 236-247.

_____, 1964c, The physical ephemeris of Mars: Wash., D.C., National Aeronautics and Space Administration, Memo. RM-3999-NASA.

Handbook of geophysics and space environments, 1965; Valley, S. L., Editor: New York, McGraw-Hill Book Co.

Harris, D., 1961, Photometry and colorimetry of planets and satellites, p. 272-342 in Planets and satellites; Kuiper, G. P., and Middlehurst, B. M., Editors: Chicago, U. of Chicago Press.

Ley, W., Von Braus, W., and Bonestell, C., 1960, Exploration of Mars: New York, Viking Press.

Miner, E. D., 1967, (Pasadena, Calif., Jet Propulsion Laboratory): private communication to R. Newburn.

Planetary coordinates for 1960-1980, 1958: H. M. Nautical Almanac Office.

Richardson, R. S., and Bonestell, C., 1964, Mars: New York, Harcourt, Brace and World, Inc.

Russell, H. N., Dugan, R. S., and Stewart, J. Q., 1945, Astronomy, v. I: Boston, New York, Ginn and Co.

Slipher, E. C., 1962, Mars: Cambridge, Sky Publishing Corp.

SECTION 2 CONTENTS

2. INTERIOR

Data Summary 3
Discussion 3
Flattening 3
Geometric Relationships 3
Dynamical Flattening 4
Optical Flattening 5
Theoretical Flattening 5
Interior Models 6
Jeffreys 1937 6
Ramsey 1948 7
Lyttleton 1963 and 1965 7
Urey 1952 8
Bullen 1966 8
Ringwood 1966 8
Conclusions 9
Cross References 11
Bibliography 12

Figures
1. Theoretical interior density profiles for Earth and Mars 10
2. Table of pressure and density distribution in the Martian interior according to Jeffreys' Hypothesis I 10

2. INTERIOR

DATA SUMMARY

Flattening:

Dynamical (preferred value)	0.00525	(Cain, 1967)
Optical	0.012	(de Vaucouleurs, 1964)

Interior models — See Figs. 1 and 2

DISCUSSION

Flattening[1]*

The flattening of a planet is the difference between the equatorial and polar radii divided by the equatorial radius. (For a more detailed description, see MacDonald, 1962.)

Geometric Relationships

Any rotating fluid body will assume a shape such that its surface is everywhere normal to the resultant of gravity and centrifugal force (Sterne, 1960). This equipotential surface will approximate a spheroid for slow rotation (Jardetzky, 1958). Real bodies may have sufficient strength in their mantles to allow their surfaces to depart somewhat from an equipotential surface or to support internal inhomogeneities.

The spheroid of revolution about an axis is given below, where

f = flattening

e = eccentricity

R = radius at geocentric latitude φ

R_E = equatorial radius

R_p = polar radius

R_m = mean radius

By definition

$$f = \frac{R_E - R_p}{R_E} = 1 - \frac{R_p}{R_E} \quad .$$

*See page 11 for list of cross references.

and

$$e = \frac{\left(R_E^2 - R_p^2\right)^{1/2}}{R_E} = \left(1 - \frac{R_p^2}{R_E^2}\right)^{1/2}$$

Thus

$$e^2 = f(2 - f)$$

and

$$f \equiv 1 - \sqrt{1 - e^2}$$

or, ignoring $0(f^2)$, $f \simeq e^2/2$;

$$R \equiv R_E \left(\frac{1 - e^2}{1 - e^2 \cos^2 \varphi}\right)^{1/2}$$

or, ignoring $0(f^2)$, $R \simeq R_E(1 - f \sin^2\varphi)$; and

$$R_m = R_E \left(1 - \frac{f}{2}\right)$$

Dynamical Flattening

Dynamical flattening refers to a term in the gravitational potential of a primary body; the equipotential surfaces described by this potential may or may not refer to the material surface of that body. The dynamical flattening of Mars is derived from consideration of the orbital perturbations of Phobos and Deimos. The theory of this motion, with improved data from Mariner IV, yields a value of 0.00525 ±0.0000092 (Cain, 1967).

The dynamical flattening of Mars is well determined and corresponds to a value theoretically reasonable for a planet with a very small amount of compression toward its center. Spectroscopic measurements agree with this value. Spectroscopic determinations also show no more CO_2 at the polar caps than at the equator.[2] If the true surface were that implied by the optical flattening value, CO_2 pressure at the caps should be several times that at the equator (Hanselman, 1965). For these reasons, therefore, the mean surface of Mars is suggested to be nearly that indicated by the dynamical flattening.

Optical Flattening

Optical flattening of the apparent planetary surface is measured directly on the image with a micrometer or heliometer or indirectly with photographic images or photoelectric scans. Most results are between 0.010 and 0.015 with recent values near 0.012, corresponding to a surface far from hydrostatic equilibrium. However, optical flattening is determined far less accurately than dynamical flattening. For the following reasons, measurements are difficult to make and are subject to many sources of systematic error and personal equation:

1) Obscuration of the planetary surface edge by the Martian atmosphere.

2) Turbulence in the Earth's atmosphere.

3) Preferential placement of crosswire relative to a bright or dark area.

4) The gibbous nature of the Martian disk.

5) Possible exaggerated equatorial diameter measurements caused by dust particles in the atmosphere during the perihelic oppositions when such measurements are characteristically made. The caps covering the polar regions should prevent the possibility of large amounts of dust at high latitudes.

6) Mars never exhibits a true polar diameter because of axial tilt.

7) Photographic images lack sharpness at image edge.

8) Photoelectric scans suffer from finite slit width, instrumental scattering, and orientation problems.

Theoretical Flattening

For a rotating body, there is a theoretical relation between the centrifugal force at its equator, the difference between polar and equatorial moments of inertia, and its flattening. This relationship depends only upon the assumption that the surface of the body is an equipotential. Hydrostatic equilibrium is not required (Sterne, 1960). Fractional difference in the acceleration of gravity at pole and equator may be substituted for the difference in moments of inertia (Clairaut's equation). Neither the local gravitational acceleration nor the difference in moments of inertia for Mars is measurable from Earth. Since they are functions of internal density distribution, these values cannot be derived theoretically. Radau's equation adds the assumption of hydrostatic equilibrium, again involving unknown moments of inertia.

A planet with all mass at the center and a homogeneous planet present near extreme limits. For a homogeneous Mars, the theoretical flattening value is slightly greater than the measured dynamical flattening, and far less than the apparent optical flattening.

Interior Models[3]

Gravity on Mars is about 0.38 times the Earth's gravity; thus topographic relief of 1.1 km on Mars suggests stresses comparable to those produced by 0.4-km relief on Earth.[4] Heiskanen's 1958 value for the ellipticity of Earth's equator (corresponding to a difference of 0.7 km between extreme equatorial radii) is an uncompensated inequality, i.e., a departure from hydrostatic equilibrium. The Moon apparently has an even greater departure. Therefore, it would not be surprising to find a similar departure on Mars. Any surface corresponding to the optical flattening, however, must be considerably out of hydrostatic equilibrium (for complete mathematical details of this theory, see Jeffreys, 1959). The large discrepancy between the preferred dynamical flattening value of 0.00525 and the optical flattening value of 0.012 is a contradiction yet to be explained.

Interior models of Jeffreys, Ramsey, Lyttleton, Urey, Bullen, and Ringwood are presented here. Figure 1 summarizes schematically various models discussed.

Jeffreys 1937

Jeffreys attempted to extend results on the internal constitution of the Earth, derived from analysis of seismological and geochemical data, to various planets in the terrestrial group. In applying the theory to Mars, Jeffreys used the following data (Earth = 1):[5] mass M = 0.1076 = 643 x 10^{24} g, diameter = 0.5313 = 6.770 x 10^{8} cm, and density = 0.7175 = 3.958 g cm^{-3}. Jeffreys considered two interior models for Mars, one with a core (Hypothesis I) and one with no core (Hypothesis II), with variation of density with pressure assumed known from Earth data. The moment of inertia I for each model was computed after obtaining the distribution laws of density ρ as a function of r, the distance from the planet's center; R is the radius of the planet.

Hypothesis I (Fig. 2)	Small iron core, 1400 km in radius; two density discontinuities, one at 1424 km and the other at 2034 km from the center of the planet.
Central pressure	~4.5 x 10^{11} dyn cm^{-2}
I/MR^2	0.3589
Flattening	1/205.3 = 0.00487 (closer to Struve's value)
Hypothesis II	No core; continuous density variation with depth, with only one density discontinuity near the surface of the planet.
I/MR^2	0.3858
Flattening	1/176.6 = 0.00566

G. de Vaucouleurs (1964) finds Hypothesis I the more plausible of the two, with the small error in flattening (2%) easily corrected by a small change in core radius.

In Jeffreys' model of the Earth, from which he partially derived his two hypotheses of the Martian interior, density varies from 3.29 g cm^{-3} at the surface to 3.69 g cm^{-3} at 474 km. At this depth a density jump to 4.23 g cm^{-3} occurs due to either a compositional change or a crystalline structure (phase) change. Density continues to increase smoothly to a depth of 2900 km, where a jump from 5.3 to 9.8 g cm^{-3} occurs at the core boundary. The central density of the Earth may be greater than 13 g cm^{-3}.

Data used by Jeffreys suggest that the Earth's upper mantle consists largely of olivine and pyroxene, which are magnesium-iron silicates. Pressure of about 1.4×10^{12} dyn cm^{-2} at the boundary of the Earth's inner core is suggested by some to be necessary for transition of complex silicates into simpler island-structure silicates such as in olivine (forsterite and fayalite). Since Jeffreys' Hypothesis I gives a central pressure of about 4.5×10^{11} dyn cm^{-2}, the possibility of a modified silicate core in Mars appears to be very unlikely.

Ramsey 1948

Ramsey has suggested that the Martian crust and core may be respectively molecular and metallic phases of a single type of material, mainly the silicates of magnesium and iron (forsterite, Mg_2SiO_4, and fayalite, $FeSiO_4$). The metallic phase may be the result of partial separation of the outer electronic valence shells of atoms, under very high pressures, into a conduction band configuration. Ramsey has further suggested that density discrepancies may be reduced by a slight compositional change with depth, the iron in silicates becoming more abundant toward the core.

Lyttleton 1963 and 1965

Lyttleton has arrived at a series of two-zone models of Mars from the known mass on the hypothesis that its composition is similar to that of the Earth, with the different zones representing phase change produced by both pressure and temperature effects, thereby extending the Ramsey hypothesis. Because of the much lower central pressure in Mars, which on almost any model must be less than 0.3×10^{12} dyn cm^{-2} (about 1/10 that for the Earth), Mars can consist of two zones only—an inner one of solid material in the same high-pressure phase as the mantle of the Earth, that is, below 413-km depth, and an outer one of solid material in the same form as the outer shell of the Earth above 413-km depth. Accordingly, on this theory Mars would be expected to be entirely solid without a liquid metallic core; and consequently, despite the closely similar angular velocity and obliquity of Mars and Earth, the theory predicted the absence of any main magnetic field before this was confirmed by Mariner IV data in July, 1965.[6]

The internal temperature is regarded as arising from release of radioactively produced energy, and because of its somewhat smaller size Mars might be expected to be at slightly lower temperatures (at comparable depths) than the Earth. The pressure at which the phase change (corresponding to the

20°-discontinuity in the Earth) occurs is known to be highly sensitive to temperature (Ringwood, 1962). For this reason the interface pressure in Mars is not at present precisely determinable. If it were known, a unique structure for the planet would emerge solely from the mass. To accord with the "best" observed radius—which is still subject to some uncertainty—the interface pressure would be about 0.08×10^{12} dyn cm^{-2} (compared with 0.14×10^{12} dyn cm^{-2} in the Earth), and the resulting structure would have about 58% of the total mass in the central region in mantle form and 42% in the outer shell, with the interface occurring at a depth of about 650 km. This configuration is also consistent (within the limits of error) with the dynamical ellipticity derived from the satellite motions, but a more accurate value of this quantity and of the radius would be required for a more stringent test of the theory.

The theory further suggests that with rising internal temperature, the depth of level of the phase discontinuity will increase to provide the requisite higher pressure, and as a result the planet will undergo slight expansion. The amount is uncertain but could well be of the order of 10 km in radius during the whole age of the planet, with a consequent increase of surface area of the order of 10^6 km^2. Thus, rifting of the extreme outer layers of Mars would be expected on this theory, though the degree to which effects of erosion might transform or remove observable traces of such rifts remains quite uncertain.[7]

Urey 1952

Urey finds that with the most probable radius value used, the dynamical value, the amount of flattening could only be satisfied if Mars is approximately homogeneous, with no core. Mariner IV magnetometer data indicate an upper limit to a probable magnetic dipole moment for Mars is 3×10^{-4} (Earth = 1), indicating the probable absence of a liquid conducting core similar to that postulated for Earth.[6]

In acceptable Mars models, it appears a dense core is either absent or very small (less than 5% of the total mass). If Urey's explanation is employed, there must be ~10% free metallic iron uniformly dispersed throughout Mars.

Bullen 1966

Bullen's computations favor a small differentiated central core, probably nickel-iron, and other Martian constituents similar to the Earth's outermost 800 km. He favors a discontinuity at about 800 km from the center of Mars, with both zones chemically homogeneous. Bondi and Marder (1965) consider partial separation in Mars a possibility.

Ringwood 1966

Ringwood concurs that Mars contains less metal than the Earth as a consequence of a higher mean state of oxidation. According to such a model, the overall ratios of iron to silicon and magnesium are the same, but Mars contains more oxygen; the iron is oxidized and exists in the silicates, not in free metal phases.

Ringwood's oxidation hypothesis suggests that Mars is composed of primordial abundances of common metals in a completely oxidized state. Density of such a material would be 3.7 g cm^{-3}, with a mean density of Mars of 4.09 g cm^{-3}. Melting of such material would not result in formation of a dense iron core and accompanying strong decrease in density of the outer regions of the planet. Ringwood suggests that the oxidation state of Mars may be similar to that of the Karoonda chondrite, which is composed mostly of magnetite and olivine $(Mg_{0.68}Fe_{0.32})_2(SiO_4)$. Karoonda contains no free metal and only a trace of carbon. This model postulates primordial abundances of radioactive elements. However, MacDonald (1962) investigated the thermal constitution of Mars and concluded the mean abundance of radioactive elements (U and Th) is substantially smaller for Mars than for Type I carbonaceous chondrites.[8]

CONCLUSIONS

Present data do not lend support to conclusive preference of one interior model over another; however, the following conclusions can be drawn:

1) Mars is a nearly homogeneous body with little or no core (near-consensus of literature).

2) Surface density is $\sim$3.3 g cm^{-3} (rough lower limit).

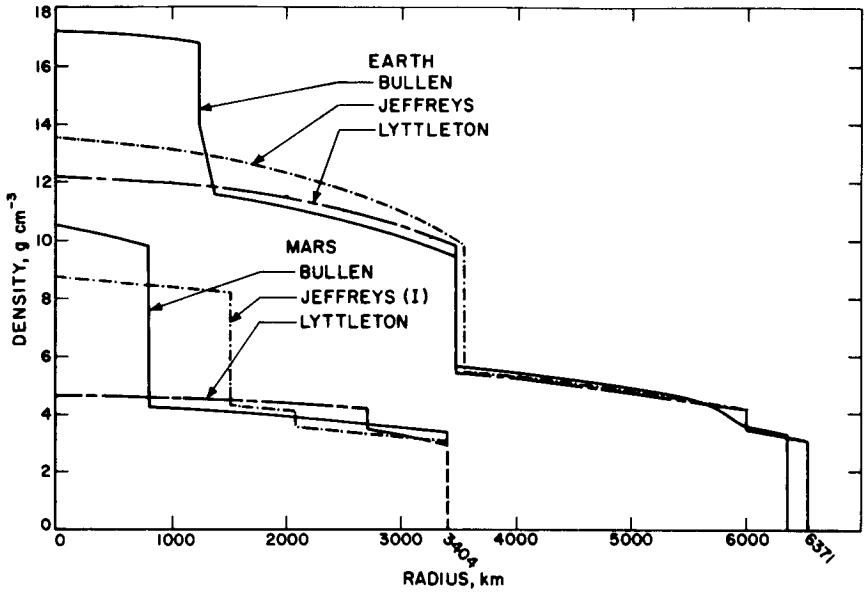

Fig. 1. Theoretical interior density profiles for Earth and Mars. (Jeffreys, 1937; Bullen, 1949, 1963)

Composition	r Distance from center of Mars, km	p Pressure, $\times 10^{10}$ dyne cm^{-2}	ρ Density, g cm^{-3}	M Mass, $\times 10^{24}$ g
Magnesium silicate Mg_2SiO_4 Olivine I	3385	0	3.29	643
	3000	4.70	3.42	477.3
	2500	10.68	3.57	310.9
			Discontinuity	
Magnesium and iron silicates $(Mg, Fe)_2SiO_4$ Olivine II ?	2034	16.22	3.69—4.23	201.3
	2000	16.69	4.24	193.9
	1500	23.69	4.35	110.7
			Discontinuity	
Iron (core)	1424	24.77	4.37—8.28	101.8
	1400	25.43	8.30	96.8
	1000	34.86	8.45	35.7
	500	42.15	8.57	4.5
	0	44.45	8.60	0.0

Fig. 2. Table of pressure and density distribution in the Martian interior according to Jeffreys' Hypothesis I. (Jeffreys, 1937)

CROSS REFERENCES

The specific section number, subject, and page number to which the reader is referred is given below.

Cross Reference	Section and Subject
[1] Flattening	1.....Physical data (data summary), p.6.
[2] Spectroscopic determinations of CO_2 at polar caps and equator	5.1.....Carbon dioxide in the atmosphere (discussion), p.4.
[3] Interior models	3.4.....Iron occurrence on the surface (discussion), p.2,3.
[4] Topographic relief	3.5.....Topographic relief differences (data summary), p.1.
[5] Physical data used by Jeffreys in 1937	1.....Current values for physical data (data summary), p.6.
[6] Magnetic field—Mariner IV magnetometer data	6.....Magnetic fields at Mars (data summary), p.3; Magnetic fields (discussion), p.7-8.
[7] Rifting of the extreme outer layers	3.5.....Linear features (discussion), p.4-5; Tectonic movement (discussion), p.9.
[8] Elements and oxides	3.4.....Terrestrial and lunar compositional data (figure), p.8.

BIBLIOGRAPHY

Bellman, R., Kagiwada, R., Kalaba, and Ueno, S., 1966, A computational approach to Chandrasekhar's planetary problem: Santa Monica, Calif., RAND Corp., RM-4991-PR.

Bondi, H., and Marder, L., 1965, The integration of the equations of planetary constitution: Geophys.J., v.10, p.69-79.

Bullen, K.E., 1949, On the constitution of Mars: Mon.Not.Roy.Astron.Soc., v.109, p.688-692.

_____, 1963, An introduction to the theory of seismology, 3d Edition: Cambridge, U.Press.

_____, 1966, On the constitution of Mars, III: Mon.Not.Roy.Astron. Soc., v.133, p.229-238.

Cain, D.L., 1967, The implications of a new Mars mass and radius, p.7-9 in Supporting research and advanced development for the period December 1, 1966-January 31, 1967: Pasadena, Calif., Jet Propulsion Laboratory, Spa.Prog.Summ.37-43, v.IV (unclassified).

de Vaucouleurs, G., 1954, Physics of the planet Mars: London, Faber and Faber Ltd.

_____, 1964, Geometric and photometric parameters of the terrestrial planets: Icarus, v.3, p.187-235.

Hanselman, R.B., 1965, Effect of Martian oblateness on atmospheric pressure distribution: Avco/Rad.

Harrison, E.R., 1966, On the origin of structure in the universe: Greenbelt, Md., Goddard Space Flight Center, May.

Heiskanen, W.A., and Vening-Meinesz, F.A., 1958, The Earth and its gravity field: New York, McGraw-Hill Book Co.

Jardetzky, W.S., 1958, Theories of figures of celestial bodies: New York, Interscience.

Jeffreys, H., 1937, The density distributions of the inner planets: Mon.Not. Roy.Astron.Soc., Geophys.Suppl., v.4, p.62-71.

_____, 1959, The Earth, its origin, history, and physical constitution, 4th Edition: Cambridge, U.Press.

Loomis, A.A., 1965, Some geologic problems of Mars: Geol.Soc.Am.Bull., v.76, p.1083-1104.

Lyttleton, R.A., 1963, On the internal constitution of the terrestrial planets: Pasadena, Calif., Jet Propulsion Laboratory, Tech.Rep.32-522.

_____, 1965, On the internal structure of the planet Mars: Mon.Not. Roy.Astron.Soc., v.129, p.21, and v.130, p.95.

MacDonald, G.J.F., 1962, On the internal constitution of the inner planets: J.Geophys.Res., v.67, p.2945-2974.

Moore, P., 1965, Guide to Mars: London, Frederick Muller Ltd.

Ramsey, W.H., 1948, On the constitution of the terrestrial planets: Mon.Not. Roy.Astron.Soc., v.108, p.406-413.

Ringwood, A.E., 1962, Prediction and confirmation of olivine-spinel transition in Ni_2SiO_4, p.457-469 in Geochim.Cosmochim.Acta, v.26: Northern Ireland, Pergamon Press Ltd.

_____, 1966, Chemical evolution of the terrestrial planets, p.41-104 in Geochim.Cosmochim.Acta, v.30: Northern Ireland, Pergamon Press Ltd.

Sterne, T.E., 1960, An introduction to celestial mechanics: New York, Interscience.

Urey, H.C., 1952, The planets, their origin and development: New Haven, Conn., Yale U.Press.

Wilkins, G.A., 1966, The determination of the mass and oblateness of Mars from the orbits of its satellites, in Proceedings of the NATO Advanced Study Institute on the mantles of the Earth and terrestrial planets, March 30-April 6, 1966: U.Newcastle-upon-Tyne, in press.

SECTION 3 CONTENTS

3. SURFACE

3.1 Thermal Properties

Data Summary 1
Surface Temperatures 1
Brightness Temperature Characteristics from Infrared Data 2
Thermal Parameter 2
Discussion 2
Cross References 9
Bibliography 10

Figures
1. Sine-function fit to a typical scan passing entirely through the extensive northern brightlands of Mars in early fall 4
2. Sine-function fit to a typical scan passing through the mixed bright and dark regions in the southern hemisphere of Mars in early spring 4
3. Diurnal variation of surface temperature on the Martian equator at perihelion 5
4. Variation of brightness temperature curve parameters with Martian latitude 6
5. Correlation of Martian surface temperature with a geometric insolation parameter 7
6. Martian surface temperature 8

3.2 Ultraviolet, Visible, and Infrared Properties

Data Summary 1
Photometric Function 1
Phase Function 1
Radiance Factor 1
Normal, Geometric, and Bond Albedo 1
Magnitude 2
Spectral Reflectivity and Distribution 2
Polarization 3
Discussion 3
Photometric Function 3
Albedo, Magnitude, and Color 4
Polarization 4
Cross References 12
Bibliography 13

3.2 (cont'd)

Figures

1. Angles in Martian albedo and magnitude consideration 6
2. Table of monochromatic albedos of Mars 6
3. Geometric albedo vs. wavelength for bright and dark areas of Mars 6
4. Geometric albedo and Bond albedo vs. wavelength for Mars 6
5. Geometric albedo map of Mars 7
6. Variation of entire Martian disk in color and brightness with rotation 9
7. Angles in Martian polarization consideration 9
8. Polarization vs. phase angle for dark areas of Mars 9
9. Polarization vs. phase angle and heliocentric longitude for the 1956, 1958, 1963, and 1965 apparitions of Mars 10
10. Table of polarization differences between northern dark spots, southern dark spots, and neighboring bright areas of Mars 11
11. Polarization differences between dark and light areas of Mars vs. Martian seasons 11

3.3 Radar Properties

Data Summary 1
Discussion 2
Elements of Radar Astronomy 2
Techniques 2
Target Radar Cross Section 2
Reflection Coefficient and Dielectric Constant 2
Directivity Factor 3
Gain and Microwave Bond Albedo 3
Martian Orbital and Physical Considerations 3
Observations and Results 4
1963-USSR Measurements 5
1963-JPL Measurements 5
1965-JPL Measurements 6
1965-AIO Measurements 7
1967-JPL Measurements 7
Observational Implications 8
Cross References 14
Bibliography 15

Figures

1. Table of important results of the 1963, 1965, and 1967 radar observations of Mars 1
2. Average Mars doppler spectrogram showing power density vs. frequency; 12.5-cm wavelength 10
3. Table of radar errors for USSR, JPL, and AIO measurements of Mars 10
4. Sub-Earth points vs. Martian latitude for 1963, 1965, and 1967 oppositions, and periods of radar observations for USSR, JPL, and AIO measurements 11

3.3 (cont'd)

5. Relative sizes of rms errors and specular component sizes for 1963-JPL and 1965-JPL measurements 11
6. Table of variation in radar reflectivity of Mars at +14° and +13° latitudes with areographic longitude of central meridian; 43- and 12.5-cm wavelengths 12
7. Table of variation in radar reflectivity of Mars at +21° latitude with areographic longitude of central meridian; 12.5- and 70-cm wavelengths 13

3.4 Chemical and Physical Properties

Data Summary 1
Composition 1
Physical Properties 1
Discussion 2
Iron Occurrence 2
Stability of Terrestrial Iron Oxides 2
Limonite 2
Goethite 2
Hematite 2
Siderite 2
Iron Oxides and Silicates on Mars 3
Water and Carbon Dioxide 3
Meteoritic and Magnetic Material 4
Sizes and Size Distribution of Material 4
Polarization, Thermal, and Radar Data 5
Mariner IV Data 5
Lunar Data 5
Bearing Strength 5
Conclusions 6
Cross References 15
Bibliography 16

Figures

1. Table of general chemical ingredients in terrestrial lavas and crustal rocks, and Surveyor lunar compositional data 8
2. Comparison of the geometric albedo of Mars with the reflectance of an oxidized basalt 9
3. Phase diagram for carbon dioxide and water 9
4. Depth of lunar rock broken by meteorite impact vs. age 10
5. Cumulative percentage of particle sizes in lunar particulate layer . . 11
6. Cumulative size-frequency distribution of particles and fragments on the lunar surface at the Surveyor I, III, V, and VI mare landing sites and the Surveyor VII highland landing site 12
7. Mosaics of the lunar surface at the Surveyor I mare site on Oceanus Procellarum and the Surveyor VII highland site north of the crater Tycho 13
8. Lunar surface bearing strength vs. penetration as interpreted from Surveyor results 14

3.5 Morphology and Processes

Data Summary 1
Topographic Relief Differences 1
Craters 1
Slope Angle Distribution 1
Freeze-Thaw Features 2
Discussion 3
Relative Elevation of Light and Dark Areas 3
Thermal Data 3
Radar Data 3
Cloud Formation Movement 3
White Patterns 4
Linear Features 4
Grid System 4
Canals 5
Craters 5
Morphology 6
Distribution 6
Processes 6
Slope Angle Distribution 7
Possible Processes and Features 9
Tectonic Movement 9
Meteorite Impact 9
Volcanic Activity 9
Thermally Activated Surface Processes 10
Thermal Creep and Fracture 10
Freeze-Thaw Processes 10
Aeolian (Wind) Action 12
Conclusions 13
Cross References 31
Bibliography 33

Figures

1. Chart of the lunar grid system 14
2. Azimuth frequency of the Martian lineaments as determined from Mariner IV pictures 14
3. Table of Martian crater statistics from Mariner IV pictures 15
4. Integral crater-frequency plot of craters recognized in Mariner IV pictures 7 to 12 15
5. Table of lunar slope angle distributions 16
6. Lunar slope angle distributions for maria and for topographic highs in mountainous terrain 16
7. Lunar Orbiter II high-resolution photograph of lunar crater Copernicus from which some slope angle measurements were made 17
8. Table of estimated range of slope angles for topographic units within large craters 18
9. Table of topographic units within large craters 18
10. Table of estimated slope angles and cumulative percentages for total area of large lunar craters 18

3.5 (cont'd)

11. Lunar Orbiter III medium-resolution photograph of lunar crater Theophilus from which some slope angle measurements were made 19
12. Sedan Crater, Nevada test site, produced by nuclear detonation in alluvium 20
13. Danny Boy Crater, Nevada test site, produced by nuclear detonation in basalt 21
14. Pumice flats adjacent to one of the Mono Craters, California 22
15. Close view of pumice flats in Fig. 14, showing particle sizes of surface debris 23
16. The Fantastic Lava Beds, Lassen Volcanic National Park, California, showing a recent lava flow with blocky surface 24
17. Close view of lava flow front in Fig. 16 25
18. Schematic representation of the evolution of an ice wedge according to the contraction-crack theory 26
19. Diagrammatic sketch of a sand wedge in Taylor Dry Valley, McMurdo Sound, Antarctica 26
20. Non-orthogonal polygons in Mt. Shenk area, Queen Maud Range, Antarctica 27
21. Table of threshold wind velocity required to initiate motion in particles of optimum size on Earth and Mars 28
22. Table of settling velocities of spherical particles in relation to size for Earth and Mars 28
23. Table of estimated particle fall time from 6-km altitude for Earth and Mars 28
24. Mariner IV pictures 7 to 12, and the locations of Martian regions photographed in pictures 1 to 19 29

3.1 THERMAL PROPERTIES

DATA SUMMARY

Surface Temperatures (Figs. 1 through 6)

Solar constant: [1*]		
At mean distance (based on 1.952 ±0.02 for Earth outside atmosphere, Laue and Drummond, 1968)	0.841 ±0.02 cal cm^{-2} min^{-1}	
At aphelion	0.703 ±0.02 cal cm^{-2} min^{-1}	
At perihelion	1.023 ±0.02 cal cm^{-2} min^{-1}	
Surface temperature in equatorial zone during early northern fall (southern spring) at sunrise local time	170-210°K	(Kachur, 1966, from Sinton and Strong radiometric data)
Maximum, minimum, and mean brightness temperatures: [2]		
Maximum at equator:		
At perihelion	~305°K	(Kachur, 1966)
At aphelion	~270°K	(Kachur, 1966)
Minimum at equator	~170°K	(Kachur, 1966)
Mean amplitude of diurnal variation at equator	~96°K	(Öpik, 1966)†
Mean polar cap region (estimated):		
Winter	~145°K	(McClatchey, 1967)
Summer	~265°K	
Mean over entire planetary surface at mean distance	~220°K	(Öpik, 1966)†
Brightness temperature from 3.14-cm microwave data	211 ±20°K	(Giordmaine et al., 1959)

*See page 9 for list of cross references.

†Öpik corrected all his data upward by 5% to allow for an assumed surface emissivity of 0.81. This factor has been removed to place all results, except those for the polar caps, on the same basis.

Brightness Temperature Characteristics from Infrared Data [3]

1) The amplitude of light area daytime warming (sunrise-noon) is 90-112°K near perihelion but drops to 75-90°K for regions affected by dust storms.[4] The amplitude for dark areas is 80-100°K.

2) Nighttime temperatures (sunset-midnight, near-equatorial) drop 29-34°K for bright areas, 22-26°K for dust storm locales, and 8-11°K for dark areas.

3) Sunrise temperatures (near-equatorial) are 170-185°K for bright areas, 185-202°K for dust storm locales, and 190-210°K for dark areas.

4) Daytime temperatures show good correlation with a purely geometrical insolation parameter $(I_o \cos \theta)^{1/4}$ and therefore may be qualitatively predicted for any day or season.

(Kachur, 1966, analysis of Sinton and Strong data)

Thermal Parameter

The thermal parameter γ characterizes heating/cooling curves of various materials.

$$\gamma = (k\rho c)^{-1/2}$$

where

k = thermal conductivity in cal cm^{-1} sec^{-1} $°K^{-1}$

ρ = density in gm cm^{-3}

c = specific heat in cal gm^{-1} $°K^{-1}$

Units of γ are cm^2 $sec^{1/2}$ °K/gm-cal.

Thermal parameter of Martian brightlands	$\gamma \simeq 357$	(Kachur, 1966)

DISCUSSION

Sinton and Strong (1960) made radiometric temperature measurements of Mars in July 1954 between 0700 and 1400 Martian local time. The data were obtained with a Golay infrared detector using the 200-in. Hale telescope. Scan width was 1.5 sec of arc, compared with the 21-sec-of-arc disk diameter. Infrared radiation emitted by these small areas of the Martian disk was measured in the 7 to 13.5μ wavelength range. This corresponds to a "window" in the terrestrial atmosphere and the spectral region of maximum infrared emission expected for Mars.

Sinton and Strong limited their consideration of the thermal parameter γ to two scans which passed entirely through the extensive northern brightlands in the equatorial regions. They concluded that the best amplitude fit with the scan data corresponded to $\gamma = 100$; however, thermal phase was in better agreement with $\gamma = 250$. Atmospheric influences were not considered. Darklands were concluded to be 8°K warmer than light areas.[5]

Using the same data, Leovy (1966) took into account the interaction of planetary surface, atmosphere, and space in effects of radiation, conduction, and convection.[6] He derived γ values of 667 to 416 for the brightlands (depending on the atmosphere) and 667 for the darklands. Thermal conductivity of the soil was found to be less than that of the Martian atmosphere, leading Leovy to conclude that the surface is composed of 0.2- to 20-μ dust particles.[7]

Kachur (1966) studied the Martian surface thermal environment quantitatively on the basis of Sinton and Strong's radiometric temperature measurements. By a sine-function fitted to the data, blackbody surface temperatures given by these measurements were extended to sunrise and sunset. Sunrise temperatures were found to be in the 170 to 210°K range for brightlands, with dust storm locales and darklands having higher temperatures. Midday temperatures were shown to depend greatly on insolation, with the expected range of 259-269°K at aphelion to 295-305°K at perihelion. Kachur concluded that the surface of Mars has a thermally rigorous climate characterized by near-cryogenic temperature at night and large seasonally dependent temperature variations during the day. Radiation exerts major control of the thermal environment on Mars in contrast to control on Earth by extensive surface water.[8]

Diurnal variation on the equator at perihelion is shown in Fig. 3 (Öpik, 1966). Öpik's analysis (also employing Sinton and Strong's data) suggests that at the Martian equator 72% of the heat is radiated away between sunrise and sunset and only 28% at night.

Kachur (1966) considered the relative influence of atmosphere and soil surface to investigate further Leovy's conclusion that the thermal conductivity of the predominantly CO_2 Martian atmosphere was several times greater than that of the brightland soil. Using a reflectivity value of 0.30 (de Vaucouleurs, 1964), Kachur derived a γ value of 357, between Leovy's and Sinton and Strong's γ values, which were derived with a surface reflectivity value of 0.15. At night the surface temperature would be determined by the balance between radiation to space and conduction from below (probably a very small quantity). The dark areas probably cool only about 10°K during the night, while bright areas cool as much as 35°K.

Thus, the surface of Mars appears to be a poor thermal conductor characterized by a mean thermal parameter of 357 for northern light areas.

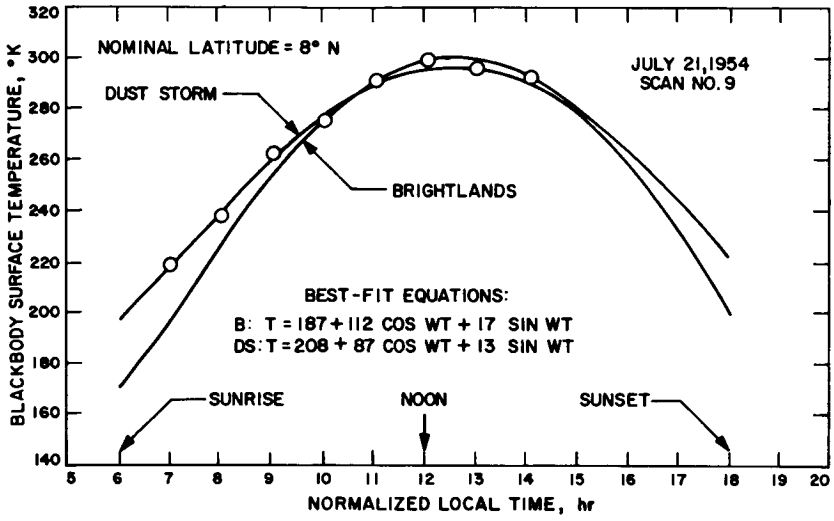

Fig. 1. Sine-function fit to a typical scan passing entirely through the extensive northern brightlands of Mars in early fall. Note the influence of local dust storms. (Kachur, 1966)

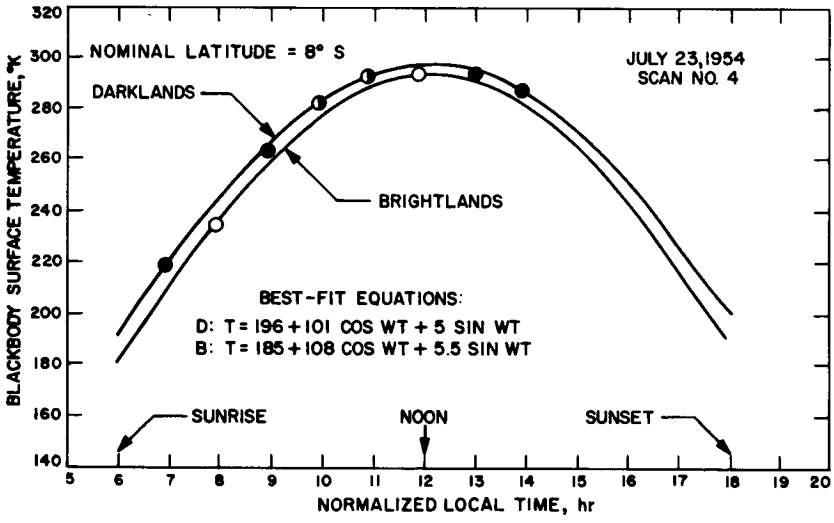

Fig. 2. Sine-function fit to a typical scan passing through the mixed bright and dark regions in the southern hemisphere of Mars in early spring. (Kachur, 1966)

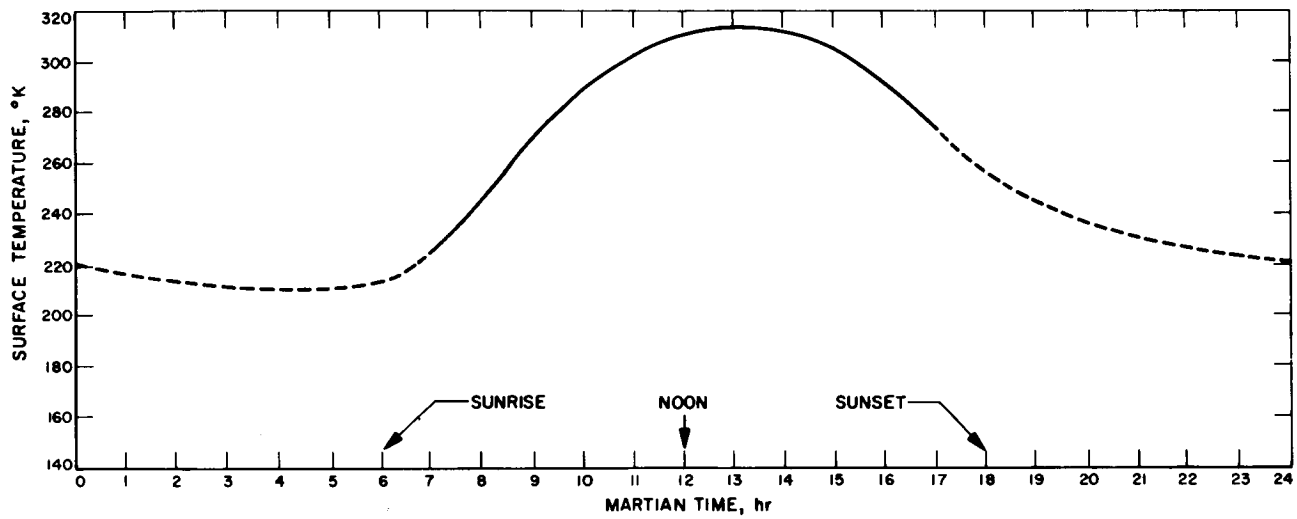

Fig. 3. Diurnal variation of surface temperature on the Martian equator at perihelion. Observed temperatures are indicated by solid line, extrapolated nocturnal temperatures by dashed line. Maximum temperature is 312°K; probable minimum at sunrise is 211°K for this warmest season. Öpik increased the measured brightness temperatures by 5% to convert them to "true" surface temperature quoted here (thus assuming an emissivity of 0.81). (after Öpik, 1966)

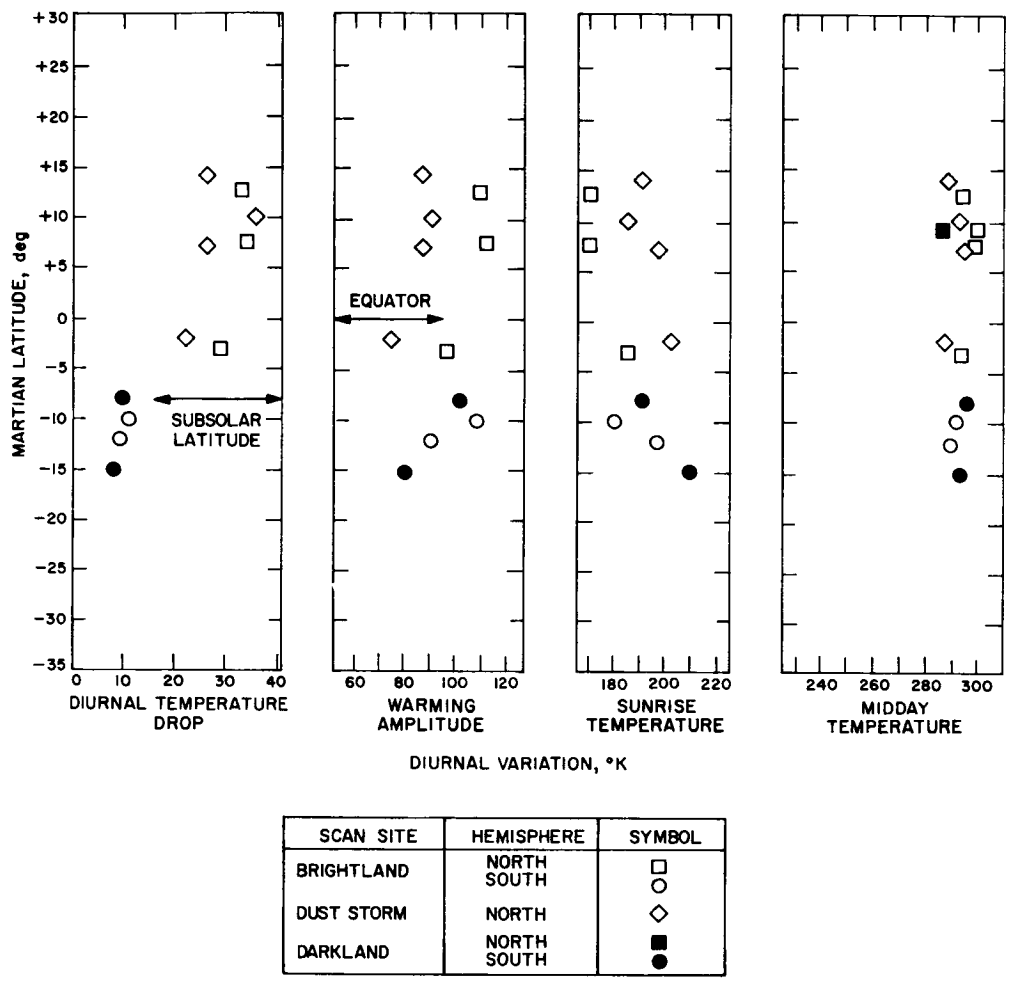

SCAN SITE	HEMISPHERE	SYMBOL
BRIGHTLAND	NORTH SOUTH	□ ○
DUST STORM	NORTH	◇
DARKLAND	NORTH SOUTH	■ ●

Fig. 4. Variation of brightness temperature curve parameters with Martian latitude. Determined from sine-function extrapolation of data over limited regions. (Kachur, 1966)

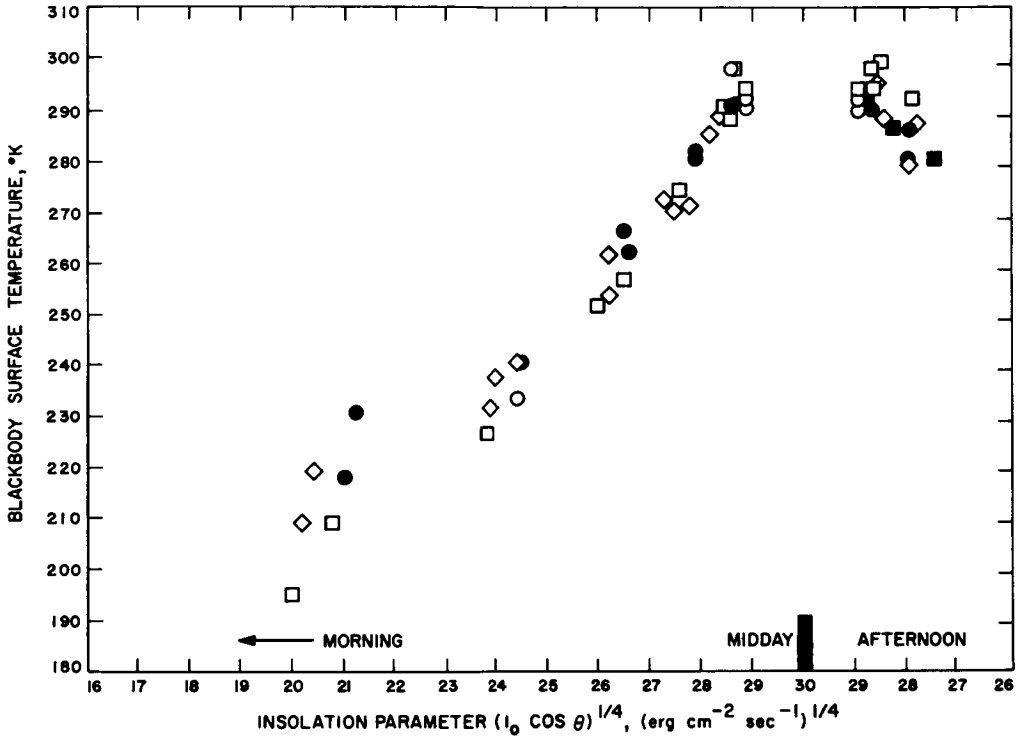

SCAN SITE	HEMISPHERE	SYMBOL
BRIGHTLAND	NORTH SOUTH	□ ○
DUST STORM	NORTH	◇
DARKLAND	NORTH SOUTH	■ ●

Fig. 5. Correlation of Martian surface temperature with a geometric insolation parameter. For 0700 to 1400 Martian local time. (after Kachur, 1966)

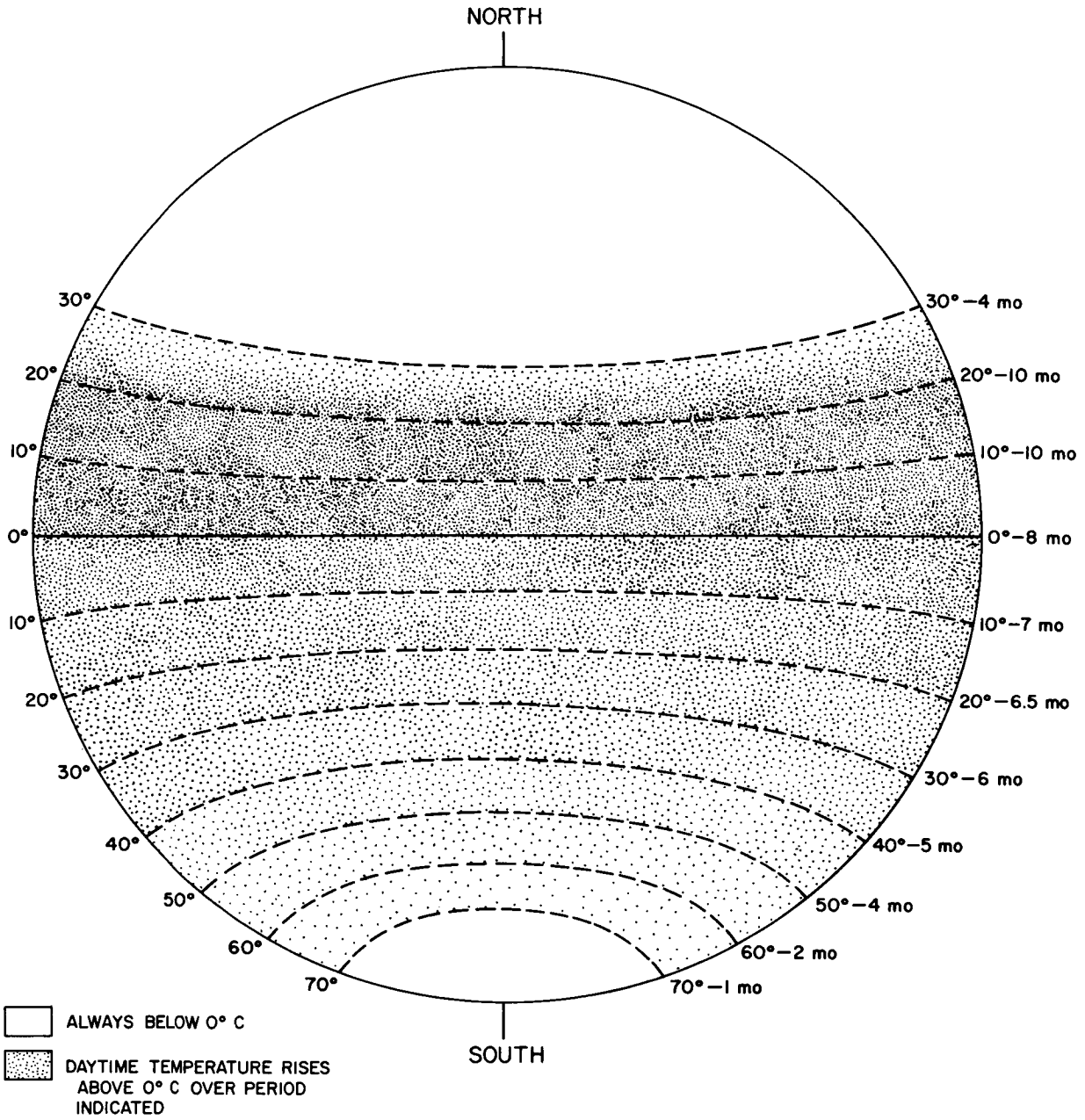

Fig. 6. Martian surface temperature. For a period of roughly two months, centered about the northern hemisphere summer solstice, temperatures over the entire surface remain below 0° C. At other seasons temperatures above 0° C occur, for at least a few daylight hours, on parts of the surface extending from -70° to +30° latitude for intervals ranging from 1 to 10 Martian months.[9] The area between 0° and +10° latitude is the most favored, with a 10-month interval in which temperatures rise daily above 0° C. Poleward of +30° and -70° surface temperatures are always below 0° C. (Leighton et al., 1967)

CROSS REFERENCES

The specific section number, subject, and page number to which the reader is referred is given below.

Cross Reference	Section and Subject
[1] Solar constant	6.....Solar electromagnetic radiation (discussion), p.5.
[2] Temperature changes	3.4.....Water and carbon dioxide on the surface (discussion), p.3. 3.5.....Crater-rim erosion (discussion), p.7; Thermally activated surface processes (discussion), p.10. 4.2.....Polar caps (discussion), p.3.
[3] Infrared data	3.2.....Ultraviolet, visible, and infrared surface properties (data summary), p.1. 6.....Absorption in the Martian atmosphere (discussion), p.6.
[4] Dust storms	4.1.....Yellow clouds (discussion), p.5; Major Martian "dust storms" (figure), p.10. 4.2.....Seasonal behavior of clouds (discussion), p.4; Seasonal changes in specific areas (figures), p.11-17; Seasonal activity maps (figures), p.19-25.
[5] Temperature difference between dark and light areas	3.5.....Thermal data—temperatures in relation to surface relief (discussion), p.3.
[6] Surface temperatures and the atmosphere	5.3.....Diurnal variation of surface and near-surface temperatures in Neubauer's model of the lower atmosphere (discussion), p.6; Diurnal, seasonal, and latitudinal variation of ground and lower atmosphere temperatures in Leovy's model (discussion), p.7; Lower atmosphere models (figures), p.10. 5.4.....The greenhouse effect (discussion), p.7.
[7] Particle sizes	3.4.....Size and size distribution of material—polarization, thermal, and radar data (discussion), p.5.
[8] Daytime air temperature at the surface—Mariner IV data	5.3.....Lower atmosphere models (figure), p.20. 5.4.....Upper Atmosphere F_2-Model (discussion), p.11.
[9] Martian months	1.....Earth-Mars calendar (discussion), p.8.

BIBLIOGRAPHY

de Vaucouleurs, G., 1964, Geometric and photometric parameters of the terrestrial planets: Wash., D.C., National Aeronautics and Space Administration, Memo. RM-4000-NASA.

Giordmaine, J.A., et al., 1959, Observations of Jupiter and Mars at 3-cm wavelength: Astron. J., v.64, n.8, p.332-333.

Kachur, V., 1966, Thermological aspects of the Martian surface environment: Mt. Prospect, Ill., Institute of Environmental Sciences, Annual Technical Meeting Proceedings Reprint.

Laue, E.G., and Drummond, A.J., 1968, Solar constant: first direct measurement: Science, v.161, p.888-891.

Leighton, R.B., Murray, B.C., Sharp, R.P., Allen, J.D., and Sloan, R.K., 1967, Mariner Mars 1964 project report: television experiment, Part I. Investigators' report, Mariner IV pictures of Mars: Pasadena, Calif., Jet Propulsion Laboratory, Tech. Rep. 32-884.

Leovy, C., 1966, Radiative-convective equilibrium calculations for a two-layer Mars atmosphere: Santa Monica, Calif., RAND Corp., Memo. RM-5017-NASA.

McClatchey, R., 1967, (Bedford, Mass., Air Force Cambridge Research Laboratories): private communication to J. de Wys.

Öpik, E.J., 1966, The Martian surface: Science, v.153, n.3733, p.255-265.

Sinton, W.M., and Strong, J., 1960, Radiometric observations of Mars: Astrophys. J., v.131, n.2, p.459-469.

Trotsky, V.S., Burov, A.B., and Alyoshina, T.N., 1968, Influences of the temperature dependence of lunar material properties on the spectrum of the Moon's radio emission: Icarus, v.8, n.3, p.423-432.

3.2 ULTRAVIOLET, VISIBLE, AND INFRARED PROPERTIES

DATA SUMMARY

Photometric Function

The photometric function $\Phi_\lambda(i,\epsilon,g)$ describes the radiance (see below) of a Martian object relative to its radiance at $i = \epsilon = g = 0°$, where i is the incidence angle, ϵ the emission angle, and g the phase angle (planetocentric angle between Sun and observer). The subscript λ indicates that the function is dependent upon wavelength.

The photometric function may also be expressed as $\Phi_\lambda(\alpha,\beta,g)$, where α is luminance longitude and β is luminance latitude. The angles α and β refer to the planetocentric coordinate system based on the instantaneous positions of the sub-observer and sub-solar points rather than to a grid system fixed with respect to the Martian surface (Fig. 1). The two sets of variables are related by the equations $\cos\epsilon = \cos\beta\cos\alpha$, and $\cos i = \cos\beta\cos(\alpha + g)$.

Phase Function

The variation with phase angle of the integrated brightness of Mars' visible hemisphere is given by the phase function $\varphi_\lambda(g)$, where

$$\varphi_\lambda(g) = \frac{1}{2\pi}\int_{-\pi/2}^{\pi/2}\int_{-\pi/2}^{\pi/2-g}\Phi_\lambda(\alpha,\beta,g)\cos\alpha\, d\alpha\, d\beta$$

Radiance Factor

The radiance factor ρ is the ratio of observed radiance of a point on the Martian surface to the radiance of a white screen placed normal to incident solar rays. Thus $\rho = \rho_o\Phi_\lambda(i,\epsilon,g)$, where ρ_o is the normal albedo.

Normal, Geometric, and Bond Albedo (Figs. 1 through 5)

Normal albedo ρ_o is the value of the radiance factor ρ at sub-observer's point of Mars at 0° phase; ρ_o varies as different points become sub-observer points at 0° phase.

Relative albedo ranges:

Light areas	0.18 to >0.3
Dark areas	<0.09 to 0.18

(from de Vaucouleurs' data)

Geometric albedo p is the average normal albedo weighted for projected area.

Bond (spherical) albedo A, sometimes referred to as Russell-Bond albedo, is the ratio of total flux reflected in all directions to total incident flux from a parallel beam (product of the geometric albedo p and phase integral q).

$$q_\lambda = 2\int_0^\pi \varphi_\lambda(g) \sin g \, dg$$

If the visual albedo A_V is defined as the albedo at 5500 Å, then $A_V = 0.159$.

Harris's (1961) monochromatic albedos of Mars are tabulated in Fig. 2. Figures 3 and 4 show wavelength dependence of the geometric albedo. Relative albedo ranges from de Vaucouleurs' data are given in Fig. 5.

Magnitude (Figs. 1 and 6)

Magnitude M is a number on an inverse logarithmic scale representing the intrinsic or apparent brightness of a celestial body; the smaller the number, the greater the brightness. 1 M = 4 db = a factor of 2.512 in brightness. The average brightness of the brightest 20 stars defines first magnitude.

Visual magnitudes:

Mars at mean opposition from Earth	V(0) = -2.01	(Harris, 1961)
Mars at 1 A.U. from Earth and from Sun; g = 0° (with Sun directly behind observer). This situation is not physically possible.	V(1,0) = -1.52	(Harris, 1961)
Sun	V(Sun) = -26.77 ±0.05	

Spectral Reflectivity and Distribution[1*] (Fig. 6)

Color indices (difference between monochromatic magnitudes at two wavelengths):	Mars	Sun
U-B	0.58	0.4
B-V	1.36	0.63
V-R	1.12	0.45
R-I	0.38	0.29

(Harris, 1961)

*See page 12 for list of cross references.

Difference between Mars
and Sun relative to visual:

U	+1.17
B	+0.71
V	0.00 (by definition)
R	-0.67
I	-0.76

(Harris, 1961)

U is magnitude in ultraviolet (3650 Å), B in blue, V in visual, R in red, and I in infrared.

Polarization (Figs. 7 through 11)

The polarization of light can be described in terms of components perpendicular and parallel to the plane of vision. By assigning a positive sign to the proportion of polarized light for the first case and a negative sign for the second, Lyot (1929) was able to describe completely the properties of the polarization of light from the whole disk of Mars by means of a single "curve of polarization."

$$P = \frac{I_1 - I_2}{I_1 + I_2} \times 100\%$$

where P is the degree of polarization, I_1 is the vibration component normal to the plane of vision (parallel to N in Fig. 7), and I_2 is the vibration component in the plane of vision (perpendicular to N in Fig. 7).

DISCUSSION

Photometric Function [2]

Mars differs from the Moon in that features on the disk vary in planetocentric angular distance from the sub-Earth point due to rotation of the planet. For example, it is assumed that the photometric function of a Martian feature may be completely determined without assuming that another feature, at a different Martian longitude, has the same photometric function. Due to the inclination of the pole of Mars, the sub-Earth point itself varies in Martian latitude from apparition to apparition. During any given Mars apparition, however, the variation is small. By observing the planet near successive oppositions, one may determine whether the photometric function is independent of latitude, except for albedo differences, as is assumed in the lunar case.

Also in contrast to the lunar case, the normal albedo may be determined directly through photometric observations of the desired Martian feature as it rotates through the sub-Earth region of the zero-phase (or near-zero-phase)

disk. The shadow of the Earth in no way interferes with illumination of Mars, even near zero phase. Extrapolation to phase zero is therefore more certain than in the lunar case, and any opposition effect should be easily observable.

Since the orbit of Mars is exterior to that of Earth, phases of Mars are limited to $\sim\pm 47°$, and extrapolation to larger phases could introduce sizable errors in the photometric function. This is further complicated by the increase in the distance of Mars and the corresponding decrease in apparent disk size as the phase angle increases. Since resolution of individual features on the disk is already seeing-limited, any decrease in apparent disk size further degrades the data.

Inasmuch as limb darkening on Mars varies with wavelength, it is probably valid to assume that the photometric function of the surface varies with wavelength, even though the major part of limb darkening may be due to the planetary atmosphere. Martian features must be observed at a number of different wavelengths to determine a complete photometric function. It is also obvious that isophotes (lines with constant radiance, except for differences in albedo) on Mars cannot possibly be meridians at any wavelength for which limb darkening is observed.

Albedo, Magnitude, and Color [3]

The geometric albedo curve rises rapidly with wavelength for light areas (Figs. 3 and 4), with flattening of the curve at about 7000 Å at an albedo of about 0.32. The dark area curve rises somewhat less sharply. (About 70% of Mars is covered by light areas, 27% by dark areas. Although not indicated by de Vaucouleurs, the remaining 3% may be the residual north polar cap.) Dark-area albedo is about half that of light areas above 5500 Å (yellow-green); bright-to-dark-area albedo ratios in green are about 2:1, in blue about 1:1. de Vaucouleurs (1964) has obtained visual geometric albedo values for the equatorial belt between latitudes ±60° (Fig. 5).

From Mariner IV pictures,[4] some taken with a green filter, some with orange, a dominant red color for those light and dark areas photographed is indicated by the relative brightness of the different frames. The Martian surface undergoes seasonal and secular variations and changes in color. Since blue-green is the complement of orange, some of the apparent color intensity may be due to contrast.

From extensive measurements, Dollfus demonstrated that the brightness of Mars decreases with the angle between the direction of illumination and the normal to the surface. He concluded that the relative darkening difference for increasing distances from the center of the disk is the same for light and dark areas and is independent of diffusion in the atmosphere (Dollfus, 1965).[5]

Polarization [6]

Using the Lyot visual fringe polarimeter and a photoelectric polarimeter, Dollfus and Focas (1966) made a polarimetric study of Mars over a period of 18 years covering nine successive apparitions. Variation of the polarization for the spectral range 1.05 to 0.47μ was examined, and the polarization

curves for the bright and dark areas of Mars were reproduced for each of the apparitions for the 0.61μ wavelength.

Observed proportions of polarization amount to a few tens of thousandths. Measurements by different stations agree to one thousandth and do not seem to depend upon observatory, observer, or instrument. Figure 9 gives curves for polarization versus heliocentric longitude and phase angle for the 1956, 1958, 1963, and 1965 apparitions.

Polarization versus phase angle for dark areas comparing equatorial markings to northern hemisphere features in Martian spring is shown in Fig. 8. The cycle of seasonal variation of dark areas polarization (Dollfus and Focas, 1966) is given in Fig. 11 resulting from data in Fig. 10.

The seasonal variation of the polarizing properties of Martian dark areas closely follows the variation of their darkness at Martian spring. Dollfus and Focas (1966) interpret this as a seasonal modification of the microscopic texture of the surface. They observed that polarization differences are greatest at the end of spring and occur principally during spring and summer of each hemisphere.

Dollfus and Focas (1966) have suggested from polarization curves for iron oxides and various sample mixtures used in laboratory studies that one possible Martian surface model which would fit the observed data would be 10- and 200-μ particle sizes of silicate material with a covering of iron oxide (goethite). This does not, however, eliminate other possible surface models.

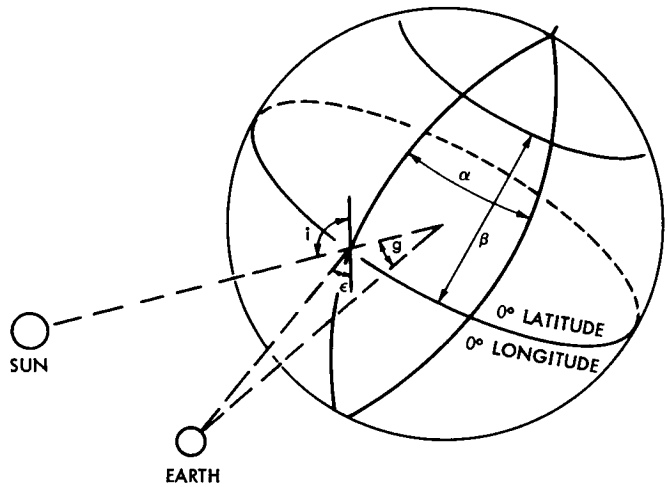

LEGEND

g = PHASE ANGLE

I = ANGLE OF INCIDENT RAYS FROM SUN

ε = ANGLE OF EMISSION TOWARD EARTH

α = LONGITUDE

β = LATITUDE

Fig. 1. Angles in Martian albedo and magnitude consideration.

λ Wavelength, Å	p(λ) Geometric albedo	q(λ) Phase integral	A(λ) Bond albedo
4050	0.049	0.95	0.047
4250	0.054	0.99	0.053
4550	0.081	1.04	0.084
4945	0.097	1.09	0.106
5430	0.131	1.19	0.16
5980	0.194	1.25	0.24
6360	0.227	1.31	0.30

Fig. 2. Table of monochromatic albedos of Mars. (Harris, 1961)

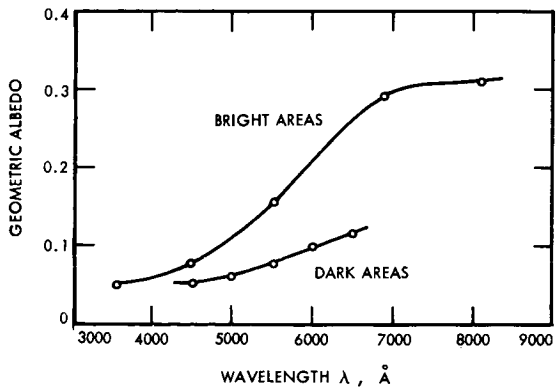

Fig. 3. Geometric albedo vs. wavelength for bright and dark areas of Mars. (Loomis, 1963)

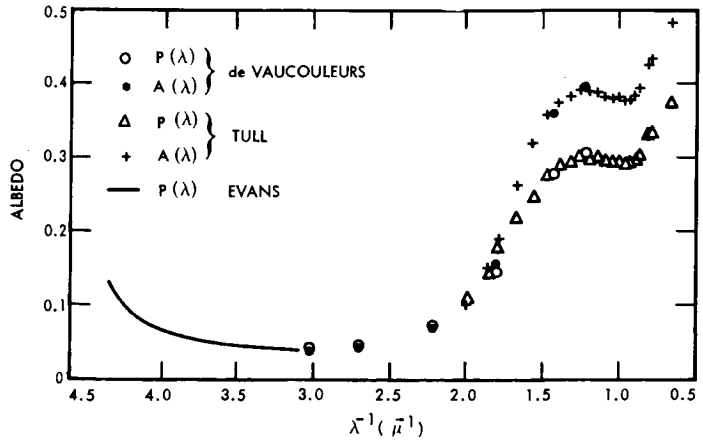

Fig. 4. Geometric albedo and Bond albedo vs. wavelength for Mars. Lower curve is geometric albedo p(λ); upper curve represents Bond albedo A(λ) = p(λ) q(λ). The curve extending to the ultraviolet from $3\mu^{-1}$ was determined by Evans from rocket spectra. (Tull, 1966)

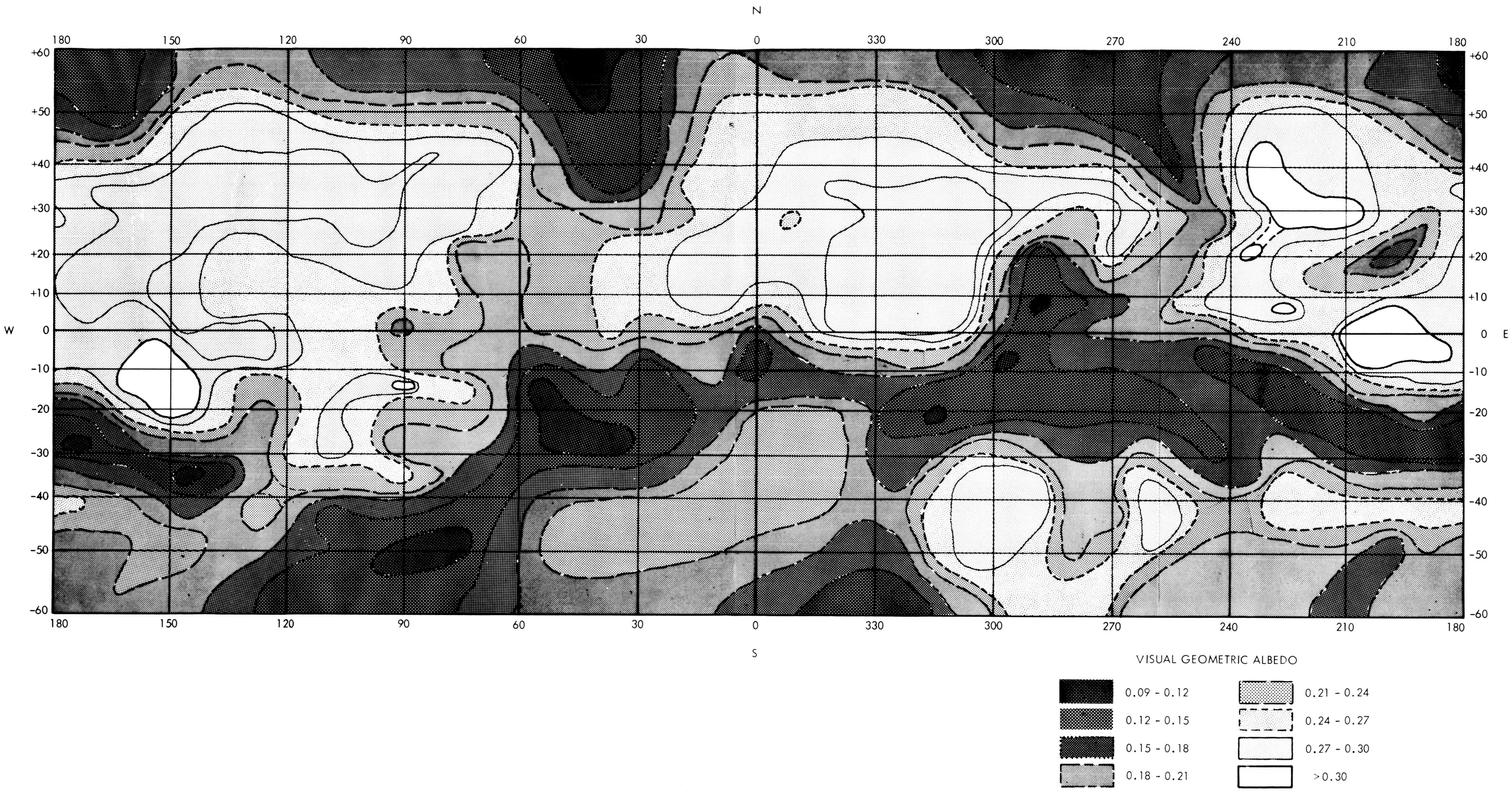

Fig. 5. Geometric albedo map of Mars. Contoured by de Wys from unpublished observational data of de Vaucouleurs.

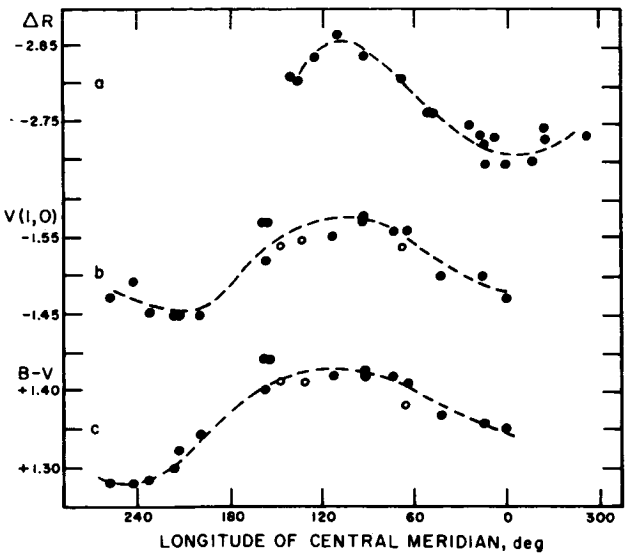

Fig. 6. Variation of entire Martian disk in color and brightness with rotation (from Harris, 1961). (a) In red light (ΔR = Mars - β Geminorum). (b) In yellow light, V(1, 0). (c) In the B-V color.

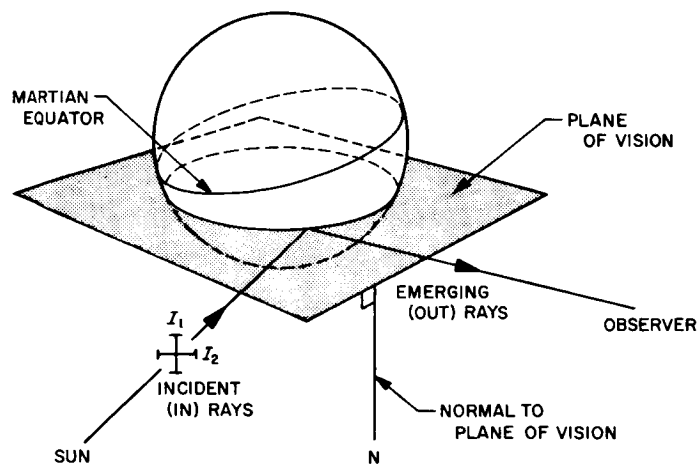

Fig. 7. Angles in Martian polarization consideration. (de Wys)

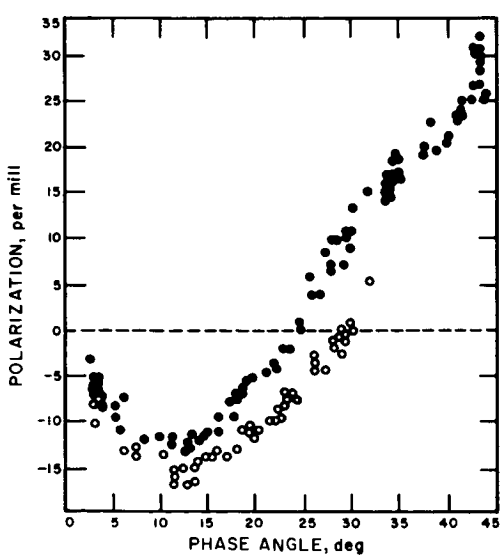

Fig. 8. Polarization vs. phase angle for dark areas of Mars. Solid circles are for equatorial markings, open circles for markings in the northern hemisphere at Martian spring. (Dollfus, 1961)

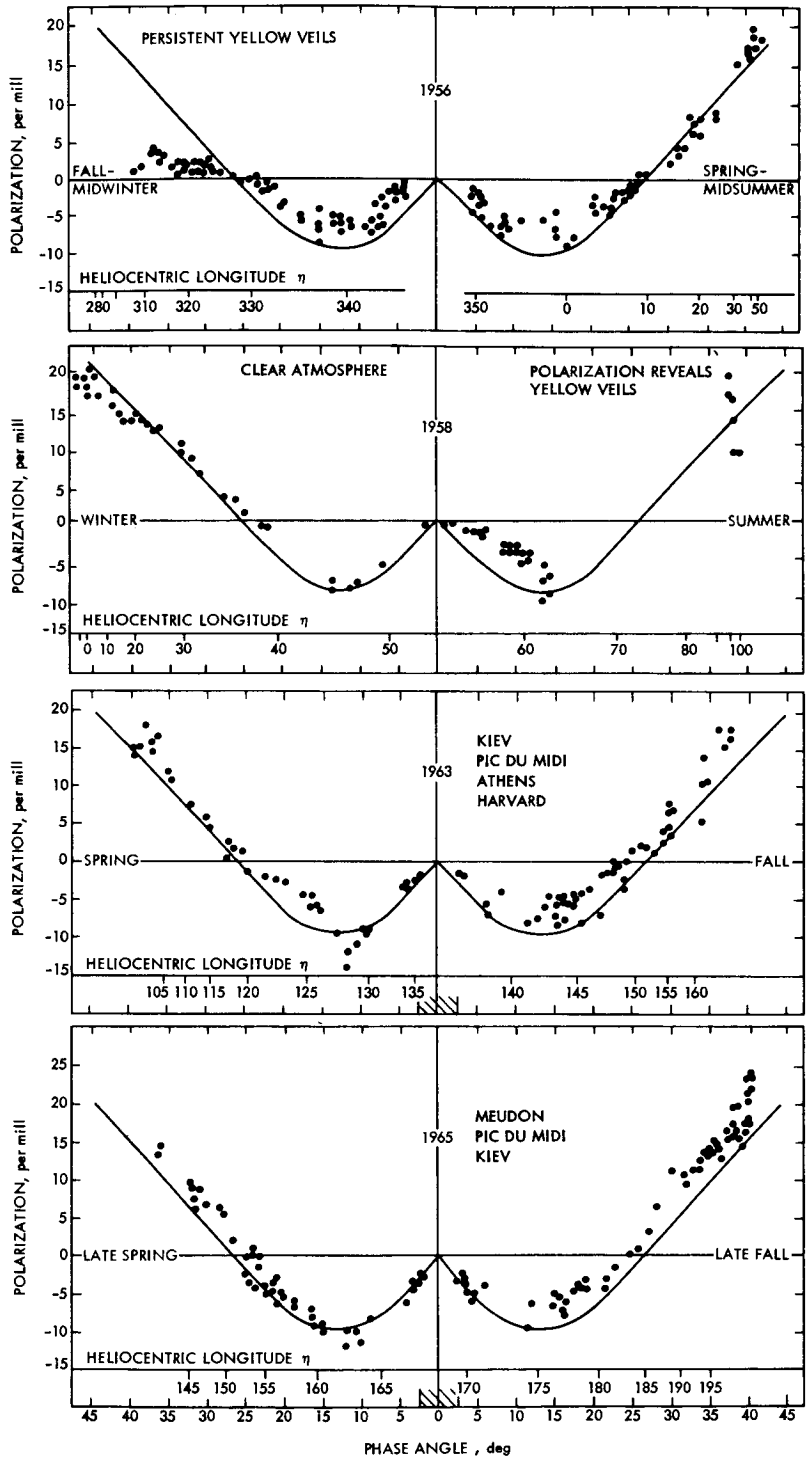

Fig. 9. Polarization vs. phase angle and heliocentric longitude for the 1956, 1958, 1963, and 1965 apparitions of Mars.[7] Martian seasons are indicated. (after Dollfus and Focas, 1966)

Year	η Heliocentric longitude (for 25° phase angle), deg	$P_N - P_S$ Polarization difference between northern and southern dark spots (for 25° phase angle), per mill	$P_N - P_O$ Polarization difference between northern dark spots and neighboring bright areas, per mill	$P_S - P_O$ Polarization difference between southern dark spots and neighboring bright areas, per mill
1948	164	-6	-4	+2
1950	197	-6	-4	+2
1952	237	-4	-1	+3
1954	253	-1	0	+1
1954	291	0	+1	+1
1956	8	+2	-0.5	-2.5
1958	36	0	0	0
1961	115	-2	-1.5	+0.5
1963	119	-2.5	-2	+0.5
1965	157	-5	-3	+2

Fig. 10. Table of polarization differences between northern dark spots, southern dark spots, and neighboring bright areas of Mars. (Dollfus and Focas, 1966)

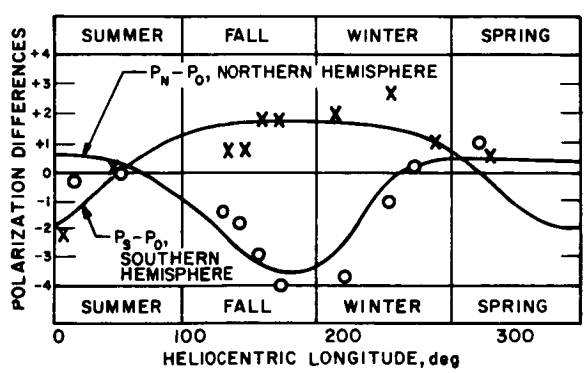

Fig. 11. Polarization differences between dark and light areas of Mars vs. Martian seasons. Data points for northern hemisphere are indicated by o's, southern hemisphere by x's. P_N-P_O and P_S-P_O are defined in Fig. 10. (This figure results from data given in Fig. 10.) (Dollfus and Focas, 1966)

CROSS REFERENCES

The specific section number, subject, and page number to which the reader is referred is given below.

Cross Reference	Section and Subject
[1] Spectral reflectivity and distribution	3.1.....Brightness temperature characteristics from infrared data (data summary), p.2 4.1.....Clouds and hazes (data summary), p.1. 6.....Solar spectral distribution (discussion), p.5, (figures), p.10,11; Absorption in the Martian atmosphere (discussion), p.6.
[2] Photometric function	1.....Planetary rotation and polar inclination (data summary), p.6,7; Oppositions and apparent disk sizes (figures), p.12,13. 3.5.....Photometric technique and elevation measurements (discussion), p.8. 5.2.....Limited usefulness of photometry in determining surface pressure (discussion), p.9,10.
[3] Albedo, magnitude, and color	1.....Physical data (data summary), p.7. 3.3.....Elevation—optical brightness and radar brightness (observational implications), p.9. 3.4.....Iron oxides and silicates (discussion), p.3. 3.5.....Elevation—thermal data and albedo differences (discussion), p.3. 4.2.....Seasonal behavior of surface features (discussion), p.5,6; Seasonal changes in specific areas (figures), p.11-17; Seasonal activity maps (figures), p.19-25.
[4] Mariner IV pictures	3.5.....Mariner IV pictures (figure), p.29.
[5] Atmosphere—general description	5.3.....Layers of the lower atmosphere (discussion), p.1,2. 5.4.....Layers of the upper atmosphere (discussion), p.1.2.
[6] Polarization	3.4.....Iron oxides and silicates (discussion), p.3; Size and size distribution of material—polarization, thermal, and radar data (discussion), p.5. 5.2.....Limited usefulness of polarimetry in determining surface pressure (discussion), p.9,10.
[7] Apparitions of Mars	1.....Earth-Mars calendars (figures), p.16,17.

BIBLIOGRAPHY

de Vaucouleurs, G., 1964, Geometric and photometric parameters of the terrestrial planets: Wash., D.C., National Aeronautics and Space Administration, Memo. RM-4000-NASA.

Dollfus, A., 1961, Polarization studies of planets, p. 343-399 in Planets and satellites; Kuiper, G.P., and Middlehurst, B.M., Editors: Chicago, U. of Chicago Press.

_____, 1965, Etude de la planete Mars de 1954-58: Ann. Astrophys., v. 28, p. 722-745.

Dollfus, A., and Focas, J.H., 1966, Polarimetric study of the planet Mars: Bedford, Mass., Air Force Cambridge Research Laboratories, Contract AF-61(052)-508, final report.

Handbook of geophysics and space environments, 1965; Valley, S.L., Editor: New York, McGraw-Hill Book Co.

Harris, D., 1961, Photometry and colorimetry of planets and satellites, p. 272-342 in Planets and satellites; Kuiper, G.P., and Middlehurst, B.M., Editors: Chicago, U. of Chicago Press.

Loomis, A.A., 1963, Some geologic problems of Mars: Pasadena, Calif., Jet Propulsion Laboratory, Tech. Rep. 32-400.

Lyot, B., 1929, Recherches sur la polarisation de la lumiere des planetes et de quelques substances terrestres: Ann. Obs. Meudon, VIII, v. 1, p. 1695.

Tull, R.G., 1966, The reflectivity spectrum of Mars in the near-infrared: Icarus, v. 5, p. 505-514.

3.3 RADAR PROPERTIES

Radar returns from Mars are predominantly direct reflections from surfaces normal to the incident radar beam. The strongest returns are usually from the sub-radar point, which may vary from +25° to -25° areographic latitude during a period of about eight years because of changes in the declination of Mars during that time. Coverage of 360° of areographic longitude requires about three weeks due to the near equality in rotational periods of Earth and Mars. A small component of power diffusely reflected from widely distributed coarse-grained material can be separated from noise to a distance of about 20° planetocentric from the sub-radar point by the JPL equipment used in 1967.

DATA SUMMARY

Attempts have been made to correlate radar reflectivity and areographic features with elevation, most notably those of Sagan et al. (1967). Preliminary results of time-delay relative ranging indicate poor correlation between reflectivity and elevation; topographic relief at +21° latitude varies from -5 to +6 km relative to the mean (Shapiro, 1968). Reliable elevation results can only come from the ranging technique. Important observational results except those on elevations are summarized in Fig. 1.

Year and facility	Wavelength, cm	Areographic latitude observed, deg	Diameter at half-power point of area of quasi-specular reflection (planetocentric angle), deg	Reflectivity[a]		Source
				Average	Range	
1963-JPL	12.5	+13	4	0.032	0.01-0.07	Goldstein and Gillmore, 1963
1965-JPL	12.5	+21	6	0.086	0.04-0.16	Goldstein, 1965; Sagan et al., 1966; Sagan et al., 1967
1967-JPL	12.5	+21	6	0.063	0.015-0.123	Carpenter, 1967
1963-USSR	43	+14[b]	~0.1 (somewhat dubious value)	0.07[b]	0.00-0.18	Kotel'nikov et al., 1964; Aleksandrov and Rzhiga, 1967
1965-AIO	70	+21	—	~0.06	0.03-0.13	Dyce, 1965

[a]Radar reflectivity is the ratio of the power received after reflection from Mars to that which would be received from a perfect reflector the size of Mars, that is, $\sigma/\pi a^2$. This quantity is also often called the relative radar cross section.

[b]The 1963-USSR measurements covered only areographic longitudes 310° to 140°.

Fig. 1. Table of important results of the 1963, 1965, and 1967 radar observations of Mars.

DISCUSSION

Elements of Radar Astronomy*

Techniques

Radar astronomy is simple in basic concept but complex in execution and detailed theory. A radar signal may be transmitted continuously, it may be coded, or it may be pulsed. Although transmitter and receiver engineering are important in practice, the frequency of the signal used is limited in principle only by the limited transparency of the Earth's atmosphere at wavelengths shorter than about 1 cm and by that of the Earth's ionosphere at wavelengths greater than about 20 m. The bandwidth of the transmitted signal may be small or large. The angular width of the transmitted beam is a function of the antenna design and may be large or small compared to the target. In the particular case of Mars the target is always very small compared to the transmitted beam. (Other experimental parameters have varied widely and have been included in the detailed discussion of observations beginning on page 4.) The radar receiver may be on the same antenna as the transmitter or on a different antenna, and there are many types of receivers and methods of data processing.

One extremely important radar technique just becoming feasible for Mars is relative ranging to the sub-radar point by measurement of the time delay between reception of successively transmitted pulses. A two-way passage of a 10-km path requires about 65 μsec for an electromagnetic wave. When the signal-to-noise ratio in a returned pulse is good enough to discriminate times of this magnitude or smaller, it is possible to begin mapping the relative altitudes of the sub-radar points.

Target Radar Cross Section

The target radar cross section σ, a concept of great importance, is defined as 4π times the ratio of the power per unit solid angle scattered back toward the transmitter to the power per unit area striking the target (Westman, 1956).

Reflection Coefficient and Dielectric Constant. The ratio of σ to the true target cross section for a perfectly smooth sphere is the reflection coefficient at normal incidence ρ_o; that is, $\sigma = \rho_o \pi a^2$, where a is the true radius of the target. For a near perfect dielectric target (conductivity zero and permeability that of free space) ρ_o can be related to the relative dielectric constant k of the target. This is a fair approximation for common terrestrial rocks and minerals. Then

$$\rho_o = \left| \frac{1 - \sqrt{k}}{1 + \sqrt{k}} \right|^2$$

*See Evans and Hagfors, 1968, for an excellent survey of the basic elements of radar astronomy.

A value for ρ_o of 0.07 implies that k is 3 under these assumptions. Usefulness of the quantity is limited by the wide variation in ρ_o over the surface, the assumptions necessary for its derivation (see the paragraphs that follow), and the lack of uniqueness in the materials which can cause a given value of k to be observed.

Directivity Factor. When the target has an irregular surface, the expression for cross section can be written $\sigma = g\rho_o\pi a^2$, where g is a "directivity factor." It has been shown by Rea et al. (1964) that g is not the gain, which can be calculated for various assumed backscattering functions, but a rather different expression of backscattering ability which is unity for a smooth dielectric sphere and which Hagfors (1964) has shown to be $g = 1 + \alpha^2$, where $2\alpha^2$ is the mean square surface slope for a sphere with a smoothly undulating surface. Thus, as applied to the quasi-specular component of the radar signal, where slopes are small, g is near unity and ρ_o is determined with some accuracy if the diffuse component can be separated from the total cross section.

Gain and Microwave Bond Albedo. Another expression for σ is given by $\sigma = G\bar{\rho}\pi a^2$, where G is the gain, i.e., the ratio of the actual backscattered intensity to that which would be obtained if the flux were scattered isotropically into 4π steradians. This gain can be calculated (8/3 for a Lambert surface) if the microwave backscattering function is assumed or could somehow be measured from a spacecraft. Now $\bar{\rho}$ is the microwave Bond albedo, which is quite distinct from the Fresnel reflection coefficient ρ_o.

Use of a Lambert surface to calculate the gain of the diffuse component of a radar return seems a reasonable approximation. When depolarization of the radar signal can be measured, as for Venus, it is possible unambiguously to separate diffuse and quasi-specular components (Carpenter, 1966), or rough estimates may be made of the relative power in quasi-specular and diffuse components by fitting scattering laws to the observations. When the quasi-specular component distinctly dominates the diffuse component, it is often assumed that $\bar{\rho} \simeq \rho_o$ (Evans and Hagfors, 1968). Such assumptions have all been used for estimating ρ_o and k in radar work.

Martian Orbital and Physical Considerations[1*]

Two factors combine to make Mars a more difficult target for radar observations than either the Moon or Venus and perhaps even more difficult than Mercury. First, the closest approach of Mars to the Earth during any given apparition varies approximately between the limits 34,000,000 and 63,000,000 mi, depending on whether the opposition is favorable (perihelic) or unfavorable (aphelic). This compares to an average closest approach (inferior conjunction) for Venus of about 26,000,000 mi. The additional distance, combined with a smaller equatorial radius—0.53 Earth radius for Mars compared with 0.96 for Venus—yields a radar return power for Mars that is from 10 (perihelic opposition) to 100 (aphelic opposition) times weaker than the returns from Venus (Pettengill, 1965).

*See page 14 for list of cross references.

The second factor which weakens radar signals returned from Mars is doppler broadening of the signal due to the comparatively rapid rotation of Mars. The doppler width for Venus is less than 1/200 that of Mars. Thus the energy per unit bandwidth of the return signal would be much smaller for Mars than for Venus, even if the total returned power were the same for both planets. The doppler width of Mercury is about 1/80 that of Mars.

In general the frequency received will be different from that transmitted because there will be a radial component of velocity between Earth and Mars. This doppler shift is important in studies of orbital mechanics but is of no planetological significance. The doppler broadening effect results from radiation reflected from the approaching limb of the planet being shifted to higher frequencies and from the receding limb to lower frequencies. A particular frequency exhibits all power reflected from a strip of Mars at a corresponding perpendicular distance from the projected axis of rotation.

A plot of the received power versus frequency is called a doppler spectrogram. Doppler spectrograms of Mars (Fig. 2) are similar to those from Venus, Mercury, and the Moon in exhibiting two components of reflection—a sharply peaked component centered at the frequency corresponding to the sub-Earth point and a shallow component falling off slowly on both sides. The peaked component is presumed due to quasi-specular reflection from a fine-grained (relative to the transmitted wavelength) surface normal to the transmitted beam. The width of this component is a measure of the median slopes present (Carpenter, 1967). The shallow component is presumed due to radiation scattered (diffused) from coarse-grained material distributed generally over the surface.[2] Topographic resolution has been about equal to the distance on the Martian surface equivalent to the width of the quasi-specular component. Integration has been required to improve the signal-to-noise ratio, resolution being reduced accordingly by the rotation of Mars during the period of integration. Ultimately, spatial resolution is dependent upon the frequency resolution of continuous wave radar and the frequency resolution and pulse width of pulsed radar.

OBSERVATIONS AND RESULTS

In each of the radar systems used, the signal was beamed at Mars for about 11 min (two-way travel time), and each transmission was followed by an 11-min reception of the reflected signal. Because of the rotation of Mars, the sub-Earth point traverses 14°.6 in Martian longitude each hour or about 2°.7 every 11 min. Thus each returned signal represents a "smeared" average of the reflected signal over 2°.7 in longitude on the Martian surface. Figure 3 tabulates values for radar errors in longitude and latitude for the 1963 and 1965 measurements. Figure 4 shows the variation in latitude of the sub-Earth points for the 1963, 1965, and 1967 oppositions of Mars. Also shown are the various periods of radar observation for USSR, JPL, and AIO investigators. Figure 5 includes the approximate uncertainty in the positions of the sub-Earth points for JPL measurements. Longitude and latitude variation is discussed in the following paragraphs where applicable.

1963-USSR Measurements (Fig. 6) (Kotel'nikov et al., 1964; Aleksandrov and Rzhiga, 1967)

Radar wavelength	43 cm (700 MHz frequency)
Period of observation	February 6 to 10, 1963
System noise temperature	Not given
Type of transmission	Alternating rectangular wave packets separated by intermissions and differing from each other by 62.5 Hz. Length of each wave packet plus intermission was 4.096 sec.
"Total" specular component:	
Frequency width	4 Hz
Planetocentric angle	0°.2 diameter
Bandwidth and resolution	80 Hz with resolution of 4 Hz
Number of observations and total integration time	48 in 8.5 hr
Average reflectivity and range	0.072 (range was 0 to 0.18)
Rms error and S/N ratio	6.5 to 12%; S/N ~2 or less

Measurements were made only from 310 through 360° to 140° Martian longitude. In addition, because of the limited number of observations and the low signal-to-noise (S/N) ratio, about all that can be said with any degree of certainty is that a Martian echo was definitely detected and that average reflectivity for the range of longitudes included in the study is of the order of 5 to 10%.

1963-JPL Measurements (Fig. 6) (Goldstein and Gillmore, 1963)

Radar wavelength	12.5 cm (2388 MHz frequency)
Period of observation	January 31 to March 2, 1963
System noise temperature	37°K
Type of transmission	CW (continuous wave); 100 kW of power on 85-ft-diameter antenna
"Total" specular component:	
Frequency width	450 Hz
Planetocentric angle	7° diameter
Bandwidth	400 Hz
Number of observations and total integration time	Over 350 in 65 hr
Average reflectivity and range	0.032 (range was 0.01 to 0.071)
Rms error and S/N ratio	1.0%; S/N ~4 (average)

The majority of the specular reflection component is contained in the 400-Hz bandwidth used, but judging from the 1965-JPL measurements there may be as little as 50% of the total (specular and diffuse) returned signal in a bandwidth this narrow. The average reflectivity and range values should thus probably be doubled to more nearly represent the total radar reflectance at 12.5 cm.

For the reflectances given, about 10 spectrograms were averaged for each 10° range in Martian longitude. Also, the Martian latitude of the sub-Earth point changed more during this particular series of runs than in any others made to date. Any attempt to assign a particular Martian longitude to any given reflectivity is therefore subject to error bars of the order of ±5°. The error bars for the latitude are somewhat more difficult to assess because all latitudes at a given longitude of the sub-Earth point have the same doppler shift in frequency and cannot be distinguished a priori in the return signal. Judging solely from the extent of the specular component in longitude and from the wandering of the sub-Earth point in latitude, it would seem that ±5° would also approximately represent the uncertainty in Martian latitude.

1965-JPL Measurements (Fig. 7) (Goldstein, 1965; Sagan et al., 1966, 1967)

Radar wavelength	12.5 cm (2388 MHz frequency)
Period of observation	Almost every night during February, March, and the first half of April, 1965
System noise temperature	27°K
Type of transmission	CW; 100 kW of power on 85-ft-diameter antenna
"Total" specular component:	
Frequency width	"Practically all" in 740 Hz
Planetocentric angle	12° diameter
Bandwidth and resolution	3700 Hz with resolution of 84 Hz
Number of observations and total integration time	Almost 1300 in ~235 hr
Average reflectivity and range	0.086 (range was 0.035 to 0.156)
Rms error and S/N ratio	2.3%; S/N ~4 (average)

Thirty-six spectrograms were plotted from the 1965-JPL measurements, each representing 10° of longitude, each the average of over 33 runs whose individual centers were within the 10° strips. The rms (root mean square) error and S/N values given apply to each individual strip. For the averaged Mars spectrogram and the average reflectivity, the S/N ratio would be larger by a factor of 6. Because of the smaller change in latitude of the sub-Earth points and the larger number of runs, the positional error bars should be about ±3° in longitude and latitude. A short discussion of the conclusions of Sagan, Pollack, and Goldstein (1967), which they based on these data, is given on page 8.

1965-AIO Measurements (Fig. 7) (Dyce, 1965)

Radar wavelength	70 cm (430 MHz frequency)
Period of observation	Under observation since November 19, 1964, but strongest returns during March, 1965
System noise temperature	Not given
Type of transmission	Pulse radar with pulse widths of 0.004 and 0.0005 sec
Specular component:	
Frequency width	Not given
Planetocentric angle	Not given
Bandwidth and resolution	Not given
Number of observations and total integration time	Not given
Average reflectivity and range	0.066 (range was 0.03 to 0.13)
Rms error and S/N ratio	Not given

As of this writing, only a preliminary report has been published for the AIO (Arecibo Ionospheric Observatory) observations of Mars. Because of the larger radar dish (1000-ft diameter), the S/N ratio should be better than that of the JPL measurements if the total integration time is comparable. The reflectance values given can at best be considered as lower bounds (within the limitations of the S/N ratio) until more is known about the bandwidth of the observations.

The reflectivity maximum near Trivium Charontis (195° longitude) and the minima near 210° and 280° longitude with relative maxima on either side of the latter seem to be features identifiable in both 1965-AIO and 1965-JPL results. However, detailed comparison of the two seems futile until more is published by the AIO investigators.

1967-JPL Measurements (Fig. 7) (Carpenter, 1967)

Radar wavelength	12.5 cm (2388 MHz frequency)
Period of observation	Almost every night during April and May, 1967
System noise temperature	20°K
Type of transmission	CW; 100 kW of power on 85-ft-diameter antenna
Receiving antenna	210-ft parabola
"Total" specular component:	
Frequency width	"Total" not given. Width at half-power point was 400 Hz.
Planetocentric angle	"Total" not given. Width of typical spectrum at half-power point was 6°.

Bandwidth and resolution	3700 Hz, resolution not given
Number of observations and total integration time	141 observations, total time not given
Average reflectivity and range	0.063 (range was 0.015 to 0.123)
Rms error and S/N ratio	Not given; S/N ~23

OBSERVATIONAL IMPLICATIONS

Important results of observations are summarized in Fig. 1 and detailed in the preceding paragraphs and the other figures. In comparison, the radar reflectivity of Venus at 12.5 cm is 0.114 (Carpenter, 1966), and the diameter, at the half-power point, of the area of quasi-specular reflection is 8° planetocentric, equivalent in area to 16° on Mars (Carpenter, 1968). This would indicate Venus is somewhat smoother than Mars on the average, but there are very large variations in this roughness over the surface of both bodies.

Interpretation of passive microwave temperatures requires a value for ϵ_λ, the emissivity at wavelength λ. It is generally assumed that $\epsilon_\lambda = 1 - \rho_\lambda$, where the values of $\sigma/\pi a^2$ quoted are used for ρ_λ at the appropriate wavelengths. Considering the wide variation of the radar reflectivity with location and the fact that it is really not $\bar{\rho}_\lambda$ (see pages 2 and 3), this is a useful but not extremely accurate procedure.

Dollfus, in a private communication quoted by Sagan, Pollack, and Goldstein (1966), estimates that the uncertainties in the configuration and positions of Martian optical features have been reduced to 2 or 3° at most, with the positions of centroids of Martian features better determined than their shapes. Since it is natural to attempt to correlate radar features with optical features, as Sagan et al. have done, the uncertainties in the positions of each must be taken into consideration. With ±3° errors in the longitude and latitude for the radar and ±2° for the optical features, any correlation between the two must involve uncertainties of the order of $\pm\sqrt{3^2 + 2^2}$, or about ±4° (Fig. 3). The relative sizes of these errors as well as the sizes of the specular reflection components for the 1963-JPL and 1965-JPL data are given in Fig. 5.

There is a small amount of uncertainty in the positions of the centroids of the spectrograms given in connection with the 1965-JPL data. This uncertainty arises from two sources: first, from the small amount of uncertainty in the relative velocity of the radar antenna and the Martian sub-Earth point and second, from the randomness of the position of the centroid due to background noise. The combined magnitude of these two factors is of the order of 1° planetocentric or less and may thus be neglected in interpretation of the data.

"For reasons of economy of hypothesis," Sagan, Pollack, and Goldstein (1967) assume that Martian dark areas are either all elevations or all depressions, and, it seems, primarily on the basis of apparent slopes in the region of Syrtis Major, the dark areas are equated to elevations.[3] This interesting "mapping" attempt seems not to be verified by more recent work with newer equipment.

Based upon the 1967-JPL radar observations, Carpenter (1967) concludes that "It would appear that the visual and radar appearance of Mars show no clear relationship and that each corresponds to a different aspect of the planet's surface." Shapiro (1968), discussing time-delay mapping of the surface, states that "An unexpected finding was the lack of a strong correlation between elevation and either optical or radar brightness." [4]

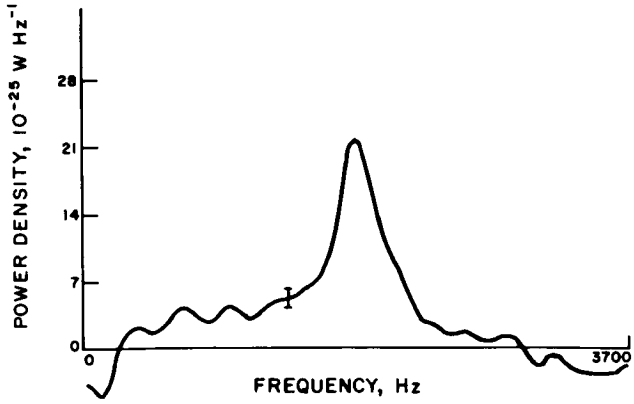

Fig. 2. Average Mars doppler spectrogram showing power density vs. frequency; 12.5-cm wavelength. 1965-JPL measurements. (Goldstein, 1965)

Radar error	Date, investigator, and wavelength			
	1963-USSR 43 cm	1963-JPL 12.5 cm	1965-JPL[a] 12.5 cm	1965-AIO 70 cm
Longitude				
Rotation	±1°.4	±1°.4	±1°.4	±1°.4
Specular component size	±0°.1	±3°.5	±3°.3	—
Averaging process, 10° strips	—	±5°	±5°	—
Estimated total, rms (Miner)	—	±5°	±3°	—
Latitude				
Inclination changes	±0°.2	±1°.3	±0°.3	±0°.1
Specular component	±0°.1	±3°.5	±3°.3	—
Estimated total, rms (Miner)	—	±5°	±3°	—

[a]Estimated error of correlation with optical features: ±4° rms.

Fig. 3. Table of radar errors for USSR, JPL, and AIO measurements of Mars. Values given are in areographic degrees.

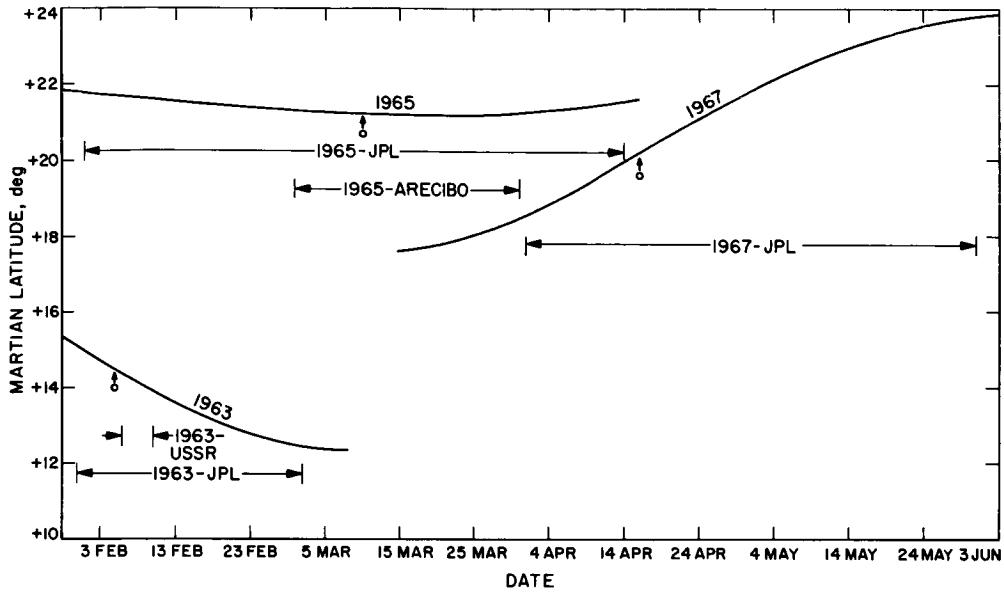

Fig. 4. Sub-Earth points vs. Martian latitude for 1963, 1965, and 1967 oppositions, and periods of radar observations for USSR, JPL, and AIO measurements. Small o's under each curve show approximate time of opposition, i.e., closest approach, of Mars for each year (American Ephemeris and Nautical Almanac, 1963, 1965, 1967).

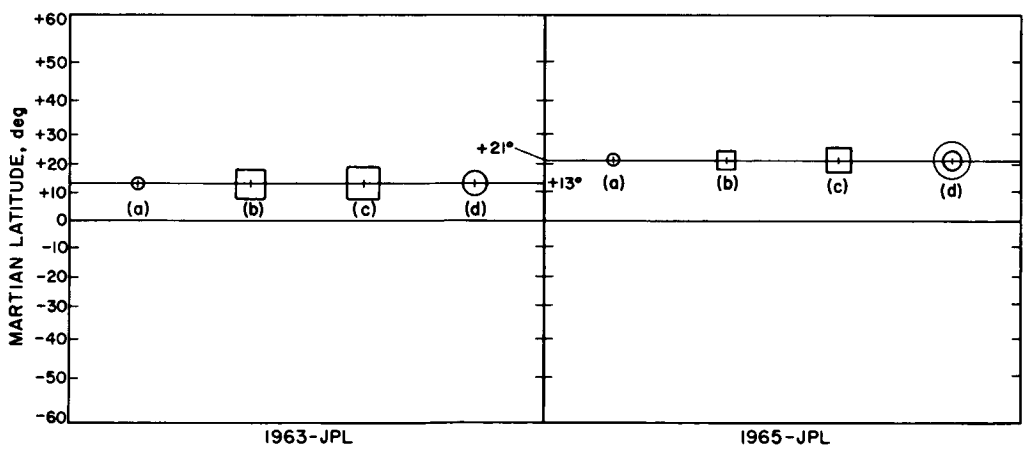

Fig. 5. Relative sizes of rms errors and specular component sizes for 1963-JPL and 1965-JPL measurements. (a) Approximate uncertainty in positions of Martian optical features. (b) Approximate uncertainty in positions of sub-Earth points for radar data given. (c) Error associated with attempted correlation between radar features and optical features: combination of (a) and (b). (d) Size of specular component as estimated by investigators (see pages 5 and 6 of text).

Longitude of central meridian, deg	Radar reflectivity		
	1963-USSR 43-cm wavelength +14° latitude		1963-JPL[a] 12.5-cm wavelength +13° latitude
	Reflectivity	Rms error	
5-15	0.08	0.065	0.019
15-25	0.09	0.085	0.033
25-35	0.18	0.07	0.031
35-45	0.04	0.065	0.023
45-55	0.05	0.07	0.018
55-65	0.11	0.07	0.019
65-75	0.03	0.07	0.015
75-85	0.08	0.06	0.021
85-95	-0.07[b]	0.07	0.025
95-105	0.00	0.075	0.010
105-115	-0.01[b]	0.085	0.031
115-125	0.19	0.075	0.039
125-135	-0.02[b]	0.085	0.019
135-145			0.026
145-155			0.035
155-165			0.032
165-175			0.015
175-185			0.023
185-195			0.015
195-205			0.050
205-215	1963-USSR measurements did not cover areographic longitudes 140° to 310°		0.019
215-225			0.033
225-235			0.039
235-245			0.043
245-255			0.064
255-265			0.055
265-275			0.062
275-285			0.071
285-295			0.057
295-305			0.039
305-315	0.16	0.12	0.026
315-325	0.09	0.10	0.012
325-335	0.06	0.10	0.023
335-345	0.10	0.12	0.035
345-355	0.10	0.065	0.031
355-5	0.12	0.075	0.044

[a]For 1963-JPL measurements, rms error is everywhere equal to ±0.01.

[b]Points distorted due to large weight of random errors.

Fig. 6. Table of variation in radar reflectivity of Mars at +14° and +13° latitudes with areographic longitude of central meridian; 43- and 12.5-cm wavelengths. 1963-USSR and 1963-JPL measurements (Aleksandrov and Rzhiga, 1967, and Goldstein and Gillmore, 1963, respectively).

Longitude of central meridian, deg	Radar reflectivity		
	1965-JPL[a] 12.5-cm wavelength +21° latitude	1965-AIO[b] 70-cm wavelength +21° latitude	1967-JPL[b] 12.5-cm wavelength +21° latitude
5	0.105	0.060	0.055
15	0.095	0.060	0.060
25	0.125	0.045	0.090
35	0.085	0.035	0.070
45	0.080	0.075	0.070
55	0.105	0.075	0.050
65	0.070	0.075	0.045
75	0.080	0.075	0.025
85	0.055	0.085	0.015
95	0.035	0.045	0.020
105	0.085	0.065	0.010
115	0.080	0.045	0.040
125	0.085	0.060	0.055
135	0.050	0.040	0.030
145	0.050	0.045	0.020
155	0.045	0.050	0.060
165	0.065	0.035	0.050
175	0.095	0.045	0.045
185	0.105	0.070	0.040
195	0.115	0.120	0.085
205	0.105	0.075	0.085
215	0.035	0.030	0.035
225	0.085	0.070	0.055
235	0.115	0.070	0.055
245	0.160	0.090	0.120
255	0.105	0.095	0.090
265	0.095	0.090	0.070
275	0.130	0.050	0.100
285	0.065	0.060	0.040
295	0.115	0.095	0.055
305	0.060	0.075	0.095
315	0.070	0.040	0.060
325	0.085	0.040	0.075
335	0.080	0.035	0.055
345	0.070	0.030	0.060
355	0.135	0.040	0.085

[a]For 1965-JPL measurements, rms error is everywhere equal to ±0.023.

[b]Rms error not given by investigators.

Fig. 7. Table of variation in radar reflectivity of Mars at +21° latitude with areographic longitude of central meridian; 12.5- and 70-cm wavelengths. 1965-JPL, 1965-AIO (Arecibo Ionospheric Observatory), and 1967-JPL measurements (Goldstein, 1965, Dyce, 1965, and Carpenter, 1967, respectively).

CROSS REFERENCES

The specific section number, subject, and page number to which the reader is referred is given below.

Cross Reference	Section and Subject
[1] Orbital and physical considerations	1.....Orbital and physical data, entire section.
[2] Fine-grained and coarse-grained material	3.4.....Size and size distribution of material—polarization, thermal, and radar data (discussion), p.5.
[3] Topographical interpretations—dark areas and slopes	3.5.....Relative elevation of light and dark areas (discussion), p.3; Slope angle distribution (discussion), p.7. 4.2.....Seasonal changes in specific dark areas (figures), p.11, 13; Seasonal activity maps (figures), p.19-25.
[4] Optical brightness	3.2.....Ultraviolet, visible, and infrared properties (data summary), p.1.

BIBLIOGRAPHY

Aleksandrov, Yu.N., and Rzhiga, D.N., 1967, Comparison of the reflectivity of Mars at 40 and 12.5 cm from radar observations during the 1963 opposition: Soviet Astronomy - AJ, v.10, p.646-649.

The American ephemeris and nautical almanac, 1963, 1965, 1967: Wash., D.C., U.S. Government Printing Office.

Carpenter, R.L., 1966, Study of Venus by cw radar—1964 results: Astron.J., v.71, p.142-152.

_____, 1967, 1967 radar observation of Mars, p.157-160 in Supporting research and advanced development for the period October 1-November 30, 1967: Pasadena, Calif., Jet Propulsion Laboratory, Spa. Prog. Summ. 37-48, v.III.

_____, 1968, (Pasadena, Calif., Jet Propulsion Laboratory): private communication to R. Newburn.

Dyce, R.B., 1965, Recent Arecibo observations of Mars and Jupiter: Radio Sci.—J.Res.NBS, v.69D, p.1628-1629.

Evans, J.V., and Hagfors, T., 1968, Radar astronomy: New York, McGraw-Hill Book Co.

Goldstein, R.M., 1965, Mars: radar observations: Science, v.150, p.1715-1717.

Goldstein, R.M., and Gillmore, W.F., 1963, Radar observations of Mars: Science, v.141, p.1171-1172.

Hagfors, T., 1964, Backscattering from an undulating surface with applications to radar returns from the Moon: J.Geophys.Res., v.69, p.3779-3784.

Kotel'nikov, V.A., et al., 1964, Radar studies of the planet Mars in the Soviet Union: Soviet Physics—Dokl., v.8, p.760-763.

Pettengill, G.H., 1965, A review of radar studies of planetary surfaces: Radio Sci.—J.Res.NBS, v.69D, p.1617-1623.

Rea, D.G., Hetherington, N., and Mifflin, R., 1964, The analysis of radar echoes from the Moon: J.Geophys.Res., v.69, p.5217-5223.

Sagan, C., Pollack, J.B., and Goldstein, R.M., 1966, Radar doppler spectroscopy of Mars, I. Elevation differences between bright and dark areas: Wash., D.C., Smithsonian Inst. Astrophys. Obs., Spec. Rep. 221.

_____, 1967, Radar doppler spectroscopy of Mars, I. Elevation differences between bright and dark areas: Astron.J., v.72, p.20-34.

Shapiro, I.I., 1968, Radar observations of the planets: Sci. Am., v.219, n.1, p.28-37.

Westman, H.P., Editor, 1956, Reference data for radio engineers: New York, International Telephone and Telegraph Corp.

3.4 CHEMICAL AND PHYSICAL PROPERTIES

The only data available for the determination of Martian surface composition are spectral reflectance and polarization curves, which suggest a result but often do not uniquely define one. Similarly, there is some indication of the physical condition of large areas of the Martian surface from polarization and thermal conductivity studies implying the presence of fine particles. Information presented in this section has been derived from interpretations of related Martian and lunar observations and from laboratory studies.

DATA SUMMARY

Composition[1*]

Extrapolating from what occurs on the Earth, material components on the Martian surface may include volcanic and extruded material (lava), outgassing sublimates, and meteoritic materials of all types, including dust. The chemical ingredients are virtually the same in all terrestrial lava types but vary considerably in relative proportions. Figure 1 is a tabulation of chemical ingredients in terrestrial lava and crustal rocks and also includes lunar compositional information from the Surveyor alpha-scattering instruments. Outgassing and reaction products that may be present on the Martian surface include carbonates (calcite, magnesite, and dolomite), sulfur, clays, sericite, opal, and talc. The composition and density of the meteoritic flux in the vicinity of Mars have not been measured. Meteoritic minerals found on Earth are given in many standard reference works, e.g., Mason (1962). Observations indicate the possible large-scale presence of basic basaltic-type rock stained and/or mixed with iron oxides (Adams, 1968).

Physical Properties

Particle sizes (<1 mm)	See Fig. 5 (theoretical study based on lunar data)
Size-frequency distribution of particles, fragments, and blocks ($\gtrsim$1 mm)	See Fig. 6 (lunar analog, Surveyor data)
Preferred static bearing strength (lunar analog):	
Up to 1-mm depth	$<0.1 \times 10^5$ dyn cm^{-2} (from imprints of small rolling fragments)
1- to 2-mm depth	0.2×10^5 dyn cm^{-2} (from imprints of alpha-scattering instrument sensor head, Surveyor VII)

*See page 15 for list of cross references.

At about 2-cm depth	1.8×10^5 dyn cm^{-2} (from imprints of crushable block, Surveyors VI and VII)
At 5-cm depth	4.2 to 5.5×10^5 dyn cm^{-2} (from footpad penetration analysis, Surveyor I)
10^5 dyn cm^{-2} = 1 Newton cm^{-2} (N cm^{-2})	(Choate et al., 1968)

Deep deposits of windblown dust having far lower bearing strength could exist in wind shadows.

DISCUSSION

Iron Occurrence

Some models suggest that Mars has not been differentiated to the extent that a nickel-iron core has formed, but rather that it is a fairly homogeneous planet. Since there is still controversy about the nickel-iron-core model of the Earth, this may not represent a substantial argument for the amount of surface differentiation on a planet. It has been suggested that Mars has a lower iron content than Earth, the iron being distributed throughout the planet.[2] Oxides of iron may be common on the surface; however, with the high atmospheric content of CO_2, the stable form of iron on the Martian surface could be siderite, $FeCO_3$ (O'Leary, 1967).[3]

Stability of Terrestrial Iron Oxides

Limonite. The term limonite—from the Greek meaning meadow, in allusion to its occurrence as bog ore in meadows and marshes—applies to a natural hydrated iron oxide mixture, frequently occurring with impurities. Most commonly, a limonite deposit includes the minerals goethite and lepidocrocite as well as iron oxides and hydroxides of undetermined crystallization and hydration.

Goethite. Goethite, $Fe(OH_3)$, is the stable iron oxide under ground-water conditions all over the Earth. Alkaline solutions stabilize goethite and other hydrates. Goethite may form from hydrolysis of silicates and hydration of hematite. In the laboratory a 10% weight loss (of water) is necessary to convert goethite to hematite (Loomis, 1967).

Hematite. Both hematite, Fe_2O_3, and goethite occur naturally in terrestrial soils. However, where hematite coexists with goethite (tropics) it probably is not stable. Hematite may be formed by baking, as a surface product of goethite, but would not rehydrate each time it rains; therefore, hematite would be expected in areas of dry climate with average temperatures of 60 to 70° F. Hematite may also be formed by the weathering of magnetite, Fe_3O_4.

Siderite. Siderite, $FeCO_3$, occurs in large deposits in terrestrial sedimentary rocks. Crystalline specimens are found in sulfide ore veins formed hydrothermally. Siderite is slightly soluble in cold hydrochloric acid.

Iron Oxides and Silicates on Mars[4]

A large amount of observational data on the geometric albedo of Mars as a function of wavelength has accumulated during the past decade, with excellent agreement among the many workers. These data are summarized in Fig. 2, modified from McCord and Adams (1968). The curve exhibits two major features: a strong broad absorption reaching a minimum below 0.4μ and a shallow broad absorption centered near 1.0μ. In some data there has been a hint of a very weak broad feature near 0.87μ. Such broad features are characteristic of electronic transitions in solids (Adams, 1968).

Early attempts to identify materials responsible for the characteristic Martian spectral reflectance were little more than educated guesses because of the lack of good laboratory comparison spectra of rocks and minerals. Identifications are always complicated by the strong dependence of intensity of the spectral features upon particle size.

The best interpretation today is that the blue absorption is due to ferric ions in the oxide or semi-hydrated form (McCord and Adams, 1968), while the 1μ absorption is due to ferrous ions in a silicate lattice (Adams, 1968). The so-called "limonite band" at 0.87μ is also caused by ferric ions but is not necessarily caused only by that ion as limonite. An excellent match with Martian observations is given by Adams' laboratory curve for an oxidized basalt, shown as the solid line in Fig. 2. Adams' preparation technique involved oxidation with dilute nitric acid, which dissolved some magnetite and resulted in precipitation of ferric oxides and hydroxides as a stain on the rock particles.

A great deal of laboratory work and telescopic observation are still needed to strengthen contemporary theories about the Martian surface. It is unlikely that detailed surface composition can be obtained short of in situ analysis. Nevertheless, there is a reasonable indication, well grounded in observation and laboratory study, that large areas of Mars may be partiallv composed of materials similar to terrestrial basic basalts stained and/or mixed with iron oxides.

Water and Carbon Dioxide[5]

On the phase diagram (Fig. 3) it can be seen that under prevailing Martian conditions H_2O could occur briefly in the liquid state from >0° to about 5 or 10° C.* The liquid phase, being subject to rapid evaporation, would exist for only short time periods in this restricted temperature range, and the solid phase, if at the surface, would outgas rapidly. Water in either the liquid or solid state would not be detected by spectroscopic methods presently being used. Observed radar data are not inconsistent with water ice, which has a dielectric constant of 3.2. Since only a trace of water vapor (in the atmosphere of Mars) has been observed spectroscopically and solid water ice would rapidly outgas, liquid or solid water appear to be possible but improbable surface features.

*Phase diagram relationships are based on pure H_2O and CO_2. Any water on Mars probably would contain dissolved salts and CO_2, thus changing the relationship somewhat.

The polar caps are probably mostly solid CO_2 with possibly a core of H_2O ice (Fig. 3). A dark band appears at the edge as the cap begins to recede. This has often been interpreted as melt water, but it seems unlikely that such could really be the case. One of many hypotheses about the nature of the wave of darkening, which moves from the pole to across the equator in Martian spring, is that a melting process of a superficial layer of crystalline H_2O and immediate evaporation or other freeze-thaw phenomena may be indicated.[6] If volcanism is present on Mars, liquid H_2O may exist in adjacent subsurface areas. Any liquid surface H_2O on Mars would contain dissolved CO_2 and thus would become a dilute carbonic acid.

According to a discussion of Martian observations and phase diagram relationships of CO_2 and H_2O (Wade and de Wys, 1968), observed frost phenomena could represent an H_2O sublimate since frost patches have been observed to endure through an entire day and to withstand the accompanying thermal regime.

Mean annual temperatures for all latitudes on Mars are below the freezing point for water, and in polar and subpolar areas theoretical calculations show that temperatures drop below the condensation point for CO_2 during the winters. Small quantities of ice particles could accumulate in cracks which extend below the annual 0° C isotherm and survive. In fact the possibility of perennially frozen ground cannot be ruled out.[7] On the other hand, any CO_2 crystals that settle to such depths will vaporize because of the warmer environment a few centimeters below the surface.

Meteoritic and Magnetic Material[8]

In the Martian areas photographed by Mariner IV, crater density estimates have varied considerably with the counter, depending upon his interpretation of the pictures. The Mariner IV experimenter team has concluded that the most optimistic count results in a crater number density slightly smaller than that of the lunar highlands (Leighton et al., 1967). Sharp (1968) has noted considerable evidence of modification of Martian craters, however, and concludes that erosion or deposition have substantially modified them compared with lunar highlands craters. If impacts are the cause of most Martian craters, an amount of meteoritic debris exceeding that postulated for the Moon may be present (Fig. 4). From Surveyor magnet data (de Wys, 1968) and from that of the alpha-scattering instrument (Turkevich et al., 1968), meteoritic iron addition to the lunar surface material tested appeared to be less than 0.25%. If meteoroid fluxes are 4 to 26 times greater for Mars (Sharp, 1967), there will be a much greater percentage of magnetic material. If this is indeed the case, the surface material will have a higher specific gravity, and this will affect mechanical properties to some extent.

Sizes and Size Distribution of Material

There is no direct information on particle size-frequency distribution curves for Martian surface material. The lunar model may be used as the closest analog (Figs. 5 and 6).

Polarization, Thermal, and Radar Data [9]

Dollfus and Focas (1966) indicate that an excellent fit to their polarimetric data can be obtained by mixtures of iron oxide particles of all sizes smaller than 200 μ, in which smaller particles envelop the larger ones. A finely pulverized or highly porous surficial layer is also indicated by the thermal parameters. Kachur (1966) suggests that the thermal regime on Mars will produce extensive cracking with accompanying particle-size reduction.

Radar data for Mars indicate a 6°-diameter (planetocentric) area of intense reflection from the planet with a wavelength of 12.5 cm and a 0°.2-diameter area with 40-cm wavelength. This is quite a drop in the size of the area giving intense reflection, a considerably greater area-size change than for the lunar returns. This has been interpreted as due to far more surface roughness on Mars on a scale of 12.5 cm than on a scale of 40 cm. Unfortunately the 40-cm data are very poor.

Mariner IV Data

The resolution is about 3 km on the best of the Mariner IV pictures of the Martian surface; therefore, no direct data are obtained as to the particulate layer. Erosion of crater rims appears to be more active than on lunar crater rims. This suggests more fine-grained material, although if processes are chiefly mass wastage or thermal creep activity, information concerning the fine-grained element is not indicated. A softening of the rim outlines could suggest covering by a fine-grained particulate layer. However, since the resolution is no better than 3 km and a surface haze may have been present (Murray, 1967), this is at best one possibility.

Lunar Data

Lunar surface material at the five widely separated Surveyor landing sites is granular, slightly cohesive, and predominantly fine-grained. Approximately 95% of the soil at these sites is finer than the 1-mm resolution of the television camera. Within the visible size range there is a uniform distribution of particle sizes ranging from the 1-mm camera resolution up to the largest blocks present, which are several meters in diameter. Cumulative size-frequency distribution curves for each Surveyor site are shown in Fig. 6. Figure 7 shows sectors of the lunar surface at the Surveyor I and VII sites. At all Surveyor sites there is a greater percentage of coarse fragments surrounding large craters than occurs on surfaces where large craters are absent. The shapes of the large blocks range from angular to subrounded. Angular blocks mostly rest on the surface with little or no burial, whereas rounded blocks appear to be partly buried.

Bearing Strength

Lunar soil at the five Surveyor landing sites was found to be remarkably similar in bearing strength (Fig. 8) and other physical properties. Based on a Surveyor footpad ~30 cm in diameter with a soil penetration of about 5 cm, bearing strength is 4.2 to 5.5 $\times 10^5$ dyn cm^{-2}. Bearing strength based on the much smaller effective surface area (5 cm × 2.5 cm) of the Surveyor III soil

mechanics surface sampler was 2×10^5 dyn cm^{-2} for a soil penetration of 2.5 cm (Scott and Roberson, 1967). The increase of lunar bearing strength with depth as determined from the five Surveyor missions is given on pages 1 and 2.

It is expected that bearing strength of most Martian surfaces will more closely resemble the Moon than the Earth. The great diversity and complexity of Earth's surface materials and their wide range of bearing strengths are not anticipated on Mars. However, it is not expected that the Martian surface will exactly duplicate the Moon. For example, lunar soils were found uniformly to have a small cohesion, the value probably being about 10^4 dyn cm^{-2}. This cohesion is probably associated with the vacuum environment (the lunar atmospheric pressure is estimated to be $\sim 10^{-13}$ Earth atmospheres) or possibly in some cases with sintering caused by energetic particle bombardment.[10] Bearing strength of the top few centimeters of lunar soil is derived mainly from soil cohesion, whereas at progressively greater depths bearing strength is derived mainly from the greater internal friction of the more densely packed soil.

On Mars surface soils may also have cohesion. Such cohesion, however, would probably be caused by water molecules adhering to soil-particle surfaces, not by vacuum sticking, and could therefore vary as the abundance of water varied—both with place and time on the Martian surface.[10]

The bearing strength of Martian soils with cohesion could be assumed conservatively to be the same as lunar soils. For Martian soils that are essentially cohesionless, an Earth analog of soils found in active dune sands and fine ash deposits around geologically recent volcanoes can be used. For loose soils with very low cohesion, surface bearing strength varies with grain size because coarse-grained soils (i.e., sand-sized) assume denser packing at the surface during deposition than do fine-grained soils (i.e., silt-sized). Examples of fine, loosely packed surface soils with low bearing strength are the ash deposits on the flats surrounding Cinder Cone in the Lassen Volcanic field and the ash field west of the 8443-ft peak at Mono Craters in California. The yellow clouds of Mars[11] and the polarization data indicate the probable existence of considerable material of very small particle size, a great deal of it smaller than 200 μ, much of it smaller than 50 μ. Collections of such fine dust in completely dry sites could prove quite hazardous to landing machinery, particularly on inclines or in dunes with surfaces approaching the angle of repose (34°).

CONCLUSIONS

1) A finely divided particulate surface layer appears to be indicated, with little composition difference between light and dark areas. Iron oxides are probably common, perhaps as a desert-varnish-type coating on silicate grains. Basaltic-type material is probably common, perhaps as lava flows as well as small grains.

2) Size-frequency distribution curves for volcanic debris and impact debris may serve as upper and lower extremes for the Martian surface material.

3) At present the lunar bearing strength data may be considered as a best estimate for the Martian surface. Deep, soft deposits of windblown dust, however, could exist in wind shadows.

4) Many investigators hypothesize a greater meteoroidal flux at Mars than at the Moon, although there is little agreement on the magnitude of the difference. There is no direct evidence of flux differences, as the age and origin of Martian craters are not firmly established.

5) The polar caps are probably mostly CO_2 ice with a possible core of H_2O ice.

Elemental compositions

Element	Terrestrial crustal rocks,[a] weight % (Holmes, 1965)	Lunar surface material,[b] atomic % (Turkevich et al., 1968): Mare Tranquillitatis: Surveyor V, Sample 1	Mare Tranquillitatis: Surveyor V, Sample 2	Sinus Medii: Surveyor VI	Tycho area: Surveyor VII, sample 1
Carbon, C		<3	<3	<2	<2
Oxygen, O	46.60	58 ±5	56 ±5	57 ±5	58 ±5
Silicon, Si	27.72	18.5 ±3	19 ±3	22 ±4	18 ±4
Aluminum, Al	8.13	6.5 ±2	6.5 ±2	6.5 ±2	9 ±3[d]
Iron, "Fe"[e]	5.00	13 ±3[g]	13 ±3[g]	5 ±2	2 ±1
Calcium, "Ca"[f]	3.63			6 ±2	6 ±2
Magnesium, Mg	2.09	3 ±3	3 ±3	3 ±3	4 ±3
Sodium, Na[h]	2.83	<2	<2	<2	<3
Potassium, K	2.59				
Titanium, Ti	0.44				
Hydrogen, H	0.14				
Phosphorous, P	0.12				
	99.29				

Elemental compositions expressed as oxides

Oxide	Terrestrial lavas, weight % (Bullard, 1962): Acid lava	Intermediate lava	Basaltic lava	Terrestrial crustal rocks,[a] weight % (Holmes, 1965)	Lunar surface material,[c] weight % (Turkevich et al., 1968): Mare sites: Surveyors V and VI	Highland site: Surveyor VII
Silica, SiO_2	≥70	59	<49	59.26	50	50
Alumina, Al_2O_3	12-15	16	16	15.35	14[d]	21
Iron oxides Fe_2O_3	≤3	7	12	3.14	16	7
Iron oxides FeO				3.74		
Lime, CaO		6	9	5.08	15	15
Magnesia, MgO		3	6	3.46	5	7
Soda, Na_2O (alkali)	6-8	4	<3	3.81	—[h]	—[h]
Potash, K_2O (alkali)		2		3.12		
Titania, TiO_2				0.73		
Water, H_2O				1.26		
Phosphorous pentoxide, P_2O_5				0.28		
				99.23		

[a] Average composition.

[b] Preliminary analytical results of each alpha-scattering experiment. (The alpha-scattering method of chemical analysis can provide quantitative information on all major elements in a sample except hydrogen, helium, and lithium.)

[c] Consistent with preliminary analytical results of each alpha-scattering experiment. (These data were inferred from elemental results; the alpha-scattering instruments were not designed to provide direct information about the chemical state of the elements measured.)

[d] The value for aluminum for sample 1 on Surveyor VII has previously been reported as 8 ±3%; additional data analysis indicates 9 ±3% is more nearly correct. The Al_2O_3 value for the mare sites is slightly higher than that (13%) reported earlier by the experimenters. The difference arises from rounding-off errors in the earlier analyses.

[e] For lunar surface material, "Fe" here denotes elements with mass numbers between approximately 47 and 65 and includes, for example, Cr, Fe, and Ni.

[f] For lunar surface material, "Ca" here denotes elements with mass numbers between approximately 30 and 47 and includes, for example, P, S, K, and Ca.

[g] The Surveyor V "Fe" and "Ca" groups have not yet been resolved; however, a lower limit of 3% of "Fe" can be set for each of the samples.

[h] The presence of Na in lunar surface material has not been established with certainty. Na_2O could be present in amounts up to 3% by weight in the mare samples and 4% in the highland samples.

Fig. 1. Table of general chemical ingredients in terrestrial lavas and crustal rocks, and Surveyor lunar compositional data.

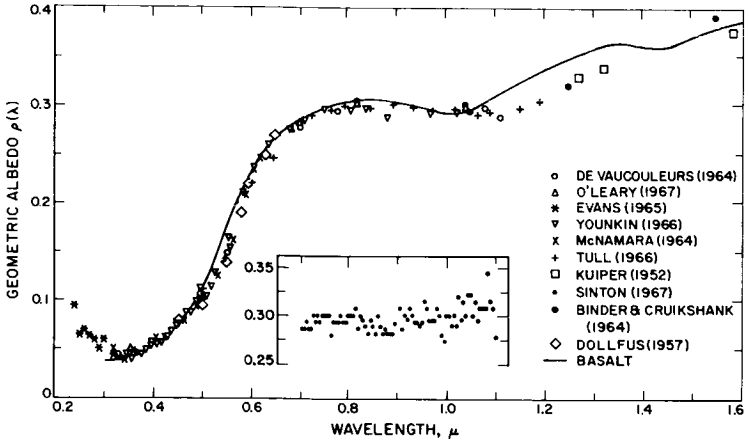

Fig. 2. Comparison of the geometric albedo of Mars (adapted from McCord and Adams, 1968) with the reflectance of an oxidized basalt (Adams, 1968). The basalt measurement was made on an integrating sphere. The specimen, a powder finer than 100 μ, consisted of 50% Little Lake basalt and 50% Boulder County basalt. Oxidation was by treatment in dilute HNO_3, which partially dissolves and oxidizes small grains of magnetite.

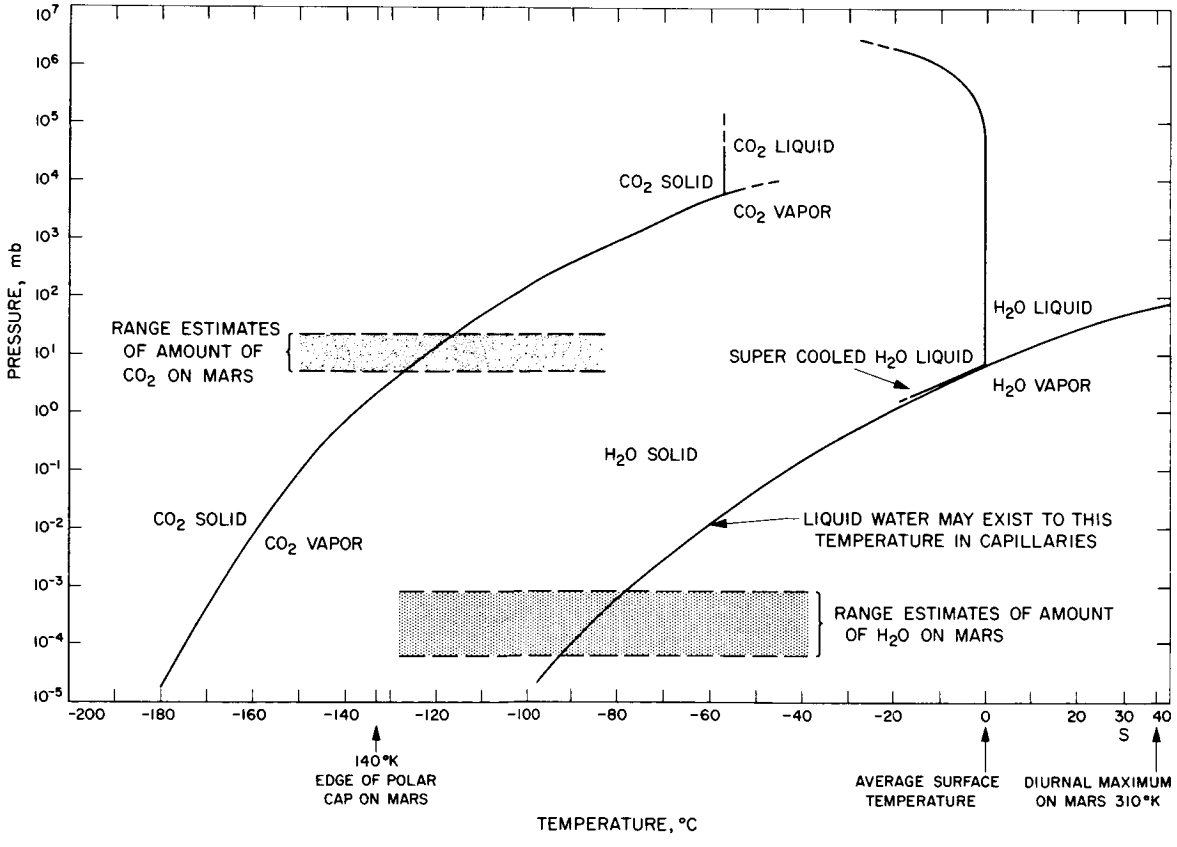

Fig. 3. Phase diagram for carbon dioxide and water. Linear-log plot. (Wade and de Wys, 1968)

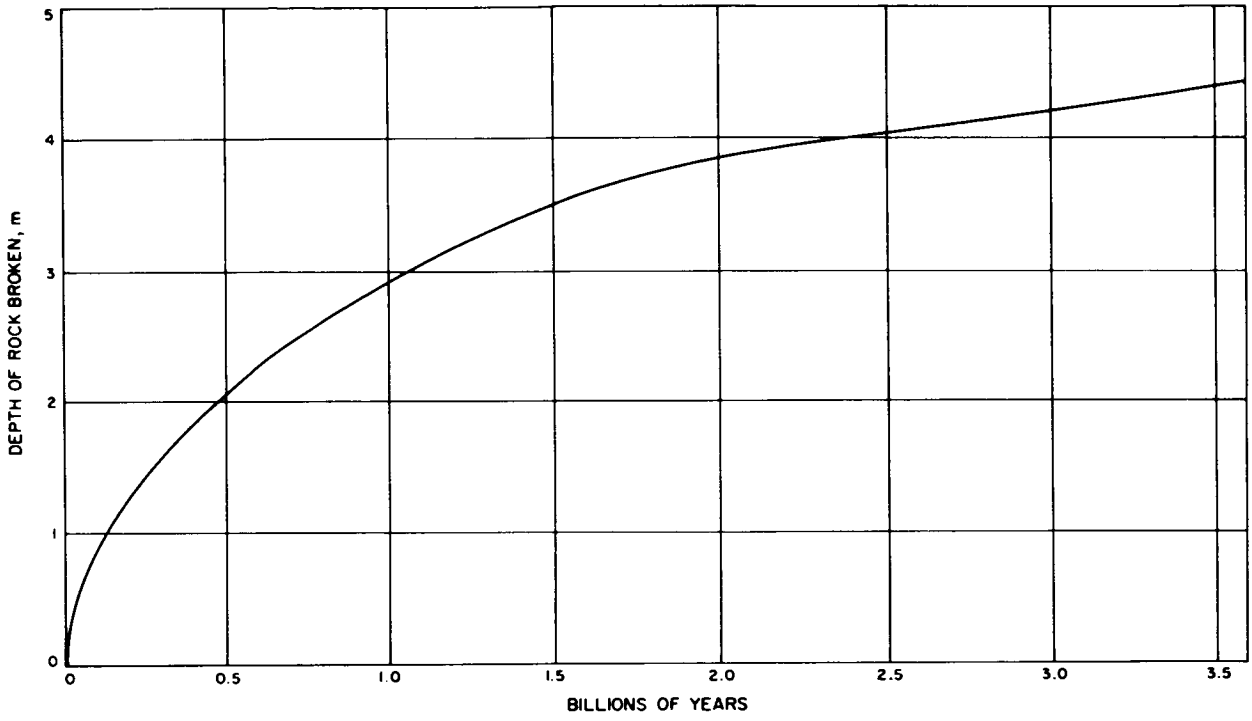

Fig. 4. Depth of lunar rock broken by meteorite impact vs. age. Depth of particulate layer estimated by the curve does not include porosity factor. Recalculation by Choate (1966) of Meloy and Faust (1965) data obtained through a computer comminution study.

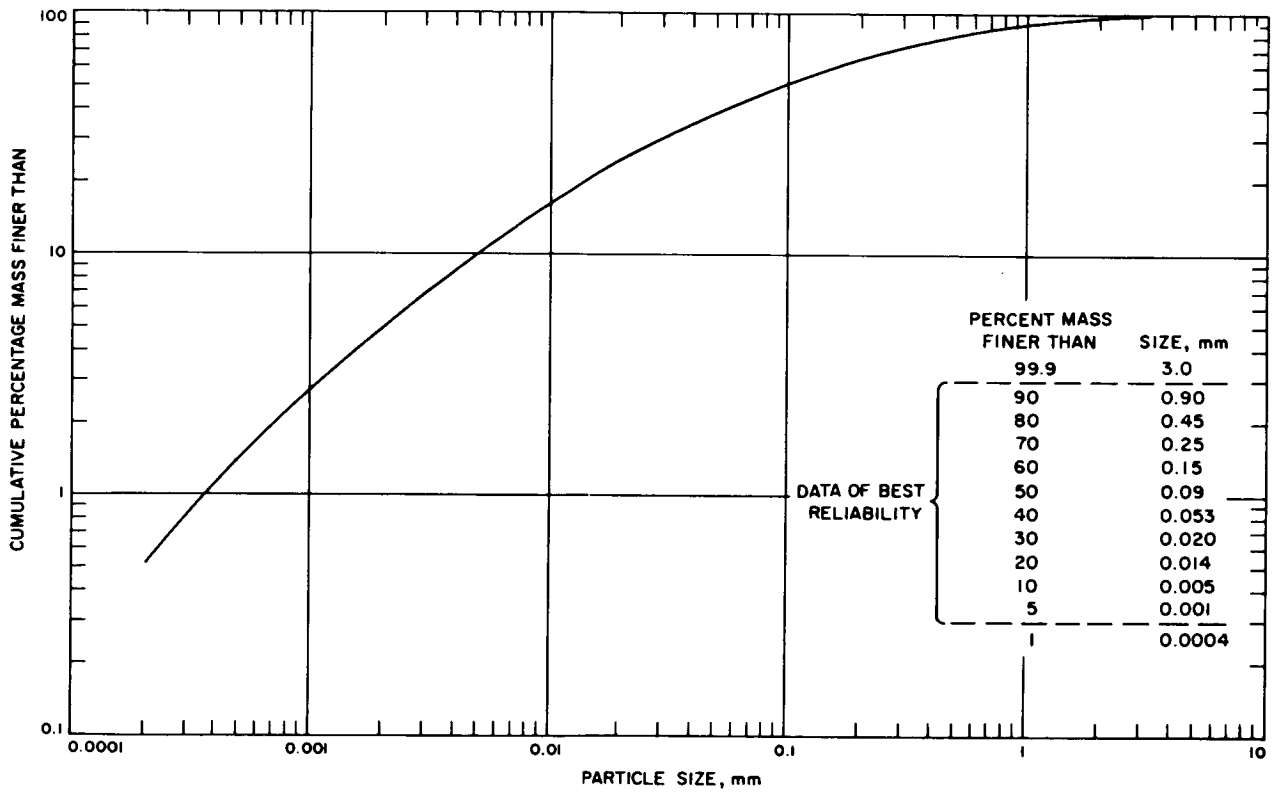

Fig. 5. Cumulative percentage of particle sizes in lunar particulate layer. Plotted by Choate (1966) from original computer comminution study data furnished by T. P. Meloy.

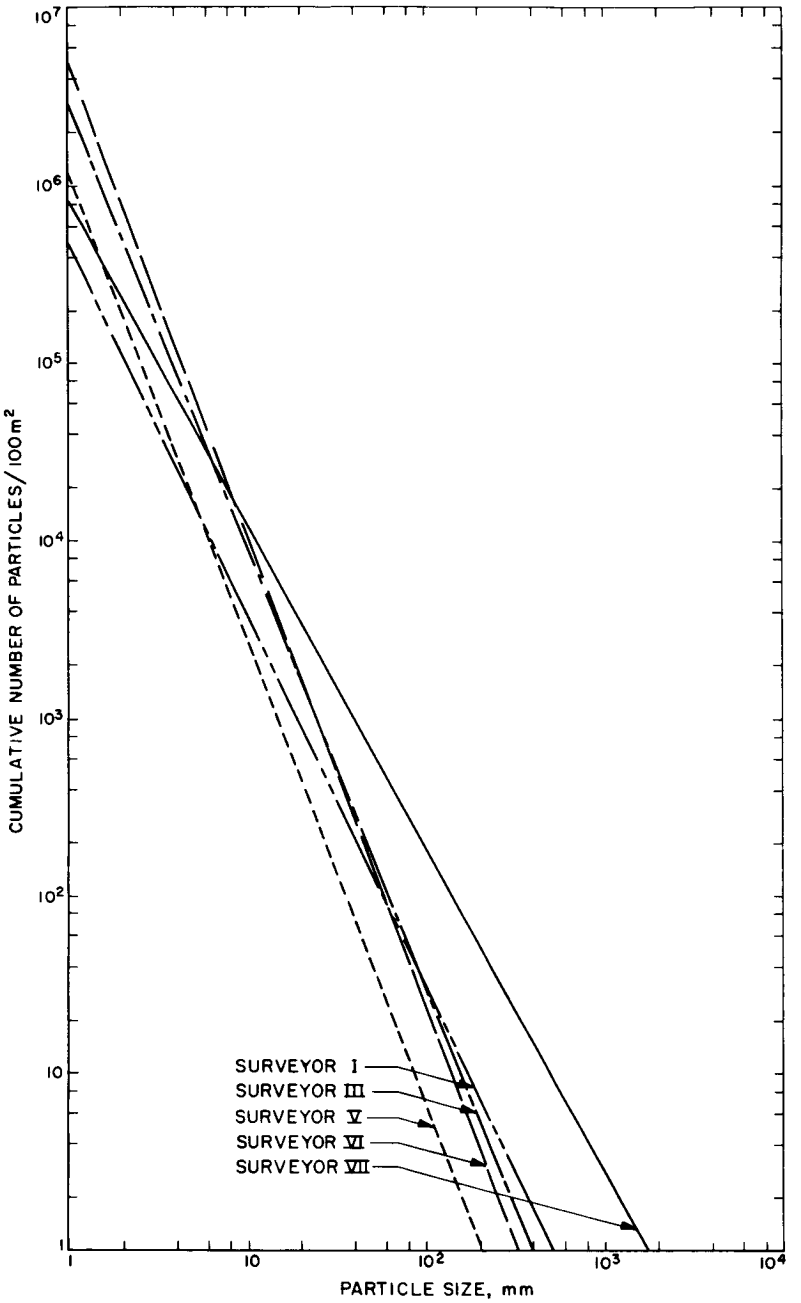

Fig. 6. Cumulative size-frequency distribution of particles and fragments on the lunar surface at the Surveyor I, III, V, and VI mare landing sites and the Surveyor VII highland landing site. (Rennilson et al., 1966; Shoemaker et al., 1967a, 1967b, 1968; Morris et al., 1968)

Fig. 7. Mosaics of the lunar surface at the Surveyor I mare site on Oceanus Procellarum (left) and the Surveyor VII highland site north of the crater Tycho (right). Each mosaic covers a 36° sector and extends from the spacecraft to the horizon. The lunar surface in view from both spacecraft is covered by soil which is predominantly fine-grained, as shown in Fig. 6. Soil at the Surveyor VII site is somewhat coarser than that at the four mare sites.

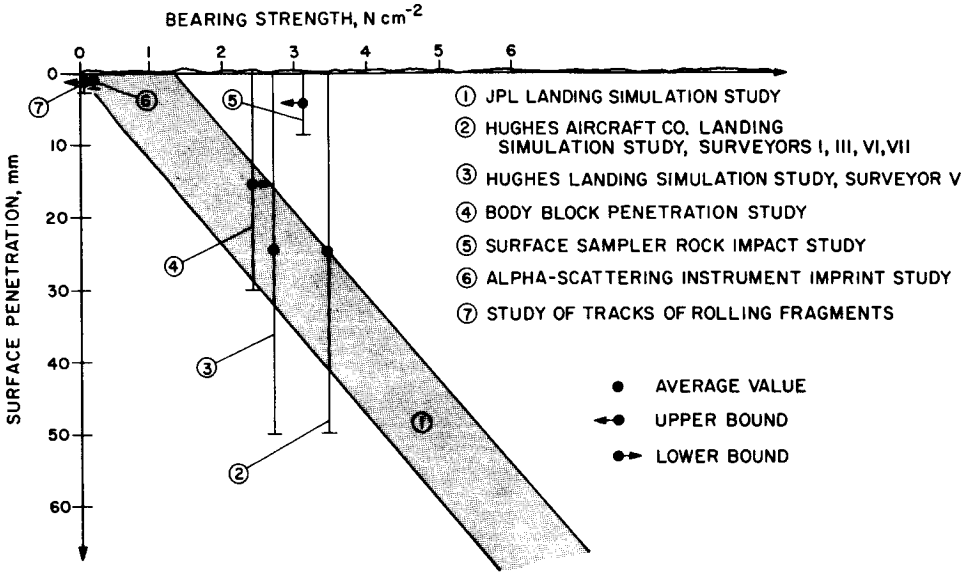

Fig. 8. Lunar surface bearing strength vs. penetration as interpreted from Surveyor results. Data designated ①, ②, and ③ were obtained from analytical simulations of spacecraft landings on surfaces with variable bearing strength and friction characteristics: estimate ① is based on a soil with a linearly increasing static bearing strength; estimates ② and ③ are based on a compressible soil with a constant bearing strength. Estimates ④ through ⑦ are based on indications of bearing strength obtained from indirect measurements during the actual missions. (Christensen et al., 1968)

CROSS REFERENCES

The specific section number, subject, and page number to which the reader is referred is given below.

Cross Reference	Section and Subject
[1] Chemical composition of the surface	3.5.....Possible surface processes and features (discussion), p.9.
[2] Iron content of the interior	2.....Interior models (discussion), p.6-9.
[3] Forms of surface iron	4.1.....Yellow clouds (discussion), p.5-7.
[4] Iron oxides—spectral and polarization characteristics	3.2.....Albedo, magnitude, and color (discussion), p.4; Polarization (discussion), p.5.
[5] Water and carbon dioxide on the surface	5.1.....Observed atmospheric constituents (data summary), p.1; Carbon dioxide (discussion), p.3-5; Water vapor (discussion), p.5,6.
[6] Polar caps, wave of darkening, frost, freeze-thaw phenomena	4.2.....Seasonal activity (data summary), p.1; Seasonal changes in specific areas (figures), p.11-17; Seasonal activity maps (figures), p.19-25. 3.5.....Freeze-thaw processes (discussion), p.9,10.
[7] Temperatures	3.1.....Surface temperatures (data summary), p.1, and brightness temperature characteristics (data summary), p.2; Surface temperature (figure), p.8. 5.3.....Ground air temperatures and lower atmosphere models (figures), p.10-20.
[8] Meteoritic material	3.5.....Cratering processes (discussion), p.6; Meteorite impact (discussion), p.9; Mariner IV pictures (figure), p.29.
[9] Particle sizes—interpretations from observational data	3.1.....Thermal properties (discussion), p.3. 3.2.....Polarization (discussion), p.5. 3.3.....Radar properties (discussion), p.4.
[10] Bearing strength	6.....Energetic particles and sintering—solar wind protons (discussion), p.8. 3.5.....Freeze-thaw features (data summary), p.2.
[11] Dust and the yellow clouds	3.5.....Wind action (discussion), p.12. 4.1.....Yellow clouds (discussion), p.5-7.

BIBLIOGRAPHY

Adams, J.B., 1968, Lunar and Martian surfaces: petrologic significance of absorption bands in the near infrared: Science, v.159, p.1453-1455.

Binder, A.B., and Cruikshank, D.P., 1964, Comparison of the infrared spectrum of Mars with the spectra of selected terrestrial rocks and minerals: Comm. Lunar Planet., v.2, p.193-196.

Bullard, F.M., 1962, Volcanoes in history, in theory, in eruption: Austin, Tex., U. of Tex. Press.

Choate, R., 1966, Physical properties and soil mechanics of particulate layer, Sec. 3.2.1 in Surveyor project lunar scientific model: Pasadena, Calif., Jet Propulsion Laboratory, Proj. Doc. 54, Rev. 1.

Choate, R., et al., 1968, Lunar surface mechanical properties, p.77-134 in Surveyor VII mission report, Part II. Science results: Pasadena, Calif., Jet Propulsion Laboratory, Tech. Rep. 32-1264.

Christensen, E.M., et al., 1968, Mechanical properties of the lunar surface material as interpreted from Surveyor landing data and soil observations: paper presented by F.B. Sperling at American Geophysical Union Meeting, Wash., D.C., April 8-11, 1968.

de Vaucouleurs, G., 1964, Geometric and photometric parameters of the terrestrial planets: Icarus, v.3, p.187-235.

de Wys, J. Negus, 1968, Magnet data, in Surveyor project final report, Part II. Science results: Pasadena, Calif., Jet Propulsion Laboratory, Tech. Rep. 32-1265.

Dollfus, A., 1957a, Etude photometrique des contrees sombres sur la planete Mars: CR Acad. Sci., v.244, p.1458-1460.

_____, 1957b, Proprietes photometrique des contree desertique sur la planete Mars: CR Acad. Sci., v.244, p.162-164.

_____, 1966, Contribution au colloque Caltech-JPL sur la Lune et les planetes: Mars, p.288-304 in Proceedings of the Caltech-JPL lunar and planetary conference, September 13-18, 1965: Pasadena, Calif., Jet Propulsion Laboratory, Tech. Memo. 33-266.

Dollfus, A., and Focas, J.H., 1966, Polarimetric study of the planet Mars: Bedford, Mass., Air Force Cambridge Research Laboratories, Contract AF-61(052)-508, final report.

Evans, D.C., 1965, Ultraviolet reflectivity of Mars: Science, v.149, p.969-972.

Guerin, P., 1962, Spectrophotometric study of the reflectivity of the center of the Martian disk at opposition and the nature of the violet layer: Planet. Space Sci., v.9, p.81-87.

Holmes, A., 1965, Principles of physical geology, 2d Edition: New York, Ronald Press.

Kachur, V., 1966, Thermological aspects of the Martian surface environment: Mt. Prospect, Ill., Institute of Environmental Sciences, Annual Technical Meeting Proceedings Reprint.

Kuiper, G.P., 1952, Atmospheres of the Earth and planets, 2d Edition: Chicago, Ill., U. of Chicago Press.

Leighton, R.B., Murray, B.C., Sharp, R.P., Allen, J.D., and Sloan, R.K., 1967, Mariner Mars 1964 project report: television experiment, Part I. Investigators' report, Mariner IV pictures of Mars: Pasadena, Calif., Jet Propulsion Laboratory, Tech. Rep. 32-884.

Loomis, A.A., 1967, Stability of iron oxides on Mars: oral presentation at Caltech Mars Seminar, Pasadena, Calif.

Mason, B., 1962, Meteorites: London, New York, Wiley and Sons.

McCord, T.B., and Adams, J.B., 1968, (Pasadena, Calif., Caltech and Jet Propulsion Laboratory): private communication of material being prepared for formal publication.

McNamara, D.N., 1964, Narrow band photometry of stars, planets and satellites: Downey, Calif., North American Aviation, Inc., Space and Information Systems Division, Space Sciences Laboratory, Rep. SID 64-78, No. 52156-64.

Meloy, T.P., and Faust, L.H., 1965, Final report: lunar surface roughness and comminution study—JPL contract no. 950919: Milwaukee, Wis., Allis-Chalmers Mfg. Co., Space and Defense Sciences Dept.

Morris, E.C., Batson, R.M., Holt, H.E., Rennilson, J.J., Shoemaker, E.M., and Whitaker, E.A., 1968, Television observations from Surveyor VI, p. 9-45 in Surveyor VI mission report, Part II. Science results: Pasadena, Calif., Jet Propulsion Laboratory, Tech. Rep. 32-1262.

Murray, B.C., 1967, (Pasadena, Calif., Caltech): oral communication at Caltech Mars Seminar, Pasadena, Calif.

O'Leary, B.T., 1967, Mars: visible and infrared studies and the composition of the surface: Berkeley, Calif., U. of Calif., dissertation.

Rennilson, J.J., Dragg, J.L., Morris, E.C., Shoemaker, E.M., and Turkevich, A., 1966, Lunar surface topography, p. 7-44 in Surveyor I mission report, Part II. Scientific data and results: Pasadena, Calif., Jet Propulsion Laboratory, Tech. Rep. 32-1023.

Scott, R.F., and Roberson, F.I., 1967, Soil mechanics surface sampler: lunar surface tests, results, and analyses, p. 69-110 in Surveyor III mission report, Part II. Scientific results: Pasadena, Calif., Jet Propulsion Laboratory, Tech. Rep. 32-1177.

Sharp, R.P., 1967, (Pasadena, Calif., Caltech): oral communication to J. de Wys.

_____, 1968, Surface processes modifying Martian craters: Icarus, v.8, p.472-480.

Shoemaker, E.M., Batson, R.M., Holt, H.E., Morris, E.C., Rennilson, J.J., and Whitaker, E.A., 1967a, Television observations from Surveyor III, p.9-67 in Surveyor III mission report, Part II. Scientific results: Pasadena, Calif., Jet Propulsion Laboratory, Tech.Rep.32-1177.

_____, 1967b, Television observations from Surveyor V, p.7-42 in Surveyor V mission report, Part II. Science results: Pasadena, Calif., Jet Propulsion Laboratory, Tech.Rep.32-1246.

_____, 1968, Television observations from Surveyor VII, p.9-76 in Surveyor VII mission report, Part II. Science results: Pasadena, Calif., Jet Propulsion Laboratory, Tech.Rep.32-1264.

Sinton, W.M., 1967, On the composition of Martian surface materials: Icarus, v.6, p.222-228.

Tull, R.G., 1966, The reflectivity spectrum of Mars in the near-infrared: Icarus, v.5, p.505-514.

Turkevich, A., et al., 1968, The alpha-scattering chemical analysis experiment on the lunar missions, in Surveyor project final report, Part II. Science results: Pasadena, Calif., Jet Propulsion Laboratory, Tech.Rep.32-1265.

Wade, F.A., and de Wys, J.Negus, 1968, Permafrost features on the Martian surface: Icarus, v.9, p.175-185.

Younkin, R.L., 1966, A search for limonite near-infrared spectral features on Mars: Astrophys.J., v.144, p.809-818.

3.5 MORPHOLOGY AND PROCESSES

DATA SUMMARY

Topographic Relief Differences[1*]

Preliminary results of radar ranging suggest large scale elevation differences of at least 12 km at +21° latitude (Shapiro, 1968). Locally, cratering is known to cause substantial relief differences. This and other sources of relief include:

Crater floors relative to surrounding terrain	Up to several kilometers
Crater rims relative to surrounding terrain	Up to perhaps a kilometer or more
Fault zones - graben, fissures, fractures	If Mars is tectonically active, deformation and fracturing may be expected at scales from centimeters to kilometers.
Patterned ground	See freeze-thaw features on page 2.

Craters

Crater counts, sizes, types, and shapes given below are based on interpretations of Mariner IV pictures.

Counts:	
In Mariner IV pictures 3-16	86 definite; 272 probable; 278 possible (Leighton et al., 1967)
Total Martian surface	~100,000 larger than 4 km in diameter
Sizes	Up to at least 180 km in diameter
Types and shapes	Circular, hexagonal, and other polygonal forms; with and without central peaks; scalloped; slump terraces; linear or circular arrangements of craters; dimple; ghost; combinations

Slope Angle Distribution

Theoretical slope angle distributions for large flatlands, basins, and valleys and for topographic highs in mountainous Martian terrain are based upon lunar measurements and are shown in Figs. 5 and 6. Theoretical slope angle distribution for inner walls, terraces, floors, and central peaks of large young craters, also based upon lunar measurements, is given in Fig. 8. Baseline data and other details are discussed on pages 7 through 9.

*See pages 31 and 32 for list of cross references.

Freeze-Thaw Features

The Martian environment appears to be favorable for freeze-thaw processes which could modify the microtopographic surface features (Wade and de Wys, 1968). The resultant patterned ground could be recognized by means of imagery of sufficient resolution, giving information of fundamental importance on Martian surface conditions. Possible dimensions of ground patterns, suggested from terrestrial analog, are presented below.

Ground pattern: Polygonal shape with single and double rims

	Polygons	Troughs	Rims
Maximum width	10-30 m	2.0 m	2.0 m
Average width	20 m	1.0 m	1.5 m
Maximum depth (height)	1.5 m	1.5 m	(1.5 m)
Average depth (height)	1.0 m	1.0 m	(0.5 m)

Sand wedges: Up to 5 m wide; up to 5 m deep

Distribution:

- Planetary: May be general; no preference for light or dark areas
- Topographic relationship: To be expected in basins, lowlands, and plateaus; not to be expected on slopes >30° to 35°
- Latitudinal preference: Greater polygon population to be expected in equatorial area, especially in +10° to +20° latitudes

Polygon population:

- Seasonal change: None
- Visibility in spring: May have frost deposition in troughs
- Visibility in summer: Disappearance of frost in troughs in lower latitudes

Effect on bearing strength: [2]

- Upper particulate layer: No effect at depths ≤10 cm upon surface soil bearing strength (3 to 5 psi)
- Lower particulate layer: May involve permafrost at depths >10 cm

Depth of upper surface of possible permafrost:

- Minimum: 10 cm
- Maximum: 3 m
- Average: 1 m

DISCUSSION

Relative Elevation of Light and Dark Areas

A belt of dark "maria" encircles Mars between -5° and -40° latitude. Maria are distributed throughout the north and south polar regions. Despite the name there is no evidence that Martian maria have properties in common with lunar maria. The north polar regions appear to be flatter than the south as indicated by the irregular melt line around the south polar cap and by isolated white areas that appear to be cloud cover or possibly surface condensates in the south polar region. There is no clear correlation of type of area with roughness or elevation in these direct observational data.

Thermal Data

Sinton and Strong (1960) concluded that the radiometric (infrared) temperature of dark areas is 8°K higher than that of brighter areas; atmospheric influences were not considered. Assuming an adiabatic lapse rate of ~4.9° km^{-1} for an all CO_2 atmosphere of 10-mb surface pressure, it has been speculated that the observed difference in temperature means a relief difference of 1.6 km. However, Mintz (1961) showed that differences in temperature between surface and air directly above the surface (~2 m) may be as great as 63°C. In a more tenuous atmosphere like that of Mars the difference could be even greater. Therefore, the surface temperature does not appear to be a valid indication of elevation.[3] It may merely reflect albedo differences between dark and light areas.[4]

Radar Data [5]

Preliminary results of relative ranging experiments show elevation differences of at least 12 km at +21° latitude (Shapiro, 1968). Correlation between reflectivity and elevation is poor. Sagan, Pollack, and Goldstein's (1967) interpretation correlating dark areas with high areas was not confirmed but, if anything, contraindicated.

Cloud Formation Movement [6]

Circulation patterns and cloud movement may give some indication of surface relief. On Earth clouds tend to form over mountains and on windward sides of topographic relief. With movement over high areas and descent of air masses, clouds disappear. There is disagreement on the relative elevation of Martian dark and light areas on the basis of cloud relationships. Wells (1965, 1966) concludes that dark areas are higher than light areas. O'Leary and Rea (1967) also support the concept that dark areas are higher on the basis that temporary bright patch formations are clouds. A 10-km range is suggested by them based on the rate of CO_2 deposition. Miyamoto (1966) concludes that dark areas are lower than "deserts." Two features to be looked for would be diversion of air masses by topography and consistent formation of clouds on the windward side of dark features. Results from the Lowell Cloud Study, when available, may contribute to solution of the problem.

It has often been noted that yellow clouds appear to be deflected by dark areas (Antoniadi, 1930; Sagan and Pollack, 1968). Sagan and Pollack (1968)

suggest "this might be accomplished by guiding the prevailing winds along the lowlands," their feeling being that the dark areas are highlands.

White Patterns [6]

Seasonal whitening of certain Martian areas, apparently due to either a cloud cover or a white condensate, may be an indication of topography. White-covered Nix Olympica is in the Amazonis Desert; Ophir-Candor-Tharsis is often brilliantly white. Miyamoto (1966) interprets this as a mountain range. He suggests that Dioscuria and Cydonia Deserts north of the canal line are probably a mountain range or high plateau.

In northern spring, Protonilus-Ismonius Lacus-Deuteronilus mark the southern border of the polar cloud layer. When the polar cap retreats, it is uneven and the brilliance is not uniform. This may also give indications of elevations. On such a basis Novus Mons near the south pole has been considered to be a mountain (Antoniadi, 1930).

Tombaugh (1966) suggests that the whiter and more persistent an area is, the higher the topographic level. He states that white areas tend to avoid maria, except in cases of haze, and further suggests that the Albor area on the Elysium Plateau is the highest land on the planet. It tends to whiten more than any other area in equatorial latitudes. On the other hand Sagan and Pollack (1968) have suggested exactly the opposite, stating that the lowlands are the coldest areas and that it is there frost is formed persistently.

In Mariner IV picture 11 (Fig. 24) the white patches in the northeast quadrant may be frost. That portion of the frame is over a dark area of Mare Sirenum while the remaining portion is in a lighter area. This would be in agreement with the concept of the dark areas being elevated.

Linear Features [7]

In Mariner IV pictures there are several different types of linear features: some light, some dark; some narrow and sharp, some broader with less defined edges. Major and minor grid systems are visible, as are patterned linear features, polygonal patterns, meandering arcuate markings, single and concentric rings, and radiating linear features. (See Fig. 24 for Mariner IV pictures 7 to 12.)

Grid System

A lunar tectonic grid system is thought by some to exist in roughly northeast-southwest and northwest-southeast directions (Fig. 1). The major Martian linear features in Mariner IV pictures reveal a similar northeast-southwest and northwest-southeast grid system with some apparent branching visible, possibly more in the northeast-southwest direction (Fig. 2). Shorter linear markings on Mars also lie in northeast-southwest and northwest-southeast directions, again with some branching, although branching possibly occurs more in the northwest-southeast direction. Observed patterned linear features may be due in part to the intersection of shorter linear markings.

Canals

The Italian astronomer Schiaparelli in 1877 gave the name 'canali' to dark, narrow, more or less continuous markings he observed crossing the bright areas of Mars. This was rather poorly translated into English as 'canals.' Lowell and his coworkers proceeded to discover more and more canals in the years following 1894, until their maps showed several hundred single and double canals and many multiple intersections called 'oases' or 'lakes' by them. Some canals can be photographed when the Earth's atmosphere is sufficiently stable and transparent, but these appear as rather broad objects under the best of conditions. Antoniadi, Maginni, and others concluded that with adequate aperture the canals visually break up into a series of discontinuous structures (or spots). Certainly the dark coloring of the canals comes and goes with the season in many cases, and an actual continuous linear structure of the features has not been substantiated to date by Mariner IV pictures.

The best that can be said with certainty today is that there are apparently linear features on the disk of Mars that are relatively permanent, though varying in visibility with season, and that can in many cases be photographed as objects apparently 100 km or more wide and up to 4000 km in length. Their actual width and continuity are in question. Their nature is as yet completely speculative.

Tombaugh (1950) suggested oases were the result of asteroidal impacts and canals the result of crustal fracturing caused by the impacts. McLaughlin (1954) proposed a volcanic origin for most Martian features and depicted the canals as ash deposits. Gifford (1964) suggested the canals might be chains of sand dunes such as those occurring in the Earth's Sahara Desert. Sagan and Pollack (1966) suggest they "are ridge systems or associated mountain chains analogous to similar features in the terrestrial ocean basins." Adequate photography is necessary for a more determinative interpretation.

Craters

Observing visually with the Yerkes Observatory 40-in. refractor, using an eyepiece giving a power of 1100, Mellish in 1916 recorded "many small craters and one large one 200 miles [320 km] in diameter at latitude about -50°" (Mellish, 1966). Even earlier, Barnard's records of observations with the 36-in. refractor at Lick Observatory during the 1892-1893 opposition of Mars showed craters appearing as dark circular patches (Mellish, 1966).

Mariner IV pictures (Leighton et al., 1967) revealed that craters of various shapes with diameters ranging up to at least 180 km exist on the surface of Mars. Picture 13 shows a feature which may be the rim of a crater 350 km in diameter. It would appear that the area photographed by Mariner IV in Pictures 7 through 11 (Fig. 24) is comparable in crater density and distribution to the lunar highlands, but with greater modification and possibly fewer smaller craters. There is no apparent crater density difference between dark and light areas. Depth-versus-diameter comparison (Sharp, 1968) suggests Martian craters are significantly more shallow than freshly formed lunar craters. Crater wall slopes up to 19° are suggested by Murray (1967) based on measurements of one 25-km-diameter crater. A summary of crater statistics is given in Fig. 3.

Morphology

Types and shapes of craters are listed on page 1. Binder (1966) found that out of 69 well preserved craters with diameters greater than 10 km in pictures 7 through 14, nine have recognizable central peaks. This would indicate that about 13% of larger Martian craters (in the area examined) have central peaks. Central-peak probability for lunar post-maria craters is 11.7% (Binder, 1966). Martian crater rims appear overall to be more eroded and floors of the craters appear to be more filled in than in many lunar craters. Craters do not appear to be recent. A number of the Martian craters have an obvious polygonal shape, as do many lunar craters.

Distribution

A dense crater-on-crater population is present in Mariner IV pictures. The crater count from these pictures (Leighton et al., 1967) indicated a density somewhat less than that in the lunar highlands; their density curve would suggest a total of about 100,000 craters on the planet. Independent counts by Marcus (1968) show a crater population virtually identical to that of the lunar highlands. Crater count results are given in Figs. 3 and 4. According to Leighton et al. (1967) the three principal features of the integral crater-frequency curve (Fig. 4) are:

1) In the 20- to 60-km size range the slope of the curve approximates that for the Moon, and the absolute abundance of the Martian craters (upper limiting curve) approaches that of the lunar uplands.

2) In the largest size classes there is an apparent dearth of Martian craters. This may, in reality, reflect the limited areas covered by the individual Mariner pictures.

3) Below 20 km there is a genuinely lower abundance and/or systematic change to smoother craters on Mars.

Of the 22 frames transmitted by Mariner IV, pictures 7 through 11 show the greatest number of craters with the greatest clarity. Resolution was $\lesssim 2.5$ km in the best Mariner IV picture (each data point = 1.2 km). The high Sun angle (29°-49° zenith distance in these pictures) eliminates most shadows, making crater counting and slope angle determination difficult. Crater detectability is affected below 20-km diameter. Pictures 7 through 12, which form three partially overlapping pairs, are reproduced as Fig. 24. The figure also shows the location of these pictures on a globe of Mars.

Processes

There is some controversy concerning the origin of lunar and Martian craters, with opinion spread between impact and volcanic origins.[8] On Earth, Meteor Crater in Arizona is accepted as a bonafide impact relic and similarities between its morphology and lunar craters have been cited to suggest an impact origin for many of the latter (Shoemaker, 1962). Meteorites, both singly and in clusters, have undoubtedly impacted the Martian surface. Objects of all sizes from fine particles to asteroidal bodies may have contributed to cratering, debris, and distribution of ejecta. The meteorite flux for Mars has

been suggested as 4 to 26 times that for the Moon, but there is no direct data or agreement on this. If the origin of any Martian crater is other than impact, and/or if the surface morphology is not a balance between crater formation and erosion, crater counts cannot be used validly to establish the flux rate or to interpret the age of the surface. Martian craters are similar to lunar craters in density counts, general morphology (including central peak frequencies), and distribution. Lunar Orbiter photographs of the Moon appear to show considerable evidence of volcanism; by analogy volcanic craters are expected on Mars. Resolution in the Mariner IV pictures of Mars is insufficient, however, to delineate examples of any definitely volcanic type of crater.

Slump and thermal creep may be important factors in the apparent erosion of Martian crater rims. The rigorous thermal environment with resulting expansion and contraction caused by diurnal temperature changes as large as about 130° C may cause a slow migration of material downslope.[9] Sharp (1968) suggests the migration rate may be in excess of 1.5 cm yr^{-1} on a 17° slope. On a slope at the angle of repose (~34°), however, the rate may be as high as 25 to 30 cm yr^{-1} for a 5-cm rock. Slump and settling of surface debris may be further abetted by seismic effects resulting from meteoritic impact, but the quantitative importance of this effect is unknown.

Wind may also play a role in altering crater rims and filling crater floors. If particles are lifted and carried by winds in the tenuous atmosphere, they could also fill craters. Under proper conditions deflation by the wind may produce shallow depressions.[6]

Lava fill in the crater floors is another possibility; the resolution of Mariner IV pictures does not confirm or deny such a possibility. Crater rims may be areas of secondary cratering, e.g, the scalloped crater in picture 11, Fig. 24. Slump around the crater rim could also account for the scalloped appearance.

Slope Angle Distribution

In estimating slope angles or slope angle distributions on Mars, the Mariner IV pictures are useful qualitatively but not quantitatively. We know of no way to measure slope angles directly from the Mariner IV pictures with any reasonable accuracy. Ways in which differences in elevations or slope angles normally can be measured from photographs include measurement of parallax in stereopairs, measurement of length of shadows cast by topographic features, and measurement of surface brightness on individual photographs and use of the photometric technique for elevation determination (Rindfleisch, 1965) where the photometric function is known or assumed.

None of the above techniques can be used with the Mariner IV pictures. Stereo coverage in the pictures is limited to picture margins, where image quality is too poor to use. Sun angle in most of the pictures that contain useful imagery is too high to have shadows cast by topographic features expected on Mars. Good image quality occurs in only three Mariner IV pictures where shadows are likely to exist, i.e., where Sun angle is less than 35° (pictures 13, 14, and 15; Sun angles 33°, 30°, and 24°, respectively). However, in none of these three pictures do dark areas of low illumination look different from areas of low illumination in any of the other Mariner pictures. In pictures 1 through

12 angle of the Sun above the horizon is greater than 40°. In pictures 16, 17, 18, and 19 where Sun angles are low—21°, 14°, 10°, and 2°, respectively—image quality is too poor to be useful. In summary, in none of the Mariner IV pictures have any of the dark areas of low illumination been positively identified as a shadow.

The photometric technique for determining differences in elevation cannot be used with Mariner IV pictures for two reasons. First, cameras aboard the Mariner IV spacecraft were not calibrated in such a way that return data could be incorporated into the photometric technique for elevation measurement, and second, the photometric function for Martian surfaces is not known with sufficient accuracy to be useful (Willingham, 1967).[10]

Because slope angles on Mars cannot be measured with reasonable accuracy from any existing data, estimates must be based on geologic reasoning. The assumption is made here that the Moon is a better analog for Mars than the Earth. On Earth water is the principal agent in erosion and in sediment deposition. On Mars, as on the Moon, water as an erosional or depositional agent has not been present—at least not in the recent geologic past.[11] On Earth wind is an important agent for transport of dry, loose, clay-sized to sand-sized particles. On Mars, where atmospheric density is estimated to be a hundredth of Earth's atmosphere, the efficiency of wind to transport material must be low. The irregularly occurring yellow clouds in Mars' atmosphere have generally been interpreted as dust storms, thus indicating that transport of fine materials probably does occur.[6] Such transport may be the only erosion agent different for Mars than for the Moon.

Lunar Orbiter photographs of the Moon show very clearly that rock outcrops on the Moon are rare and that the Moon is covered with a layer of loose material whose average depth is probably greater than 5 m. Only two geologic agents can logically account for this deposit: impact by meteorites and/or deposition of volcanic pyroclastic ash, lapilli, and bombs. Both agents have probably been active throughout the Moon's history but probably not with equal intensities. The same agents should also have been active on Mars. Mariner IV pictures in fact indicate that the crater-marred surface of Mars is very similar to the Moon. Various factors, however, may make the ratio of relative activity of these two agents different for Mars than for the Moon.

The "best estimate" of slope angle distribution for large flatlands, basins, and valleys on Mars (Figs. 5 and 6) is taken directly from the values measured from the last frame received from each of the P_1 and P_3 cameras aboard Rangers VII, VIII, and IX before impact on the Moon (Choate, 1966). Impact points were in Mare Cognitum, Mare Tranquillitatis, and the floor of the large, partly filled crater Alphonsus, respectively. The slope angle distribution values shown in Fig. 5 and plotted in Fig. 6 are based on a 3.8-m baseline and represent averages of approximately 70,000 data points. Although the impact area of Ranger VIII is somewhat smoother than for Rangers VII and IX, the slope angle distribution curves for the three areas are remarkably similar (Choate, 1966).

The estimate of slope angle distribution for topographic highs in mountainous Martian terrain (Figs. 5 and 6) is based on measurements of the horizon formed by the lunar Carpathian Mountains in the Lunar Orbiter II

photograph, frame H-162 (Fig. 7). Measurements were made on an enlarged print developed to accentuate contrast at the horizon. Slope angles were measured at constant horizontal increments; distribution values are based on 193 measurements. Length of the horizontal distance covered was 51 km, and baseline length was approximately 250 m. Though the baseline length—controlled by scale of the photograph—was 250 m, field experience and study of other Lunar Orbiter photographs indicate that the slope angle distribution for mountain flanks would not change substantially even for baselines as short as 3 m (a factor of $\sim 10^{-2}$).

The best estimate of slope angle distribution for inner walls, terraces, floors, and central peaks of large young Martian craters ($\gtrsim$5-km diameter) is given in Fig. 8. (The percent of area for each topographic unit in a representative large crater is shown in Fig. 9, and mean values for slope angles for total area of large craters are given in Fig. 10.) Distribution was determined by measurements and estimations made principally on photographs of the lunar craters Copernicus (Fig. 7) and Theophilus (Lunar Orbiter III, frame M-78; Fig. 11). The ranges in area percentage (Fig. 10) for each type of terrain were made sufficiently broad to include most large lunar craters.

Possible Processes and Features

Tectonic Movement

Crustal stresses imposed either internally or externally will generally be relieved through movement, which can appear as peripheral faulting around craters, ring faults and parallel faults causing subsidence blocks and basins (graben), linear and echelon faulting, or major faulting due to subsurface readjustment. The existence of craters virtually assures the existence of faults in the Martian surface.

Meteorite Impact [8]

The topography produced by meteorite impact depends primarily upon the impacting energy and nature of the target material. The mechanics of cratering have been studied in both laboratory and field investigations. The cratering problem for impacts of fairly large size is effectively modeled by subsurface nuclear detonations. Possible variations in topography that may be expected to result from impact in loose, uncompacted material and in hard, dense basalt are shown in Figs. 12 and 13 (Nordyke and Wray, 1964). Impact in loose material produces gentle, hummocky rim deposits and inner crater slopes at the angle of repose for loose material ($\sim 34°$). In contrast, an impact in basalt produces large blocks in both rim and bowl deposits.

Volcanic Activity

There have been several reports of bright, temporary phenomena on Mars. Typical examples of transient spots and flares have been discussed by Katterfel'd (1966) and tabulated elsewhere in this document;[12] these all were observed to occur over or near dark areas. The most probable explanation of such sightings seems to be volcanic activity. Out of the nine listed sightings between 1937 and 1958, three occur in Edom Promontorium, two in Solis Lacus,

two in Tithonius Lacus, and one each in Nix Tanaica and Sithonius Lacus. Hellas is also mentioned in one of the Edom Promontorium sightings.

In the case of the Moon, the surface of which closely resembles Martian areas photographed by Mariner IV, over 600 transient events have been compiled (Middlehurst, 1968; Burley and Middlehurst, 1966), more than 200 of which occur in or around Shröeter's Valley. This recurrence in a restricted locality is strongly suggestive of volcanism rather than meteorite impact.

Ranger IX pictures of the lunar crater Alphonsus indicate how one type of volcanism can be expected to modify the pre-existing surface around dark halo craters. The older surface appears to be covered by dark pyroclastic material; former irregularities in it are smoothed out.

By analogy with volcanic deposits on Earth, wide variations in Martian topography will result from volcanic activity. Possibly the two extremes, between which all other cases might be expected to lie, are ash or pumice deposits and aa (blocky) lava flows. The pumiceous gravel flats adjacent to northern Mono Craters in California (Figs. 14 and 15) are an example of the first type. The surface is smooth with variations in relief no greater than a few centimeters over distances of 10 m. The other extreme, a blocky lava flow, is illustrated by the Fantastic Lava Beds in Lassen Volcanic National Park, California (Figs. 16 and 17). Local relief is as great as 10 m, many slopes are ~45°, and the surface is mantled with blocks up to a meter or two in diameter (individual blocks may be vesicular). Roughness of this scale, however, is insignificant compared with irregularities in the macroscopic flow surface. No examples of aa flow are evident in any lunar photographs to date.

Thermally Activated Surface Processes

Thermal Creep and Fracture. Sharp (1968) has provided a comprehensive review of the effects of thermal creep and fracture expected on Mars' surface. Because of the apparent paucity of liquid water on the surface, at least at present, freeze-thaw action or chemical weathering are ruled out as significant debris-producing mechanisms. However, if water ice is present even in slight amounts in the surface material, the process of spalling will be accentuated and greater disintegration of rock fragments will occur.[11] Rock fragmentation arising from diurnal heating is also probably ineffective. Terrestrial experiments show that large temperature changes are required (200-300°C), whereas the fluctuations on Mars are at most only of the order of 130°C.[9] Along with action of the wind, debris transport by alternate thermal contraction and expansion may be the important mechanism of downslope debris transport. The process would be more effective on Mars than on the Moon because the frequency of thermal fluctuation is 30 times as great.

Freeze-Thaw Processes. On Mars the temperature regime and the evidence for water indicate a significant probability of perennially frozen ground. That it underlies large areas of the Martian surface has been suggested by several investigators (Kachur, 1966; Leighton and Murray, 1966). If it exists, this permafrost probably constitutes a zone which has an upper limit some few centimeters to tens of centimeters below the surface and which extends to depths of some tens of meters.

It has been speculated that the presence of permafrost on Mars might be manifested in "patterned ground"—similar to that in frigid zones on Earth—which would be the result of the growth of ice- or dust-filled cracks (wedges) occasioned by drastic freeze-thaw processes. The greatest effects of Martian freeze-thaw processes would occur at the equator where the temperature range is greatest. Figure 18 shows the evolution of an ice wedge according to the contraction-crack theory. Inasmuch as no "active layer" in the strict sense would be present and there would be no supply of melt water, the process of wedge formation on Mars would have to be similar to the sand-wedge formation shown in Fig. 19 and summarized in the following paragraphs.

During the winter months, the cold wave would penetrate the surface aggregate to the frozen zone. Horizontal tensional stress would be generated there, and eventually it would be relieved by vertical fracturing. The fine material from the aggregate above would settle into the small fractures no more than 2 to 3 mm wide. Expansion to its original volume would be attempted by the material of the frozen zone during the following spring and summer. Because the cracks would now be filled with rock detritus, this would not be possible, and the compressional forces would be relieved by upturning of the frozen strata. In the course of time a trough would develop above each wedge and subsequently parallel ridges would form bordering the troughs (Wade and de Wys, 1968).

The process of sand-wedge formation may be assisted to a limited extent by accumulation of new ice in the open cracks. Observations in Siberia have shown that ice veins grow without liquid water nourishment owing to the accumulation of hoar frost at depth in the cracks (Shumskii, 1964). This process is possible in the postulated Martian environment. Also, an open crack may acquire ice filling by water arriving in the frost zone from below and being transported upward by capillary action (Grawe, 1936). A sand-ice or composite-type wedge would be formed by this intermixing of sand and new ice by either of these methods.

Because of the assumed, fairly homogeneous nature of the permafrost and its low plasticity, a non-orthogonal network of troughs and ridges should outline unfractured polygons on Mars (Wade and de Wys, 1968). In areas underlain by permafrost, sand-wedge polygons should develop on the surface. These polygons may originally be as much as 20 to 30 m in diameter and the ridges up to 1.5 m in height. Sand wedges may grow to widths of 10 m. Most in Antarctica are less than 5 m wide. In depth they may extend 2 to 5 m. One type of patterned ground in the terrestrial Antarctic is shown in Fig. 20.

Polygons develop on sloping as well as flat surfaces. Over a period of time, because of the downhill migration of the surface layer under gravity-controlled processes, the ridges become elongated in the direction of slope and produce "stone stripes." A well developed polygonal pattern would not be expected on slopes greater than the angle of repose (34°).

A fuller account of terrestrial freeze-thaw phenomena and their possible manifestations on Mars is given by Wade and de Wys (1968).

Aeolian (Wind) Action

The most widely accepted explanation of the Martian yellow clouds is that they are composed of small particles raised into the atmosphere by wind storms.[6] The wind velocity required to initiate particle motion is a function of both particle size and atmospheric parameters. For typical Martian conditions a particle about a half millimeter in diameter is easiest to move; both larger and smaller particles require a greater wind velocity to initiate motion directly (Ryan, 1964). These data are summarized in Fig. 21. Large particles can initiate motion in smaller particles through collisions, and in fact large particles tend to bounce along near the surface in a process called saltation while the smaller particles, once airborne, are carried aloft and can be moved great distances. If there is an upward wind component equal to or greater than the settling velocity, a particle will remain airborne, and small particles may remain in the atmosphere for days or weeks. Settling velocities in an atmosphere of Martian characteristics for particles of various sizes are given in Fig. 22. Fall times, assuming no vertical wind, are given in Fig. 23.

Vertical winds may be caused primarily by thermal convection, principally a daytime phenomenon. Nevertheless, such vertical winds typically have velocities of ~2 m sec^{-1} according to the theory of Leovy and Mintz (1968) and may reach 6 m sec^{-1} according to Gierasch and Goody (1968). Such winds easily could carry particles as high as the tropopause during the daylight hours.[13] Only particles larger than ~50 μ would settle to the ground during a 12-hr night. Furthermore, there is unlikely to be abundant precipitation on Mars to clear the atmosphere. The horizontal range of particles with diameters smaller than 50 μ may be determined only by circulation patterns. The range of larger particles should be more limited, those from 50 to 100 μ in diameter being limited to the distance wind can carry them in half a day, while particles larger than a few hundred microns will just saltate except under the most violent temporary conditions.

Particulate matter may be thrown into the air by meteorite impact or by volcanic eruptions. These are not normally considered "storms" but could indeed be a significant source of atmospheric particles.

Persistent winds on Mars might produce "desert pavement" by the winnowing of fine material from otherwise unsorted debris. Where there is strong wind and a supply of debris for sand blasting, wind-faceted pebbles or ventifacts might be produced. Winds blowing freely over the surface of Mars may transport large amounts of material outside the areas of origin before settling. This process is known as deflation and may give rise to shallow, closed depressions in otherwise arid regions.

In areas where wind-transported material is deposited, large accumulations (dunes) of dust may occur because of changes in topography or because of vegetation.[14] There are many types of dunes, with varied morphology and circumstances of origin, and the reader is referred to standard texts in Geology for details, e.g., Gilluly et al. (1959) and Bagnold (1960).

CONCLUSIONS

Observational information about the Martian surface is extremely limited, and virtually all of it is large scale (horizontal resolution poorer than 3 km). Improved radar work and new space probes are expected to improve this situation, but today "morphology and processes" is necessarily part theory and part speculation grounded in a small bit of observation.

Radar has confirmed large elevation differences, and Mariner IV has given crater statistics down to a few kilometers for somewhat less than 1% of the Martian surface. Spectroscopy has indicated the existence of a very small amount of water vapor in the atmosphere, and theory indicates a reasonable possibility of permafrost beneath the surface. Informed speculation predicts the possibility of patterned ground. Data from several disciplines indicate the probable presence of finely divided material on parts of the Martian surface, and there is therefore speculation about various aeolian processes involving these small particles. At our present state of knowledge Sec. 3.5 is necessarily one of discussion rather than one of firm conclusions.

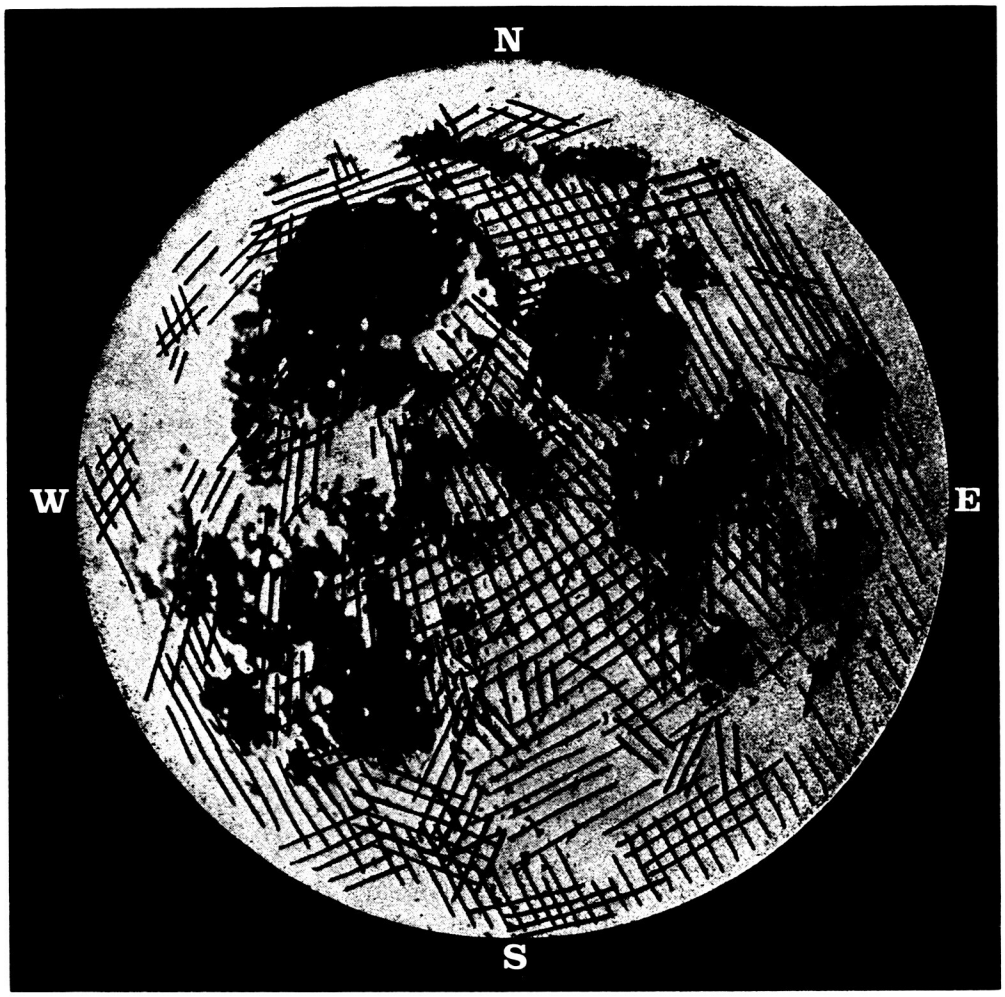

Fig. 1. Chart of the lunar grid system. (Fielder, 1961)

Fig. 2. Azimuth frequency of the Martian lineaments as determined from Mariner IV pictures. Group A are those lineaments north of -36° latitude (pictures 7 to 12) (Fig. 24); group B are those lineaments south of -36° latitude (pictures 13 to 15). (Binder, 1966)

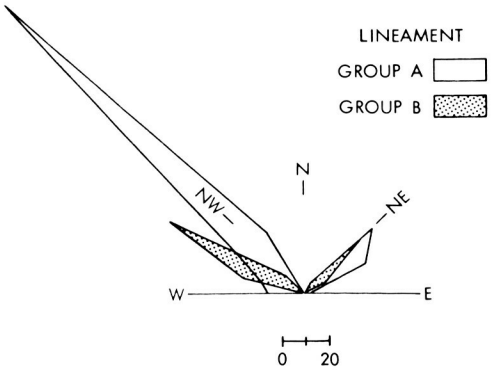

Mariner IV picture no.	Number of definite craters[a]	Number of probable craters[b]	Number of possible craters[c]	Total number of craters	Smallest craters identified, km	Largest crater identified, km	Number of craters with central peaks	Number of craters with polygonal outlines
3 and 4	5	37	46	88	6	80	1	0
5 and 6	9	40	43	92	5	64	6	2
7 and 8	18	45	52	115	4	180	7	10
9 and 10	19	67	46	132	4	123	11	10
11 and 12	20	42	35	97	3	175	8	9
13 and 14	12	19	36	67	6	58[d]	4	4
15 and 16	3	22	20	45	7	114	2	3
	86	272	278	636			39	38

[a]Definite implies the experimenters believe at least 99% of this group will be confirmed by subsequent investigation.

[b]Probable implies the experimenters believe at least 90% of this group will be confirmed by subsequent investigation.

[c]Possible implies the experimenters believe at least 50% of this group will be confirmed by subsequent investigation.

[d]Picture 13 shows a feature which may be the rim of a crater 350 km in diameter.

Fig. 3. Table of Martian crater statistics from Mariner IV pictures. (Leighton et al., 1967)

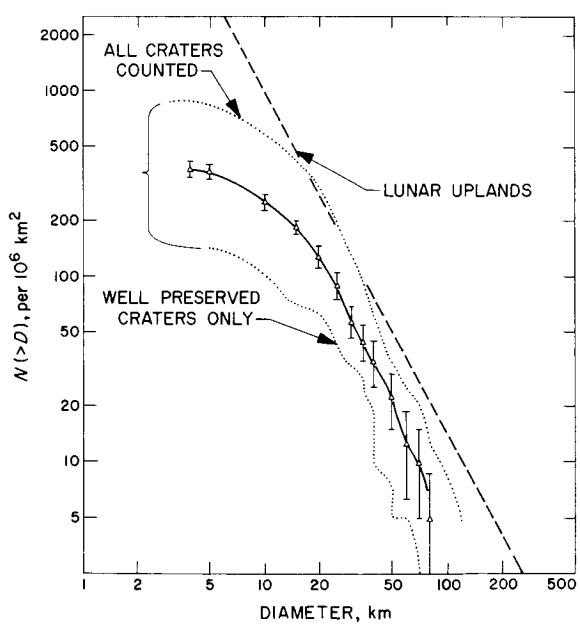

Fig. 4. Integral crater-frequency plot of craters recognized in Mariner IV pictures 7 to 12 (Fig. 24). The upper and lower dotted lines give liberal (75% certainty) and conservative limits (99%). The solid line includes the definite and probable categories, estimated to be 90% certain; error bars are based on statistical fluctuation only. The lunar uplands curve (dashed) is based on data of Trask (1966). (Leighton et al., 1967)

Slope angle, deg	Cumulative percent greater than		Slope angle, deg	Cumulative percent greater than	
	Topographic highs in mountainous terrain	Mare-like areas		Topographic highs in mountainous terrain	Mare-like areas
0	100	100	16	28	0.27
1	95	89	17	27	0.18
2	89	68	18	24	0.13
3	84	46	19	20	
4	80	32	20	18	
5	73	22	21	12	
6	64	14	22	10	
7	61	9.4	23	8.8	
8	57	6.4	24	8.3	
9	51	4.2	25	6.7	
10	47	2.9	26	5.2	
11	45	2.0	27	3.1	
12	42	1.3	28	1.6	
13	37	0.9	29	1.0	
14	35	0.6	30	1.0	
15	33	0.4	31	0.5	

Fig. 5. Table of lunar slope angle distributions.

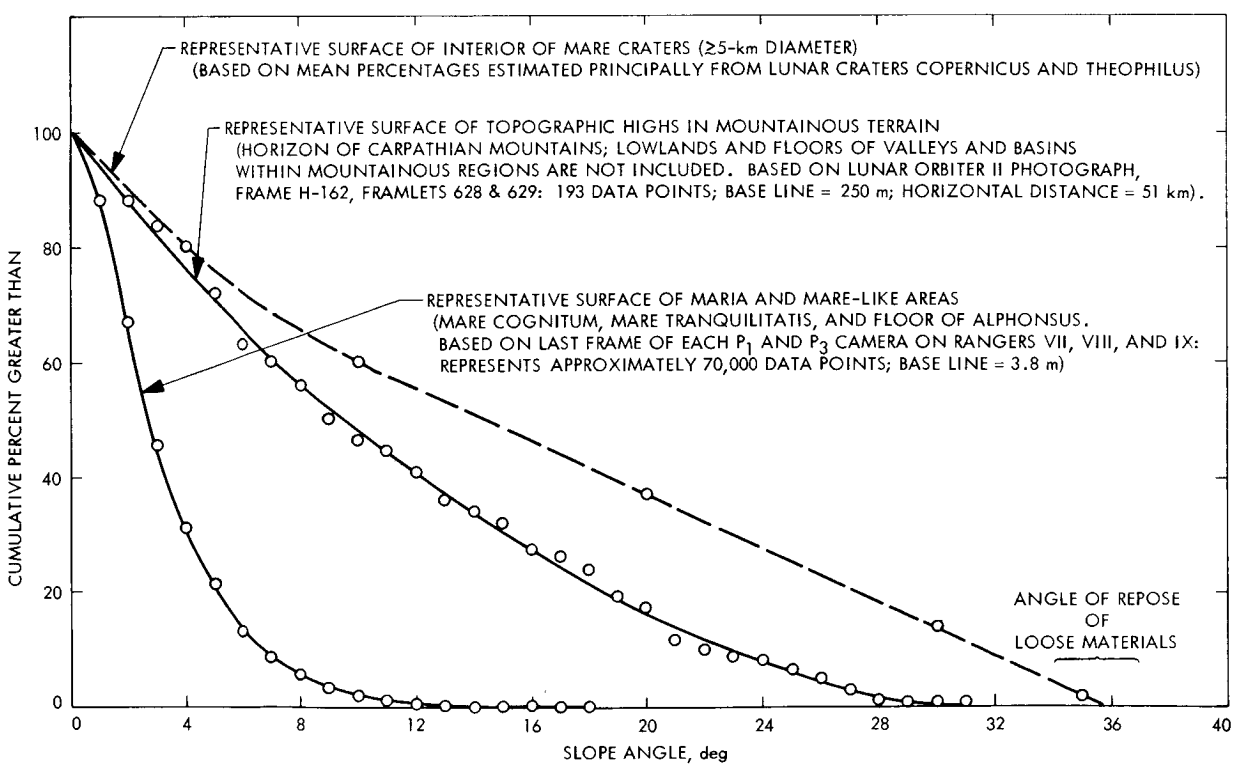

Fig. 6. Lunar slope angle distributions for maria and for topographic highs in mountainous terrain.

Fig. 7. Lunar Orbiter II high-resolution photograph (frame H-162) of lunar crater Copernicus from which some slope angle measurements were made. Distance from the horizon to the base of the photo is about 150 mi; horizontal distance across the part of the crater shown is about 17 mi. The spacecraft was 28.4 mi above the lunar surface and about 150 mi due south of the center of Copernicus when the picture was taken. (photograph by courtesy of Langley Research Center)

Slope angle range, deg	Topographic unit within larger craters, estimated percent			
	Central peaks	Crater floor	Crater terraces	Main inner crater wall
>35	<5	0	<5	<10
30-35	10-30	<5	5-10	20-50
20-30	25-55	5-15	10-30	30-65
10-20	10-40	10-30	20-40	5-15
<10	5-20	55-80	25-55	<5

Fig. 8. Table of estimated range of slope angles for topographic units within large craters (≳5-km diameter). Estimates are based on measurements of slope angles in lunar craters Copernicus and Theophilus (Figs. 7 and 11).

Fig. 9. Table of topographic units within large craters (≳5-km diameter). Percentage estimates are based on representative lunar crater Theophilus (Fig. 11).

Topographic unit	Percent of crater area
Central peaks	5
Crater floor	30
Crater terraces	45
Main inner crater wall	20

Slope angle range, deg	Central peaks		Crater floor		Crater terraces		Inner wall		Total crater area, mean percent	Mean cumulative percent
	Mean percent[a]	Percent of total crater area	Mean percent	Percent of total crater area	Mean percent	Percent of total crater area	Mean percent	Percent of total crater area		
>35	2	0.1	0	0	2	0.9	5	1.0	2.0	2.0
30-35	20	1.0	2	0.6	8	3.6	35	7.0	12.2	14.2
20-30	40	2.0	10	3.0	20	9.0	47	9.4	23.4	37.6
10-20	25	1.2	20	6.0	30	13.5	10	2.0	22.7	60.3
<10	13	0.7	68	20.4	40	18.0	3	0.6	39.7	100.0
Totals	100	5.0	100	30.0	100	45.0	100	20.0	100.0	

[a]Mean value of the range listed in Fig. 8 for each topographic unit.

Fig. 10. Table of estimated slope angles and cumulative percentages for total area of large lunar craters.

Fig. 11. Lunar Orbiter III medium-resolution photograph (frame M-78) of lunar crater Theophilus from which some slope angle measurements were made. The crater is about 104 km (64.9 mi) in diameter. (photograph by courtesy of Langley Research Center)

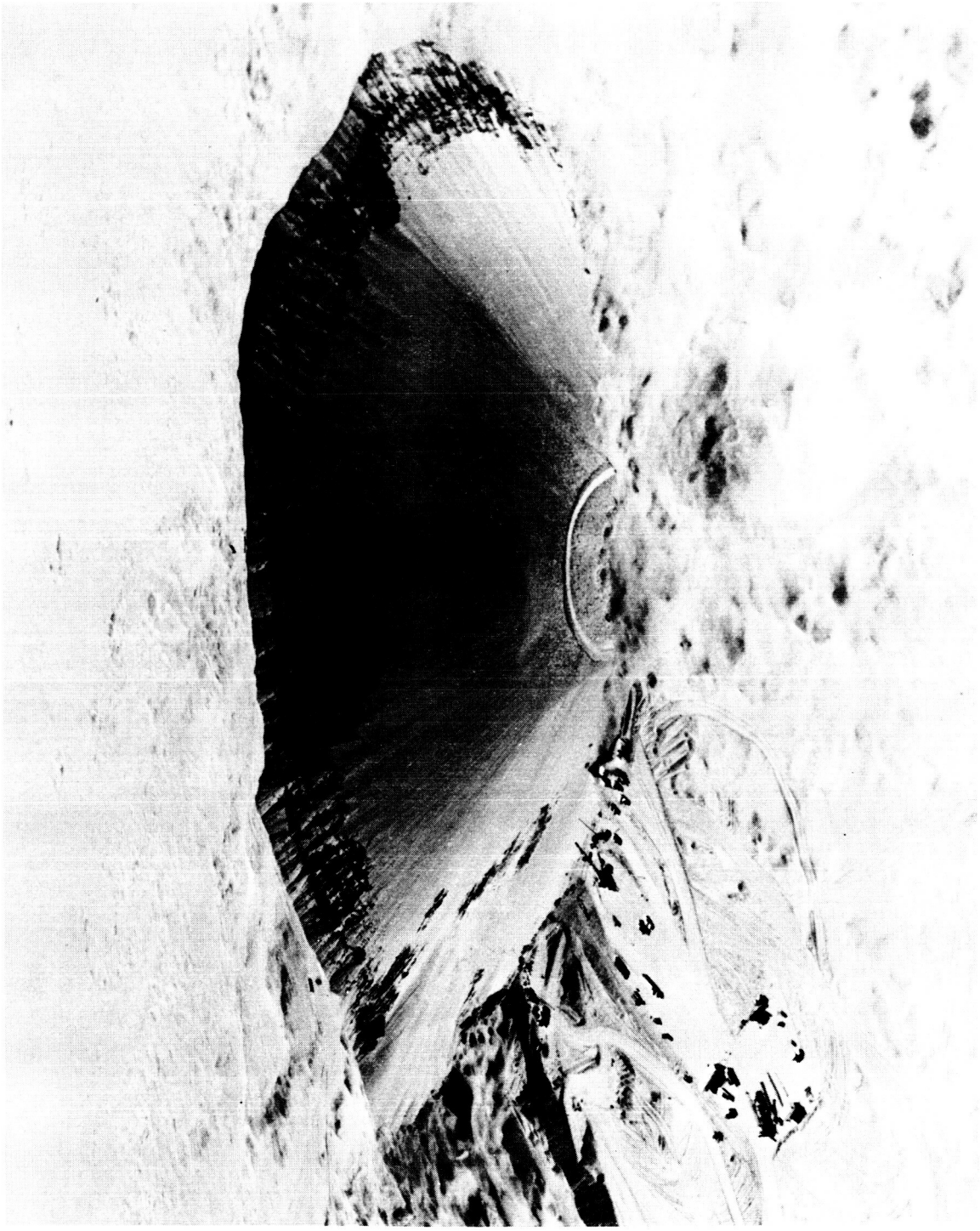

Fig. 12. Sedan Crater, Nevada test site, produced by nuclear detonation in alluvium. Blocks are absent, and loose material on inner slope is at angle of repose. Note trucks and equipment at lower left for scale. (photograph by courtesy of Lawrence Radiation Laboratory)

Fig. 13. Danny Boy Crater, Nevada test site, produced by nuclear detonation in basalt. Crater is 65 m in diameter and 19 m deep. Note trucks near crater rim for comparison with block sizes. For details see Nordyke and Wray (1964). (photograph by courtesy of Lawrence Radiation Laboratory)

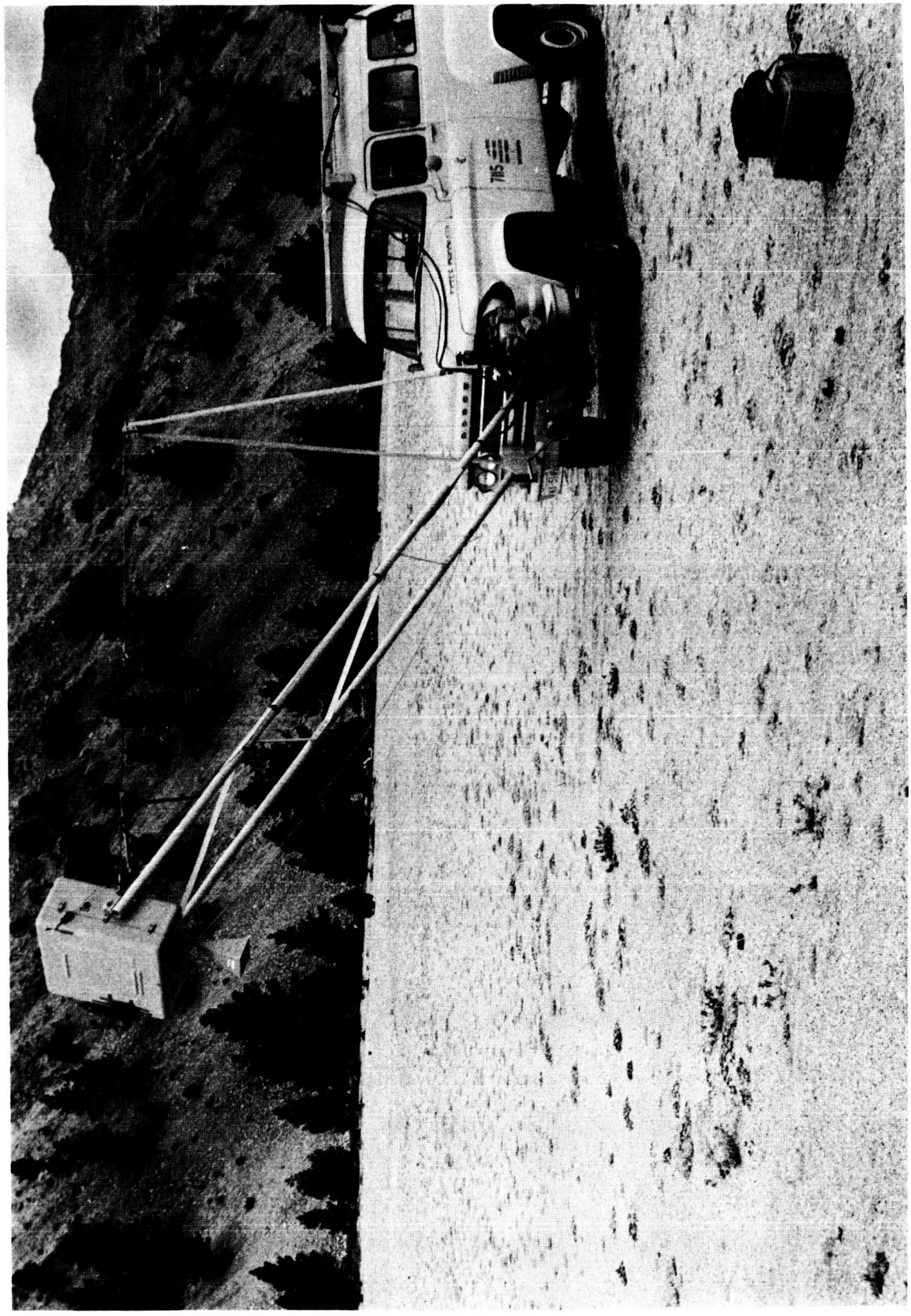

Fig. 14. Pumice flats adjacent to one of the Mono Craters, California. Total relative relief in this surface between observer and distant slope is less than 1 m (3 ft) and arises mostly from recent stream erosion.

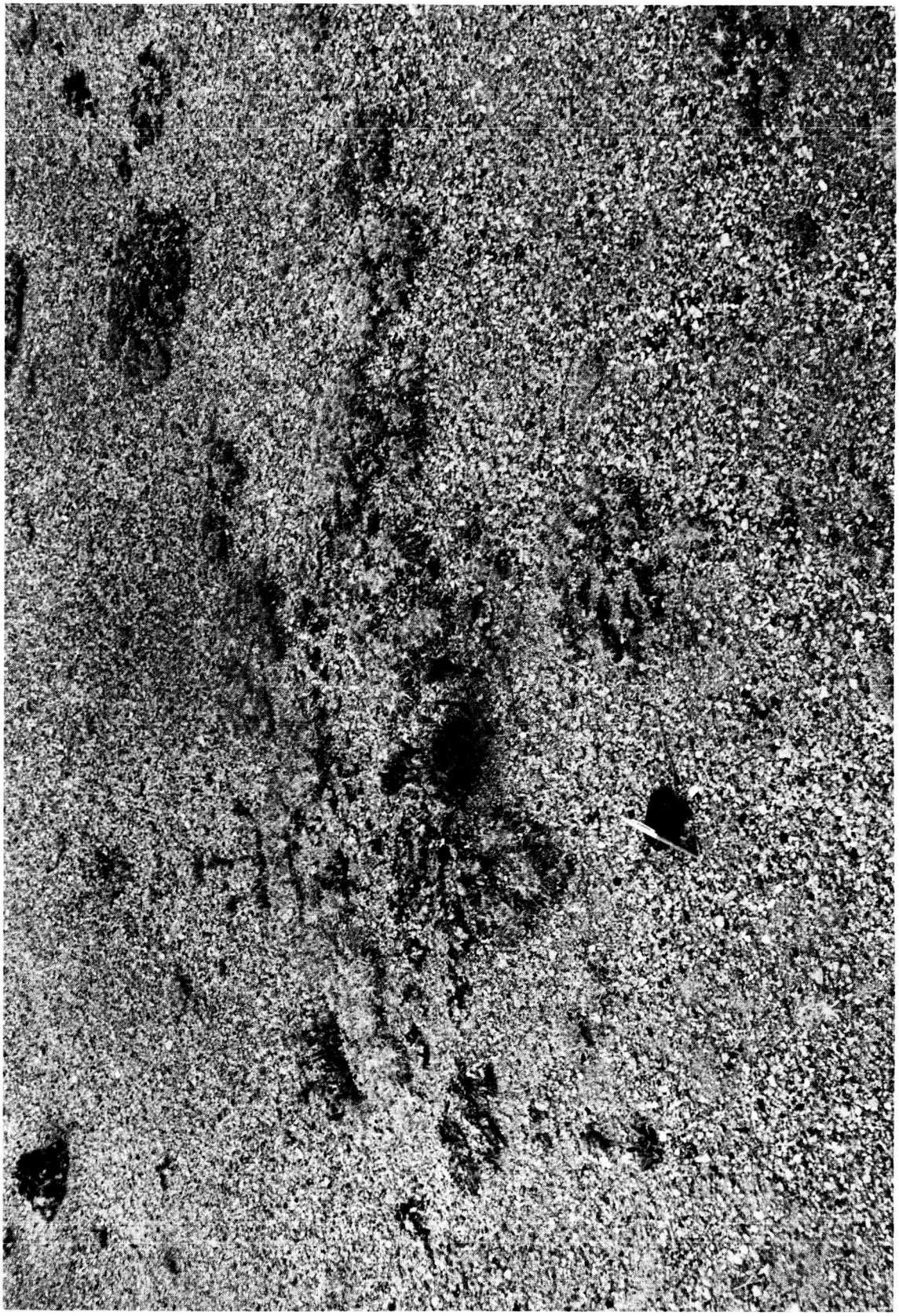

Fig. 15. Close view of pumice flats in Fig. 14, showing particle sizes of surface debris. Wind and water action have removed fine material from surface layers, leaving a coarse (up to 1-2 cm) "lag" concentrate behind.

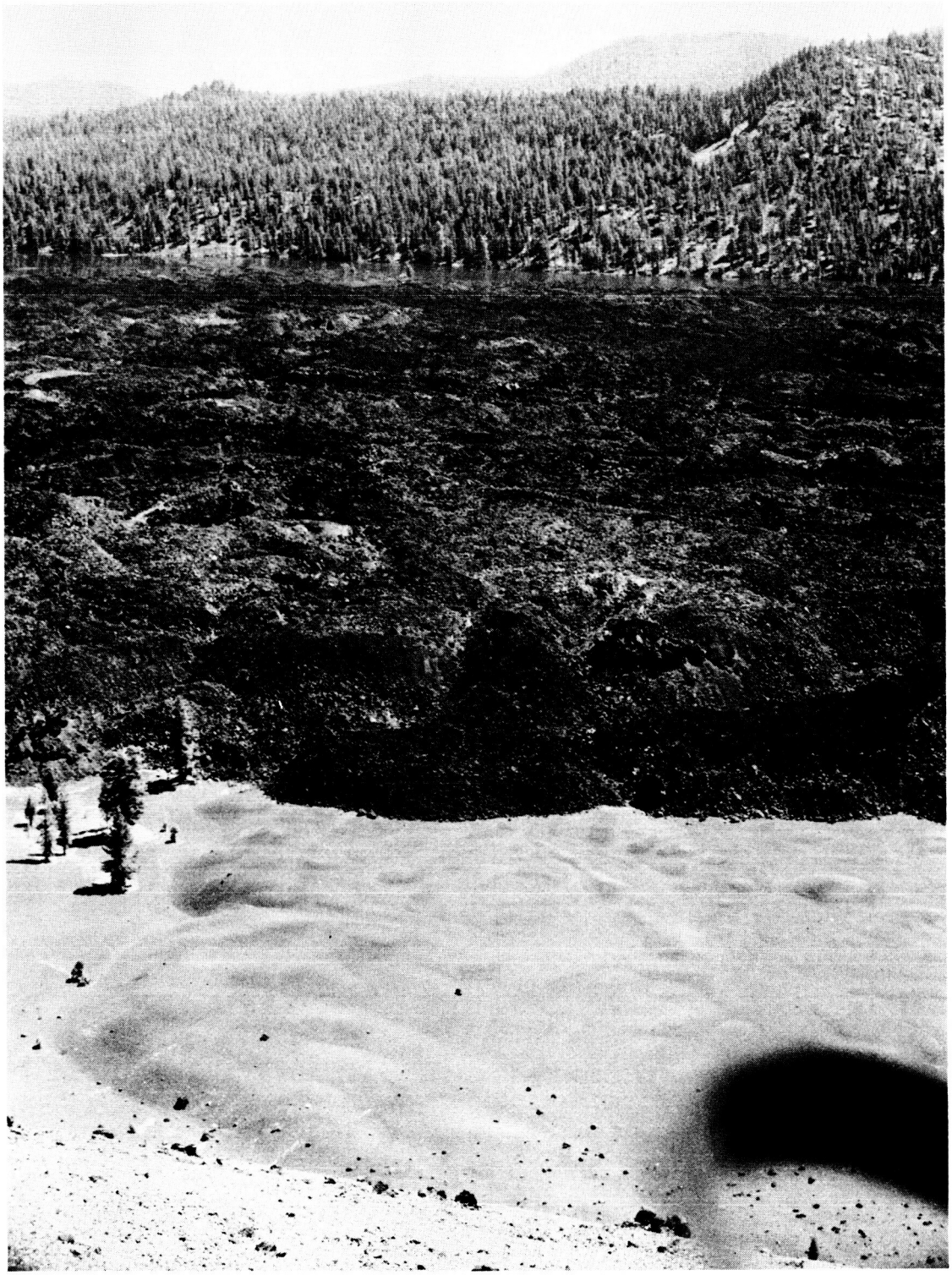

Fig. 16. The Fantastic Lava Beds, Lassen Volcanic National Park, California, showing a recent lava flow with blocky surface. Butte Lake in the distance is approximately 2 mi away from observer. Note fine ash deposits in the foreground.

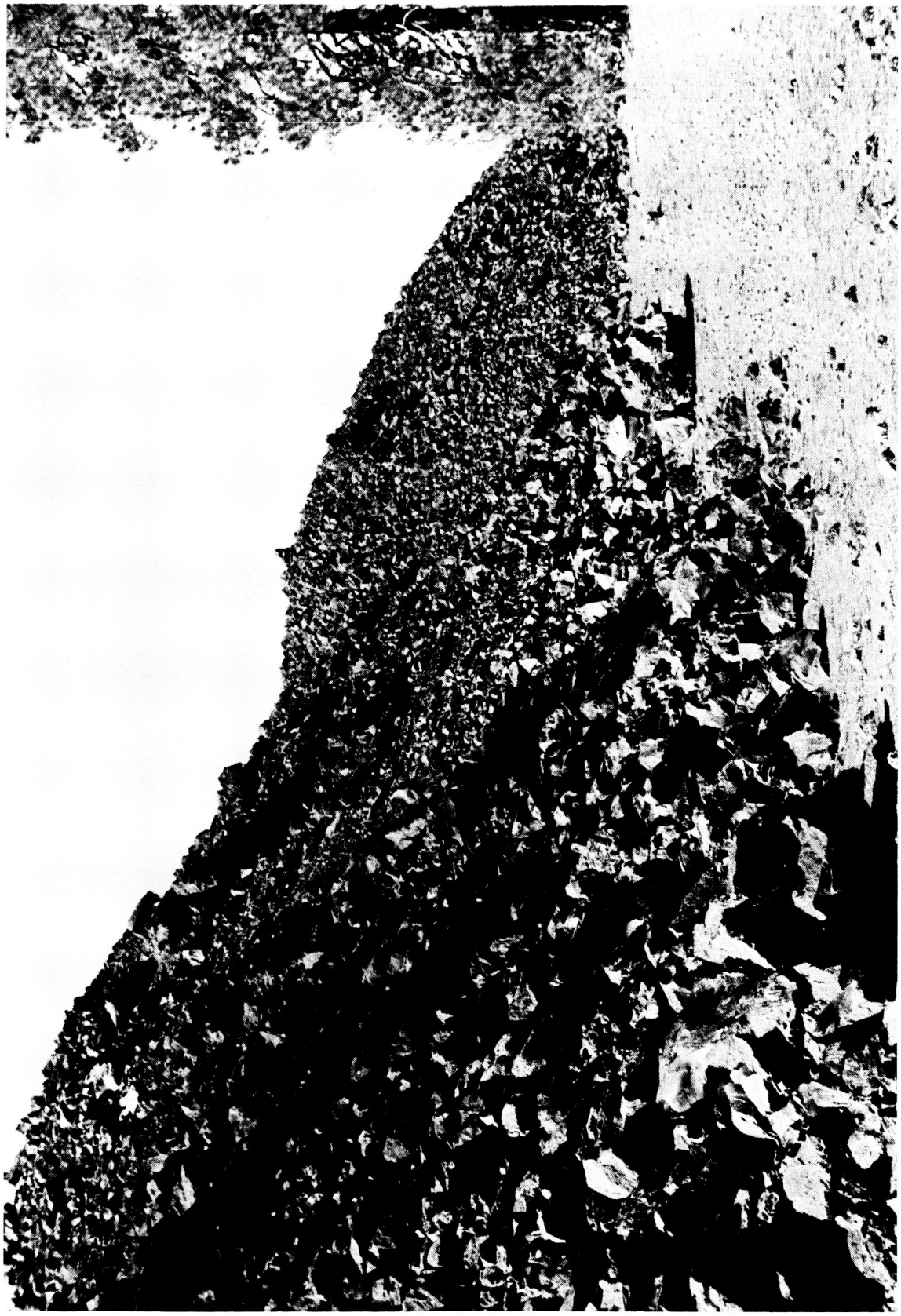

Fig. 17. Close view of lava flow front in Fig. 16. Top of the flow is about 8 m (25-30 ft) above the smooth ash surface on right. Blocks on the nearly 40° slope range in size up to approximately 1 m (3 ft) in diameter.

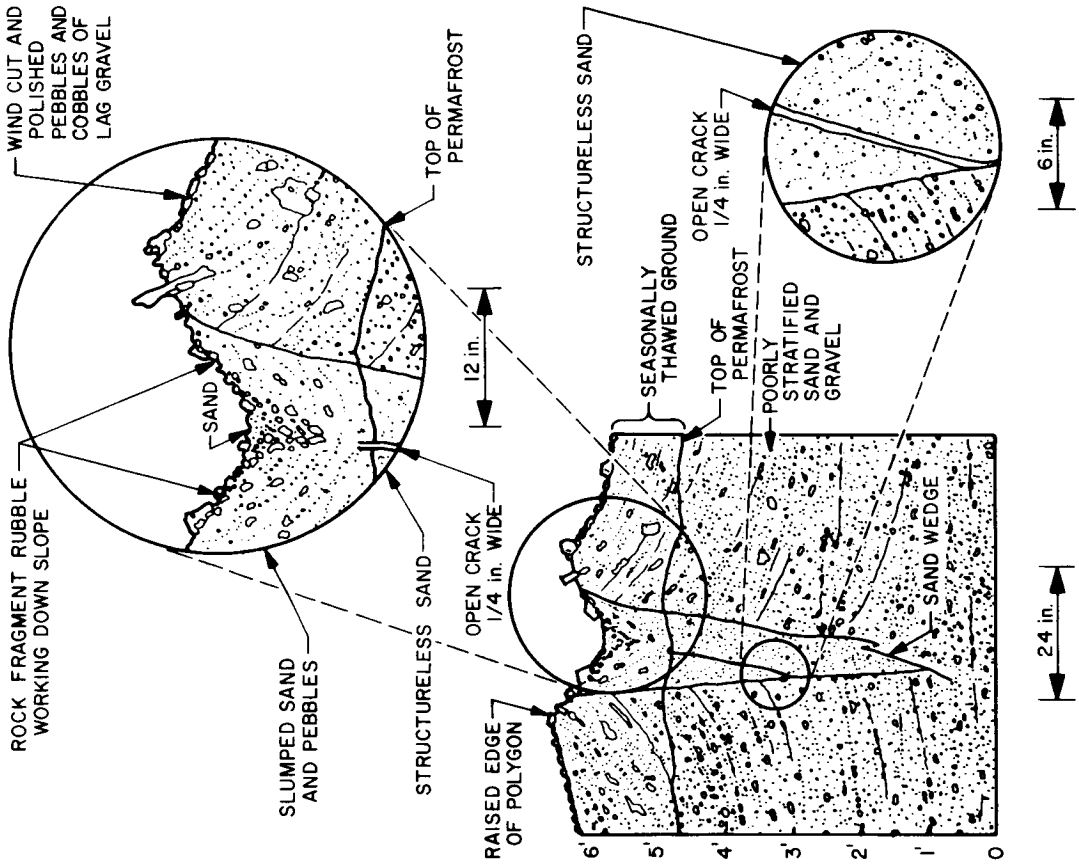

Fig. 19. Diagrammatic sketch of a sand wedge in Taylor Dry Valley, McMurdo Sound, Antarctica. (Péwé, 1959)

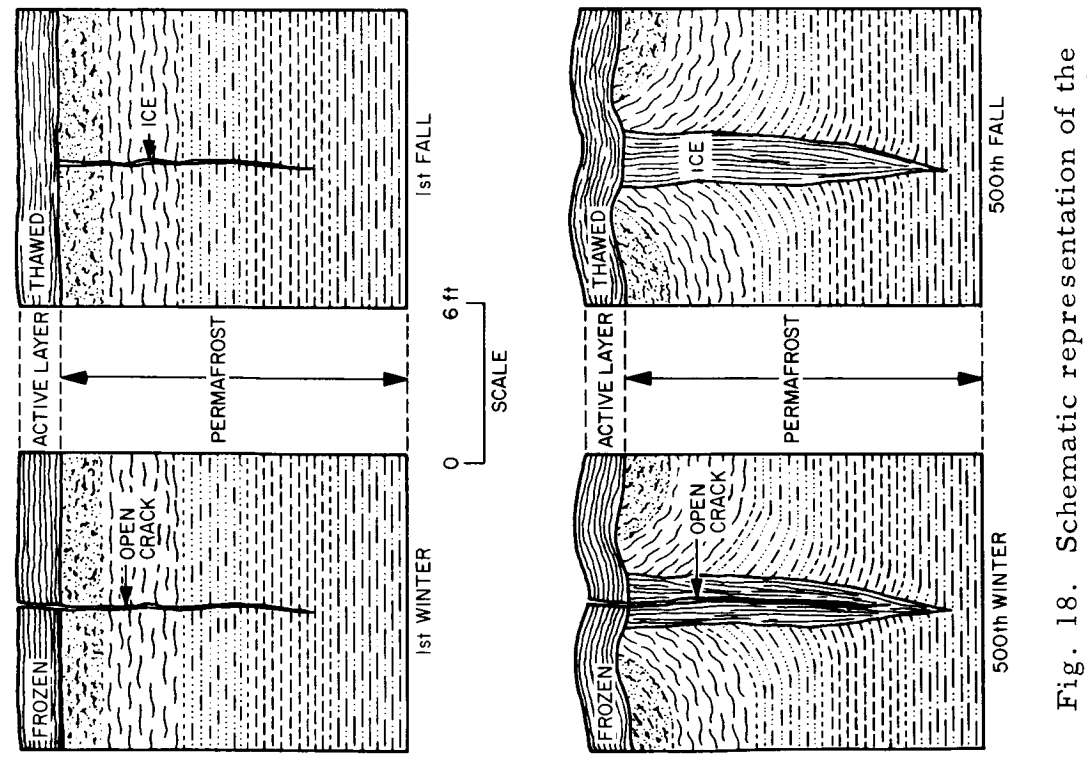

Fig. 18. Schematic representation of the evolution of an ice wedge according to the contraction-crack theory. Width of crack has been exaggerated for illustrative purposes. (Lachenbruch, 1962)

Fig. 20. Non-orthogonal polygons in Mt. Shenk area, Queen Maud Range, Antarctica. Polygons are 20 to 30 m in diameter.

Minimum values for		(1) Surface pressure, Earth: 1000 mb	(2) Surface pressure, Mars		
			25 mb	10 mb	5 mb
(1) Grain diameter (in mm) for maximum susceptibility to motion		0.08	0.4	0.5	0.7
(2) Minimum drag velocity to initiate grain movement (m sec^{-1})		0.15	1.1	2.5	4.0
(3) Horizontal wind velocity at 1-m height equivalent to minimum drag velocity (m sec^{-1})	K = 0.03 cm[a]	3.0	22	50	80
	K = 0.006 cm[a]	3.7	27	60	100

[a]K is the surface roughness characteristic, the height above the surface at which the wind velocity is zero.

Data sources:
Column (1), lines (1) and (2)—
Bagnold, 1941, p.88 and 90; for particle density of 2.65 and normal surface temperature.
Column (1), line (3)—
Bagnold, 1941; computed from equation on p.52.
Column (2), line (1)—
Galbraith, 1966, Fig.18; for grains of density 3.0 and temperature 275°K.
Column (2), line (2)—
Galbraith, 1966; interpolation from Figs. 12-14.
Column (2), line (3)—
Galbraith, 1966, Figs.33-34.

Fig. 21. Table of threshold wind velocity required to initiate motion in particles of optimum size on Earth and Mars.

Particle diameter, mm	Surface pressure, Earth: 1000 mb	Surface pressure, Mars		
		25 mb	10 mb	5 mb
10	50	—	126	165
1.0	7	16.0	17.8	21.1
0.5	4	6.4	7.0	8.0
0.1	0.6	0.44	0.51	0.55
0.05	0.2	0.12	0.14	0.17
0.01	0.008	0.006	0.009	0.014
0.005	0.002	0.002	0.004	0.006
0.001	0.00006	0.00025	0.0006	0.001

Data for Earth from Malina, 1941, Fig.8, and Bagnold, 1941, Fig.1; particle density of 2.65 and normal surface temperature assumed.

Data for Mars from Anderson, 1966, Tables 2 and 3 and Fig.7; particle density of 3.0 and surface temperature of 225°K assumed.

Dashed lines mark reversals in ratio of settling velocities on Earth and on Mars.

Fig. 22. Table of settling velocities of spherical particles in relation to size for Earth and Mars.

Grain diameter, μ	Estimated fall time from 6-km altitude			
	Surface pressure, Earth: 1000 mb	Surface pressure, Mars		
		25 mb	10 mb	5.5 mb
100	3 hours	4 hours	3.1 hours	2.9 hours
50	9 hours	17 hours	11.2 hours	9.7 hours
20	2 days	3.5 days	2.3 days	1.7 days
10	7 days	12 days	6.5 days	4.3 days
5	31 days	40 days	16.0 days	9.9 days
1	700 days	300 days	95.0 days	53.0 days

Assumed data:
Particle density of 3.0; particle shape spherical (after Anderson, 1966, p.18).
Temperature on Earth of 280°K, constant with altitude. Temperature on Mars of 230°K for 25 mb, constant with altitude; and of 225°K for 10 and 5.5 mb, decreasing upward.

Fig. 23. Table of estimated particle fall time from 6-km altitude for Earth and Mars. Absence of vertical wind on Mars is assumed.

A mosaic of the Mariner IV pictures superimposed upon a photograph of a hand-painted model of Mars. Picture 1 caught the limb, or edge, of the planet as Mariner IV observed it from a position about 8,000 miles below the plane of Mars' orbit at a slant range of 10,500 miles. As the spacecraft swept under the planet, the television scan path progressed toward the southeast and in picture 19 moved across the terminator (the light-dark boundary). The last three pictures (20, 21, and 22) were taken in complete darkness.

Picture 7

Picture 7 is wholly within the southeastern part of the bright region Zephyria, near Mare Sirenum.

Location of picture center:
- Latitude . . . . . -13°
- Longitude . . . . . 174°

Dimensions of area:
- East-west . . . . . 290 km (180 mi)
- North-south . . . . 290 km (180 mi)

Spacecraft distances:
- Altitude . . . . . 13,192 km (8,179 mi)
- Slant range . . . . . 13,582 km (8,421 mi)

Time and lighting:
- Local time . . . . . about noon
- Phase angle . . . . . 59.6° to 60.5°
- Zenith angle . . . . Sun is 29° north of the zenith

Filter . . . . . green

Overlap. . . . . Lower right corner overlaps picture 8

Time of exposure . . . 00:25:45 GMT, July 15, 1965

Picture 8

Picture 8 contains part
and the dark Mare Siren
border between these tv
trends across the middl
picture.

Location of picture cent
- Latitude . . . . . .
- Longitude . . . . . .

Dimensions of area:
- East-west 290
- North-south 275

Spacecraft distances:
- Altitude . . . . . .
- Slant range . . . . . .

Time and lighting:
- Local time . . . . . .
- Phase angle 5
- Zenith angle . . . . Sun

Filter . . . . . .

Overlap. . . . . Uppe
overla

Time of exposure . . . 00
J

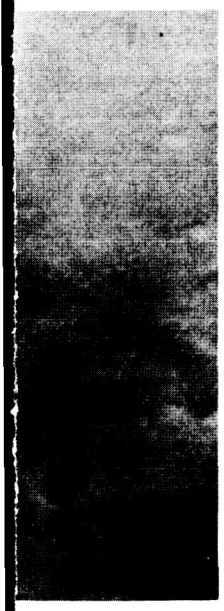

of Zephyria
num. The
o features
e of the

er:
.....-17°
.....173°

km (180 mi)
km (170 mi)

..13,056 km
(8,095 mi)
..13,373 km
(8,291 mi)

..about noon
.5° to 60.5°
is 32° north
of the zenith

..... orange

r left corner
ps picture 7

:26:33 GMT,
uly 15, 1965

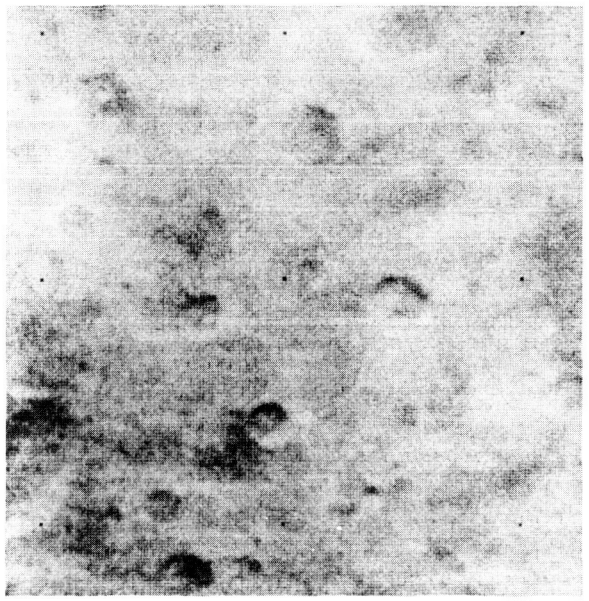

Picture 9

Picture 9 is largely in the dark area Mare Sirenum, bordering on the light area Atlantis in the southwest corner of the picture.

Location of picture center:
Latitude.....-24°
Longitude .....169°

Dimensions of area:
East-west.....275 km (170 mi)
North-south ....260 km (161 mi)

Spacecraft distances:
Altitude.....12,790 km (7,930 mi)
Slant range.....13,004 km (8,062 mi)

Time and lighting:
Local time .....about noon
Phase angle .....59.4° to 60.4°
Zenith angle .... Sun is 39° from the zenith

Filter .....orange

Overlap.....Lower right corner overlaps picture 10

Time of exposure ... 00:28:09 GMT, July 15, 1965

J. de Wys, JPL

Picture 10

Picture 10 is partly in the dark area Mare Sirenum, and largely in the light area Atlantis, which borders on Mare Sirenum in the northeast corner of the picture.

Location of picture center:
Latitude.....-27°
Longitude .....167°

Dimensions of area:
East-west.....275 km (170 mi)
North-south ....260 km (161 mi)

Spacecraft distances:
Altitude.....12,660 km (7,849 mi)
Slant range.....12,843 km (7,963 mi)

Time and lighting:
Local time .....about noon
Phase angle .....59.4° to 60.3°
Zenith angle .... Sun is 42° from the zenith

Filter .....green

Overlap.....Upper left corner overlaps picture 9

Time of exposure ... 00:28:57 GMT, July 15, 1965

Picture 11

Picture 11 probably is principally within the dark Mare Sirenum, but may be in or near the lighter area Atlantis between Mare Sirenum and Mare Cimmerium.

Location of picture center:
Latitude.....-33°
Longitude .....162°

Dimensions of area:
East-west.....275 km (170 mi)
North-south ....240 km (149 mi)

Spacecraft distances:
Altitude.....12,407 km (7,692 mi)
Slant range.....12,564 km (7,790 mi)

Time and lighting:
Local time ..... about 12:40
Phase angle .....59.3° to 60.3°
Zenith angle .... Sun is 49° from the zenith

Filter .....green

Overlap.....Lower right corner overlaps picture 12

Time of exposure ... 00:30:33 GMT, July 15, 1965

Picture 1
poorly de
dark Mar
area Atla

Location
Latitu
Longit

Dimensio
East-v
North-

Spacecraf
Altitud

Slant r

Time and
Local
Phase
Zenith

Filter ...

Overlap..

Time of e

9

Picture 12

2 probably lies across the
fined border between the
e Sirenum and the lighter
ntis.

of picture center:
le.....-36°
ude .....160°

ns of area:
vest .....275 km (170 mi)
south ....240 km (149 mi)

't distances:
e .....12,284 km
(7,616 mi)
ange .....12,446 km
(7,717 mi)

lighting:
time ..... about 12:40
angle .....59.3° to 60.2°
angle .... Sun is 52° from
the zenith

..... orange

.....Upper left corner
overlaps picture 11

xposure ... 00:31:21 GMT,
July 15, 1965

Fig. 24. Mariner IV pictures 7 to 12, and the locations of Martian regions photographed in pictures 1 to 19. North is at the top.

3

CROSS REFERENCES

The specific section number, subject, and page number to which the reader is referred is given below.

Cross Reference	Section and Subject
[1] Relief differences	1.....Physical data (data summary), p.6. 2.....Flattening (discussion), p.4; Interior models (discussion), p.6. 5.2.....Surface pressure as determined from the Mariner IV occultation experiment (discussion), p.3.
[2] Freeze-thaw features and bearing strength	3.4.....Bearing strength (discussion), p.6.
[3] Surface temperature and pressure	3.1.....Thermal properties (discussion), p.2,3. 5.2.....Surface pressure (data summary), p.1. 5.3.....Lower atmosphere (data summary), p.1; Dry-adiabatic lapse rate in the troposphere (discussion), p.2.
[4] Albedo differences	3.2.....Albedo, magnitude, and color (discussion), p.4.
[5] Radar data	3.3.....Radar results and surface relief (observational implications), p.8,9.
[6] Clouds, white patterns	4.1.....Clouds and hazes, entire section. 4.2.....The polar hoods (discussion), p.3,4; Seasonal behavior of clouds (discussion), p.4; Seasonal changes in specific areas (figures), p.11-17; Seasonal activity maps (figures), p.19-25.
[7] Linear features	2.....Planetary expansion and rifting in Lyttleton's interior model (discussion), p.8. 4.1.....The W-shaped cloud in the Tharsis region (discussion), p.5. 4.2.....Secular changes of the Nilosyrtis, Thoth, and Nepenthes canals (discussion), p.2.
[8] Meteorite impact	3.4.....Meteoritic and magnetic material (discussion), p.4.
[9] Thermal environment	3.1.....Surface temperatures (data summary), p.1, and brightness temperature characteristics (data summary), p.2.
[10] Photometric technique	3.2.....Photometric function (discussion), p.3,4.

Cross Reference	Section and Subject
[11] Water	3.4.....Water and carbon dioxide on the surface (discussion), p.3,4. 5.1.....Observed atmospheric constituents (data summary), p.1.
[12] Volcanic activity	4.1.....Green haze, gray clouds, and bright spots (discussion), p.7,8; List of observed bright flares and spots (figure), p.11.
[13] Vertical winds and thermal convection	5.3.....Physics of the troposphere (discussion), p.2,3.
[14] Accumulations of dust	3.4.....Bearing strength (data summary), p.2, (discussion), p.6.

BIBLIOGRAPHY

Anderson, A.D., 1966, Spherical particle terminal velocities in the Martian daytime atmosphere from 0 to 50 kilometer: Palo Alto, Calif., Lockheed Palo Alto Research Lab.

Antoniadi, E.M., 1930, La planete Mars: Paris, Librairie Scientifique Hermann et Cie, 6, Rue de la Sorbonne.

Bagnold, R.A., 1941, rpt 1960, The physics of blown land and desert dunes: London, Methuen and Co.

Binder, A.B., 1966, Mariner IV: analysis of preliminary photographs: Science, v.152, p.1053-1055.

Burley, J., and Middlehurst, B.M., 1966, Apparent lunar activity: historical review: Proc.Nat.Acad.Sci., v.55(S), p.1007-1011.

Choate, R., 1966, Lunar slope angles and surface roughness from Ranger photographs, p.411-431 in Proceedings of the fourth symposium on remote sensing of environment: Ann Arbor, Mich., U.of Mich. Reprinted: Pasadena, Calif., Jet Propulsion Laboratory, Tech.Rep. 32-994.

Fielder, G., 1961, Structure of the Moon's surface: Oxford, London, New York, Paris, Pergamon Press, p.190.

Galbraith, T.L., 1966, Particle transport in the Martian atmosphere: General Electric, Space Physics, Tech.Memo.8126-4.

Gierasch, P., and Goody, R., 1968, A study of the thermal and dynamical structure of the Martian lower atmosphere: Planet.Space Sci., v.16, p.615-646.

Gifford, F.A., Jr., 1964, The Martian canals according to a purely aeolian hypothesis: Icarus, v.3, p.130-135.

Gilluly, J., Waters, A.C., and Woodford, A.D., 1959, Principles of geology, 2d Edition: Freeman and Co.

Grawe, O.R., 1936, Ice as an agent of rock weathering: J.Geol., v.44, p.180-181.

Kachur, V., 1966, Thermology of the Martian surface; presented at AIAA 4th Aerospace Sciences Meeting: New York, American Institute of Aeronautics and Astronautics, AIAA Paper 66-436.

Katterfel'd, G.N., 1966, Volcanic activity on Mars: Wash., D.C., National Aeronautics and Space Administration, Tech.Transl.F-410. Translation of, 1965, Vulkanicheskaya aktivnost' na Marse: Priroda, n.8, p.103-109.

Lachenbruch, A.H., 1962, Mechanics of thermal contraction cracks and ice-wedge polygons in permafrost: Geol.Soc.Am., Sp.Paper 70.

Leighton, R.B., and Murray, B.C., 1966, Behavior of carbon dioxide and other volatiles on Mars: Science, v.153, p.136-144.

Leighton, R.B., Murray, B.C., Sharp, R.P., Allen, J.D., and Sloan, R.K., 1967, Mariner Mars 1964 project report: television experiment, Part I. Investigators' report, Mariner IV pictures of Mars: Pasadena, Calif., Jet Propulsion Laboratory, Tech.Rep.32-884.

Leovy, C.B., and Mintz, Y., 1968, Numerical simulation of the general atmospheric circulation and climate on Mars: Santa Monica, Calif., RAND Corp., Administrative Rep.AR-362-JPL.

Malina, F.J., 1941, Recent developments in the dynamics of wind-erosion: Trans.Am.Geophys.Union for 1941, p.262-284.

Marcus, A.H., 1968, Number density of Martian craters: Wash., D.C., Bellcomm, Inc., TR-68-710-1.

McLaughlin, D.B., 1954, Interpretation of some Martian features: Pub. Astron.Soc.Pacific, v.66, p.161-170.

Mellish, J.E., 1966, Letter: Sky and Telescope, v.XXXI, n.6, p.339.

Middlehurst, B.M., 1968, (U.of Ariz., Lunar and Planetary Lab.): private communication to J. de Wys.

Mintz, Y., 1961, A note on the temperature of the equatorial troposphere of Mars, in Studies of the physical properties of the Moon and planets: Santa Monica, Calif., RAND Corp., Quarterly Progress Rep.(3), RM-2769-JPL.

Miyamoto, S., 1966, Martian atmosphere and crust: Icarus, v.5, p.360-374.

Murray, B.C., 1967, (Pasadena, Calif., Caltech): oral communication to J. de Wys.

Nordyke, M.D., and Wray, W., 1964, Cratering and radioactivity results from a nuclear cratering detonation in basalt: J.Geophys.Res., v.69, p.675-689.

O'Leary, B.T., and Rea, D.G., 1967, Mars: influence of topography on temporary bright patches: Science, v.155, p.317-319.

Péwé, T.L., 1959, Sand-wedge polygons (tesselations) in the McMurdo Sound region, Antarctica—a progress report: Am.J.Sci., v.257, p.545-551.

Rindfleisch, T., 1965, A photometric method for deriving lunar topographic information: Pasadena, Calif., Jet Propulsion Laboratory, Tech.Rep. 32-786.

Ryan, J.A., 1964, Notes on the Martian yellow clouds: J.Geophys.Res., v.69, p.3759-3770.

Sagan, C., and Pollack, J.B., 1966, On the nature of the canals of Mars: Nature, v.212, p.117-121.

_____, 1968, Elevation differences on Mars: J.Geophys. Res., v.73, p.1373-1387.

Sagan, C., Pollack, J.B., and Goldstein, R.M., 1967, Radar doppler spectroscopy of Mars, I. Elevation differences between bright and dark areas: Astron.J., v.72, p.20-34.

Shapiro, I.I., 1968, Radar observations of the planets: Sci.Am., v.219, n.1, p.28-37.

Sharp, R.P., 1968, Surface processes modifying Martian craters: Icarus, v.8, p.472-480.

Shoemaker, E.M., 1962, Interpretation of lunar craters, in Physics and astronomy of the Moon; Kopal, F., Editor: New York and London, Academic Press.

Shumskii, P.A., 1964, Principles of structural glaciology (translated from Russian by D.Kraus): New York, Dover Publications, Inc., p.197.

Sinton, W.M., and Strong, J., 1960, Radiometric observations of Mars: Astrophys.J., v.131, p.459-469.

Tombaugh, C.W., 1950, Geological interpretations of the markings on Mars: Astron.J., v.55, p.184.

_____, 1965, Provisional topographic map of Mars, Mariner 4 region: University Park, N.M., N.M. State U. Observatory, TN-701-66-8.

_____, 1966, Evidence that the dark areas on Mars are elevated mountain ranges: Nature, v.209, p.1338.

Trask, N.J., 1966, Size and spatial distribution of craters estimated from the Ranger photographs, in Ranger VIII and IX, Part II. Experimenters' analyses and interpretations: Pasadena, Calif., Jet Propulsion Laboratory, Tech.Rep.32-800.

Wade, F.A., and de Wys, J.Negus, 1968, Permafrost features on the Martian surface: Icarus, v.9, p.175-185.

Wells, R.A., 1965, Evidence that the dark areas on Mars are elevated mountain ranges: Nature, v.207, p.735-736.

_____, 1966, Evidence that the dark areas on Mars are elevated mountain ranges: Nature, v.209, p.1338-1339.

Willingham, D., 1967, (Pasadena, Calif., Jet Propulsion Laboratory): oral communication to R. Choate.

SECTION 4 CONTENTS

4. OBSERVATIONAL PHENOMENA

Introduction 3

4.1 Clouds and Hazes

Data Summary 1
The Violet Layer 1
Blue Clearing 1
White Clouds 1
Yellow Clouds 1
Other Phenomena 2
Discussion 2
Early Observations 2
The Violet Layer, Blue Clouds, and Blue Clearing 2
White Clouds 5
Yellow Clouds 5
Green Haze, Gray Clouds, and Bright Spots 7
Cross References 12
Bibliography 14

Figures
1. Table of observations of Martian blue clearings 9
2. Table of major Martian "dust storms" 10
3. Table of bright flares and spots observed on Mars 11

4.2 Seasonal Activity

Data Summary 1
The Polar Caps and Hoods 1
The Dark Fringe of the Polar Caps 1
Seasonal Behavior of Clouds 1
The Wave of Darkening 1
Seasonal Behavior of Surface Features 1
Discussion 2
Polar Caps 2
The Polar Hoods 3
The Dark, Peripheral Fringe-Band-Collar of the Polar Caps 4
Seasonal Behavior of Clouds 4
The Wave of Darkening 5
Seasonal Behavior of Surface Features 5
Cross References 27
Bibliography 28

4.2 (cont'd)

Figures

1. Measured width of the south polar cap of Mars for various oppositions from 1798 to 1924 8
2. Measured width of the north polar cap of Mars for observations from October, 1964, through August, 1965 9
3. Areographic amplitude of the intensity of the dark areas of Mars . . 10
4. Table of seasonal changes on Mars in northern dark areas 11
5. Table of seasonal changes on Mars in equatorial dark areas 13
6. Table of seasonal changes on Mars in northern light areas 15
7. Table of seasonal changes on Mars in equatorial light areas 17
8. Color map of the Martian surface in northern fall-winter and southern spring-summer, with white and yellow cloud activity during these seasons 19
9. Color map of the Martian surface in northern spring and southern fall, with wave of darkening, frost, and white and yellow cloud activity during these seasons 21
10. Color map of the Martian surface in northern summer and southern winter, with wave of darkening and white and yellow cloud activity during these seasons 23
11. Map and table of Martian place-names and their locations 25

4. OBSERVATIONAL PHENOMENA

INTRODUCTION

This section of the Mars Scientific Model includes discussion of many of those aspects of the appearance of Mars which were originally discovered by direct visual observation, although current knowledge of them may have been greatly enhanced by photographic studies, photometry, polarimetry, etc. More than brief mention of these phenomena is important in order to convey a proper appreciation of Mars as a dynamic, changing world, a perspective often lost in the presentation of quantitative data and simplified theoretical models.

The first part, Sec. 4.1, encompasses discussion of such persistent but often changing phenomena as the clouds and hazes of the planet, while the second part, Sec. 4.2, is devoted to phenomena which change seasonally, such as the polar caps and the wave of darkening. Cloud activity has a seasonal character which is included in Sec. 4.2. It is hoped that a third section can be added at some future time to discuss secular changes in the Martian surface, of which there have been many during the past 100 years, the period of observations of relatively high reliability.

4.1 CLOUDS AND HAZES

Two distinct types of Martian clouds are always recognized, white clouds and yellow clouds. Some observers recognize a distinct class of blue clouds separated from white on the basis of polarization measurements and behavior. Others separate blue clouds morphologically, associating them with brighter areas in a general atmospheric haze usually called the violet layer. Still others consider blue and white clouds to be the same phenomenon. Recently gray clouds, bright spots, and a green haze have also been reported. These observational phenomena are each discussed in this section.

DATA SUMMARY

The Violet Layer

The violet layer, sometimes called the blue haze or violet haze, is thought to be a high altitude distribution of sub-micron-size particles composed of a volatile substance, perhaps CO_2 or H_2O. It contributes to atmospheric opacity sufficiently to lower surface contrast below the level where detail can be discerned in wavelengths of light shorter than about 4550 Å. Not all investigators are convinced that the violet layer really exists, attributing lack of surface detail in blue light to poor surface contrast in the blue and to poor seeing.

Blue Clearing

At times, in about a day, the atmosphere of Mars becomes clear enough for a period of one or more days for surface detail to be seen clearly at wavelengths of 4250 Å or less. This "blue clearing" of the Martian atmosphere is attributed to a temporary dissipation of the violet layer (by those who believe in the layer).

White Clouds

White clouds are those which can be photographed at short wavelengths but disappear in red or infrared photos. Sometimes an added distinction is made for certain "blue clouds" based upon behavior and polarization properties. White clouds are generally thought to be a fog of sub-micron ice particles similar to terrestrial cirrus clouds. White clouds are of all shapes and sizes, from terminator haze lasting a few hours to dense, 2000-km giants lasting days or weeks.

Yellow Clouds

Yellow clouds are those readily photographed in yellow or red light but which are not seen in blue light. They may be small, dense, orange or yellow objects lasting one or a few days, or they may start large and grow larger until they become a yellow veil covering most of Mars and lasting a month or more. Yellow clouds are believed to be clouds of dust particles, perhaps a few to 50 μ in diameter, raised by high surface winds.

Other Phenomena

Several other less well established phenomena are covered in the discussion, including bright spots or flares which, if real, may be evidence of surface tectonic activity.

DISCUSSION [1*]

Early Observations

Yellowish clouds and veils were reported by visual observers of Mars at least as early as 1809 (by Flaugergues), and white clouds were reported by Secchi in 1858 (Maginni, 1939). Such observations were made with refracting telescopes, color corrected for visual observing. Under such conditions color descriptions are quite subjective, but the differences in appearance which resulted in a distinction between yellow and white clouds were real enough.

In 1871 the dry photographic plate was developed, making astronomical photography a practical possibility rather than a stunt, as it had been during the wet plate era. The "natural" spectral sensitivity of a photographic emulsion extends from the ultraviolet to about 5200 Å, there being some dependence upon the exact ratio of halides used in the emulsion and the physical processing during manufacture. Although it was discovered by Vogel in 1873 that the range of spectral sensitivity could be extended with dyes, reasonably fast red plates were not commercially available until 1906 (Mees, 1954). Most early photography of Mars was done with "natural" blue plates exposed through a refracting telescope, color corrected in the visual (yellow) region of the spectrum. The resulting blurred images were rather discouraging.

Lowell Observatory began an experimental Martian photographic program in 1901 with "encouraging" results (Lowell, 1905). Surviving today are four plates taken in 1903 and 99 plates from 1905 of useful scientific quality (Baum et al., 1967). In 1907 Lowell described their process of extending plate sensitivity to 6800 Å and the use of a filter to isolate the yellow-green region for which their 24-in. refractor was color corrected. Many excellent photographic images were obtained in 1907, largely with an 18-in. refractor taken to Chile, where Mars came much nearer to the zenith. Some of these are reproduced in Slipher's 1962 book. Even more important was the development for use in 1909 of filters for separately isolating blue and red light (Slipher, 1962). The blue images "surprisingly" showed no detail whatsoever.

The Violet Layer, Blue Clouds, and Blue Clearing

The Lowell Observatory's featureless, blue photographic plates of 1909 mark the discovery of the violet layer. The effect could have been caused by a lack of surface contrast or by a layer in the atmosphere absorbing or scattering violet-blue light. At times, however, for periods usually lasting a few days, the atmosphere of Mars becomes quite clear in the blue region of the spectrum over part or most of the visible hemisphere. This is the so-called phenomenon

*See pages 12 and 13 for list of cross references.

of blue clearing discovered by Slipher (1937). A clearing, of course, implies the existence of a real layer in the atmosphere which can at least partially dissipate and reform in a period of the order of a day and which preferentially absorbs or scatters in the violet and blue regions of the spectrum.[2] This layer is usually called the violet layer or the blue haze. The existence of the layer is not universally accepted, and problems associated with it are discussed in the following paragraphs.

Basing his interpretations upon photographs taken through various Wratten filters, Slipher (1962) states that the violet layer begins to obscure the surface noticeably at about 4550 Å. Wilson's (1958) results suggest that there may actually be maxima in the obscuration about every 200 Å starting at somewhat longer wavelengths. These maxima would tend to be unnoticed until the surface contrast becomes small enough to be dominated by the slight atmospheric changes. Slipher (1962) found good transparency at 4250 Å during blue clearings. A complete dissipation of the violet layer, observed under perfect seeing conditions, might result in some contrast to about 3000 Å, the region where molecular scattering begins to dominate.[3] There are no published quantitative measurements. Considerable change in apparent atmospheric transparency has been seen in a few hours, with much of a hemisphere clearing in a day (Slipher, 1962). A clearing may last one or several days.

Attempts have been made to correlate blue clearings with areographic longitude, Martian season, and time from opposition. These results are given in Slipher (1962) but are not reproduced here because of considerable correlation of each with observational selection (ease of making the measurement). Some data on blue clearings are tabulated in Fig. 1.

Recently Pollack and Sagan (1967) have suggested that the rare blue clearings are due entirely to excellent seeing at times when the Martian atmosphere is cloud free and when there is an area of intrinsic high contrast near the Martian central meridian. It is certainly true that a blue clearing cannot be detected unless there is a surface region of some contrast beneath. It is equally true that good seeing is required, since bad seeing can destroy visibility of all surface detail even in the red or infrared. Nevertheless, there are periods of excellent seeing, when tremendous surface detail is easily visible in the yellow and red, and when no hint of a surface feature can be seen in blue-violet light (Capen, 1968). Furthermore, normal blue images taken in good seeing often have an irregularity, showing structure that is not correlated with surface features (Humason, 1961). Often bright areas on blue photographs correlate with white clouds seen visually. In other cases they are visible only as a thickening or brightening in the blue and violet and are sometimes called blue or violet clouds. Dollfus (1961a) prefers to reserve the term blue clouds for clouds visible only in photographs using "deep blue filters" and near the morning and evening limbs. Such blue clouds differ radically in polarization properties from white clouds or from the violet layer and typically seem to be produced by 3-μ droplets (Dollfus, 1961a). Sometimes the violet layer shows a banded structure (Slipher, 1962; Humason, 1961). In summary, blue images of Mars are far from being uniform and featureless at all times or from showing structure correlated only with surface features as would be anticipated for a pure, molecular atmosphere.

The observer of Mars "sees" the result of the combination of several phenomena occurring simultaneously. The reflectivity of the Martian surface decreases sharply from 6000 Å to 3500 Å (due probably to the presence of ferric oxides[4]), and contrast between light and dark areas is greatly reduced.[5] Somewhere near 3000 Å the light scattered by atmospheric gas molecules becomes equal to that reflected from the surface, but molecular scattering decreases toward longer wavelengths according to the λ^{-4} Rayleigh law dependence (Evans, 1965). Added to these is the light scattered by the violet layer. Even under conditions of perfect terrestrial seeing, or from a space probe, all surface detail except the polar caps and possible frost patches (which have a high constant reflectivity throughout the visible part of the spectrum) should disappear somewhere between 3000 Å and 4000 Å without any added atmospheric scattering.

Explanation of a phenomenon whose existence is not universally accepted is often controversial. Dollfus and Focas (1966) find a photometrically determined surface pressure for Mars of 30 mb. The pressure is known to be about one-third of that amount. The difference, if not instrumental, must be caused by particulate scattering.[6] The particles must have been smaller than the 4700-Å wavelength used by Focas and Dollfus for their polarimetric studies, for the particles were not so detected. Gehrels and Teska (1962) found strong polarization at times at 3200 Å and 3600 Å, varying from 1.5 to 9.8% in 7 days at 3200 Å and a constant phase, and from 0.1 to 7.6% at 3600 Å as the phase changed from 43°.3 to 36°.1. Neither of these is possible for Rayleigh scattering. Kuiper (1964) has compared these results with theoretical scattering calculations for mixtures of sizes of sub-micron ice particles with indefinite results. He notes that "pumping liquid nitrogen into an open vessel placed in very dry air" results in a blue cloud of sub-micron ice crystals (frozen by the evaporating nitrogen) having the sort of extinction properties required of the violet layer. When the air is not so dry, a white cloud results.

The most likely composition of the particles is frozen CO_2 or H_2O, both known to be present in the Martian atmosphere.[7] Wilson (1958) compared a series of low dispersion (100 Å/mm) blue spectra taken during blue clearings to an identical set taken under normal conditions. He found periodic maxima and minima in the ratio of light reflected from Mars that were exactly supplementary to light transmitted through terrestrial noctilucent clouds. Noctilucent clouds are thought to be composed of sub-micron-size, ice-coated bits of meteoritic dust (Webb, 1965).[8] It is also interesting to note that the intensity of light scattered from particles comparable in size to its wavelength characteristically goes through a number of maxima and minima.

The altitude of the violet layer is unknown. Wright's (1925) discovery that the disk of Mars appears significantly larger in the violet than in the red has been well verified (de Vaucouleurs, 1954). This effect is probably caused in significant part by the violet layer, but there is no way accurately to separate the contributions from competing effects or to know how thick the violet layer itself may be. The very fact that Mars is measurably larger in the violet suggests the layer must extend at least some tens of kilometers above the surface.

In summary, the best evidence suggests the reality of a tenuous violet layer in the Martian atmosphere which can partially dissipate or reform in a day or so. To fit various observations the volatile layer must be composed of

sub-micron-size particles. Such particles would take several years to settle out of the Martian atmosphere, so they probably must evaporate or sublime to cause a blue clearing unless some new dynamical process for particle removal can be evoked.

White Clouds [9]

Originally white clouds were defined as those which seemed white or bluish when seen visually. With the advent of filter photography it became apparent that white and blue clouds were easily photographed at short, visible wavelengths but disappeared in the red and infrared, a simple operational distinction. Differentiation between white and blue clouds is not so simple, nor is agreement general that a distinction exists; both can be photographed in the blue. Dollfus' distinction, given on page 3, was based upon location and polarimetry. Polarimetry of dense white clouds suggests they are a fog of ice particles similar to terrestrial cirrus clouds (Dollfus, 1961a). If so, the distinctions between white clouds and the material of the violet layer may be chiefly location and particle density, although white cloud particles could also differ somewhat in size distribution or even in composition.

Some white clouds are quite large, as much as 2000 km across, and remain visible for days or weeks; they may form or dissolve at their edges, may move at relatively high speeds, and have a tendency to appear above certain regions of the planet (Dollfus, 1961b).[10] They may show as bright prominences at the limb of Mars. Under excellent seeing conditions large clouds may exhibit considerable fine structure. Large clouds also may be surrounded by an even larger area of thin haze detectable only with a polarimeter.

Other white clouds are small, bright, and generally remain fixed in an isolated location (Dollfus, 1961b). These may be surrounded by a large, fainter cloud structure. The polar caps are usually said to be covered in Martian winter with a hood of clouds similar in character to these small bright clouds.

Clouds or hazes are often seen near the morning terminator of Mars; these usually disappear in a few hours. Sometimes such are also seen to form near the evening terminator. Both morning and evening hazes are seen most frequently in the Martian spring (Dollfus, 1961b).

The famous "W" cloud of Mars seems to be a peculiar white cloud. It was first observed and photographed by Slipher in 1907 and has been seen during several additional apparitions of Mars since then (Slipher, 1962). It was particularly prominent and received wide public notice in 1954. The W-shaped cloud always appears in the same place, the Tharsis region near Lacus Phoenicis, and "the main stems of the cloud pattern appear to coincide with the main canals in the area" (Slipher, 1962).[11] It must be noted that the cloud appears as a W in astronomical orientation. With north "at the top" it is an M cloud.

Yellow Clouds [12]

Yellow clouds usually appear yellow or orange when seen visually. They are easily photographed in yellow or red light but cannot be seen on blue photographs. Their disappearance in the blue may be caused by lack of contrast

and by their being lower in the atmosphere than the violet layer, essentially the same reasons for the disappearance of surface detail in blue photographs. Even in red light, yellow clouds may be difficult to see because of lack of contrast when above a Martian bright area.

It is almost universally accepted at the present time that yellow clouds are dust clouds. The arguments for such identification are to some extent of the "bootstrap" sort. Polarimetric and thermal studies of the surface indicate the probable existence there of finely divided material. The color of the clouds is somewhat different than that of the surface but not more different than might be expected of surface material dispersed in a cloud. Polarimetric studies do not disagree with the dust hypothesis (Dollfus, 1961a). No reasonable alternative suggestions have been offered. Therefore, they "must" (probably) be dust clouds.

Yellow clouds have a large range of sizes and shades of color. The most obvious are the great yellow "storms." which may grow in size until they nearly cover the planet. The great dust storm of 1956 began with local activity on August 20 (Earth date) and greatly intensified on August 28 with a "brilliant, orange colored cloud" over Noachis, according to Slipher (1962). Kuiper (1957) first saw a group of "five or six bright yellow clouds" over Mare Sirenum on August 29. The differences in descriptions of the development are probably due at least in part to the fact that Slipher was observing in Bloemfontein, South Africa, and Kuiper in west Texas; so they were seeing somewhat different parts of the planet. Both agree that by September 2 almost the entire planet was covered by a yellow veil which partially obscured most surface detail. Actually a part of the surface was still unobscured as seen from Australia on September 3 (de Vaucouleurs, 1957). There were local areas of greater opacity which completely obscured the surface. This activity reached a maximum on September 7, according to Slipher (1962), and continued to some extent until at least September 22. A third description of the 1956 storm, the greatest ever observed on Mars, is given by Dollfus (1961b). Information on other major dust storms is given in Fig. 2.

Small yellow clouds have been observed at most favorable apparitions of Mars, but they are not common. (A fairly complete plot of those recorded in the literature is shown elsewhere in this document.[10]) Some yellow clouds move and have been followed for as long as 16 days, although most disappear in a few days (Gifford, 1964). Average speeds as high as 90 km hr^{-1} have been noted (Gifford, 1964). Yellow clouds which are often detected projected beyond the limb or terminator of Mars also can display motion, and speeds as high as 135 km hr^{-1} have been recorded (Gifford, 1964).

It is generally assumed that the dust particles are raised by high winds, although meteoritic impacts[8] or volcanic activity[13] have been suggested as possible occasional (or not so occasional) contributors. It is important to recognize that high wind velocities are required to initiate movement of particles of any size, large particles (~1/2 mm) being easier for wind to move than small ones (Ryan, 1964). Even particles of optimum size require surface winds (1 m above the surface) of at least 50 m sec^{-1} to move them, assuming a 10-mb atmosphere (Galbraith, 1966). Neubauer (1966) has shown that large dust-devils (more than 100 m in diameter) may be a most efficient mechanism

for moving dust aloft. High, large-scale wind velocities are also possible, as shown by observed cloud velocities as high as 135 km hr^{-1} (Gifford, 1964). Once large particles begin to move, they collide with small particles, knocking them into the air. Dust-devils have a good upward component of velocity (Neubauer, 1966). Larger-scale winds may also have a vertical component, perhaps as great as 6 m sec^{-1} (Gierasch and Goody, 1968). There is no reason to think that dust cannot be raised from the surface, at least to the tropopause, to form yellow clouds.

The altitudes of yellow clouds have often been estimated, but the results vary wildly. They are "mostly low level objects, lying generally between 3 and 5 miles above the surface," according to de Vaucouleurs (1954). Slipher (1962) states that "most of the examples best observed and most susceptible of accurate measurement have been found at heights of 18 to 20 miles." Altitude "measurements" have generally been made on terminator clouds (clouds that remain illuminated on the dark side of the terminator because of their height above the ground) by assuming the apparent horizontal distance between cloud and terminator is a direct function of altitude. Statistical errors are quite large for the small angles involved ($\lesssim 0''.1$), and there are numerous possibilities for systematic error in such measurements.

Small yellow clouds usually last for no more than two to four days. The particles involved must be at least 1-2 μ in diameter (larger than the wavelengths of yellow and red light in which they are easily photographed). They very probably never rise higher than the tropopause. In fact particles must be at least 20 μ in diameter and rise no more than $\sim$5 km if they are to settle out of the atmosphere in four days. Therefore, yellow clouds must include many particles 20-50 μ in diameter. The yellow veils lasting a month or more can easily be accounted for by including the smaller particles.

In summary, it is certainly possible, based upon all direct and indirect observational evidence, that the yellow clouds are dust clouds. It is in fact probable that the yellow clouds are dust clouds, but there unfortunately is no direct proof that such is the case, although one would be hard pressed to offer any reasonable alternative hypothesis.

Green Haze, Gray Clouds, and Bright Spots

From time to time descriptions of "new" Martian meteorological phenomena appear in the literature. Current knowledge of Mars is sufficiently limited that something completely new is quite possible. Most such new discoveries, however, are likely to be different aspects of something already well known.

Capen (1966) has reported that there was considerable Martian atmospheric opacity in the yellow-green region of the spectrum during February and March of 1965. Filters such as the Wratten 57 or Schott GG-14, which reject most light with wavelength less than 5000 Å, usually provide a clear view or photograph of surface features. During the period mentioned, this was often not the case. Five dense, blue-white clouds were photographed in both blue and yellow-green during much of this period. It seems likely in this case that the more tenuous haze which often surrounds white clouds simply overlapped with haze from other clouds. Perhaps the haze was more dense than usual. Mars was undoubtedly

having "unusually cloudy weather," but there is no reason to look for any new physical phenomenon to explain these unusual observations.

Ley (1963) has summarized reports of strange dark-gray clouds by several of the best known Japanese observers of Mars. Four of these clouds were seen during 1950 and 1952 in an area about 500 mi across extending from Mare Sirenum across Electris to Eridania. White clouds often appear somewhat gray, but the experienced Japanese observers felt these were unique both in color and in the great height to which they appeared to rise. They have chosen to attribute the gray clouds to volcanic activity. Such a hypothesis is possible, of course, but can hardly be supported from the observations alone.

Over the years there have been a number of reports of bright spots or flares on Mars, typically lasting five or 10 minutes. Some of these reports have been from reputable, experienced observers. At least two Martian sites have reportedly exhibited repeated flares, again resulting in hypotheses of volcanic activity.[13] A brief list of flare observations and characteristics is given in Fig. 3.

Dates of clearing	Opposition date	Source
May 26-Jun 1, 1890	May 27, 1890	de Vaucouleurs, 1954
Nov 2-3, 1926	Nov 4, 1926	de Vaucouleurs, 1954
May 20-21, 1937	May 19, 1937	de Vaucouleurs, 1954
Jul 18-25, 1939	Jul 23, 1939	de Vaucouleurs, 1954
Oct 10, 1941	Oct 10, 1941	de Vaucouleurs, 1954
Nov 22, 1941	Oct 10, 1941	Slipher, 1962
Jun 13-14, 1954	Jun 24, 1954	Slipher, 1962
Jun 27-Jul 2, 1954	Jun 24, 1954	Pettit and Richardson, 1955
Aug 7 and 11, 1956	Sep 11, 1956	Slipher, 1962
Aug 23-Sep 3, 1956[a]	Sep 11, 1956	de Vaucouleurs, 1957; Slipher, 1962
Oct 26, 1956	Sep 11, 1956	Slipher, 1962
Sep 3, 1958[b]	Nov 17, 1958	Richardson and Roques, 1959
Oct 13-15, 1958	Nov 17, 1958	Slipher, 1962
Nov 6-10, 1958	Nov 17, 1958	Slipher, 1962
Nov 31, 1960; Jan 17 and 27, 1961[c]	Dec 30, 1960	Smith, 1961
Sep 26-28, 1964; Oct 3-4, 1964; Dec 30, 1964-Jan 1, 1965; Mar 8-9, 1965[d]	Mar 9, 1965	Capen, 1966

[a]This clearing occurred during the beginning of the great dust storm. Not all of the planet was covered during this period, and those dark areas visible in yellow light were almost equally visible in blue light.

[b]Note that this clearing occurred 74 days before opposition, clearly indicating the apparent association with opposition to be an effect of observational selection.

[c]A number of other dates showed lesser clearing than these three.

[d]A number of other dates showed lesser clearing than these four groups.

Fig. 1. Table of observations of Martian blue clearings.

Date	Description	Source
September-December, 1877	Schiaparelli observed vast clouds totally obscuring the "equatorial continent" between Syrtis Major and Ganges. On around the equatorial zone north of Mare Sirenum and Mare Cimmerium everything was veiled but not totally obscured.	Maginni, 1939, p.323-325
July, 1909	A large part of the visible disk was covered by a yellow veil (grayish in some areas). Fine detail in polar cap areas showed seeing was excellent in spite of lack of detail in the center of the disk.	Maginni, 1939, p.318-320
Oct 11-20, 1911	A large, yellowish-white cloud covering some 350,000 km^2 was seen over Libya on Oct 11 moving southeast at about 30 km hr^{-1}. It slowed to a stop and dissipated over Eridania on Oct 20.	de Vaucouleurs, 1954, p.339-341
Nov 3-Dec 23, 1911	An orange yellow veil covered the entire region south of Syrtis Major and Sinus Sabaeus as far west as Thaumasia, and persisted for weeks.	Maginni, 1939, p.321-322
Apr 12-May 15, 1920	"Yellow photographs recorded vast bright areas across the Martian disk, especially over the Syrtis Major area 260° to 32° longitude near the equator."	Capen, I.O.M. to J. A. Stallkamp, March 19, 1966
Jul 9-12, 1922	The storm appeared on Jul 9 south of Margaritifer Sinus and soon covered "about 400,000 square miles." It drifted northwest at 6-12 mi hr^{-1} and gradually thinned, showing only as a faint veil on Jul 12.	Slipher, 1962, p.106-107
Nov 28, 1928	According to Maginni, "More than a veil, this was a wide luminous ring, a vast golden yellow circular zone enwrapping the planet's disk." He says nothing about its duration.	Maginni, 1939, p.322-323
Nov 12-28, 1941	A large cloud grew over Libya on Nov 12 and began moving south. On Nov 15 Slipher saw it as a vast system of several clouds more than 1000 km across. It was last seen over Phaethontis on Nov 28. de Vaucouleurs describes it as yellowish or pinkish except on Nov 13, when it appeared bluish-white.	de Vaucouleurs, 1954, p.339-341; Slipher, 1962, p.108-109
January, 1944	A yellow veil was seen in the south polar region. The planet was little observed during this wartime aphelic opposition and little information is available.	Dollfus, 1961b, p.564
Aug 20-Sep 22, 1956	Details are given in the main body of the text.	Slipher, 1962; Kuiper, 1957; de Vaucouleurs, 1957

Fig. 2. Table of major Martian "dust storms."

Date	Observer	Instrument and Observatory	Location of flare or spot	Characteristics and duration
Jun 4, 1937	Sitzuo Mayeda	8-in. reflector	Close to Sithonius Lacus; +55° lat., 240° long.	Considerably brighter than the polar cap and the white clouds. Flickered like a star, and after 5 min it was hidden from view (possibly due to rotation of the planet). (See Saheki, 1955.)
Dec 8, 1951	Tsuneo Saheki	8-in. reflector, planetarium at Osaka, Japan	Western portion of equatorial Tithonius Lacus	Brighter than the north polar cap. Flickering light and stellar brightness of the 6th magnitude for 5 min. It then began to be extinguished and changed into a grayish cloud having a diameter of more than 300 km. The entire phenomenon lasted about 40 min. (See Saheki, 1955.)
Jul 1, 1954	Tsuneo Saheki	8-in. reflector, planetarium at Osaka, Japan	Edom Promontorium (at the equator)	In 10 sec the color changed from a whitish-yellow to a bright, pure white, and then changed to yellowish-white. Duration of the flare was 5 sec. (See Saheki, 1955.)
Jul 24, 1954	Clark McClelland	13-in. refractor, Allegheny Obs. of Pittsburgh University, Penn.	Edom Promontorium	Flare was visible for about 58 sec. In the opinion of the observer, it was caused by a volcanic eruption.
Nov 5, 1958	Sadao Murayama	20-cm refractor, National Science Museum in Tokyo, Japan	South of Tanais Plateau, southwestern edge of Aphrodite Mare (Acidalia); +35° lat., 42° long.	Small but very bright spot, white in color. Lasted about 5 min. From Jul 23 to Aug 3, 1954, a similar white spot was observed at the same location by Tsuneo Saheki in the form of a very bright, small cloud.
Nov 6, 1958	Sigeji Tanabe	8-cm reflector, Sitsuoke, Japan	Southern edge of Tithonius Lacus	Brightness same as for the polar cap for 4 min.
Nov 10, 1958	Sanenobu Fukui	25-cm reflector, Kobe, Japan	Northeastern part of Solis Lacus	Brightness same as for the polar cap for 5 min. Diameter of spot (according to a figure) about 250 km.
Nov 21, 1958	Tsuneo Saheki	—	Northern edge of Hellas and Edom Promontorium	Two bright spots. Visibility below 5 according to the standard scale.
Nov 21, 1958	Itsiro Tasaka	32.5-cm reflector, Vakayama, Japan	Northern edge of Hellas and Edom Promontorium	The same spots as above, but visibility 6÷7. Yellowish-white cloud over northern part of Hellas. Both flares lasted about 5 min, together with phases of increase and decrease in brightness—15 min. After several minutes, the flares reappeared.

Fig. 3. Table of bright flares and spots observed on Mars. (from Katterfel'd, 1966)

CROSS REFERENCES

The specific section number, subject, and page number to which the reader is referred is given below.

Cross Reference	Section and Subject
[1] Clouds and hazes—discussion	5.3.....Assumptions made in deriving Lower Atmosphere Models I, II, and III (discussion), p.8. 5.4.....Assumptions made in deriving Upper Atmosphere F_1-Model (discussion), p.10, 11, and F_2-Model (discussion), p.12.
[2] Absorption by the violet layer (the blue haze)	6.....Absorption in the Martian atmosphere (discussion), p.6.
[3] Molecular (Rayleigh) scattering	5.4.....Physics of the upper atmosphere (discussion), p.2.
[4] Ferric oxides	3.4.....Iron oxides and silicates on the surface (discussion), p.3.
[5] Surface reflectivity	3.2.....Spectral reflectivity and distribution (data summary), p.2; Albedo, magnitude, and color (discussion), p.4.
[6] Surface pressure and particulate (non-Rayleigh) scattering	5.2.....Surface pressure (data summary), p.1; Limited usefulness of photometry and polarimetry in determining surface pressure (discussion), p.9, 10.
[7] CO_2 and H_2O	5.1.....Observed atmospheric constituents (data summary), p.1. 3.4.....Water and carbon dioxide on the surface (discussion), p.3, 4; Phase diagram for carbon dioxide and water (figure), p.9.
[8] Meteoritic dust	3.4.....Meteoritic material—meteoroid fluxes for Mars (discussion), p.4.
[9] White clouds	3.5.....Relative elevation of dark and light areas—cloud formation movement (discussion), p.3, and white patterns (discussion), p.4.
[10] White and yellow cloud seasonal activity	4.2.....Seasonal behavior of clouds (discussion), p.4; Seasonal changes in specific areas (figures), p.11-17; Seasonal activity maps (figures), p.19-25.

Cross Reference	Section and Subject
[11] Canals	3.5.....Linear features (discussion), p.4,5. 4.2.....Secular changes of the Nilosyrtis, Thoth, and Nepenthes canals (discussion), p.2.
[12] Yellow clouds	3.1.....Surface temperatures in dust storm locales (data summary), p.2, (figures), p.4,6,7. 3.2.....Polarization studies revealing yellow veils in 1956 and 1958 (figure), p.10. 3.4.....Surface constituents and particle sizes (conclusions), p.6,7. 3.5.....Cloud formation movement (discussion), p.3,4; Wind action (discussion), p.12; Wind velocity/particle movement/particle settling data (figures), p.28. 5.2.....Surface pressure (data summary), p.1. 5.3.....Neubauer's convective atmospheric model—dust-devil formation (discussion), p.5,6.
[13] Volcanic activity	3.5.....Cratering processes (discussion), p.6,7; Volcanic activity (discussion), p.9,10.

BIBLIOGRAPHY

Baum, W.A., et al., 1967, Mars cloud survey report no. 1: Flagstaff, Ariz., Lowell Observatory, Planetary Research Center.

Capen, C.F., 1966, The Mars 1964-1965 apparition: Pasadena, Calif., Jet Propulsion Laboratory, Tech. Rep. 32-990.

_____, 1968, (Pasadena, Calif., Jet Propulsion Laboratory): private communication.

de Vaucouleurs, G., 1954, Physics of the planet Mars: London, Faber and Faber.

_____, 1957, Photographic observations in 1956 of the blue clearing on Mars: Pub. Astron. Soc. Pacific, v. 69, p. 530-532.

Dollfus, A., 1961a, Polarization studies of the planets, Chapter 9 in Planets and satellites, Vol. III of The solar system; Kuiper, G.P., and Middlehurst, B.M., Editors: Chicago, U. of Chicago Press.

_____, 1961b, Visual and photographic studies of the planets at the Pic du Midi, Chapter 15 in Planets and satellites, Vol. III of The solar system; Kuiper, G.P., and Middlehurst, B.M., Editors: Chicago, U. of Chicago Press.

Dollfus, A., and Focas, J.H., 1966, Polarimetric study of the planet Mars: Bedford, Mass., Air Force Cambridge Research Laboratories, Contract AF-61(052)-508, final report.

Evans, D.C., 1965, Ultraviolet reflectivity of Mars: Science, v. 149, p. 969-972.

Galbraith, T.L., 1966, Particle transport in the Martian atmosphere: General Electric, Space Physics, Tech. Memo. 8126-4.

Gehrels, T., and Teska, T.M., 1962, The wavelength dependence of polarization: Comm. Lunar Planet. Lab., v. 1, n. 22, p. 167-177.

Gierasch, P., and Goody, R.M., 1968, A study of the thermal and dynamical structure of the Martian lower atmosphere: Planet. Space Sci., v. 16, n. 5, p. 615-646.

Gifford, F., 1964, A study of Martian yellow clouds that display movement: Mon. Weather Rev., v. 92, p. 435-440.

Humason, M.L., 1961, Photographs of the planets with the 200-inch telescope, Chapter 16 in Planets and satellites, Vol. III of The solar system; Kuiper, G.P., and Middlehurst, B.M., Editors: Chicago, U. of Chicago Press.

Katterfel'd, G.N., 1966, Volcanic activity on Mars: Wash., D.C., National Aeronautics and Space Administration, Tech. Transl. F-410. Translation of, 1965, Vulkanicheskaya aktivnost' na Marse: Priroda, n. 8, p. 103-109.

Kuiper, G.P., 1957, Visual observations of Mars, 1956: Astrophys.J., v.125, p.307-317.

_____, 1964, Infrared spectra of stars and planets, IV. The spectrum of Mars, 1-2.5 microns, and the structure of its atmosphere: Comm. Lunar Planet.Lab., v.2, n.31, p.79-112.

Ley, W., 1963, Watchers of the skies: New York, Viking Press.

Lowell, P., 1905, The canals of Mars—photographed: Lowell Obs.Bull., v.1, n.21, p.134-135.

_____, 1907, On a new means of sharpening celestial photographic images; and applied with success to Mars: Lowell Obs.Bull., v.1, n.31, p.182-185.

Maginni, M., 1939, Il planeta Marte: Milan, Italy, Ulrico Hoepli, Editore-Librario della Real Casa, 400 p.

Mees, C.E.K., 1954, The theory of the photographic process, Rev.Edition: New York, Macmillian Co.

Neubauer, F.M., 1966, Thermal convection in the Martian atmosphere: J.Geophys.Res., v.71, p.2419-2426.

Pettit, E., and Richardson, R.S., 1955, Observations of Mars made at Mt. Wilson in 1954: Pub.Astron.Soc.Pacific, v.67, p.62-73.

Pollack, J.B., and Sagan, C., 1967, An analysis of Martian photometry and polarimetry: Wash., D.C., Smithsonian Inst.Astrophys.Obs., Spec. Rep.258.

Richardson, R.S., and Roques, P.E., 1959, An example of the blue clearing observed 74 days before opposition: Pub.Astron.Soc.Pacific, v.71, p.321-323.

Ryan, J.A., 1964, Notes on the Martian yellow clouds: J.Geophys.Res., v.69, p.3759-3770.

Saheki, T., 1955, Martian phenomena suggesting volcanic activity: Sky and Telescope, v.XIV, n.4, p.144-146.

Slipher, E.C., 1937, An outstanding atmospheric phenomenon on Mars: Pub. Astron.Soc.Pacific, v.49, p.137-140.

_____, 1962, Mars, the photographic story: Cambridge, Mass., Sky Publishing Corp., and Flagstaff, Ariz., Northland Press.

Smith, B.A., 1961, Blue clearing during the 1960-61 Mars apparition: Pub. Astron.Soc.Pacific, v.73, p.456-459.

Webb, W.L., 1965, Morphology of noctilucent clouds: J.Geophys.Res., v.70, p.4463-4475.

Wilson, A. G., 1958, Spectrographic observations of the blue haze in the atmosphere of Mars: Santa Monica, Calif., RAND Corp., Rep. P-1509.

Wright, W. H., 1925, Photographs of Mars made with light of different colors: Lick Obs. Bull., XII, n. 366, p. 48-61.

4.2 SEASONAL ACTIVITY

DATA SUMMARY

The Polar Caps and Hoods (Figs. 1 and 2)

The Martian polar caps appear to be deposits of some solid substance, most probably CO_2 (and small amounts of H_2O), condensing during the fall and winter in each hemisphere and then subliming during the spring and summer. The polar hoods are white clouds which hide the polar regions when photographed in blue or violet light during the fall and winter. Typical time behavior of these features is shown below. Lines indicate typical periods when these features are visible. Lengths of seasons are given in Earth days.

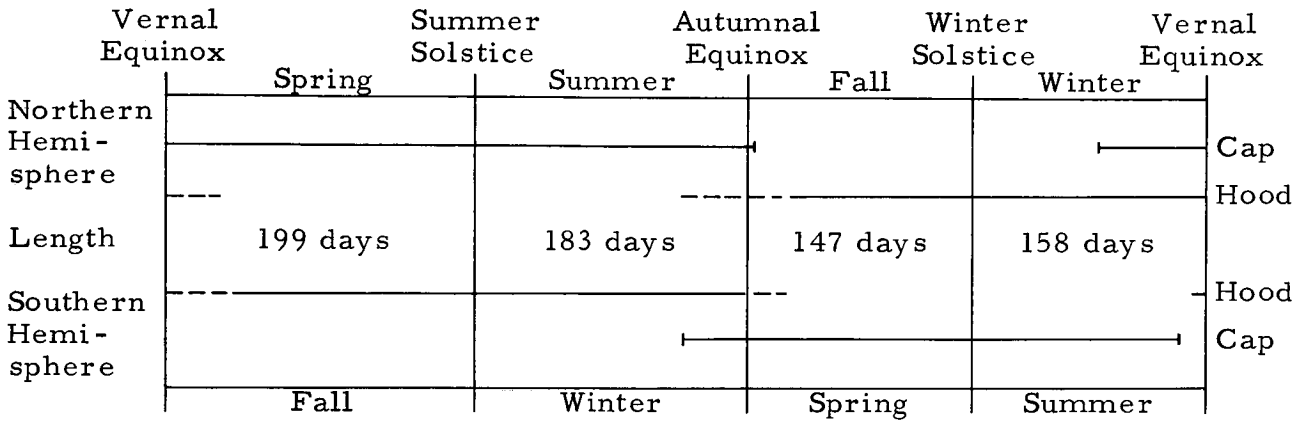

The Dark Fringe of the Polar Caps

During the time either polar cap is retreating, a dark fringe develops adjacent to it. The cause of the fringe is unknown. It seems to be real, not just a subjective effect of contrast, and may be related to the wave of darkening (q.v.).

Seasonal Behavior of Clouds

See Figs. 8 through 10.

The Wave of Darkening (Fig. 3)

The wave of darkening is "a progressive albedo decline of the Martian dark areas starting in local springtime from the edge of the vaporizing polar ice cap and moving towards and across the equator" (Sagan and Houghey, 1966).

Seasonal Behavior of Surface Features

Besides intensity (albedo) changes, dark areas show change in color, shape, size, and internal appearance, while light areas also change in color and structure. These changes are best shown in detailed descriptions of the changes occurring in individual areas (Figs. 4 through 7) and in a series of color maps (Figs. 8 through 10).

DISCUSSION

The first known drawings of Mars showing features which can definitely be identified are Christiaan Huygens' maps of November 28, 1659, definitely showing Syrtis Major, and of August 13, 1672, showing the south polar cap (Ley, 1963). J. D. Cassini saw both caps in 1666. The first astronomer to realize that both the polar "white spots" and the equatorial dark areas changed in appearance from opposition to opposition was Giacomo Filippo Maraldi, who observed every opposition of Mars from 1672 until at least 1719 (Ley, 1963). For more than 250 years, then, it has been realized that Mars is a changing world, and famous planetary astronomers such as W. Herschel, Schroeter, Beer and Von Mädler, Secchi, Lockyer, Kaiser, Dawes, and Proctor studied this planet, which appeared more Earthlike than any other. The modern period of good maps and really useful records of surface changes began with Schiaparelli's work during the excellent opposition of 1877.

Mars undergoes many sorts of change. There are the apparent changes as seen from Earth caused by the rotations of Mars and Earth and by the tremendous variation in the distance separating the two planets.[1*] Because the axes of Earth and Mars point in different directions, the sub-Earth point on Mars changes through almost 50° of areographic latitude, causing a great change in perspective. During this time there are also more subtle changes in appearance caused by changes in the photometric coordinates.[2] There are changes caused by the appearance and disappearance of various meteorological phenomena such as are discussed in Sec. 4.1. Some of these phenomena are not completely random but appear to be somewhat a function of season. Changes in polar caps and in the appearance and photometric properties of Martian dark areas are obvious seasonal changes and the primary subject of this section.

Mars also exhibits long term changes, usually called secular changes even though they are often reversed in a few decades. It is important but sometimes difficult to separate secular changes from the apparent changes caused by changes in perspective, particularly when only drawings or qualitative descriptions of past conditions are available. Nevertheless, such changes are very real. For example, the Lowell photographs of 1907 show a very strong, obvious Nilosyrtis canal, whereas Nepenthes is weaker and Thoth requires a bit of imagination to see (Slipher, 1962). Schiaparelli's map of 1879 shows the Nilosyrtis canal almost as an elongation of Syrtis Major itself, while Thoth and Nepenthes are very weak (Schiaparelli, 1929). Today the situation is completely reversed, with Thoth and Nepenthes the strongest, most easily photographed canals on Mars, while photographing Nilosyrtis is a rare coup. In fact Thoth and Nepenthes are now so broad the term canal is rather inappropriate.[3] The most valuable contribution of the old literature is in such studies of secular change.

Polar Caps

The first recognition (in 1784) that the variation in the "white polar spots" of Mars is seasonal and the suggestion that the spots are true polar caps of snow and ice were due to the famous William Herschel (Ley, 1963; Slipher, 1962). Measurements of the waxing and waning of the caps, begun by Herschel,

*See page 27 for list of cross references.

have shown little change over a period approaching 200 years. Figure 1, compiled by Slipher (1962), shows the regression of the south cap as observed through many seasons. Each year the regression reaches an irregular structure called the Mountains of Mitchel at a latitude of about -73° on the same seasonal date (Slipher, 1962). The south cap does not retreat with a perfectly circular edge, however. During the regression numerous irregularities in the edge, detached pieces, and channels into the cap appear, possibly caused by topographic irregularities (Maginni, 1939).[4] Basing his interpretations upon studies of the heat load and regression rate, de Vaucouleurs (1954) has suggested that only a central plateau covering about 15 areocentric degrees is a true cap and that the rest is a much thinner ring which may not completely or uniformly cover the ground.[5] de Vaucouleurs' actual numbers are out of date since they are based on assumed H_2O ice.[6] The last remnant of the south cap is located at about -83°.5 latitude and 30° longitude rather than at the pole.

There is considerable difference in the north and south polar caps of Mars caused by the asymmetry in Martian seasons. The south cap is formed during the long, 382 (terrestrial) days of southern fall and winter when Mars is near aphelion, and it covers more than 70 areocentric degrees at greatest extent (extending beyond latitude -55°). The north cap is formed during the short, warmer 305 (terrestrial) days of northern fall and winter when Mars is near perihelion, and it usually measures only about 53° at maximum extent (Slipher, 1962). According to Maginni (1939) the south cap disappears completely every summer about 136 days after the southern summer solstice, leaving behind a dark polar region. Slipher (1962) says it sometimes disappears but more often does not. There is also disagreement about the north cap, Maginni (1939) stating it disappears 188 days after northern summer solstice, Slipher (1962) saying it never shrinks to less than 6° in breadth. Capen's (1966) observations of the 1964-1965 apparition indicate a 6° minimum size. The remnant of the north cap is also slightly displaced from the pole, about 3° (Maginni, 1939). The northern polar region surface is a light area.

Capen's (1966) regression curve of the north cap is given as Fig. 2. It agrees very well with earlier curves derived by Antoniadi in 1899, 1901, and 1903, as quoted by Maginni (1939). The north cap also displays some irregularity as it shrinks. For example, in 1888 and in 1918 the north cap appeared to divide into two unequal pieces as it regressed (Maginni, 1939). Olympia, a bright region at +80° latitude and 210° longitude, remains white for some time after the cap pulls away from it. Olympia remains visible an average of 100 days.

Quantitative photometric and polarimetric data on both polar caps and hoods have been given by Focas (1962).

The Polar Hoods [7]

During the fall and winter in either hemisphere of Mars the polar areas appear covered by a very large hood of clouds, often somewhat dull bluish-white in color and with an irregular diffuse edge. The clouds usually appear large and bright in violet and blue photographs, although varying considerably in extent from day to day. Yellow and red pictures may show a much smaller bright region, the cap beneath the hood, or they may show almost nothing. In the spring and summer, however, polar cap pictures are brilliant and sharp in red

light, the caps remaining constant in size from night to night except for the very gradual regression, and they usually appear with only slightly reduced contrast in blue light. A beautiful series of photographs illustrating these points has been published by Slipher (1962).

The southern polar hood reached latitudes of -42°, -40°, and -44°—equivalent to breadths of 96°, 100°, and 92°—in 1909, 1922, and 1954, respectively (Slipher, 1962). On December 18, 1960, when Mars was 10 (terrestrial) days beyond its vernal equinox, both polar hoods came below 35° latitude in their hemispheres, each covering more than 110 areocentric degrees. On the equinox of July 17, 1922, the southern hood came down to -26° latitude. Very near the time spring begins, however, the polar hood breaks up, leaving beneath it the much smaller true polar cap.

The Dark, Peripheral Fringe-Band-Collar of the Polar Caps

A dark fringe surrounding the retreating polar caps is said to have been seen first by Beer and von Mädler as early as 1830 (Slipher, 1962). The fringe is not seen when a polar cap is at its maximum extent nor is one visible during the slow, final demise of a cap (de Vaucouleurs, 1954). During the time of retreat, however, a zone most often described as bluish develops contiguous to the cap, reaching its greatest width at the time of maximum rate of vaporization (de Vaucouleurs, 1954).

The dark fringe seems to be more than just an effect of contrast between the brilliant cap and its relatively dull surroundings. Quantitative studies by de Vaucouleurs and by Dollfus identified a contrast effect but confirmed the reality of the fringe (de Vaucouleurs, 1954). The behavior of the fringe may be identical to other areas of the planet that take part in the wave of darkening.

The dark fringe has sometimes been called the melt zone, implying it to be an area where liquid water exists for a brief time, wetting the ground before evaporating.[6] The best current values for surface pressure[8] and water vapor abundance make this interpretation seem unlikely.

Seasonal Behavior of Clouds (Figs. 8 through 10)

The general nature and properties of Martian clouds are discussed in Sec. 4.1. The polar hoods are seasonal white clouds. A few additional facts which seem to be correlated with seasons are presented here.

The really "great" Martian dust storms which covered a large part of the visible disk, notably those of 1877, 1909, 1922, and 1956, all occurred when Mars was near perihelion. It has been suggested that large-scale dust storms are more likely at the time of greatest heating when Mars is near perihelion (de Vaucouleurs, 1954).[9]

White area activity (including ground "frost" and low level atmospheric "fogs," which are impossible to separate by simple visual observation) reaches a peak when the polar caps are small (Capen, 1966), a time when atmospheric water vapor appears relatively abundant (Schorn et al., 1967).[6] Frost activity recurs frequently in certain areas, as shown in the second overlay on Fig. 9.[4]

The Wave of Darkening

The wave of darkening has been described as "a progressive albedo decline of the Martian dark areas (but not the bright areas) starting in local springtime from the edge of the vaporizing polar ice cap, and moving towards and across the equator" (Sagan and Houghey, 1966). There is firm quantitative evidence that dark areas darken during the Martian spring, reaching maximum darkness after the summer solstice.[10] Whether the darkening occurs as a "wave" from the pole has been argued. A statistical analysis by Pollack, Greenberg, and Sagan (1967) showed that while there are areas which "violate the concept of an invariable wave," there is "a very significant correlation of latitude with time of maximum darkening."

The waves start alternately from the two polar caps at half-year intervals, cross the equator, and fade at about 22° latitude in the opposite hemisphere from which they began (Focas, 1962). The rate of propagation is variable but averages about 35 km per terrestrial day. The time from beginning of darkening to maximum darkening is 0.30 to 0.35 Martian years in the circumpolar and temperate areas, 0.30 years at the boundary of the equatorial zone, and 0.15 years in the equatorial area (Focas, 1962). The total duration of darkening—minimum to maximum and fading back to minimum—is 0.67 Martian years in the circumpolar areas for the wave proceeding from the north cap and 0.55 years for the north wave at its southern limit. The wave proceeding from the south cap lasts 0.50 Martian years in the circumpolar area and 0.40 years at its northern limit (Focas, 1962).[11]

The average "intensity" of dark areas on Mars increases from pole to equator. The additional intensity resulting from the wave of darkening decreases from poles to equator. This is balanced by the fact that two waves affect the equatorial regions. The behavior of the wave of darkening is shown diagrammatically in Fig. 3 taken from Focas (1962). An average behavior is also shown as overlays on Figs. 9 and 10.

The cause of the wave of darkening is most commonly thought to be water vapor, released from the vaporizing polar cap, that somehow interacts with the surface material or with "vegetation" to cause the darkening.[6] Other explanations have generally involved seasonal transport of dust on and off of dark areas. Both classes of explanation of the wave of darkening are, at best, hypotheses, lacking detailed mechanism let alone quantitative prediction. Pollack, Greenberg, and Sagan's (1967) statistical analysis is unable to differentiate between the two types of hypotheses. The wave of darkening remains one of Mars' greatest enigmas.

Seasonal Behavior of Surface Features[12]

The wave of darkening is a "statistical thing" differing in its effect from area to area and in no sense an inviolable description of even the behavior of intensity of all dark areas. Besides such albedo changes there are color changes and even changes in shape, size, and internal appearance of the various dark areas. Bright areas also show seasonal changes in color and sometimes in structure. These changes in individual northern and equatorial areas have been summarized in a series of figures prepared by C. Capen for this document (Figs. 4 through 7).

Color is a very subjective thing. There are over 150 discriminable colors (hues) in the visible spectrum, times some 450 steps in brightness and 15 to 165 steps in saturation that can be detected by the human eye (Chapanis, 1965). Even with practice an individual can learn to discriminate only 12 or 13 hues on an absolute basis, as opposed to differentiation or interpolation using color chips or some other comparative method (Chapanis, 1965). In addition, when dealing with areas that are very small in angular extent next to brighter areas of a different color, peculiar physiological effects come into play which may completely change the apparent hue (Schmidt, 1959). The descriptions of color in Figs. 4 through 7 are those of an experienced Mars observer with excellent color vision, but they should be accepted with due reservation.

Winter colors of dark areas tend to be very subdued, often grayish or brownish hues. Lack of contrast sometimes causes features to disappear. Blue-greens, yellow-greens, and blacks appear common in late spring. The canals, which react to the wave of darkening like any dark area, become prominent in spring. Summer is a period of deepening color with changes to purples, browns, and grays, which fade as summer progresses. Fall is a drab period very like winter.

The color base-maps (Figs. 8 through 10) are based upon filter photography, color photography, and visual studies. Color saturation has been increased to aid reproduction. The maps represent a useful description of seasonal change on Mars, but again the colors should be accepted with due reservation.

An overlay giving names and locations of prominent Martian features is included as Fig. 11 and can be used with any of the color base-maps. A list of names and coordinates of the features appears with Fig. 11.

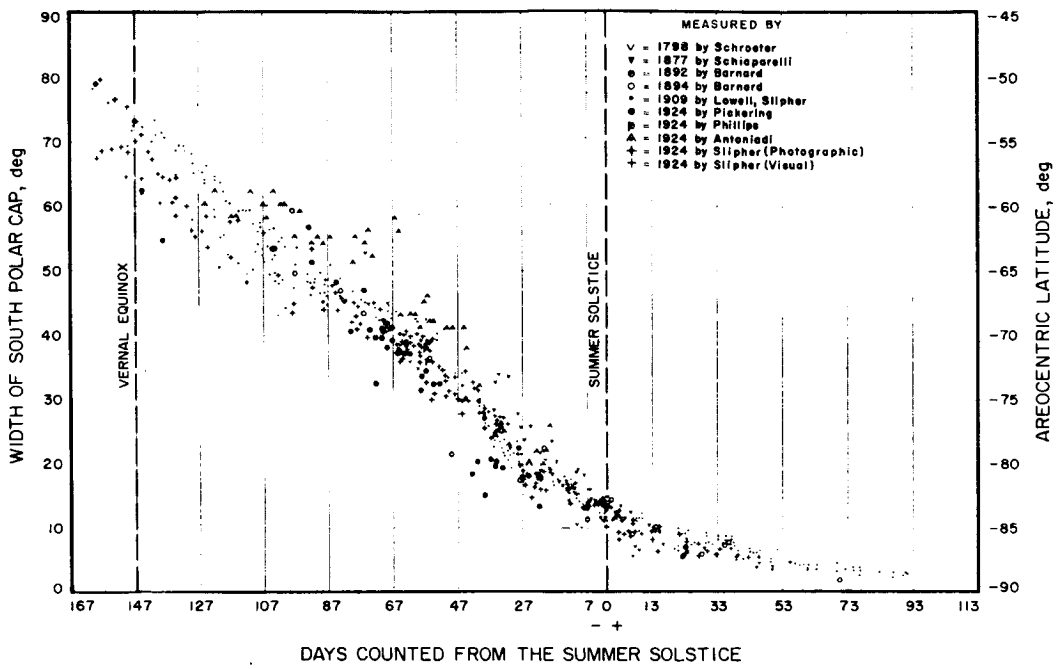

Fig. 1. Measured width of the south polar cap of Mars for various oppositions from 1798 to 1924. This figure embraces the Martian season from before the vernal equinox to 94 days after the summer solstice. Other measures derived from drawings in 1781, 1783, 1815, 1830, 1845, and 1862 were checked with those shown here, but no notable deviations were found other than accidental errors attributable to optical limits of the observer's telescope. The plotted measures shown in the figure agree very well indeed, and the deviations in the measures by the same observer are of about the same order as those that occur between different observers. This study revealed no evidence of any irregularity in the melting of the south cap at any of these oppositions during this long period of observation. (Slipher, 1962)

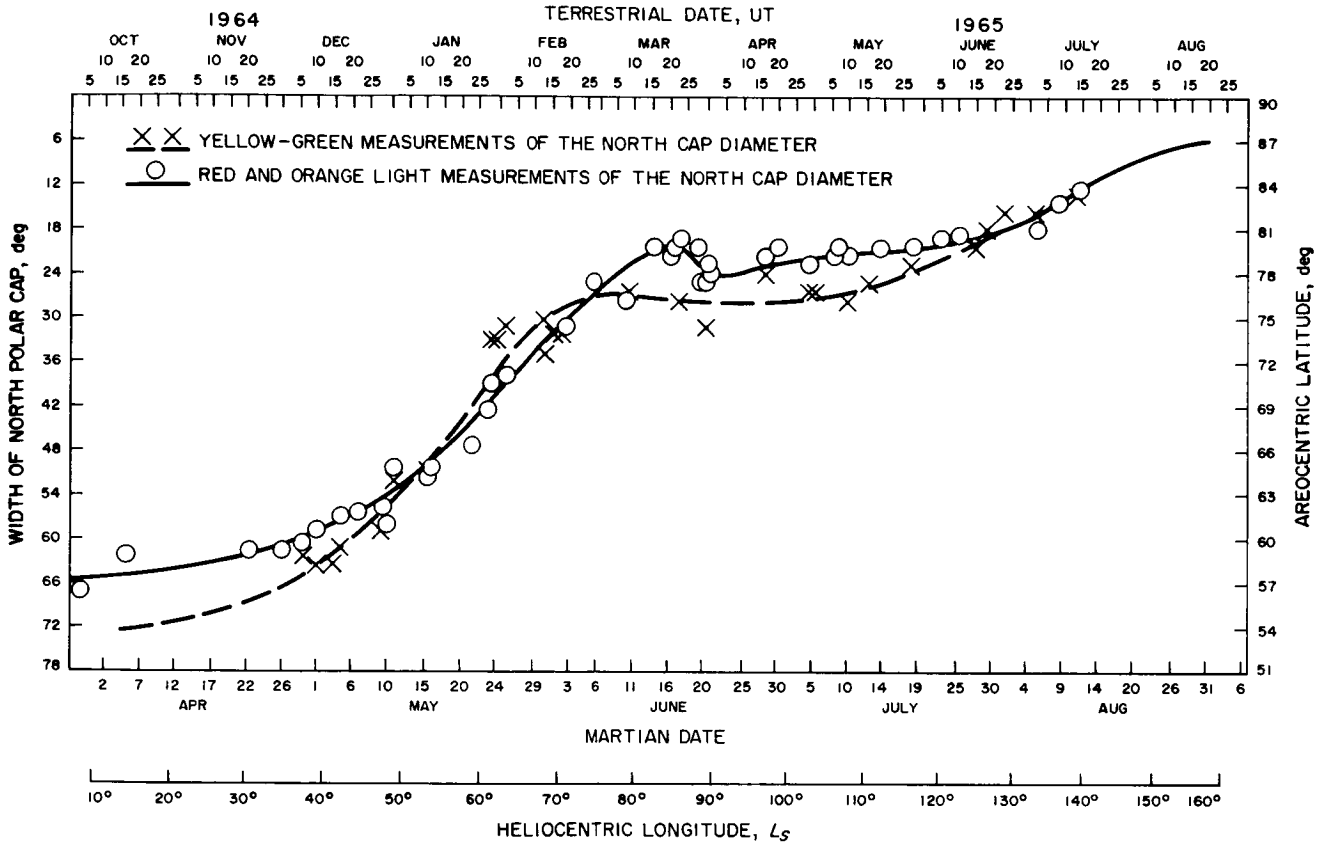

Fig. 2. Measured width of the north polar cap of Mars for observations from October, 1964, through August, 1965. Martian dates are rough seasonal equivalents to their terrestrial counterparts.[11] (Capen, 1966)

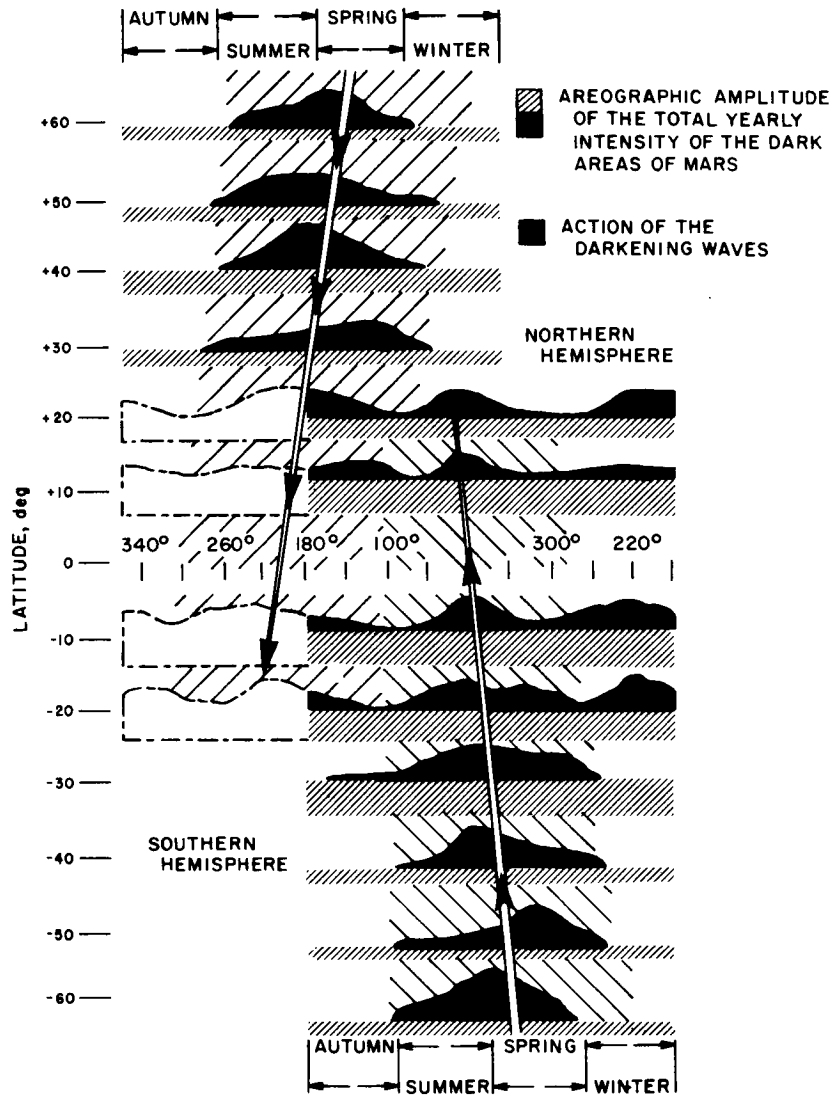

Fig. 3. Areographic amplitude of the intensity of the dark areas of Mars. Lineated areas show the average intensity of the dark areas contained within the corresponding areographic latitudes but do not include the variation of intensity resulting from the action of the darkening waves. Black areas show the increase of the average intensity of the dark areas resulting from the action of the darkening waves. The abscissas represent the Martian year and the ordinates the ratio Bs/Bc. (Bs is brightness at a measured spot; Bc is brightness at a reference spot in the center of the Martian disk.) These data have been computed on the basis of 7200 determinations of the ratio Bs/Bc made by Focas for 36 dark areas of Mars on 663 negatives of this planet taken at Pic du Midi during the period 1941-1958. (Focas, 1962)

Area and location (center of area)	Martian season	Type of change: Color	Type of change: Shape and size	Map
Mare Acidalium +50° latitude, 35° longitude	Spring	Dark gray, blue-gray, with oasis gray-green; gray in general	Boundaries weak	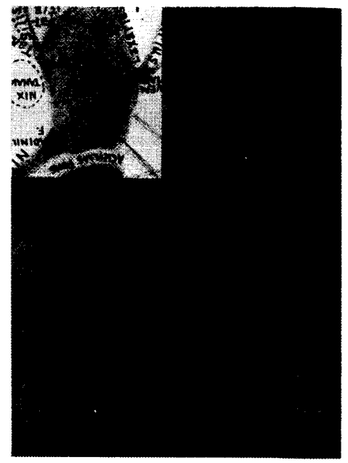
	Summer	Black-green central area; large, gray-green oases; changes to gray-green at end of summer	Large, swollen in size	
	Fall	Lightens to blue-gray, losing contrast; still dark, variated	Borders fade	
	Winter	Grays and browns	Center fades to match edges	
Niliacus Lacus +32° latitude, 32° longitude	Spring	Dark gray unmapped oasis; late: dark gray green	Internal changes in shape; borders and center darken	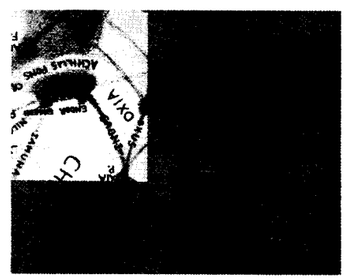
	Summer	Dark green	Swollen in size; looks larger	
	Fall	Dark gray		
	Winter	Gray	Borders weak	
Mare Boreum (Baltia-Boreum) +65° latitude, 85° longitude	Spring	Dark gray; blue tint and black shades as cap melts; black blue		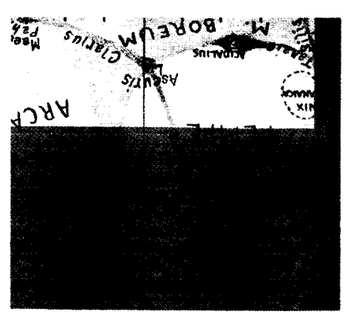
	Summer	Black-blue		
	Fall	Less contrast; dark gray		
	Winter	Dark gray		

Notes: Maps are from the ALPO map compiled by D. P. Avigliano (Sky and Telescope, September, 1956, p.502-503). Maps have been rotated here to place north at the top.

Area and location (center of area)	Martian season	Type of change: Color	Type of change: Shape and size	Map
Propontis Complex +50° latitude, 170° longitude	Spring	Darker gray	Highly complex changes in shape	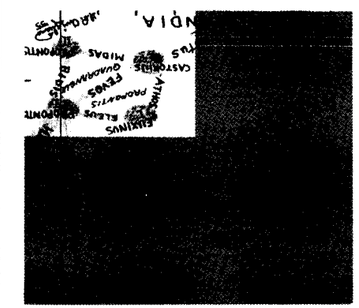
	Summer	Green-black; loses green in late summer	Shape: oases swollen, canals dark and seasonal canal structure; Size: larger oases	
	Fall	Dark gray to black	Fading shape	
	Winter	Mid-gray shade	Shape: simple parallelogram with corner oases; Size: small weak oases, not connected	
Nodus Laocoontis-Alcyonius +30° latitude, 255° longitude	Spring	Very active; A: gray-green to black-green; B: small, black-green oasis; C: intense, saturated green; D: not seen		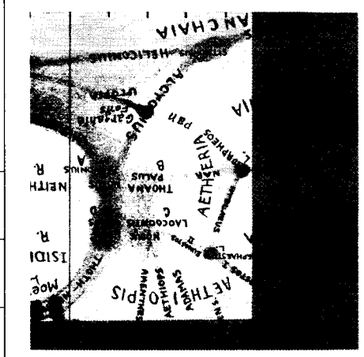
	Summer	C: black-green, darker	C: most color-saturated (green) on Mars, 1964-65	
	Fall	C: fades, gray-green; others gray		
	Winter	Inactive; A and C seen; medium gray		
Utopia-Boreosyrtis +50° latitude, 270° longitude	Spring	Increase in contrast; dark gray 61 hue	Internal structure changes in size	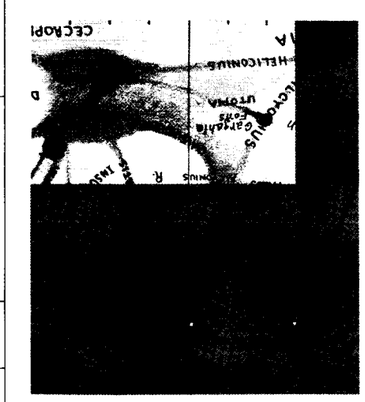
	Summer	General: dark blue-gray; early: green tint; mid-summer: intense blue-black with variations, dark browns, olive drabs, ochre		
	Fall	Fading contrast; dark gray		
	Winter	Dark gray		

Fig. 4. Table of seasonal changes on Mars in northern dark areas.

Area and location (center of area)	Martian season	Type of change: Color	Type of change: Shape and size	Map
Meridiani Sinus 0° latitude, 0° longitude	Spring	Dark gray shade		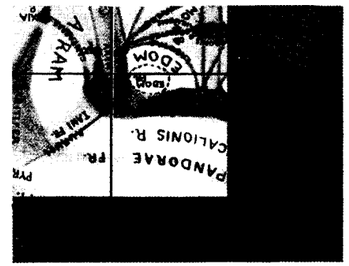
	Summer	Black shade	Shape: Caret* extension toward Cantabras; Size: Fastigium Aryn fills in (darkens) between two canal Carets (does not become black)	
	Fall	Dark gray to black	W. Caret dims; no change in size	
	Winter	Sometimes black-blue	Size: Fastigium Aryn becomes light	
Margaritifer Sinus -10° latitude, 25° longitude	Spring	Early: dark gray shade; late: blue-green hue + dark gray		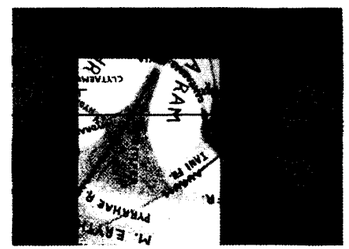
	Summer	Black-green hue	Internal canal changes in size	
	Fall	Changes back to dark gray + mottled brown		
	Winter	Dark gray + mottled dark brown		
Aurorae Sinus -12° latitude, 60° longitude	Spring	Early: black shade; late: black-blue		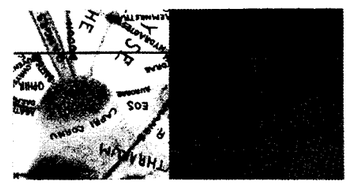
	Summer	Black-blue		
	Fall	Black and dark gray shade		
	Winter	Dark gray		
Trivium Charontis-Cerberus I +15° latitude, 200° longitude	Spring	Medium dark gray and brown tints; olive drab with darkening wave; takes on intense black later	Size: below normal contrast, 1964-65	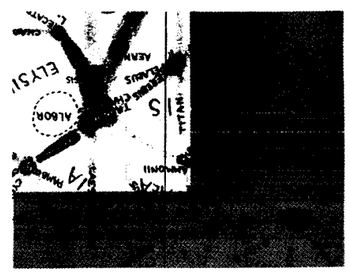
	Summer	Stays black		
	Fall	Dark gray and brown		
	Winter	Medium dark gray and brown tints		

*Term used to designate root-like darkening toward canal.

Area and location (center of area)	Martian season	Type of change: Color	Type of change: Shape and size	Map
Mare Cimmerium -30° latitude, 200° longitude (equatorial and southern area)	Spring	Medium dark gray with dark brown and medium gray		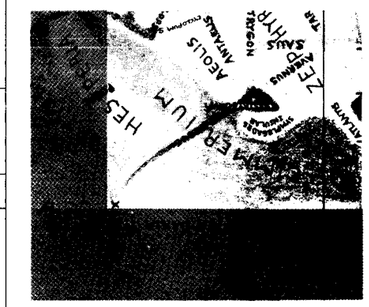
	Summer	Changes to dark brown with blue-gray streaks	Edges: N.E. Gomer Sinus has been increasing in size	
	Fall	Dark blue-gray		
	Winter	Nondescript medium dark gray with dark brown and medium gray streaks		
Mare Tyrrhenum-Iapygia -15° latitude, 270° longitude	Spring	Purple and dark brown	Carets increase in contrast; no change in shape	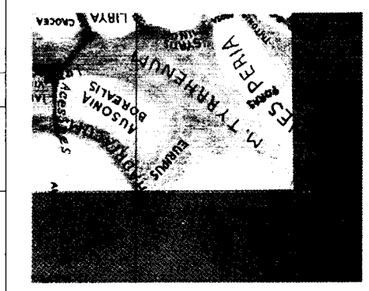
	Summer	No change		
	Fall	Fading purple and mottled brown; also grays	Carets decrease in contrast	
	Winter	Medium gray with mottled brown hues; most prominent and colorful feature on Mars		
Syrtis Major +11° latitude, 290° longitude	Spring	Green-blue; blue-green; late: bright, saturated blue		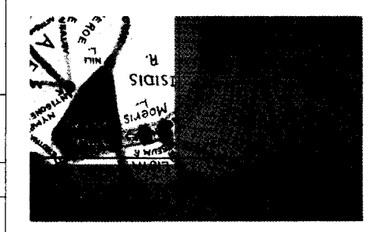
	Summer	Dark blue-black; late: returns to blue-green	No tip esp.	
	Fall	Green-blue		
	Winter	Dark gray-green		
Sabaeus Sinus -10° latitude, 330° longitude	Spring	Intense black-blue hue	Size: very stable, high contrast area	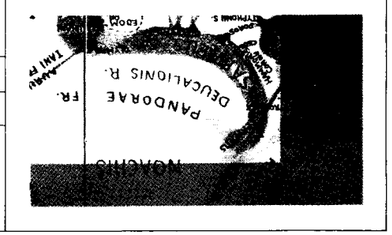
	Summer	Black-green hue		
	Fall	Dark gray shade		
	Winter	Dark brown-gray		

Notes: Maps are from the ALPO map compiled by D. P. Avigliano (Sky and Telescope, September, 1956, p. 502-503). Maps have been rotated here to place north at the top.

Fig. 5. Table of seasonal changes on Mars in equatorial dark areas. Seasons refer to northern hemisphere.

Area and location (center of area)	Type of change	Map
Cydonia-Ortygia +50° latitude, 0° longitude	Normal ochre desert color south of Novem Viae in Nix Cydonia; exhibits diurnal seasonal whitening	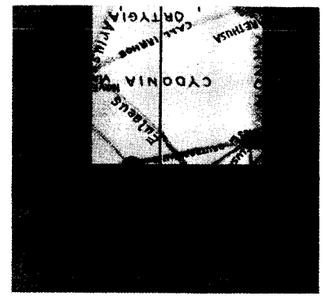
Tempe +40° latitude, 70° longitude	Large ochre region; filling-in in Tempe canal (secular); Nix Tanaica exhibits diurnal seasonal whitening	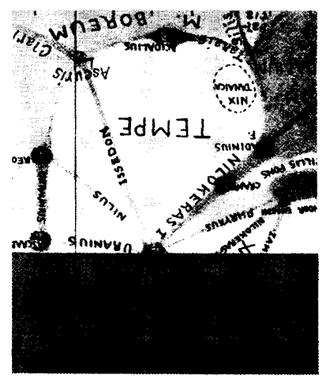
Arcadia, Scandia +45° latitude, 135° longitude	Arcadia: large ochre area, over which recurrent afternoon clouds form; yellow dust clouds have been observed Scandia: dark ochre; some seasonal darkening; sometimes filled in, appears similar to maria	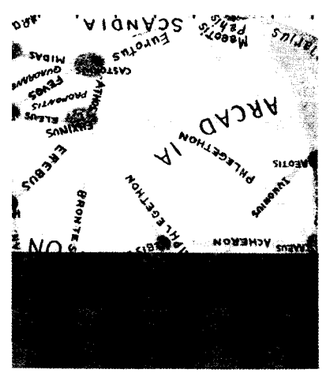

Area and location (center of area)	Type of change	Map
Phlegra, Cebrenia-Aetheria +45° latitude, 210° longitude	Phlegra: variable color hues ranging from light to dark ochre, and yellowish; exhibits seasonal darkening due to filling-in Cebrenia-Aetheria: normal ochre region	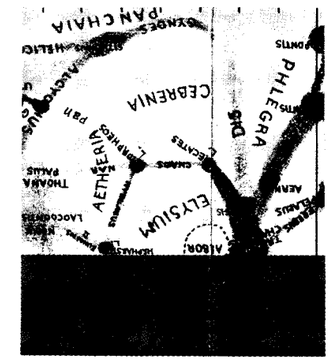
Dioscuria +50° latitude, 320° longitude	Normal ochre area; no seasonal changes observed	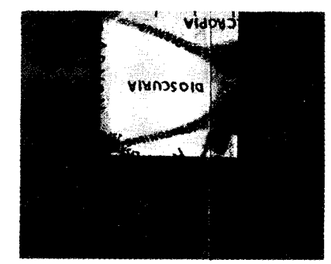
Panchaia-Cecropia +65° latitude, 180-340° longitude	Normally dark ochre region; darkening during spring; light ochre in late summer, fall; covered by polar cap in winter; within Cecropia (+65° latitude, 275-315° longitude) a large, white, oval frost patch has been observed from time to time	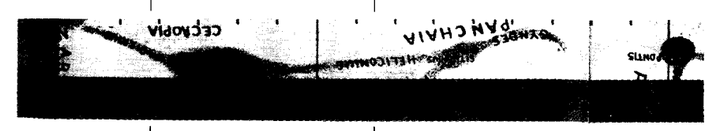

Notes: Maps are from the ALPO map compiled by D. P. Avigliano (Sky and Telescope, September, 1956, p.502-503). Maps have been rotated here to place north at the top.

Fig. 6. Table of seasonal changes on Mars in northern light areas.

Area and location (center of area)	Type of change	Map
Aram, Chryse, Xanthe +10° latitude, 30° longitude	Aram: light ochre; seasonal whitening Chryse: normal desert ochre hue Xanthe: known to whiten in some areas	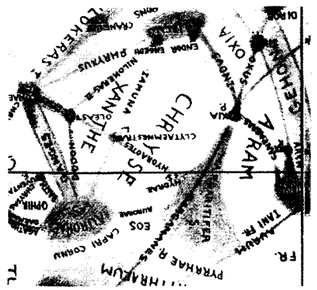
Candor-Tharsis +10° latitude, 90° longitude	Normal ochre hue; clouds are generated in this region; entire region becomes seasonally whitened	
Thaumasia (Eye-of-Mars) -30° latitude, 90° longitude	Variegated colored area with hues ranging from dark orange, light ochre, to yellow; seasonal local-area whitening; sometimes covered by yellow clouds	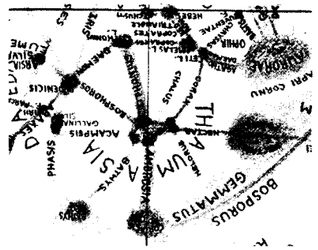
Daedalia -15° latitude, 125° longitude	Normal ochre color; some seasonal darkening (local oasis and canal structure)	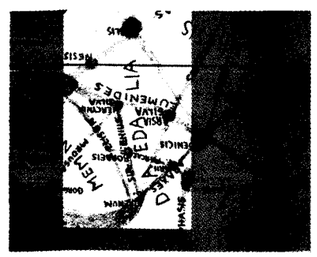

Area and location (center of area	Type of change	Map
Memnonia-Mesogaea area -10° latitude, 160° longitude	Normal ochre color; seasonal whitening known to occur on southern border of Memnonia	
Amazonis +20° latitude, 60° longitude	Very bland, featureless area (Tempe-Arcadia similar); recurrent cloud activity; Nix Olympica in Amazonis becomes seasonally whitened (historically known); yellow clouds have been observed in this region	
Zephyria, Aeolis -10° latitude, 200° longitude	Zephyria: normal ochre color Aeolis: light region; possibly some whitening at times	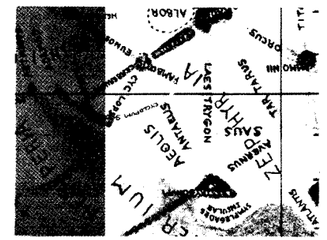
Elysium, Aethiopis +20° latitude, 235° longitude	Elysium: normal light ochre (Albor area gray-white); becomes dazzling white during late spring with rapid regression of north polar cap; diurnal retreat of whitening leaves pink tint Aethiopis: normal ochre color	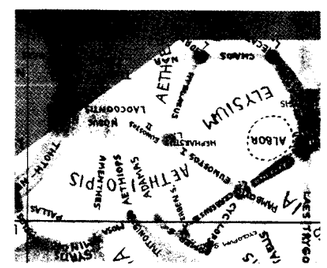

Area and location (center of area)	Type of change	Map
Hesperia -20° latitude, 235° longitude	Dark ochre narrow area; shows some seasonal filling-in (darkening)	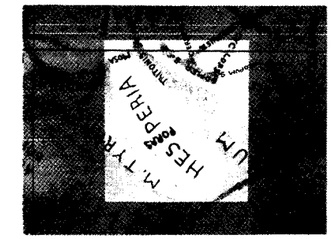
Libya-Crocea, Isidis Regio-Neith Regio area +20° latitude, 280° longitude	Libya-Crocea: ochre region; displays seasonal morning whitening and blue limb haze Isidis Regio-Neith Regio: light ochre desert regions; much morning seasonal whitening and limb haze	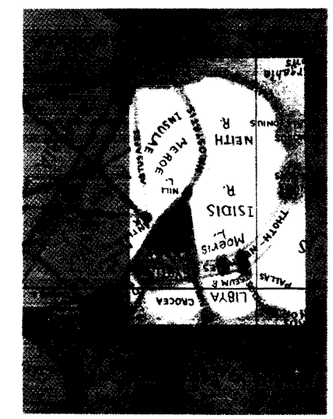
Aeria, Arabia-Eden, Edom +20° latitude, 330° longitude	Aeria: yellowish hue with enclosed Nymphaeum being gray-white shade; similar characteristics to Elysium-Albor area; may become pink around Nymphaeum Arabia-Eden: normal ochre color; morning limb frost has been observed in Eden area Edom: light desert area; seasonal whitening	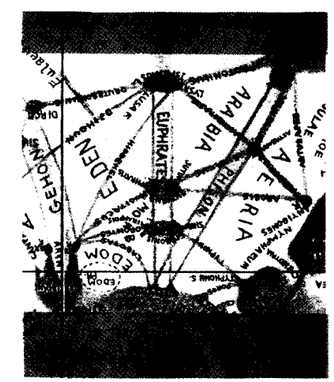

Notes: Maps are from the ALPO map compiled by D. P. Avigliano (Sky and Telescope, September, 1956, p. 502-503). Maps have been rotated here to place north at the top.

Fig. 7. Table of seasonal changes on Mars in equatorial light areas.

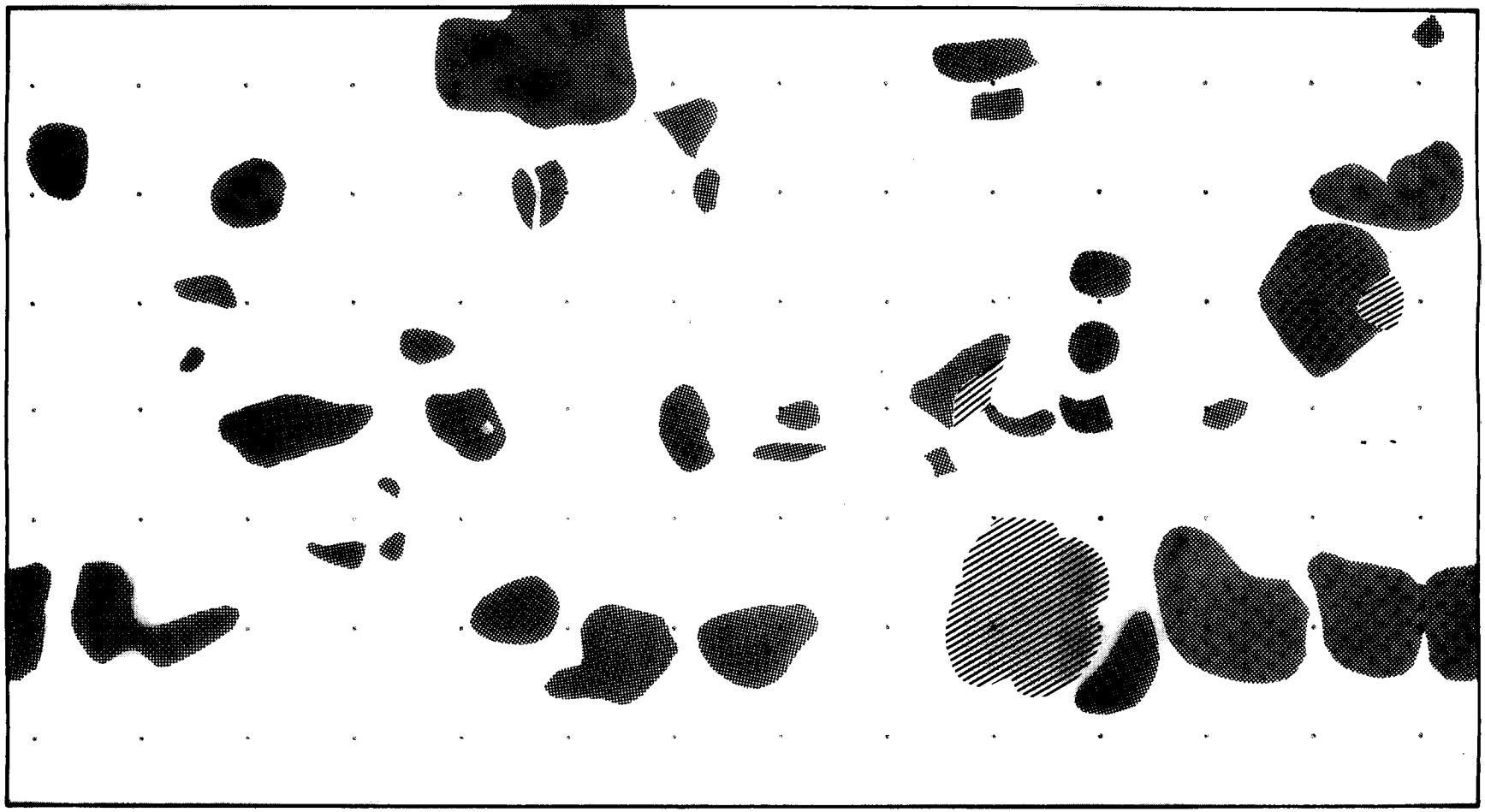

FROST

N. SPRING, S. FALL

recurrent frost

more persistent frost cover through the Martian day

JPL 606-1

APRIL 1, 1967

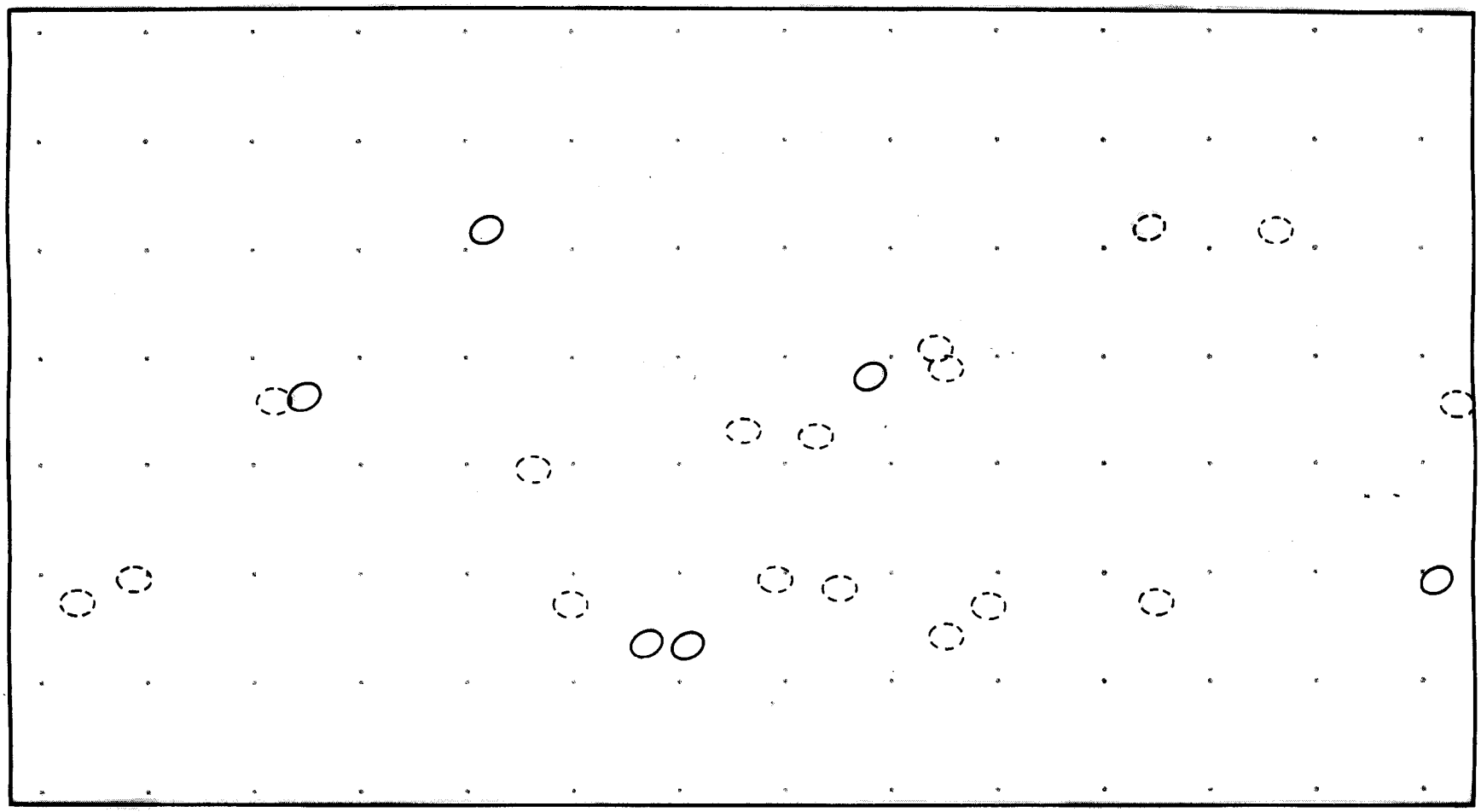

WHITE CLOUDS ◯ & YELLOW CLOUDS ◌

N. SPRING, S. FALL

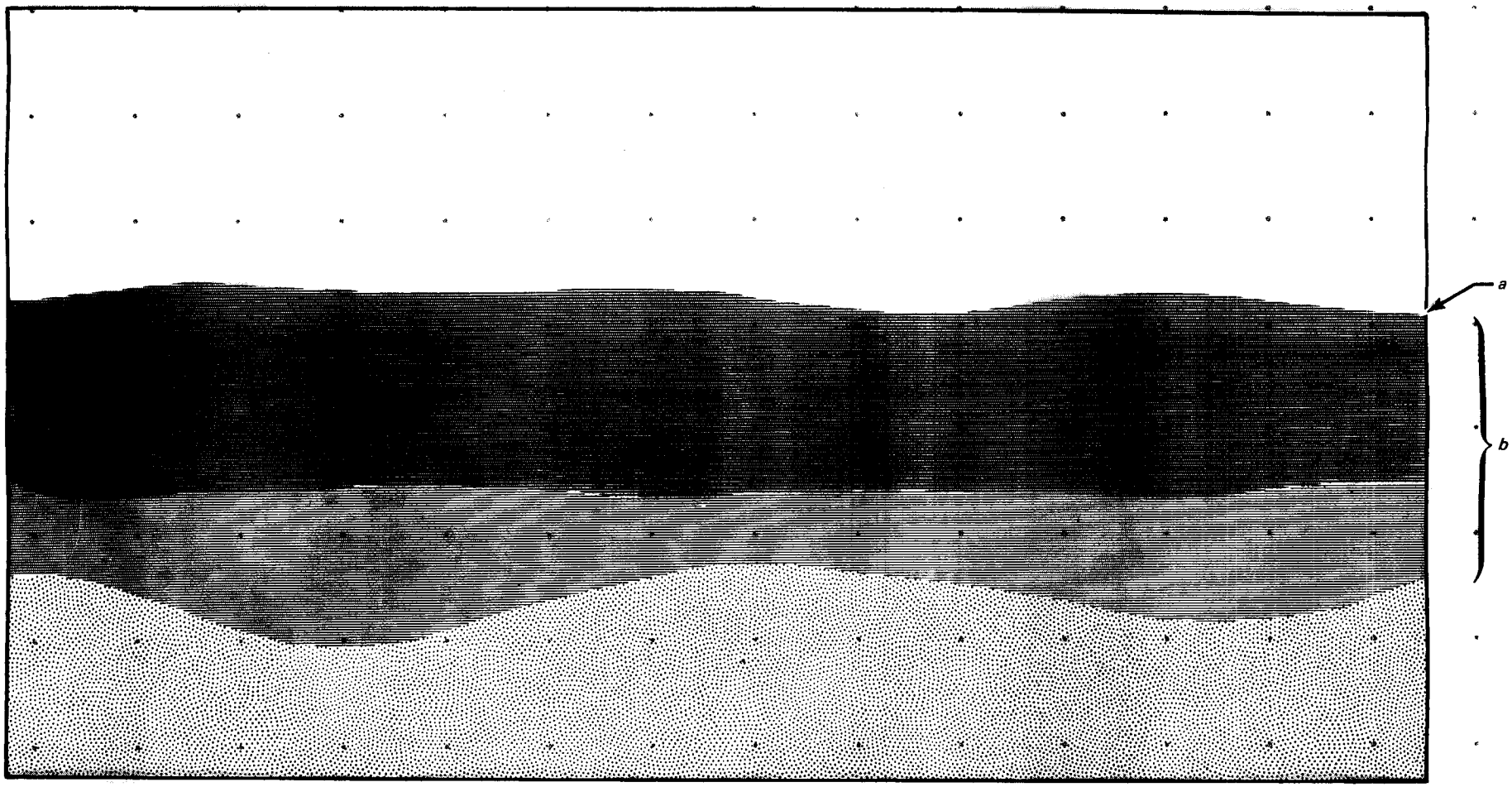

WAVE OF DARKENING

N. SUMMER, S. WINTER

a: northern extent of southern wave
b: at maximum darkening

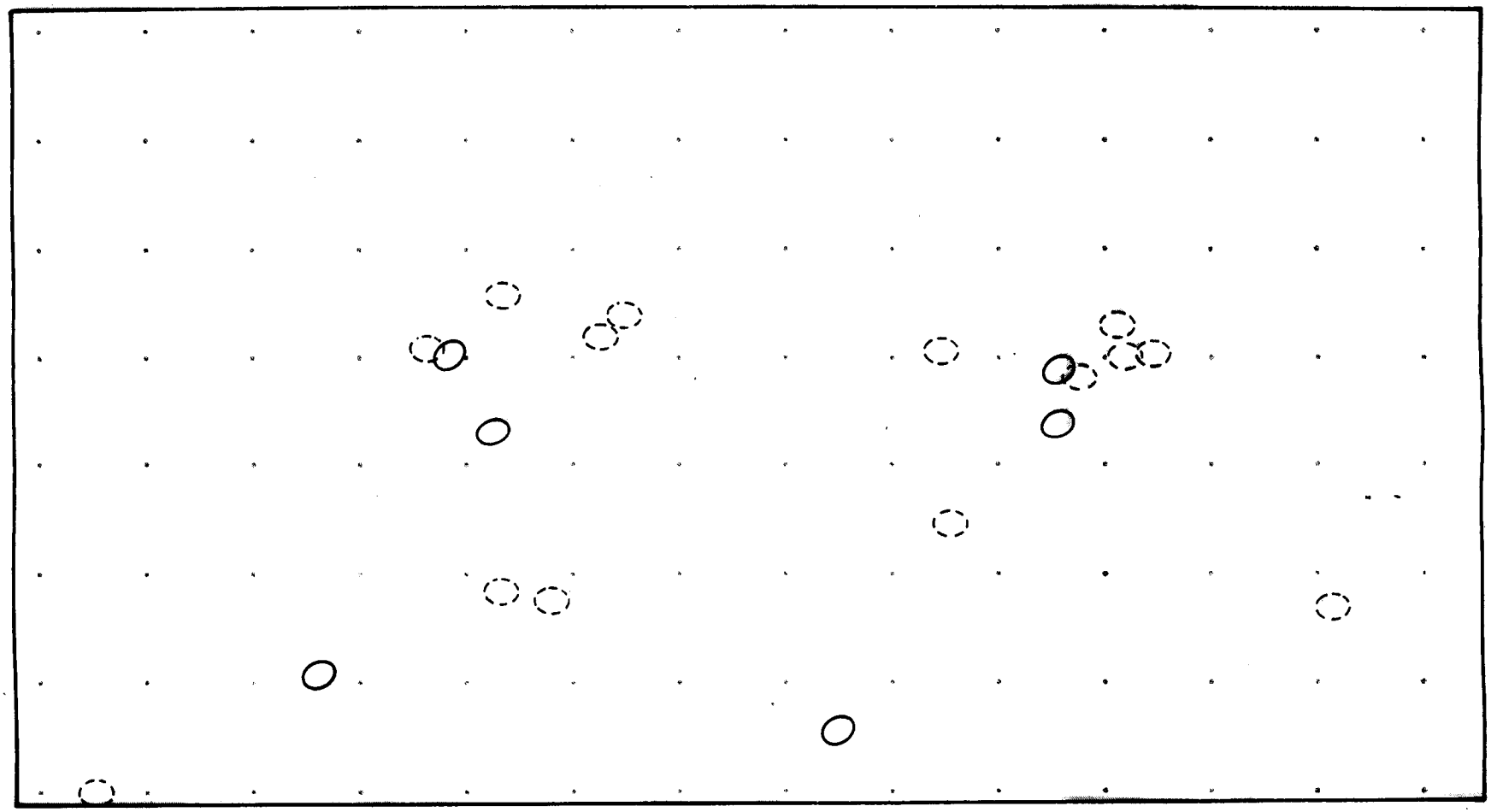

WHITE CLOUDS & YELLOW CLOUDS

N. SUMMER, S. WINTER

JPL 606-1

APRIL 1, 1967

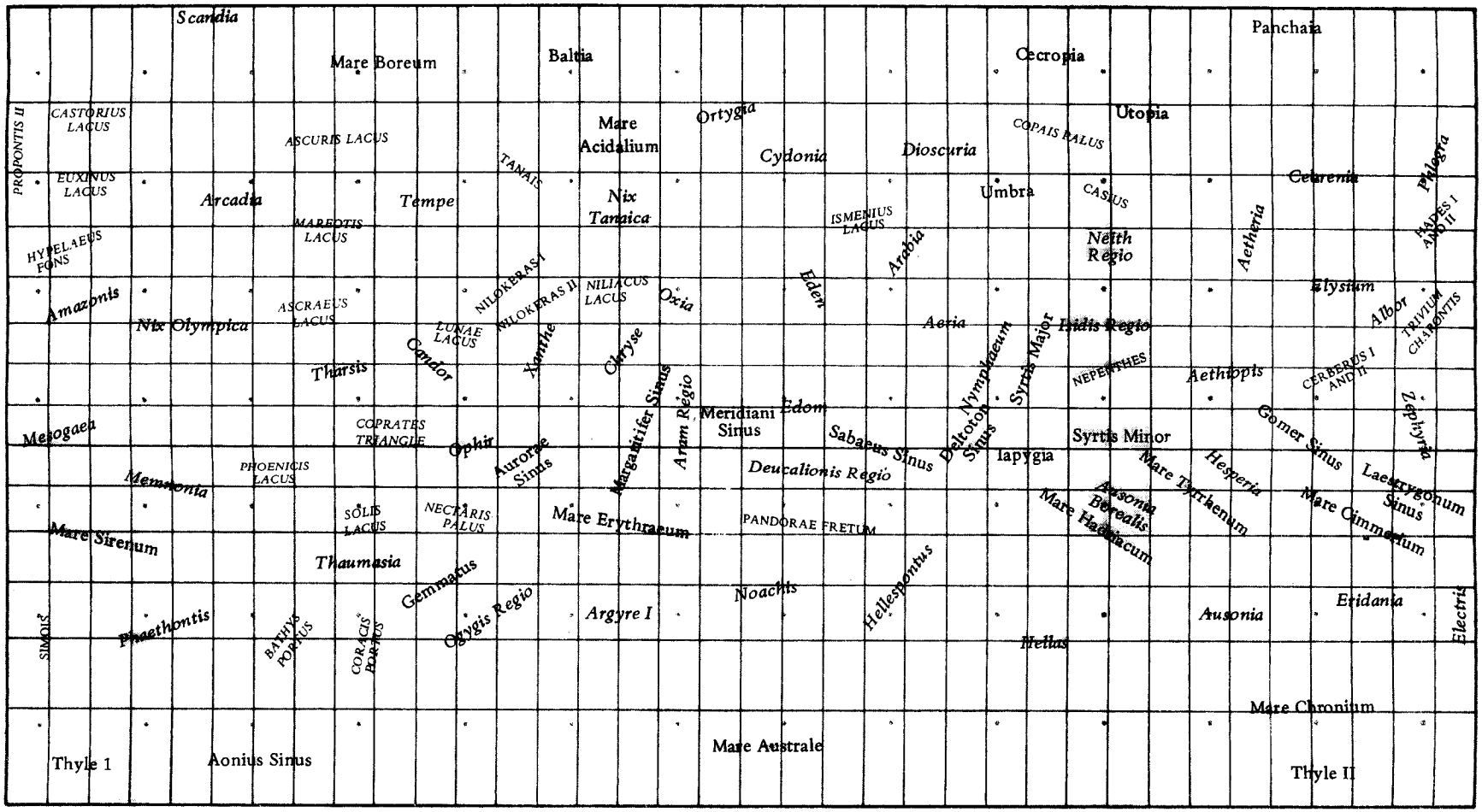

JPL 606-1
APRIL 1, 1967

PLACE-NAMES OF SURFACE FEATURES

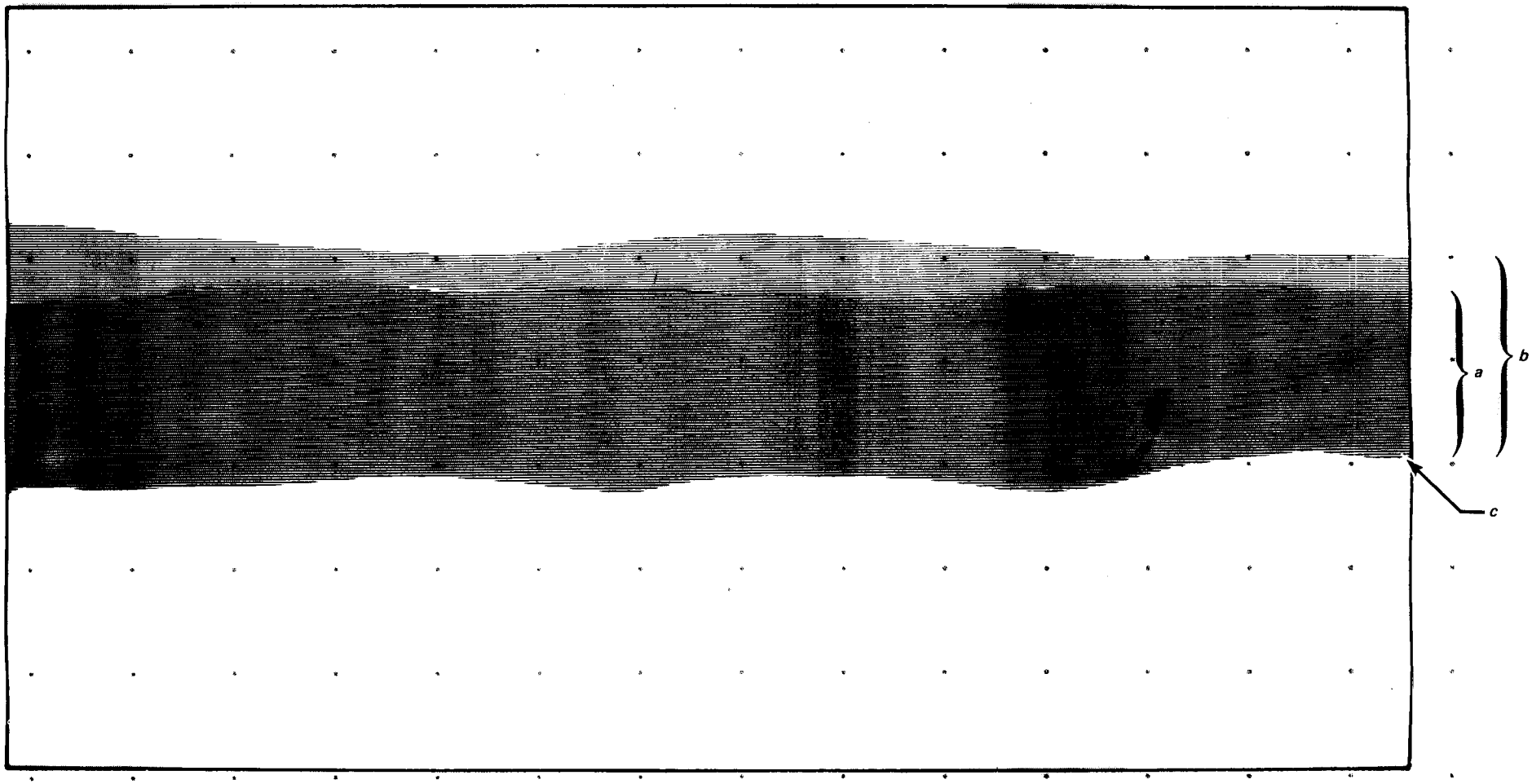

WAVE OF DARKENING

N. SPRING, S. FALL

a: affected every 6 months
b: at maximum darkening
c: southern extent of

JPL 606-1

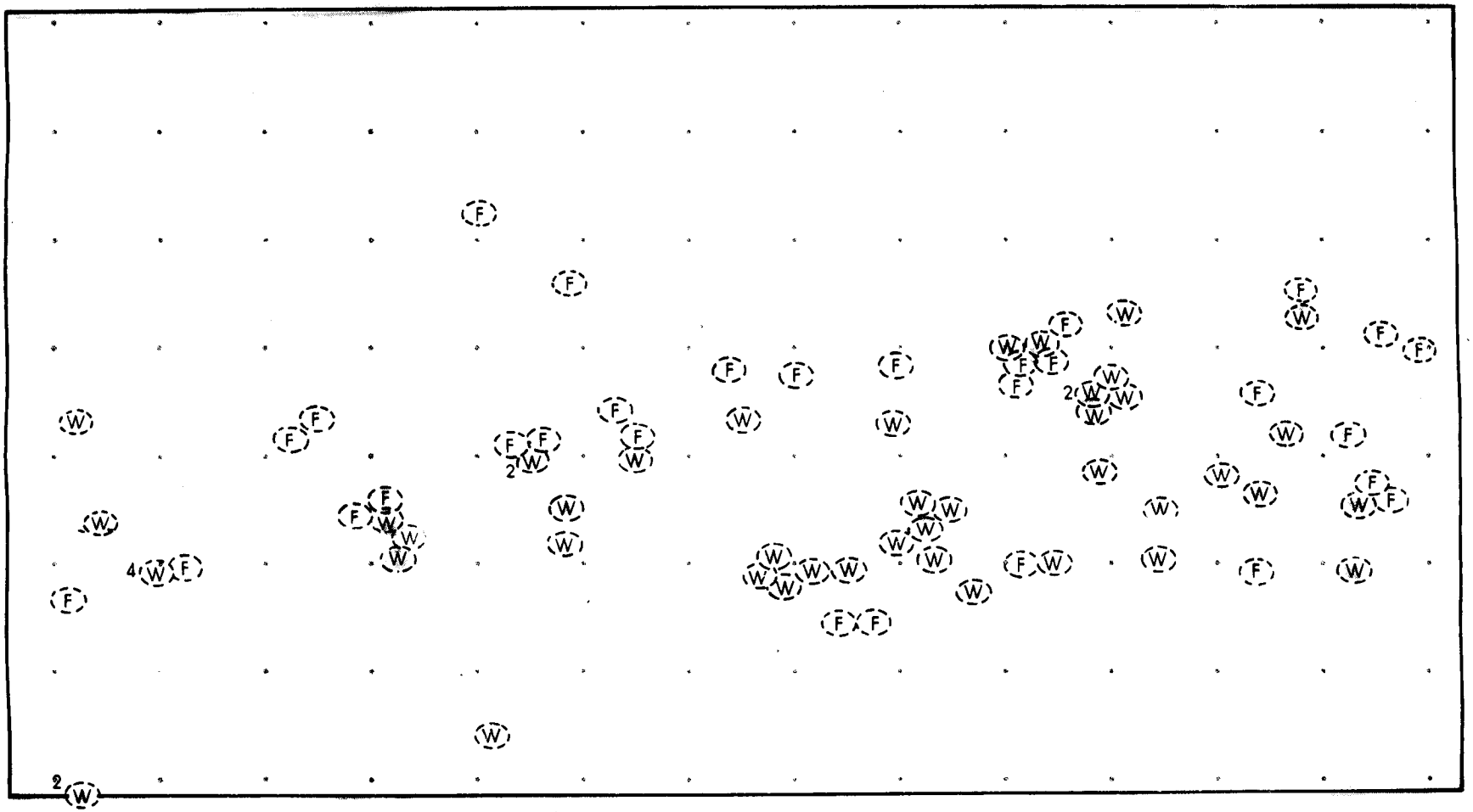

YELLOW CLOUDS

N. FALL-WINTER, S. SPRING-SUMMER

JPL 606-1

APRIL 1, 1967

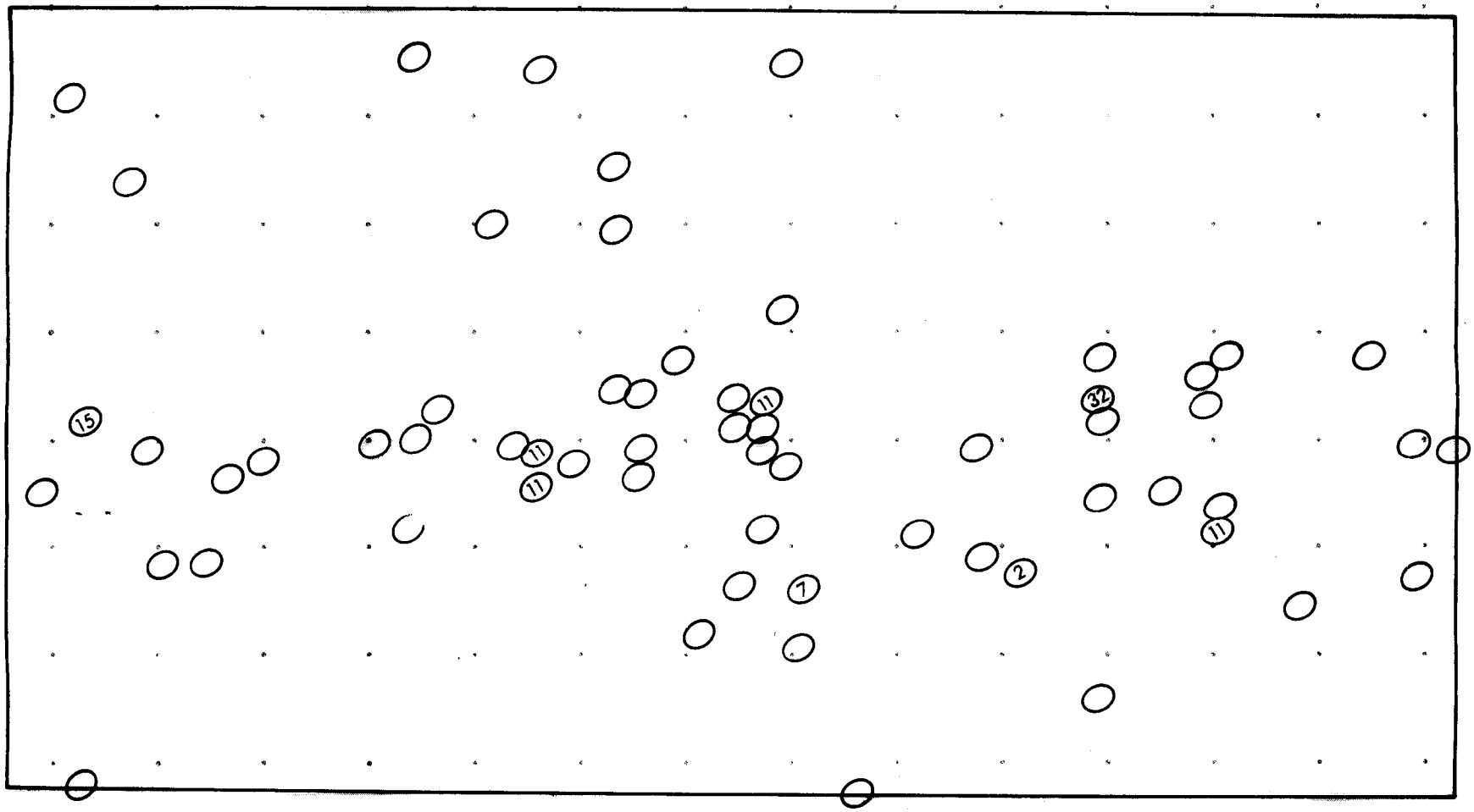

WHITE CLOUDS

N. FALL-WINTER, S.SPRING-SUMMER

JPL 606-1

APRIL 1, 1967

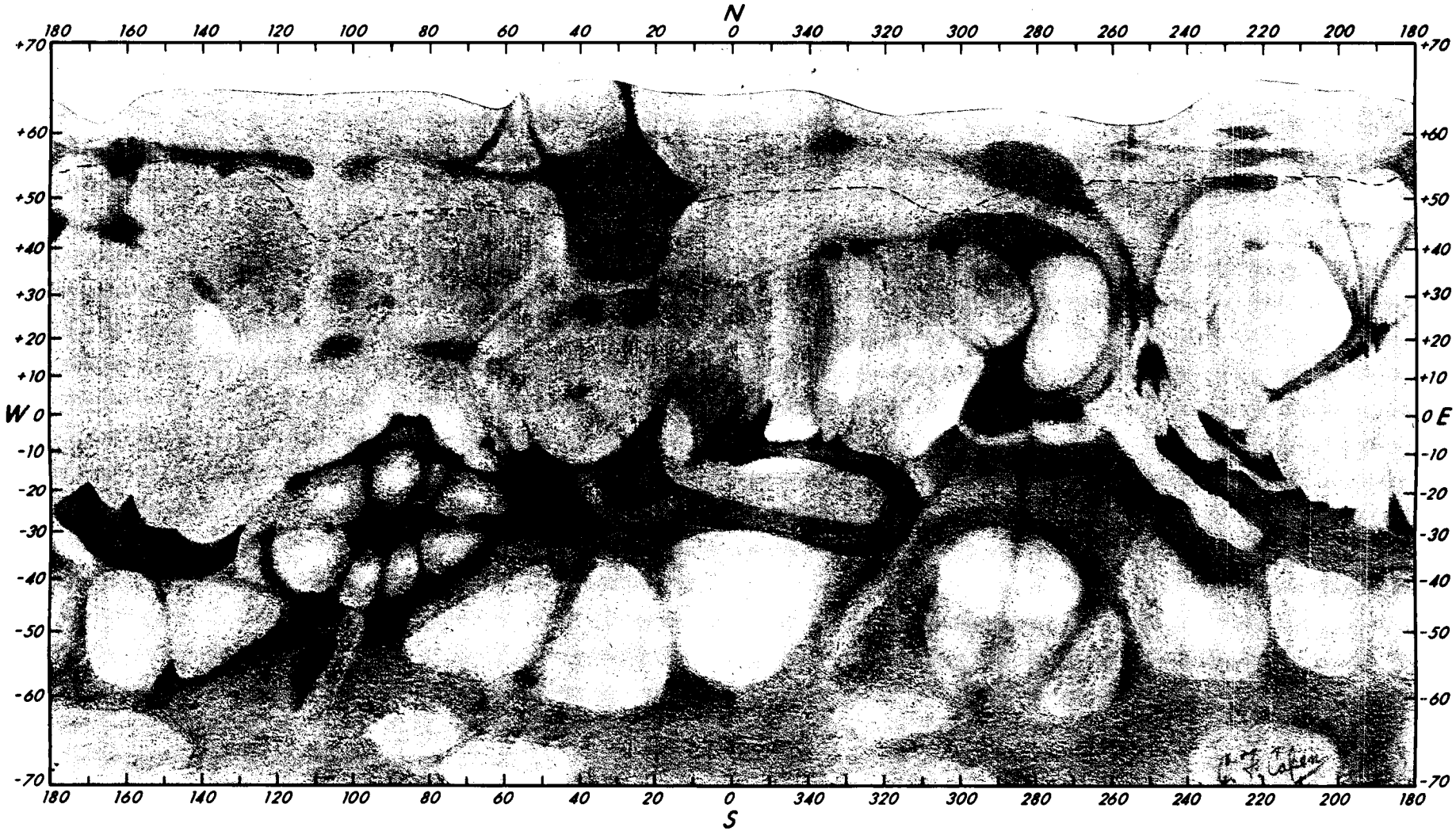

THE MARTIAN SURFACE

NORTHERN FALL-WINTER, SOUTHERN SPRING-SUMMER

JPL 606-1
C. CAPEN, JPL
APRIL 1, 1967

Fig. 8. Color map of the Martian surface in northern fall-winter and southern spring-summer, with white and yellow cloud activity during these seasons. The color map was compiled from observational data by C. F. Capen (color contrasts of features were necessarily increased to aid reproduction). The Mercator format was obtained from the International Astronomical Union (Ashbrook, 1958) and from de Vaucouleurs' map (1965) and areographic coordinates (1961a, 1961b, 1962).

JPL 606-1
C. CAPEN, JPL
APRIL 1, 1967

THE MARTIAN SURFACE

NORTHERN SPRING, SOUTHERN FALL

Fig. 9. Color map of the Martian surface in northern spring and southern fall, with wave of darkening, frost, and white and yellow cloud activity during these seasons. The color map was compiled from observational data by C. F. Capen (color contrasts of features were necessarily increased to aid reproduction). The Mercator format was obtained from the International Astronomical Union (Ashbrook, 1958) and from de Vaucouleurs' map (1965) and areographic coordinates (1961a, 1961b, 1962).

C. Capen,
J. de Wys, JPL

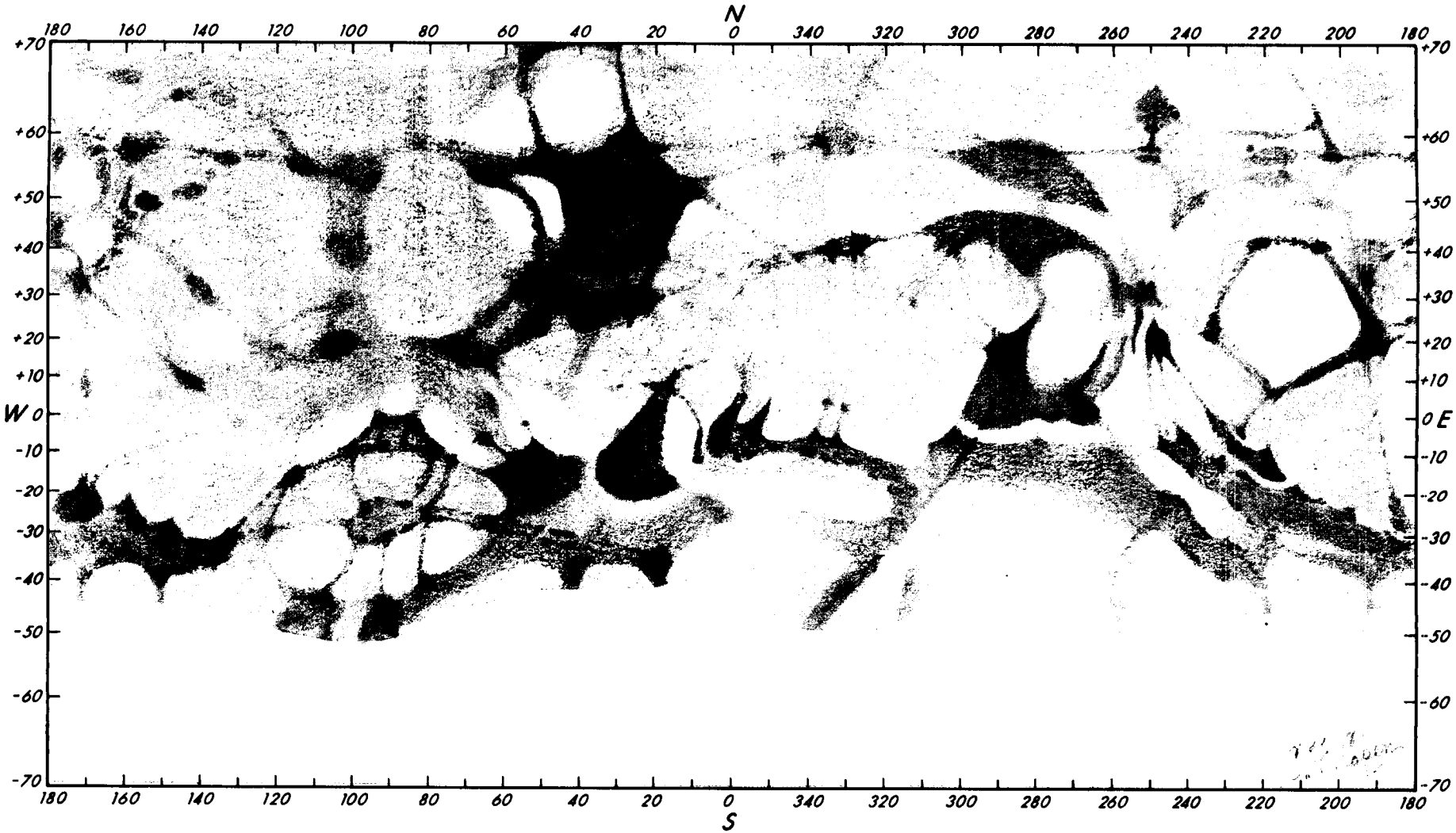

JPL 606-1
C. CAPEN, JPL
APRIL 1, 1967

THE MARTIAN SURFACE

NORTHERN SUMMER, SOUTHERN WINTER

Fig. 10. Color map of the Martian surface in northern summer and southern winter, with wave of darkening and white and yellow cloud activity during these seasons. The color map was compiled from observational data by C. F. Capen (color contrasts of features were necessarily increased to aid reproduction). The Mercator format was obtained from the International Astronomical Union (Ashbrook, 1958) and from de Vaucouleurs' map (1965) and areographic coordinates (1961a, 1961b, 1962).

C. Capen, J. de Wys, JPL

A	° Lat, ° Long
Acadinius Fons (Acadinus): oasis	+40, 41
Acampsis: canal	-30, 105
Acesines: canal	-30, 290
Acheron: canal	+22, 120
Achillis Fons (Craneum Fons): oasis	+30, 52
Achillis Pons: light promontorium	+36, 32
Acidalia Depressio (Acidalia Fons): oasis	+50, 38
Acidalium, Mare: mare	+50, 35
Acidalius Fons: oasis	+57, 65
Adamas (Serpentinus): canal	+12, 240
Aeolis: desert	-10, 212
Aeria: light desert	+18, 312
Aernos Fons: oasis	+33, 192
Aesacus (Dis): canal	+45, 200
Aetheria: desert	+40, 240
Aethiopis: desert	+10, 245
Aethiops: canal	+10, 248
Agathodaemon: canal	-12, 72
Albis Lacus: oasis	+20, 139
Albor; on Elysium plateau: light area	+21, 209
Alcyonius: canal	+45, 250
Alcyonius, Nodus: large oasis	+35, 260
Alpheus: canal	-40, 290
Amazonis: desert	+20, 160
Ambrosia: canal	-35, 90
Amenthes: canal	+10, 251
Ammonii Fons: oasis	+10, 175
Antaeus: canal	-10, 205
Antigones Fons: oasis	+20, 296
Aonius Sinus: mare	-60, 105
Arabia: desert	+32, 320
Aram Regio (Thymiamata): light desert	+5, 12
Araxes: canal	-25, 120
Arcadia: desert	+45, 130
Arethusa Lacus: oasis	+62, 333
Argyre I: desert plateau	-48, 35
Argyroporos: canal	-40, 10
Arius: canal	+55, 15
Arnon (Euphrates-Arnon): canal	+50, 333
Arosis: canal	+18, 310
Arsenius Lacus: oasis	+68, 153
Arsia Silva: oasis	-5, 120
Ascania Pons: oasis	+38, 158
Ascraeus Lacus: oasis	+20, 99
Ascuris Lacus: oasis	+53, 88
Astaborae Fons: oasis	+33, 309
Astaboras I and II: canals	+30, 310
Astusapes: canal	+33, 298
Athos: canal	+48, 157
Atlantis: desert	-28, 175
Aurorae (Auroral Promontorium; Fretiem): canal	-8, 40
Aurorae Sinus: mare	-10, 55
Aurum: canal	-12, 10
Ausonia: desert plateau	-48, 250
Ausonia Borealis: light desert plateau	-28, 275
Australe, Mare: mare	-70, 0
Avernus: canal	-15, 185
B	
Baltia: mare	+60, 35
Bathys: canal	-35, 100
Bathys Portus: oasis	-42, 106
Bay of Furca (Fastigium Aryn); within Gehon double canal	0, 0
Biblis Fons: oasis	+10, 130
Bidis: canal	+50, 180
Borbeis Fons: oasis	-21, 128
Boreosyrtis: mare	+55, 285
Boreum, Mare: mare	+63, 80
Bosporus: mare	-40, 60
Bretis: canal	-4, 63
Brontes: canal	+25, 160

C	° Lat, ° Long
Callirrhoe: canal	+55, 0
Callirrhoes Sinus (Novem Fons; Novem Viae): oasis	+50, 19
Candor: desert	+5, 75
Cantabras: canal	+10, 10
Capri Cornu: strait	-20, 60
Casius; within Mare Casius: canal	+41, 270
Casius, Mare (Wedge-of-Casius): mare	+45, 270
Castorius Lacus: oasis	+55, 157
Cebrenia: desert	+47, 220
Cecropia region	+65, 300
Cenotria (Enotria): desert	0, 305
Ceos: canal	-8, 318
Ceraunius: canal	+30, 99
Cerberus I and II: canals	+10, 215
Ceti Lacus: oasis	-10, 75
Chalus: canal	-20, 85
Chaos: canal	+38, 220
Charis: strait	-40, 325
Chronium, Mare: mare	-60, 200
Chrysas: canal	-5, 70
Chryse: desert	+10, 30
Chrysorrhoas: canal	+10, 80
Cimmerium, Mare: mare	-30, 200
Clarius: canal	+57, 100
Clytaemnestrae Lacus: oasis	+12, 46
Coloe Palus: oasis	+40, 305
Copais Palus; within the Boreosyrtis mare: large oasis	+54, 290
Coprates: canal	-8, 90
Coprates Triangle: oasis complex	-5, 90
Coracis Portus: oasis	-44, 90
Corax: canal	-20, 80
Craneum Fons (Achillis Fons): oasis	+30, 52
Crocea: desert	-5, 290
Cyclops: canal	0, 220
Cydonia: desert	+50, 355
Cydonia, Nix: plateau	+46, 18
D	
Daedalia: desert	-15, 125
Daemon: canal	-12, 102
Dardanus: canal	+40, 55
Dargamanes: canal	-20, 40
Deltoton Sinus: mare	-5, 310
Deucalionis Regio: light desert region	-15, 350
Deuteronilus: canal	+40, 350
Dioscuria: desert	+50, 320
Dirce Fons: oasis	+35, 5
Dis (Aesacus): canal	+45, 200
Djihoun (Oxus II): canal	+35, 0
Dodon: canal	+5, 58
Dosaron: canal	0, 300
Draco: canal	+10, 90
E	
Echus Lacus: oasis	0, 90
Eden (Moab): desert	+25, 350
Edom and Edom Promontorium: desert plateau	0, 350
Electris: desert plateau	-48, 190
Eleus: canal	+45, 168
Elison: canal	-20, 135
Elusa Fons; within Ismenius Lacus: oasis	+40, 336
Elysium: plateau	+25, 215
Endor Fons (Endoris): oasis	+29, 26
Engedii Fons: oasis	+29, 38
Eos: mare	-12, 40
Eosphoros: canal	-20, 100
Erebus: canal	+27, 180
Eridania: desert plateau	-45, 215
Erythraeum, Mare: mare	-25, 40

	° Lat, ° Long
Eulaeus: canal	+48, 10
Eumenides: canal	-10, 125
Eunostos I and II: canals	+20, 230
Euphrates (Euphrates-Arnon): double canal	+40, 333
Euphratis Lacus; within Juturna Fons: oasis	+20, 335
Euripus	-30, 260
Eurotus: canal	+58, 125
Euxinus Lacus: oasis	+44, 159
Eye-of-Mars (Solis Lacus): multi-oasis	-28, 90
F	
Fastigium Aryn (Bay of Furca); within Gehon double canal	0, 0
Ferentinae Lacus: oasis	+38, 132
Fevos: canal	+50, 165
Fortuna: canal	+10, 95
G	
Gaesus: canal	-27, 210
Gallinaria Silva: oasis	-26, 113
Ganges: double canal	+10, 65
Gargahie Fons: oasis	+45, 250
Garrhuenus: canal	-30, 30
Gehon: double canal	+15, 0
Gemmatus: mare	-38, 73
Gigantum Sinus: mare	-23, 160
Gigas: canal	-15, 155; +15, 115
Gomer Sinus: mare	-5, 230
Gordii, Nodus: oases	-5, 140
Gorgon: canal	-20, 150
Gorgonum Sinus: mare	-30, 150
Granicus (Grantcus): canal	+50, 192
Great Martian Desert (Amazonis-Arcadia-Tempe-Tharsis)	+30, 120
Gyndes: canal	+58, 220
H	
Hades I and II: canals	+40, 180
Hadriacum (Hadriaticum), Mare: mare	-35, 280
Hammonis Cornu: strait	-15, 320
Hebes Lacus: oasis	0, 85
Hebrus: canal	+65, 155
Hecates Lacus: oasis	+35, 210
Heliconius: canal	+55, 260
Hellas: plateau	-46, 295
Hellespontica Depressio: mare	-55, 340
Hellespontus	-40, 320
Helorus: canal	-33, 80
Hephaestus Lacus: oasis	+20, 234
Hercynia Silva: oasis	-10, 130
Hesperia: light area	-20, 235
Hiddekel: canal	+20, 350
Hougerius Lacus: oasis	+20, 120
Hyblaeus: canal	+30, 232
Hydrae Sinus: mare	-1, 33
Hydraotes: canal	+5, 40
Hypelaeus Fons (Hypelaei): oasis	+30, 180
I	
Iamuna (Jamuna): canal	+20, 48
Iani Fretum: strait	-10, 10
Iapygia: mare	-12, 290
Iapygia Viridis: desert	-20, 303
Ilissus: canal	+68, 130
Indus: canal	+22, 20
Ionium, Mare: mare	-25, 310
Iris: canal	-10, 105
Iseum Fons: oasis	+5, 272
Isidis Regio: desert	+20, 275
Ismenius Lacus: multi-oasis	+40, 333

Issedon: canal	
Iunonius: canal	
J	
Jamuna (Iamuna): canal	
Jordanis Fons: oasis	
Juturna Fons: oasis	
Juturna Lacus; within Juturna oasis	
Juventae Fons: oasis	
K	
Kedron: canal	
L	
Labeatis Lacus: oasis	
Labotas: canal	
Laestrygon (Laestrigon): can	
Laestrygonum Sinus: mare	
Laocoontis (Lacoontis), Nodus large oasis	
Laxartes: canal	
Lex Fons: oasis	
Libya: desert	
Lovis Lacus: oasis	
Lunae Fons: oasis	
Lunae Lacus: oasis	
Lysa Fons; within Ismenius La	
Lysis: canal	
M	
Maeotis Palus: oasis	
Mare Acidalium	
Mare Australe	
Mare Boreum	
Mare Casius (Wedge-of-Casiu	
Mare Chronium	
Mare Cimmerium	
Mare Erythraeum	
Mare Hadriacum (Hadriaticum	
Mare Ionium	
Mare Serpentis	
Mare Sirenum	
Mare Tyrrhenum	
Mareotis Lacus: oasis	
Margaritifer Sinus: mare	
Maricae Lacus: oasis	
Medusa: canal	
Medusae Fons: oasis	
Melas Lacus: oasis	
Melos: canal	
Memnonia: desert	
Meridiani Sinus (Dawes Bay;	
mare	
Meroe Insulae: desert	
Mesogaea: desert	
Midas: canal	
Moab (Eden): desert	
Moeris Lacus: double oasis	
Morpheos Lacus: oasis	
Mosa: canal	
Mountains of Mitchel	
N	
Nar: canal	
Nectar: canal	
Nectaris Palus: oasis	
Neith Regio: desert	
Nepenthes (Thoth-Nepenthes):	
Nereidum Fretum: strait	
Nesis Fons: oasis	
Nili Lacus: oasis	
Niliacus Lacus: multi-oasis	

	° Lat, ° Long
.....	+40, 80
.....	+25, 115
.....	+20, 48
.....	+33, 20
.....	+20, 333
Fons:	
.....	+20, 331
.....	-2, 65
.....	-5, 81
.....	+40, 72
.....	+5, 345
l	0, 200
.....	-22, 197
.....	+25, 250
.....	+65, 30
.....	+5, 5
.....	0, 279
.....	+18, 111
.....	-15, 290
.....	+20, 65
cus: oasis	+40, 332
.....	+18, 62
.....	+62, 115
.....	+50, 35
.....	-70, 0
.....	+63, 80
s)	+45, 270
.....	-60, 200
.....	-30, 200
.....	-25, 40
).....	-35, 280
.....	-25, 310
.....	-25, 325
.....	-35, 155
.....	-20, 250
.....	+36, 99
.....	-10, 25
.....	+5, 165
.....	-20, 140
.....	-9, 166
.....	-10, 76
.....	0, 270
.....	-20, 146
urca):	
.....	-5, 0
.....	+35, 295
.....	0, 170
.....	+54, 168
.....	+25, 350
.....	+8, 275
.....	+35, 225
.....	0, 250
.....	-73, 290
.....	+35, 235
.....	-27, 75
.....	-30, 63
.....	+38, 280
canal	+20, 265
.....	-35, 40
.....	0, 138
.....	+23, 290
.....	+30, 32

	° Lat, ° Long
Nilokeras I: canal	+32, 60
Nilokeras II: canal	+20, 50
Nilosyrtis: canal	+33, 285
Nilus: canal	+30, 80
Nix Cydonia: plateau	+46, 18
Nix Olympica	+25, 135
Nix Tanaica: plateau	+50, 50
Nixis: canal	+45, 30
Noachis: desert plateau	-30, 355
Nodus Alcyonius: large oasis	+35, 260
Nodus Gordii: oases	-5, 140
Nodus Laocoontis (Lacoontis): large oasis	+25, 250
Novem Fons (Novem Viae; Callirrhoes Sinus): oasis	+50, 19
Nubis Lacus: double oasis	+23, 260
Nymphaeum: plateau	+10, 308
O	
Ogygis Regio: desert plateau	-50, 60
Oleaster Lacus: oasis	+13, 58
Olympia: light region	+80, 210
Olympia Fons; within Meridiani Sinus: oasis	-10, 359
Olympica, Nix	+25, 135
Ophir: desert	-10, 67
Orcus: canal	+15, 180
Orontes: canal	+10, 345
Orosines: canal	-15, 304
Ortygia region	+65, 0
Oxia: desert	+30, 15
Oxia Palus: oasis	+12, 18
Oxus: canal	+23, 13
P	
Pallas: canal	+3, 265
Pambotis Lacus: oasis	+10, 212
Pan: canal	+44, 240
Panchaia region	+65, 220
Pandorae Fretum: strait	-20, 345
Parcae: canal	-21, 125
Pavonis Lacus: oasis	+12, 118
Peneus: canal	-48, 290
Phaethontis: desert plateau	-45, 150
Phasis: canal	-35, 112
Phison (Phison-Vexillum): double canal.	+20, 320
Phlegethon: canal	+40, 130
Phlegra: desert	+50, 190
Phoenicis Lacus: oasis	-12, 111
Phrygius Lacus: oasis	+5, 151
Phryxus: canal	+25, 50
Pierius: canal	+58, 315
Poras: canal	-20, 235
Poros: canal	-5, 320
Propontis I: oasis	+45, 180
Propontis II: oasis	+55, 179
Propontis Quadrangle: oasis complex...	+50, 170
Protei Lacus: oasis	-30, 40
Protonilus: canal	+42, 320
Pyriphlegethon: canal	+30, 140
Pyrrhae Regio: desert	-18, 30
R	
Rhesus: canal	-2, 288
Rhyndacus: canal	+62, 198
S	
Sabaeus Sinus: mare	-10, 330
Saus: canal	-10, 180
Scamander: canal	-47, 200
Scandia: desert	+64, 145
Scythes (Silia): canal	+68, 75
Semiramidis Lacus; within Sirbonis	

	° Lat, ° Long
Palus: oasis	+10, 335
Serpentis, Mare: mare	-25, 325
Sigeus Portus: double oasis	-5, 335
Silia (Scythes): canal	+68, 75
Siloe Fons: oasis	+30, 10
Simois: canal	-50, 165
Sirbonis Lacus; within Sirbonis Palus: oasis	+10, 331
Sirbonis Palus: oasis	+10, 333
Sirenius: canal	-20, 129
Sirenum, Mare: mare	-35, 155
Sirenum Sinus: mare	-30, 125
Sirii Fons: oasis	-22, 115
Sitacus: canal	+15, 345
Sithonius Lacus: oasis	+55, 235
Solis Lacus (Eye-of-Mars): multi-oasis.	-28, 90
Strongyle Insula	-20, 310
Stygis Lacus: oasis	+30, 198
Stymphalius Lacus: oasis	+55, 202
Styx: canal	+34, 195
Symplegades Insulae: desert	-27, 195
Syrtis Major: mare	+10, 290
Syrtis Minor: mare	-5, 255
T	
Tanaica, Nix: plateau	+50, 50
Tanais: canal	+53, 50
Tartarus: canal	0, 185
Tempe: desert	+40, 70
Tempes: canal	+45, 155
Tharsis: desert	+10, 100
Thaumasia (Eye-of-Mars): desert	-30, 90
Thermodon: canal	-50, 145
Thoana Palus: oasis	+33, 250
Thoth (Thoth-Nepenthes): canal	+20, 265
Thyle I region	-65, 150
Thyle II region	-65, 230
Thymiamata (Aram Regio): desert	+5, 12
Tiphys Fretum: strait	-57, 260
Titan: canal	+20, 175
Titanum Sinus: mare	-23, 170
Tithonius: canal	-20, 92
Tithonius Lacus: oasis	-8, 95
Triton: oasis	+7, 265
Tritonis Sinus: mare	-5, 245
Trivium Charontis: multi-oasis	+20, 200
Typhon: canal	+5, 320
Typhonii Sinus: mare	-2, 314
Tyrrhenum, Mare: mare	-20, 250
U	
Ulysses: canal	0, 112
Umbra: mare	+45, 290
Uranius: canal	+20, 85
Utopia region	+62, 250
V	
Vexillum (Phison-Vexillum): double canal	+35, 310
W	
Wedge-of-Casius (Mare Casius): mare..	+45, 270
X	
Xanthe: desert	+18, 50
Xanthus: canal	-45, 233
Y	
Yaonis Fretum: strait	-40, 315
Z	
Zea Lacus: oasis	-48, 290
Zephyria: desert	-10, 190

Notes:

Coordinates listed here for Martian features indicate the approximate center of the feature. The table is an aid in generally locating a feature but should not be considered a source of exact areographic coordinates.

Conventionally, the terms suggesting water are assigned to the darker Martian markings, i.e., Fons (spring), Fretum (strait), Lacus (lake), Mare (sea), Palus (swamp), Portus (harbor), and Sinus (gulf). Those terms applicable to land are usually used for the lighter areas and the bright reddish or yellowish areas, i.e., Insula (island), Promontorium (cape), and Nix (white). Other terms include Depressio (depression) and Regio (region).

Fig. 11. Map and table of Martian place-names and their locations. Map is for use with Figs. 8 thru 10.

BIBLIOGRAPHY

Ashbrook, J., 1958, The new IAU nomenclature for Mars: Sky and Telescope, v.XVIII, n.1, p.23-25.

Capen, C.F., 1966, The Mars 1964-1965 apparition: Pasadena, Calif., Jet Propulsion Laboratory, Tech.Rep.32-990.

Chapanis, A., 1965, Color names for color space: Am.Sci., v.53, p.327-346.

de Vaucouleurs, G., 1954, Physics of the planet Mars: London, Faber and Faber.

_____, 1961a, Sources of areographic coordinates 1909-1954: Harvard College Obs., Sci.Rep.No.2, ARDC Contract AF19(604)-7461, AFCRL 257.

_____, 1961b, Areographic coordinates for 1958: Harvard College Obs., Sci.Rep.No.4, ARDC Contract AF19(604)-7461, AFCRL 818.

_____, 1962, Precision mapping of Mars: La Physique des Planetes, Colloque International Universite de Liege.

_____, 1965, Charting the Martian surface: Sky and Telescope, v.XXX, n.4, p.196-201.

Focas, J.H., 1962, Seasonal evolution of the fine structure of the dark areas of Mars: J.Planet.Space Sci., v.9, p.371-381.

Ley, W., 1963, Watchers of the skies: New York, Viking Press.

Maginni, M., 1939, Il planeta Marte: Milan, Italy, Ulrico Hoepli, Editore-Librario della Real Casa, 400 p.

Pollack, J.B., Greenberg, E.H., and Sagan, C., 1967, A statistical analysis of the Martian wave of darkening and related phenomena: J.Planet.Space Sci., v.15, p.817-824.

Sagan, C., and Houghey, J.W., 1966, Launch opportunities and seasonal activity on Mars, in Biology and the exploration of Mars; Pettendrigh, C.S., Vishniac, W., and Pearman, J.P.T., Editors: Wash., D.C., Natl.Acad.Sci.Res.Council, Pub.1296.

Schiaparelli, G.V., 1929, Le opere di G.V.Schiaparelli, Tomo I: Milan, Italy, Ulrico Hoepli.

Schmidt, I., 1959, Visual problems in observing the planet Mars: Proc.Lunar Planet.Exploration Coll., v.1, n.6, p.19-22.

Schorn, R.A., et al., 1967, High dispersion spectroscopic observations of Mars, II. The water-vapor variations: Astrophys.J., v.147, p.743-752.

Slipher, E.C., 1962, Mars, the photographic story: Cambridge, Mass., Sky Publishing Corp., and Flagstaff, Ariz., Northland Press.

SECTION 5 CONTENTS

5. ATMOSPHERE

Introduction 5

5.1 Atmospheric Composition

Data Summary 1
Observed Constituents 1
Assumed Constituents 2
Possible Constituents 2
Discussion 3
Observed Constituents 3
Carbon Dioxide 3
Water Vapor 5
Carbon Monoxide 6
Sinton Bands 7
Assumed Constituents 7
Argon 7
Molecular Nitrogen 7
Atomic Oxygen 7
Molecular Oxygen 8
Ozone 8
Possible Constituents 8
Oxides of Nitrogen 8
Methane and Related Compounds 9
Ammonia 9
Carbonyl Sulfide 9
Cross References 10
Bibliography 11

5.2 Surface Pressure

Data Summary 1
Discussion 1
Spectroscopic Results 1
Occultation Experiment Results 3
Methods of Surface Pressure Determination 4
Spectroscopy 4
Occultation 8
Photometry and Polarimetry 9
Conclusions 10
Cross References 12
Bibliography 13

5.3 Lower Atmosphere

Data Summary 1
Discussion 1
Layers of the Lower Atmosphere 1
Physics of the Lower Atmosphere 2
Troposphere 2
Stratosphere and Mesosphere 4
Contemporary Models of the Lower Atmosphere 5
Types of Models 5
Convective 5
Radiative 6
Convective-Radiative 6
Lower Atmosphere Models I, II, and III 8
Conclusions 9
Cross References 21
Bibliography 22

Figures
1. Table of ground air temperatures for Mars referred to northern seasons 10
2. Lower Atmosphere Model I for ground air temperatures 180, 190, 200, and 210°K 11
3. Lower Atmosphere Model I for ground air temperatures 220, 230, 240, and 250°K 12
4. Lower Atmosphere Model I for ground air temperatures 270 and 290°K 13
5. Lower Atmosphere Model II for ground air temperatures 180, 190, 200, and 210°K 14
6. Lower Atmosphere Model II for ground air temperatures 220, 230, 240, and 250°K 15
7. Lower Atmosphere Model II for ground air temperatures 270 and 290°K 16
8. Lower Atmosphere Model III for ground air temperatures 180, 190, 200, and 210°K 17
9. Lower Atmosphere Model III for ground air temperatures 220, 230, 240, and 250°K 18
10. Lower Atmosphere Model III for ground air temperatures 270 and 290°K 19
11. Table of contemporary models for lower atmosphere of Mars 20

5.4 Upper Atmosphere

Data Summary 1
Discussion 1
Layers of the Upper Atmosphere 1
Physics of the Upper Atmosphere 2
Photodissociation Region 2
Ionosphere 3
Ionization Processes 4
Thermal Processes 6

5.4 (cont'd)

Contemporary Models of the Upper Atmosphere 8
Preliminary E-Model 8
F_1-Model 9
F_2-Model 11
Conclusions 13
Cross References 20
Bibliography 21

Figures

1. Upper Atmosphere F_1-Model: table of calculated neutral number densities and temperatures vs. altitude 14
2. Upper Atmosphere F_1-Model: ion and electron density vs. altitude 14
3. Upper Atmosphere F_1-Model: temperature vs. altitude 15
4. Upper Atmosphere F_1-Model: neutral density vs. altitude 16
5. Upper Atmosphere F_1-Model: profiles of photoionization rate of neutral constituents 16
6. Upper Atmosphere F_2-Model: table of calculated neutral and electronic number densities and temperature vs. altitude 17
7. Upper Atmosphere F_2-Model: number density of electronic and neutral constituents vs. altitude 17
8. Upper Atmosphere F_2-Model: temperature vs. altitude 17
9. Table of significant reactions in the Martian ionosphere for a pure CO_2 lower atmosphere 18
10. Table of incident solar flux densities at Mars and absorption cross sections for selected wavelength regions 18
11. Table of models for upper atmosphere of Mars based on Mariner IV results 19

5. ATMOSPHERE

INTRODUCTION

That Mars has an atmosphere was well appreciated by astronomers of the 19th century, who saw a disk with fuzzy edges, brilliant polar caps that came and went, and even what appeared to be clouds or haze that at times obscured the surface. By the turn of the century the great Princeton astronomer, Charles A. Young, had authored a standard textbook which included interpretations of planetary atmospheres. He made the following statement which presents the best opinion available at the time, although by modern standards the reasoning is not exactly flawless:

> "This (Mars) atmosphere, however, contrary to opinions formerly held, is probably much less dense than that of the Earth, the low density being indicated by the infrequency of clouds and of other atmospheric phenomena familiar to us upon the Earth, to say nothing of the fact that, since the planet's superficial gravity is less than two fifths of the force of gravity on the Earth, a dense atmosphere would be impossible."*

The atmosphere of a planet is an immensely complex thing, an order of magnitude more complex than an ordinary hot stellar atmosphere where only atoms need be considered. (Some molecules become important in the coolest stars.) Not only does a planetary atmosphere consist largely of molecules, but even matter in liquid or solid state may be present. Furthermore, a planetary atmosphere is in a perpetually nonisotropic radiation field, as insolation varies with planetary rotation and revolution. We have really begun to understand the Earth's atmosphere only as it has been penetrated by aircraft, balloons, and rockets. If we demand perfect accuracy, a "simple" 24-hr weather prediction for a terrestrial city is still beyond our practical capabilities, due to lack of sufficient radiosonde data to properly delineate boundary conditions for the problem and to lack of electronic computers with sufficient speed to solve the equations involved even at the rate at which the physical phenomena are occurring.

Fortunately the real engineering needs of our space program are not so great as our scientific curiosity. In the pages that follow an attempt is made to define those gross atmospheric parameters most needed for a successful entry into the Martian atmosphere and a landing (intact) on the Martian surface. These data will be refined as additional observational and theoretical results become available. Meanwhile, an attempt is made to assess realistically the probable errors in the results presented.

---

*Young, C. A., 1902, p.361-371 in Manual of astronomy: Mars: Boston, Mass., Ginn and Co.

5.1 ATMOSPHERIC COMPOSITION

DATA SUMMARY

Observed Constituents

Carbon dioxide, water vapor, and carbon monoxide have been observed in the atmosphere of Mars. (The source of an unidentified 3.45μ band observed in a spectrometer tracing of Mars has not yet been determined.) Carbon dioxide seems to be the main constituent and could constitute more than 90% or as little as 50% of the Martian atmosphere. A significant amount of the remainder may be argon or possibly nitrogen, although there is no observed evidence to support this assumption. The abundance of each of the observed constituents is given below.

Carbon dioxide, CO_2	Abundance may be variable.
Best value	90 ±25 m atm. (The quoted error is a probable error.) 90 m atm = 6.7 mb = 5.1 torr.
Extreme possibilities	Best value of CO_2 abundance could conceivably vary by half, from 45 to 135 m atm.
Water vapor, H_2O	Amount and distribution are variable.
Best model	H_2O begins to appear over a melting polar cap, reaches a concentration of perhaps 15 μ of precipitable water, and starts to move toward the equator. A concentration of perhaps 20 to 30 μ is reached over most of the planet. It starts to drop as a new polar cap begins to form in the opposite hemisphere, soon becoming undetectable (<10 μ).
Extreme possibilities:	
Probability <5%	Apparent H_2O detection may be entirely due to coincidences and/or experimental error.
Probability ≈50%	Distribution may not be as given in best model.
Probability <5%	H_2O concentration may at times be >100 μ of precipitable water.
Carbon monoxide, CO	Best value is 10 cm atm. No error analysis is yet available.
Sinton Bands	3.45μ band unidentified and may not be real. 3.69μ and 3.58μ bands due to telluric HDO and do not originate on Mars.

Assumed Constituents

The assumption that a significant amount of the Martian atmosphere other than carbon dioxide may be argon or possibly nitrogen is based on terrestrial analogy. The existence of atomic oxygen, molecular oxygen, and ozone is assumed based on photodissociation and photochemical theory. There is no observed evidence of the presence of the following constituents in the Martian atmosphere. Theoretical abundance values are given.

Argon, Ar	<40 m atm, theoretical upper limit.
Molecular nitrogen, N_2	<20 m atm.
Atomic oxygen, O	No estimate. Dominates in exosphere.
Molecular oxygen, O_2	<70 cm atm; possibly ~10 μ atm according to theoretical calculations.
Ozone, O_3	Possibly ~0.1 μ atm according to theoretical calculations.

Possible Constituents

Attempts to positively identify oxides of nitrogen, methane and/or methyl compounds, formaldehyde, ammonia, and carbonyl sulphide in the Martian atmosphere have been unsuccessful. Spectroscopic upper limits on the abundance of these possible constituents have been set and are given below. It must be stressed, however, that there is no reliable observational or theoretical evidence affirming the existence of <u>any</u> oxide of nitrogen on Mars.

Oxides of nitrogen:	Best upper limit	Conservative upper limit
Nitrogen dioxide, NO_2	10 μ atm	100 μ atm
Nitrogen dioxide, N_2O_4	10 μ atm (theoretical)	100 μ atm
Nitric oxide, NO	30 cm atm	200 cm atm
Nitrous oxide, N_2O	1 mm atm	1 cm atm
Nitrous acid, HNO_2	2 mm atm (theoretical)	2 cm atm
Methane, CH_4	<1 mm atm	
Formaldehyde, HCHO	<3 mm atm	
Ammonia, NH_3	<1 mm atm	
Carbonyl sulfide, COS	<2 mm atm	

DISCUSSION

Observed Constituents

Carbon Dioxide [1*]

Carbon dioxide was the first (and for may years the only) gas detected spectroscopically in the Martian atmosphere. Kuiper (1952) found the 1.57μ and 1.60μ bands on a spectrometer tracing of Mars made October 7, 1947, and added the discovery of the 1.96μ, 2.01μ, and 2.06μ bands when Mars was near opposition in February, 1948.[2] These bands are all very strong and are present in both Martian and terrestrial atmospheres.

Kuiper's initial attempt to give an abundance took no account of pressure differences between Martian and terrestrial atmospheres and was quite inadequate. The disentangling of the superimposed absorptions was handled more properly by Grandjean and Goody (1955), who used Kuiper's data to derive a pressure-concentration product $P_s^2 C_v = 1.6 \pm 0.5 \times 10^2$ mb^2. A concentration cannot be derived from a strong band alone.[3] Using the then available surface pressure figures, Grandjean and Goody found the CO_2 concentration to be about 2% by volume. (Using modern values for the pressure,[4] the concentration becomes roughly 150%.) Considering the relatively poor resolution in these pioneering infrared spectra and the fact that the theory used made no allowance for such refinements as temperature differences or the proper individual damping constants for each atmosphere, the result is excellent, giving the right order of magnitude.

In 1963, while searching for (and finding) water vapor in the Martian atmosphere, Spinrad, Münch, and Kaplan discovered on the same plate a number of faint spectral lines in the 8700-Å region which are not present in solar spectra (Kaplan et al., 1964). These proved to be lines of the very weak $5\nu_3$ band of CO_2, a band so weak that it should not have appeared at all unless the CO_2 abundance of Mars were much higher than previously thought by astronomers. Such proved to be the case, and Kaplan, Münch, and Spinrad derived a CO_2 abundance for Mars of 50 ±20 m atm assuming a 200°K Martian temperature and based upon that one plate (Kaplan et al., 1964). A detailed calibration by Owen of the same plate corrected the Kaplan, Münch, and Spinrad air-mass function and allowed for doubling back of the band,[5] thereby resulting in a revised abundance value of 46 ±20 m atm (Owen, 1964). Most of the large probable error arose from the uncertainty in the measurement of the one plate of Mars upon which all of the elaborate theory depended.

Several groups made serious attempts to determine CO_2 abundance during the 1964-1965 Mars apparition. Their results are presented at the top of the following page. The errors quoted are estimated by the individual authors to be the total probable error including known sources of systematic error as well as the random errors of measurement.

---

*See page 10 for list of cross references.

CO_2 abundance, m atm	Technique and amount of data	Observers
68 ±26	Photoelectric scan of 1.05μ band on 60-in. McMath solar telescope; eight "blocks" of data used, taken March 17 through May 21, 1965.	Belton et al., 1966
65 ±20	Photographic on 82-in. Struve reflector; four plates of 8700-Å band at 4.2 Å/mm and one plate of 1.05μ band at 10.7 Å/mm, all taken March 13 through 19, 1965.	Owen, 1966
90 ±27	Photographic of 8700-Å band; eight plates at 4.1 Å/mm with 82-in. Struve reflector from December 24, 1964, through May 24, 1965; five plates at 4.1 Å/mm with 120-in. Lick reflector from February 18 through June 10, 1965.	Spinrad et al., 1966

Work has continued during the 1967 apparition of Mars. A major advance has been the first application of Fabry-Perot interference spectrometry to the problem. (For a general discussion of the technique see Vaughan, 1967.) Using the very high resolution available with a Fabry-Perot instrument used in conjunction with a coudé spectrograph (as premonochromator), Münch (1967) recently reported an abundance of 110 m atm of CO_2. With perhaps three times the resolution of previous observations, this result should be of relatively high accuracy.

The work of Leovy (1966a, 1966b), which showed that the temperature in the Martian polar regions might be low enough to freeze CO_2,[6] and the work of Leighton and Murray (1966), implying this indeed to be the case, have raised the question of whether the CO_2 abundance in the Martian atmosphere might be variable (and if so, how variable?). That question cannot yet be answered positively, but future Earth-based work including additional spectrography, temperature measurement of the polar caps when their aspect is satisfactory, and reflection spectra of the caps themselves should solve the problem.

Question has been raised (Hanselman, 1965) of the possibility of variation in surface pressure from equator to pole, resulting from the geometric surface of Mars not being an equipotential surface.[7] Spinrad et al. (1966) suggest they "could probably detect a deviation from concentric spheroids describing the atmosphere and planetary surface amounting to more than one scale height (~9 km)." Schorn (1967) states that his best new plates indicate at least as much CO_2 at the equator as at the poles rather than perhaps 15% as much as might be suggested if the apparent optical flattening were a true Martian surface. No variation of surface pressure with latitude should be considered unless new evidence is forthcoming to indicate such a need.

Weak-line theory is very straightforward and perfectly understood.[5] New laboratory calibrations of absolute line strength have been carried out by three groups, two working on the λ8700 band (Rank et al., 1964; Boese et al., 1965) and one on the λ10,500 band (Burch et al., 1965). The λ8700-band workers agree very closely, with no more than 10% difference in their values. All parties were fully aware of the small corrections for overlapping lines and for temperatures (all used roughly 200°K) (see Belton et al., 1966, for minor difference). As much care as possible was taken in deriving the radiation's mean path length in the Martian atmosphere. The probable errors quoted in the tabulation on page 4 should therefore be considered realistic ones. The main sources contributing to these errors are the actual observations and their reduction—the difficulty in measuring the equivalent width of very weak noisy lines.

In photographic work the personal choice of where to draw the line representing the solar continuum is a major source of error. In effect such a choice must also be made for photoelectric work, although the choice may then be more mental than visual. Improvement will come from additional observations to add to the statistics and from improved techniques. The most important improvements in technique include the application of Fabry-Perot spectrometry and especially of the Connes-type Michelson interferometry to the problem. The latter technique is currently being applied by P. Connes, J. Connes, Kaplan, and Benedict, but results are not yet available.

The value quoted on page 1 accepts the complete validity and error probabilities of the 1964-1965 work on CO_2 abundance. The 1967 Fabry-Perot result is averaged in at half the total weight of the other observations with the probable error remaining the same as before its addition. The one major doubt in this work is the possibility of a real seasonal variation in abundance of CO_2. The worst case quoted allows for such a possibility since the atmosphere certainly never completely disappears and observations have also been made when both caps were small.

Water Vapor

The question of the existence of water vapor in the atmosphere of Mars is a classic one in planetary spectrography. Pioneer studies were carried out at Lowell and Lick Observatories shortly after the turn of the century and at times yielded apparently positive results, probably due to inadequate equipment and technique. Adams and his co-workers at Mt. Wilson gave considerable attention to the problem between 1925 and 1943, at times with apparently positive results but always with large probable errors. A review of these efforts is given by de Vaucouleurs (1954). More recent unsuccessful attempts at H_2O detection are reviewed by and include that of Spinrad and Richardson (1963).

The 1962-1963 apparition of Mars resulted in two independent reports of successful H_2O detection on Mars. Spinrad, Münch, and Kaplan, working at the 100-in. Mt. Wilson reflector, obtained a spectrogram of the 8200-Å water band at a dispersion of 5.6 Å/mm. It showed 11 lines with satellites at the doppler displacement appropriate to Mars, several of them apparently free of blends with other terrestrial or solar lines (Spinrad et al., 1963). Detailed analysis gave the abundance as 14 ±7 μ of precipitable water. The analysis was based on

about one-third of the length of the lines, namely, that part covering the polar region (Kaplan et al., 1964). Working with a 50-cm (20-in.) reflector at the scientific station on the 3600-m (12,000-ft) Jungfraujoch in Switzerland, Dollfus used a Lyot filter and half-wave plate to alternately isolate the 1.4μ band and two adjacent bands. He then subtracted the terrestrial component as determined from measurements of the Moon and other objects. His result was an average over the planet of 200 μ of precipitable water (Dollfus, 1963). With recalibration the value from the same observations was later reduced to 45 μ (Dollfus, 1965).

An intensive observing program was carried out by Schorn et al. during the 1964-1965 apparition of Mars in an attempt to refine the previous result (Schorn et al., 1967). Over a 9-month period, 19 well-exposed spectrographic plates were obtained at McDonald and Lick Observatories at dispersions of 4.09 and 4.14 Å/mm, respectively. Those taken from September through mid-November, 1964, showed no water vapor; those taken during late December and January indicated about 15 μ of precipitable water in the northern hemisphere only. The season was late spring in the north on Mars.[8] Further measurements were impossible until May due to insufficient doppler shift (small relative radial velocity) around opposition, which occurred during March. During May and June, 10 to 25 μ of water were detected in both hemispheres, perhaps more of it in the southern hemisphere than the northern. The season was early summer in the north. A new series of observations is being carried out during the 1967 apparition by Schorn and co-workers. Much future work is needed.

Observation of water vapor on Mars is extremely difficult, and the quantitative results very uncertain. The doppler-shift technique is at least potentially more accurate than the gross-band-strength technique used by Dollfus, which is dependent upon the difference of two quantities similar in magnitude, as well as upon a difficult calibration. Sufficient care was taken by the doppler-method experimenters in avoiding confusion of weak water lines with weak Fraunhofer and/or terrestrial lines to make the identification of water vapor seem relatively secure. The intrinsic nonlinearity of the photographic plate and the difficulty of measuring the equivalent widths of lines as weak as the Martian water lines leave the quantitative results very much in question, particularly those results having to do with distribution in the atmosphere as a function of season. It is difficult to ignore the possibility that distribution results would not have become available without the guidance of prior knowledge of the Martian seasons. It must be emphasized that the meager amount of water in the atmosphere tells us little about the possibility of subsurface H_2O (water or ice) on Mars.[9]

Carbon Monoxide

Although small amounts of carbon monoxide could be predicted for the Martian atmosphere from the dissociation of CO_2, no detection had been made nor even seemed possible until the practical development of instrumentation for Fourier spectroscopy by J. and P. Connes (1966). Working with spectra taken by the Connes, Kaplan has now made positive identification of CO on Mars (Kaplan, 1967b). His very rough preliminary abundance estimate is that the concentration is one part in 10^3, or roughly 10 cm atm; the CO is almost certainly well mixed throughout the atmosphere, not just confined to a layer.

Sinton Bands

In 1957 Sinton reported the presence of three bands at 3.43μ, 3.56μ, and 3.67μ (later revised to 3.45μ, 3.58μ, and 3.69μ) in a spectrometer tracing of Mars made with the 200-in. Palomar reflector. These were generally attributed to some compound with a C-H bond, although such interpretations were far from completely satisfactory (Rea et al., 1963). Recently, rather positive identification with telluric HDO has been made of the 3.58μ and 3.69μ features (Rea et al., 1965). The source of the 3.45μ band, the weakest of the three, remains unknown. Future work using the techniques of Fourier spectroscopy should decide if this band really exists in the Martian atmosphere and may perhaps reveal enough structure to facilitate identification.

Assumed Constituents

Argon

Argon has no spectral lines in regions of the spectrum accessible from the Earth's surface, yet there has been a general assumption that some argon should be present in the atmosphere of Mars. On Earth argon has resulted mainly from decay of potassium 40.[10] If Mars has undergone the same process of differentiation and surface concentration as the Earth, one might expect to find an argon abundance in the Martian atmosphere proportional to its surface area relative to the Earth. The surface area of Mars is roughly 28% of that of Earth. Since Earth has about 9.5 mb of argon, Mars might be expected to have 2.5 mb. In fact, we have no certain knowledge of the history of the crust of Mars. It is generally assumed today that whatever part of the Martian atmosphere is not CO_2 is mainly argon; this is not unreasonable.

Molecular Nitrogen

At one time molecular nitrogen was thought to be the major constituent of the Martian atmosphere. Like argon, N_2 has no detectable absorption features in the accessible spectrum, so this was simply a guess by terrestrial analogy. As relatively accurate surface pressure and CO_2 abundance have become known, it has been realized that there is no room left for any large amount of nitrogen. The 1965 occultation measurement by Mariner IV has suggested doubt that nitrogen can even constitute a large fraction of that lesser part of the atmosphere which is not CO_2 (Kliore et al., 1966). Geophysical theory suggests there should be N_2 on Mars. The best judgment based on observation is that it very probably constitutes less than 20% of the Martian atmosphere and could constitute much less.

Atomic Oxygen

In photodissociation of CO_2 one atom of atomic oxygen is created for each molecule of carbon monoxide. Atomic oxygen is so extremely reactive, however, that only a very small steady state abundance can exist in the chemosphere where it is created. It may be the chief constituent of the Martian exosphere, where it would diffuse by virtue of being the lightest gas that could not easily escape from Mars, and where it would remain without reacting because the low density would result in few collisions.[11]

Molecular Oxygen

The search for molecular oxygen on Mars is second only to that for water vapor in age and expended effort. The searches of Adams, Dunham, and St. John at Mt. Wilson during the period 1926-1934 have been summarized by Dunham (1952). The results of the searches were negative. A more recent search by Kaplan, Münch, and Spinrad was also negative and resulted in an upper limit of 70 cm atm (Kaplan et al., 1964). It is known from photochemical theory that at least some O_2 must be present in the atmosphere of Mars. If Martian O_2 is only that amount present as a result of the photochemical steady state,[11] then the abundance may be four to five orders of magnitude less than the current upper limit set by the lack of spectroscopic detection. Geophysical theory indicates that most oxygen in the Earth's atmosphere is biotic in origin. Therefore, the low abundance on Mars is not too surprising.

Ozone

Some ozone must also be formed as a result of atmospheric photochemical interactions.[11] Unlike the terrestrial case, O_3 may occur generally in the atmosphere below perhaps 30-km altitude rather than being concentrated in a layer near 40 km (as on Earth) or higher (Marmo et al., 1965). The abundance, however, would be one to two orders of magnitude lower than even the very low O_2 abundance (Marmo et al., 1965). Evans' rocket study of Mars in the ultraviolet seems to indicate considerable transparency from 2400 to 3000 Å, a definite confirmation of very low ozone abundance (Evans, 1965).[12]

Possible Constituents

Oxides of Nitrogen

In 1960, Kiess, Karrer, and Kiess presented "A New Interpretation of Martian Phenomena," a claim that many observational results of long standing were due to the presence of the various oxides of nitrogen on Mars. That paper contained no new observational results, being simply a rediscussion of previous results of others. Virtually each statement in the paper has since proved untenable. The paper is mentioned because it unfortunately resulted in a concern about nitrogen oxides which has not been dispelled.

Sinton (1961), Kaplan (1961), and Huang (1961) immediately objected to Kiess, Karrer, and Kiess' work, Sinton and Kaplan on observational grounds and Huang on theoretical grounds. In an attempt at rebuttal Kiess, Karrer, and Kiess (1963) showed a section of microphotometer tracings of Mars and the Sun. This proved chiefly that their Martian spectrogram exhibited a very poor signal-to-noise ratio. The 1963 paper also contained a statement that 1 to 2 mm atm was sufficient NO_2 to account for many of the observed effects. Meanwhile, a new observational study by Spinrad set an upper limit of 1 mm atm for the NO_2 abundance in the Martian atmosphere (Spinrad, 1963). This was later reduced to an upper limit of 8 μ atm by Marshall (1964). Another detailed observational study by O'Leary indicated very conservatively that the upper limit of NO_2 abundance was no more than 0.1 mm atm (O'Leary, 1965). Still another study by Owen indicates Marshall's value is on very firm ground (Owen, 1966).

Kuiper (1964) has made spectrographic searches for N_2O and NO; these are the bases of the quoted best upper limits of these substances. Sagan et al. (1965) set theoretical limits on NO and HNO_2 based on observed NO_2 limits. They also set limits on N_2O_4 based on the well-known relationship between monomer (NO_2) and dimer (N_2O_4). Very recently Lippincott et al. (1967) performed a thermodynamic equilibrium calculation with a large assumed N_2 abundance and found all oxides of nitrogen to be several orders of magnitude lower in abundance than the best upper limits given here. For a cool, relatively tenuous, transparent atmosphere such as that present on Mars, equilibrium calculations are less convincing than they might otherwise be, nonequilibrium situations being a common possibility.

Oxides of nitrogen on Mars, if present, certainly do not appear to exist in sufficient quantity to be of biological significance or of gross "mechanical" significance, i.e., having significant effect on entry mechanics, heat transfer, etc. They could possibly play a significant role in ionospheric structure, perhaps through formation and dissociative recombination of NO^+.[13] Future interferometric studies will considerably refine all of these results.

Methane and Related Compounds

The possible existence of methane and/or various methyl compounds has been discussed by Kaplan (1967a) based upon Fourier spectroscopy of Mars, and his current feeling is that confirmation is still needed to assure proper identification of the features in question. Kuiper (1964) has placed upper limits of 1 mm atm and 3 mm atm on the Martian methane and formaldehyde abundance, respectively.

Ammonia

Kuiper (1964) has tested for ammonia in three wavelength regions: the 1.515μ, 1.98μ, and 2.2 to 2.3μ bands. He places an upper limit of 1 mm atm on the ammonia abundance.

Carbonyl Sulfide

Kuiper (1964) has looked for carbonyl sulfide in the very strong band at 2.44μ. The abundance, if any, must be much less than 2 mm atm.

CROSS REFERENCES

The specific section number, subject, and page number to which the reader is referred is given below.

Cross Reference	Section and Subject
[1] Carbon dioxide in the atmosphere	3.4.....Carbon dioxide on the surface (discussion), p.4.
[2] Opposition	1.....Oppositions (figures), p.12, 13.
[3] Strong-band data and CO_2 concentration	5.2.....Surface pressure—spectroscopic results (discussion), p.1-3.
[4] Surface pressure values	5.2.....Surface pressure (data summary), p.1.
[5] Weak CO_2 band and weak-line theory	5.2.....Spectroscopy (discussion), p.6.
[6] Temperature in the polar regions	3.1.....Surface temperatures (data summary), p.1; Martian surface temperature (figure), p.8. 5.3.....Ground air temperatures (figure), p.10.
[7] Geometric surface of Mars	2.....Dynamical flattening (discussion), p.4.
[8] Martian seasons	1.....Calendar of Earth-Mars equivalent dates for 1964 and 1965 (figure), p.17. 4.2.....Seasonal activity maps (figures), p.19-25.
[9] Surface and subsurface H_2O (water or ice)	3.4.....Water on the surface (discussion), p.3-4. 3.5.....Freeze-thaw processes (discussion), p.10, 11.
[10] Argon and potassium 40—planetary differentiation and surface concentration	3.4.....Terrestrial and lunar surface compositional data (figure), p.8. 2.....Interior models (discussion), p.6-9.
[11] Atomic oxygen, molecular oxygen, and ozone	5.4.....Photodissociation region (discussion), p.2, 3.
[12] Transparency in the ultraviolet	6.....Absorption in the Martian atmosphere (discussion), p.6.
[13] Formation and dissociative recombination of NO^+	5.4.....Ionization processes (discussion), p.4-6; Upper Atmosphere Preliminary E-Model (discussion), p.8, 9.

BIBLIOGRAPHY

Belton, M.J.S., and Hunten, D.M., 1966, The abundance and temperature of CO_2 in the Martian atmosphere: Astrophys.J., v.145, p.454-467.

Boese, R.W., Miller, J.H., and Inn, E.C.Y., 1965, The $5\nu_3$ band of carbon dioxide R-branch integrated intensity: Astrophys.J., v.142, p.1272-1273.

Burch, D.E., Gryvnak, D.A., and Patty, R.R., 1965, Absorption by CO_2 between 8000 and 10,000 cm^{-1} (1-1.25 micron region): Newport Beach, Calif., Aeronutronic Div. of Philco-Ford Corp., Pub.U-3200.

Connes, J., and Connes, P., 1966, Near-infrared planetary spectra by Fourier spectroscopy, I.Instruments and results: J.Opt.Soc.Am., v.56, p.896-910.

de Vaucouleurs, G., 1954, The spectrographic quest for water vapor, Chapter III in Physics of the planet Mars, Part III: London, Faber and Faber.

Dollfus, A., 1963, Mesure de la quantité de vapour d'eau contenue dans l'atmosphere de la planete Mars: CR Acad.Sci., v.256, p.3009-3011.

_____, 1965, Analyse des mesures de la quantité de vapour d'eau dans l'atmosphere de la planete Mars: CR Acad.Sci., v.261, p.1603-1606.

Dunham, T., 1952, Spectroscopic observations of the planets at Mt. Wilson, Chapter XI in The atmospheres of the Earth and planets, Rev.Edition; Kuiper, G.P., Editor: Chicago, U.of Chicago Press.

Evans, D.C., 1965, Ultraviolet reflectivity of Mars: Science, v.149, p.969-972.

Grandjean, J., and Goody, R.M., 1955, The concentration of carbon dioxide in the atmosphere of Mars: Astrophys.J., v.121, p.548-552.

Hanselman, R.B., 1965, Effect of Martian oblateness on atmospheric pressure distribution: Avco/Rad.

Huang, S., 1961, The problem of nitrogen peroxide in the atmospheres of planets: Pub.Astron.Soc.Pacific, v.73, p.446-451.

Kaplan, L.D., 1961, On the Kiess, Karrer, and Kiess interpretation of planetary spectra, p.62-64 in Quarterly technical progress rep. (3): Santa Monica, Calif., RAND Corp., RM-2769-JPL.

_____, 1967a: Conference, "The surface of Mars," New York, Goddard Institute for Space Studies, Feb.2-4, 1967.

_____, 1967b, (Pasadena, Calif., Jet Propulsion Laboratory): private communication.

Kaplan, L.D., Münch, G., and Spinrad, H., 1964, An analysis of the spectrum of Mars: Astrophys.J., v.139, p.1-15.

Kiess, C.C., Karrer, S., and Kiess, H.K., 1960, A new interpretation of Martian phenomena: Pub.Astron.Soc.Pacific, v.72, p.256-267.

_____, 1963, Oxides of nitrogen in the Martian atmosphere: Pub.Astron.Soc.Pacific, v.75, p.50-60.

Kliore, A.J., Cain, D.L., Levy, G.S., Eshleman, V.R., Fjeldbo, G., and Drake, F.D., 1966, Preliminary results of the Mariner IV occultation measurement of the atmosphere of Mars, p.257-266 in Proceedings of the Caltech-JPL lunar and planetary conference, September 13-18, 1965: Pasadena, Calif., Jet Propulsion Laboratory, Tech.Memo.33-266.

Kuiper, G.P., 1952, Planetary atmospheres and their origin, Chapter XII (esp. p.358-361) in The atmospheres of the Earth and planets, Rev.Edition; Kuiper, G.P., Editor: Chicago, U.of Chicago Press.

_____, 1964, Infrared spectra of stars and planets, IV. The spectrum of Mars, 1-2.5 microns, and the structure of its atmosphere: Comm. Lunar Planet.Lab., v.2, n.31, p.79-112.

Leighton, R.B., and Murray, B.C., 1966, Behavior of carbon dioxide and other volatiles on Mars: Science, v.153, p.136-144.

Leovy, C., 1966a, Note on thermal properties of Mars: Icarus, v.5, p.1-6.

_____, 1966b, Mars ice caps: Science, v.154, p.1178-1179.

Lippincott, E.R., Eck, R.V., Dayhoff, M.D., and Sagan, C., 1967, Thermodynamic equilibria in planetary atmospheres: Astrophys.J., v.147, p.753-764.

Marmo, F.F., Shardanand, and Warneck, P., 1965, Ozone distribution in the atmosphere of Mars: J.Geophys.Res., v.70, p.2270-2271.

Marshall, J.V., 1964, Improved test for NO_2 on Mars: Comm.Lunar Planet. Lab., v.2, n.35, p.167-173.

Münch, G., 1967: Caltech meeting of the Astronomical Society of the Pacific, Pasadena, Calif., June 29-30, 1967.

O'Leary, B.T., 1965, A revised upper limit of NO_2 in the Martian atmosphere: Pub.Astron.Soc.Pacific, v.77, p.168-177.

Owen, T., 1966, The composition and surface pressure of the Martian atmosphere: results from the 1965 opposition: Astrophys.J., v.146, p.257-270.

Owen, T.C., 1964, A determination of the Martian CO_2 abundance: Comm. Lunar Planet.Lab., v.2, n.33, p.133-140.

Rank, D.H., Fink, V., Foltz, J.V., and Wiggins, T.A., 1964, Intensity measurements on spectra of gases of planetary interest—H_2, H_2O, and CO_2: Astrophys.J., v.140, p.366-373.

Rea, D.G., Belsky, T., and Calvin, M., 1963, Interpretation of the 3- to 4-micron infrared spectrum of Mars: Science, v.141, p.923-927.

Rea, D.G., O'Leary, B.T., and Sinton, W.M., 1965, Mars: the origin of the 3.58 and 3.69-micron minima in the infrared spectra: Science, v.147, p.1286-1288.

Sagan, C., Hanst, P.L., and Young, A.T., 1965, Nitrogen oxides on Mars: Planet.Space Sci., v.13, p.73-88.

Schorn, R.A., 1967, (Pasadena, Calif., Jet Propulsion Laboratory): private communication.

Schorn, R.A., Spinrad, H., Moore, R.C., Smith, H.J., and Giver, L.P., 1967, High dispersion spectroscopic observations of Mars, II. The water-vapor variations: Astrophys.J., v.147, p.743-752.

Sinton, W.M., 1957, Spectroscopic evidence for vegetation on Mars: Astrophys.J., v.126, p.231-239.

_____, 1961, An upper limit to the concentration of NO_2 and N_2O_4 in the Martian atmosphere: Pub.Astron.Soc.Pacific, v.73, p.125-128.

Spinrad, H., 1963, The NO_2 content of the Martian atmosphere: Pub.Astron. Soc.Pacific, v.75, p.190-191.

Spinrad, H., Münch, G., and Kaplan, L.D., 1963, The detection of water vapor on Mars: Astrophys.J., v.137, p.1319-1321.

Spinrad, H., and Richardson, E.H., 1963, High dispersion spectra of the outer planets, II. A new upper limit for the water vapor content of the Martian atmosphere: Icarus, v.2, p.49-53.

Spinrad, H., Schorn, R.A., Moore, R., Giver, L.P., and Smith, H.J., 1966, High dispersion spectroscopic observations of Mars, I. The CO_2 content and surface pressure: Astrophys.J., v.146, p.331-338.

Vaughan, A.H., Jr., 1967, Astronomical Fabry-Perot interference spectroscopy: Ann.Rev.Astron.Astrophys., v.5, p.139-166.

5.2 SURFACE PRESSURE

DATA SUMMARY

Spectroscopic analysis and the 1965 Mariner IV occultation experiment are the major sources of Martian surface pressure data. Photometry and polarimetry, the classical methods of pressure determination, are valid techniques for studying the surface of Mars but cannot alone give a useful surface pressure for the planet.

Best value (from spectroscopic measurements): 9^{+5}_{-2} mb. (The quoted error is a probable error.)

The pressure may be variable. There may be local elevations of a half scale height (4 km) or more above the mean surface equipotential.[1*]

Values quoted by the Mariner IV experimenters (from occultation data):

Composition	Immersion	Emersion
100% CO_2 [2]	4.9 ±0.8 mb	7.6 ±1.3 mb
80% CO_2, 20% Ar	5.2 ±0.8 mb	8.2 ±1.3 mb

The higher emersion pressure should be adopted on the likely possibility that it presents a more representative elevation on the planet.

DISCUSSION

Spectroscopic Results

To get a spectroscopic pressure, it is necessary to combine the CO_2 abundance[3] ω with a pressure-abundance product ωP_s from strong-line data. The CO_2-band groups near 1.6μ and near 2μ are convenient for this purpose. The original Martian spectroscopic pressure determination by Kaplan, Münch, and Spinrad (1964) was based upon 2μ data of Sinton (1963) and of Kuiper (1963), although reference was also made to the original 1.6μ discovery data of Kuiper (1952). Owen and Kuiper's 1964 surface pressure determination was based upon a careful laboratory calibration of 1.6μ data. Prior to new observations made during the 1964-1965 Mars apparition, all surface pressure values that followed depended upon rediscussion of observations of these groups plus some new laboratory line strengths. All of these numbers thus rested on an inadequate

*See page 12 for list of cross references.

observational base, and most contained small errors in calculations as well. They should therefore be discarded, although the few observations themselves are appropriate for reduction with the new data. The Stratoscope observations (Danielson et al., 1964) are eliminated from consideration, as suggested by Chamberlain and Hunten (1965), because of poor resolution, possible mislocation of the continuum, and other difficulties.

Each of the three teams which derived a new CO_2 abundance from new weak-line observations[3] also derived a new surface pressure based upon the best strong-line data available to them. The pertinent quantity to discuss then is the strong-line data, not the pressures variously derived. The most important new development in strong-line data was actually a theoretical one in which Gray (1966) managed a detailed fit to both laboratory and terrestrial CO_2 in the 2μ region with a random Elsasser band model, making allowances for 31 vibrational transitions. She then applied the model to the existing data of Kuiper (1964) and of Moroz (1964) to derive a new pressure-abundance product. Using true pressure, rather than effective broadening pressure, her result was $\omega P_s = 420 \pm 100$ mb (m atm).

Unfortunately the spectra available were of very low resolution. Low resolving power applied to a complex spectrum almost inevitably results in a depression of the apparent solar continuum, and such has proved to be the case here. Preliminary analysis by Kaplan (1967) of new interferometric spectra taken with the Connes spectrometer (Connes and Connes, 1966) indicates that the true equivalent widths (see spectroscopy discussion) are about twice the values on the Kuiper and the Moroz spectra. The effective pressure-abundance product $\omega P_{s,\,eff.}$ then becomes ~1000 mb (m atm). The damping constant for CO_2 self-broadening differs from that for broadening by nitrogen or argon. Self-broadening by CO_2 is 20% more efficient than broadening by nitrogen (it was thought to be 120% until 1966), and broadening by nitrogen is 20 to 25% more efficient than broadening by argon. Considering nitrogen and argon in equal abundance to make up that fraction of the Martian atmosphere which is not CO_2, the relationship between effective and true pressure is approximately $P_{s,\,eff.} = P_s(1 + 0.3\alpha)$, where α is the fraction of CO_2 by volume. The true pressure-abundance product ωP_s then becomes ~830 mb (m atm) with less than 10% error for $0.4 < \alpha < 0.9$.

The best study of the 1.6μ region remains the semi-empirical approach of Owen and Kuiper (1964). New observations of the 1.6μ bands are mentioned by Owen (1966). They differ little from the older results, increasing the equivalent width of the Martian contribution from 15.8 to 16.2 Å. The latter is equivalent to a product $\omega P_s = 585$ mb (m atm).

Gray (1967) has looked briefly at very high resolution Fourier spectra of the 1.6μ region taken by the Connes. These again indicate that $\omega P_{s,\,eff.}$ ~1000 mb (m atm) with a very large probable error.

The technique used by Gray (1966) is potentially by far the most accurate of spectroscopic studies of the strong CO_2 bands. The error due to unknown composition is small. Owen must contend with the same compositional problem in deciding which gases to introduce into the tube. Additional uncertainty is introduced in this latter case by the impossibility of realizing the long paths

and low pressures actually present on Mars. Extrapolations to low pressures are made more difficult by the compositional uncertainty.

In summary, strong-band spectroscopic data are somewhat improved today over that available at the time of the original spectroscopic pressure determination. With the certain knowledge that CO_2 constitutes at least half the atmosphere and probably much more, the damping constant uncertainty is minimized. Today it seems quite conservative to suggest $\omega P_s = 800 \pm 300$ (p.e.) mb (m atm), which implies a surface pressure of about 9 ±5 (p.e.) mb. In fact certain combinations of ωP_s and ω are not allowed by the data, namely, those which predict a total pressure less than the partial pressure of CO_2. The partial pressure of 90 - 25 = 65 m atm of CO_2 is ~5 mb. Therefore, the spectroscopic surface pressure is given as 9^{+5}_{-2} (p.e.) mb.

Again it must be remembered that the CO_2 abundance may be variable, and as a result the total surface pressure may also vary. Any conceivable surface pressure variation should be fully encompassed by the 2σ (two standard deviations) level of confidence, which is three times the probable error quoted above.

Occultation Experiment Results

The other major source of surface pressure data is the Mariner IV occultation experiment. Although the quantity measured by the occultation technique (index of refraction) is measured very accurately, it is somewhat removed from the parameter in question, the surface pressure (see pages 8 and 9). The results are a (fortunately weak) function of assumed composition. They are also a weak function of the atmospheric model (temperature profile) invoked to fit the data.

The results of immersion and emersion differ significantly, the latter resulting in considerably higher surface pressure values of 7.6 ±1.3 mb (100% CO_2) and the recommended 8.2 ±1.3 mb (80% CO_2, 20% Ar) (Kliore et al., 1967). The emersion point also appears to be perhaps 5 km nearer to the center of mass of Mars (Kliore et al., 1967). Although topographic relief is reasonable to invoke, at least part of this difference is certainly due to the oblateness (flattening) of Mars. There are conflicting figures for this,[4] the preferred dynamical flattening of 0.00525 (Cain, 1967) placing the emersion point 2.8 km nearer the center of mass than the immersion point (Kliore et al., 1967). The actual difference may be considerably smaller than 5 km since the probable error in the altitude is more than half the total amount. The pressure errors themselves are very small, however, and a real difference in height of the surfaces for which the pressures were measured is probably needed to explain the difference of some two standard deviations between immersion and emersion data.*

*Mariner IV immersion and emersion data were obtained above Electris and Mare Acidalium, respectively.[5]

Methods of Surface Pressure Determination

Spectroscopy*

An astronomical spectrogram consists of a photograph of a dispersed continuum of illumination, produced by the Sun in this case, usually with certain relatively discrete wavelengths more or less missing (more exactly, weakened). These are absorption features corresponding to the natural absorbing frequencies of atoms or molecules between source and detector. In the spectra of Mars the absorbers may be in the Sun (Fraunhofer lines), in the atmosphere of Mars, or in the Earth's atmosphere. There is no CO_2 on the Sun, so any solar interference is caused by the chance occurrence of absorption lines at the same frequency due to something other than CO_2. Because of the doppler effect, the same frequencies on different bodies shift slightly with respect to each other on a spectrogram if the bodies have any relative radial velocity.

If a microdensitometer tracing is made of a single absorption line and the densities are converted to intensities, the results may be somewhat bell shaped and usually will be fairly symmetrical.

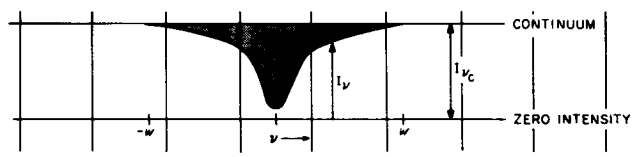

Assuming the continuum intensity to be essentially constant over the interval of integration, the total absorption A in the line (the shaded area) can then be written

$$A = \int_{-w}^{w} \left(I_{\nu_c} - I_\nu \right) d\nu = I_{\nu_c} \int_{-w}^{w} \left(1 - \frac{I_\nu}{I_{\nu_c}} \right) d\nu$$

where ν is the frequency, I_ν the intensity at ν, and I_{ν_c} the continuum of intensity. The parameter 2w marks the total width of the line, something which may be very difficult to determine in practice. The effect of finite instrument resolution (instrument profile) is a complication which will not be discussed here except to note that it causes line shapes to spread but leaves total absorption unaltered (although it may help cause nearby lines to make that absorption difficult or impossible to measure).

*For details of spectroscopic theory, see the references, especially Kondrat'yev (1965) and Goody (1964).

Total absorption is generally expressed in terms of equivalent width W, the width of an equivalent square line of zero intensity everywhere within the line. In other words, $A = I_{\nu_c} W$, and

$$W = \int_{-w}^{w} \left(1 - \frac{I_\nu}{I_{\nu_c}}\right) d\nu$$

At a particular frequency ν, I_{ν_c} starts through a gas, but only I_ν comes out — a typical case of mass absorption. Thus

$$I_\nu = I_{\nu_c} \exp(-\tau_\nu) = I_{\nu_c} \exp\left(-\int_0^x \alpha_\nu \rho dx\right)$$

where τ_ν is the optical depth, α_ν the mass absorption coefficient, ρ the number density, and x the path length through the gas. Then

$$W = \int_{-w}^{w} \left[1 - \exp\left(-\int_0^x \alpha_\nu \rho dx\right)\right] d\nu$$

At this point it is necessary to consider the form or forms taken by the mass absorption coefficient. Each spectral line due to freely radiating or absorbing atoms has a natural width determined by the finite lifetime of the state, a consequence of radiation damping. To this natural width will be added a doppler width produced by random motion of the atoms, a function of their kinetic energy, i.e., temperature. The line may be broadened further by encounters with perturbing neighbors (collision broadening), a function of pressure and temperature. Magnetic fields are responsible for Zeeman splitting, while the fluctuating electric fields due to charged particles may cause Stark broadening. Other causes of line broadening range from nuclear to gross motional effects such as high speed rotation or turbulence. In the case of Mars, only doppler and collision broadening need be considered.

If the damping constant is properly defined, collision damping and radiation damping can be evaluated with the same so-called dispersion equation

$$\alpha_\nu = \frac{\pi e^2}{mc} f \frac{\frac{\Gamma}{4\pi^2}}{(\nu - \nu_o)^2 + \left(\frac{\Gamma}{4\pi}\right)^2}$$

where m is the mass of the electron, e its charge, c the speed of light, f the oscillator strength for the transition in question, and Γ the corresponding damping constant. Here it must be understood that $\Gamma = \Gamma$ radiation + 2S, where S is the number of damping collisions per second, a quantity which is a function of the pressure. This is the so-called Lorentz profile exhibited by a line dominated by collision broadening or by natural broadening. It is in fact only an approximation for collision broadening; accurate calculations show broadened lines to be both slightly shifted in frequency and slightly asymmetric. Doppler broadening, on the other hand, follows a Maxwellian distribution (assuming equilibrium exists) and takes the form known as a doppler profile:

$$\alpha_\nu = \left(\frac{M}{2\pi kT}\right)^{1/2} \frac{c}{\nu} \exp\left[\frac{Mc^2}{-2kT}\left(\frac{\nu - \nu_o}{\nu}\right)^2\right]$$

where M is the mass of the molecule in question, k the Boltzmann constant, and T the temperature. These expressions may be easily combined into one equation for the absorption coefficient which includes all three broadening mechanisms (see Chapter 3 of Kondrat'yev, 1965, or of Goody, 1964).

The entire problem then reduces to finding workable approximations for the particular problem at hand. For example, consider the case pertinent to the very weak CO_2 lines discussed in Sec. 5.1.[3] If the optical depth is very small

$$\int_0^x \alpha_\nu \rho dx \cong \rho x \alpha_\nu$$

and

$$e^{-\rho x \alpha_\nu} \cong 1 - \rho x \alpha_\nu$$

so

$$W = \rho x \int_{-w}^{w} \alpha_\nu d\nu$$

Assuming each individual CO_2 line does not overlap its neighbor under the existing conditions, the integration may in effect be from minus to plus infinity. But, ignoring any doppler contribution,

$$\int_{-\infty}^{\infty} \frac{\frac{\Gamma}{4\pi^2}}{\left(\nu - \nu_o\right)^2 + \left(\frac{\Gamma}{4\pi}\right)^2} d\left(\nu - \nu_o\right) = 1$$

Thus

$$W = \rho x \frac{\pi e^2}{mc} f$$

Here, $(\pi e^2/mc)f$ are usually combined and called the line strength S, a quantity which in principle could be calculated but in practice is measured in the laboratory with a tube containing (in this case) CO_2. The factor ρx is the mass of absorbing material per unit area, usually written in terms of the amount of material in a vertical column ω times a multiplier η to allow for the actual atmospheric path traversed by the radiation. Therefore (rearranging), the CO_2 abundance $\omega = W/\eta S$, where W is measured on a photographic plate, η is calculated, and S is determined in the laboratory; as might be expected for a very weak line, the absorption is linearly proportional to the number of absorbers. Actually, the intrinsic width of these CO_2 lines is so small that they begin to saturate slightly, and a small doppler correction was introduced by the experimenters who determined the CO_2 abundance.[3]

The case discussed in the preceding paragraph was extremely simple. The lines were so weak there was no terrestrial contamination, they were far enough apart to avoid significant overlap with other lines and thus were treated as individual absorption lines, and the spectra to be measured exhibited sufficiently high resolution, precluding a smear of all the lines in the band (plus other lines not part of the band). The extension of this single-line theory to stronger lines is a bit involved mathematically but simple in principle (see Chapter 3 of Kondrat'yev, 1965). The difficulty occurs when lines become strong enough to begin to overlap.

Carbon dioxide is a molecule with a complex rotation-vibration spectrum; each band contains many lines, and the bands often overlap. To make a pressure determination, a pressure-broadened line must be observed. In principle both abundance and pressure could be determined by observing two different strong bands. In practice the abundance is much more easily and accurately determined with a very weak line or a group of weak lines to add statistical accuracy, and the pressure is then determined from that abundance and one strong band. It is necessary to consider the entire band because overlap prevents use of only one or a few lines of the band. It should be noted here that general use is made of the Curtis approximation, which states that mean pressure derived from a pressure-broadened line in an atmosphere in hydrostatic equilibrium is just half the surface pressure.

Since a real molecular band is quite complex, various band models have been developed in an attempt to make atmospheric transmission problems more tractable. Perhaps the simplest model, developed by Elsasser, is a band consisting of equally spaced lines of equal intensity. A more realistic band model results from probability theory and allows positions and intensities of lines in a band to be nearly random. The quantum mechanical relations governing the actual positions and intensities are so complex as to justify this "unusual" procedure first undertaken by Goody. This approach has been developed further by Kaplan, Godson, and others. Details and references to the original papers are given in Chapter 3 of Kondrat'yev (1965) and Chapter 4 of Goody (1964).

For the specific problem of CO_2, Gray (1966) has used an idea of Kaplan's for a random Elsasser band model in which the lines within a band are uniform, but the contributing bands are randomly spaced. This is important since it offers a means of separating Martian and terrestrial CO_2, both of which show up in strong-band spectra but are displaced by doppler shift. Other workers have generally used a less sophisticated approximation due to Grandjean and Goody (1955), Goody (1964), and the careful empirical work done by Owen and Kuiper (1964).

Much reference is made in quantitative spectroscopy to the curve of growth, which is a plot of abundance-times-pressure versus equivalent width for an individual band or line. It is a plot for which the various approximations discussed may each describe a small section. In theory it could be derived from basic principles. In fact it is usually rooted entirely in laboratory work wherever molecules are involved, although the laboratory results may be theoretically modified or extrapolated to reach conditions not attainable in the laboratory.

Occultation

When an electromagnetic wave passes through a planetary atmosphere, its amplitude, phase, and direction are changed. The ease of measurement and interpretation of these changes depends greatly on the frequency involved. Unfortunately there has never been an accurate observation of the optical occultation of a relatively bright star by Mars, although such observations have been made for Venus and Jupiter. A successful experiment at microwave frequencies (2300 MHz) was carried out by Kliore, Cain, Levy, Eshleman, Fjeldbo, and Drake using the communication system of the Mariner IV spacecraft (Kliore et al., 1965).

In a modern phase-coherent communication system with the frequency reference on Earth, extremely precise measurements of change in phase can be made, while direction and precise power loss are much more difficult to determine. The integrated refractive index along the ray path followed by the signal transmitted by a spacecraft through a planetary atmosphere is a direct function of the measured phase change (Kliore and Tito, 1967). The actual refractive index profile as a function of altitude can be determined if the atmosphere is assumed spherically symmetric and the index is small enough to ignore bending of the ray (Fjeldbo and Eshleman, 1965). As the atmosphere penetrated by the signal becomes denser, the refractive index increases, bending of the ray increases, and some knowledge of the spacecraft trajectory is needed to correctly allow for the effective increase in atmospheric path (Fjeldbo and Eshleman, 1965). If the atmosphere is non-spherical, the refractive index profile can still be determined if the shape of the atmosphere (planet) is known, as well as the trajectory of the transmitting spacecraft with respect to that atmosphere.

The refractive index profile is a function of the electron density and of the neutral particle density. If the ionosphere is separated in altitude from the bulk of the neutral atmosphere, confusion is unlikely.[6] In an ideal experiment at least two frequencies will be transmitted since the refractive index of the neutral atmosphere is virtually independent of frequency while that of the ionosphere varies inversely as the square of the frequency (Fjeldbo and Eshleman, 1965).

Assuming ionospheric effects have been removed, the refractive index profile of the neutral atmosphere is available to attempt fits with density profiles or the equivalent. (In most literature, reference is made to refractivity, which is just the refractive index minus one.) The simplest procedure to follow is to assume an exponential profile for refractivity with height in the lower atmosphere (Fjeldbo and Eshleman, 1965). Then $N(h) = N_s \exp(-h/H)$, where N_s is surface refractivity, H is a constant scale height, and h is altitude. This is equivalent to assuming an isothermal atmosphere. With the added prior knowledge that the bulk of the atmosphere must be CO_2 plus spectroscopic undetectables such as N_2 and Ar, a mass density and pressure may be calculated for each of a small family of compositional possibilities.

If the exponential assumption is inadequate to fit the observed profile of refractivity, then similar calculations may be done based on more complex model atmospheres having linear or adiabatic temperature lapse rates up to a certain elevation with an isothermal atmosphere above. In general, a reasonable fit to the data can be obtained without complex assumptions. The surface pressure results are not a strong function of the assumed model. Similarly, this technique is not a good one for attempting to obtain a detailed profile of the lower atmosphere of a planet. The more that is known about an atmosphere from independent studies, the more useful the occultation technique becomes in precisely defining certain quantities, since the quantities actually measured are measured with great precision.

Photometry and Polarimetry [7]

The attempt physically to measure the surface pressure on Mars was begun by D. Menzel in 1925 (Menzel, 1926). His method of mean albedos, a photometric method of determination, implied that the surface pressure was less than 50 to 60 torr, but the method contained four major assumptions which caused its later rejection by de Vaucouleurs and others. Lyot (1929) made the first attempt at a polarimetric determination of the surface pressure and found it to be less than 18 torr. Again, however, unverifiable assumptions were involved in the determination. A detailed resume of all the photometric and polarimetric determinations was made by de Vaucouleurs in 1954. After carefully pointing out all the assumptions and possibilities for error in all of these determinations, de Vaucouleurs nevertheless arrived at the conclusion that "the result (surface pressure P_s) cannot be far from $P_s = 64 \pm 3$ (p.e.) torr = 85 ± 4 (p.e.) mb."

The foremost exponent of planetary polarimetry since the death of Lyot has been his pupil Dollfus. Although primarily interested in surface properties, Dollfus has given various values of atmospheric mass (surface pressure), the most recent one being 30 mb assuming no haze component (Dollfus, 1966). In fact there very probably is a haze component which would further reduce the given value. [8]

A detailed critique of the entire surface pressure problem has recently been given by Chamberlain and Hunten (1965). The following paragraphs summarize their conclusions.

In even the best polarimetric work done to date it is assumed that surface polarization variation across the disk is wavelength independent, that the phase-angle and zenith-distance dependences of surface brightness are independent, and worst that the atmosphere is a pure Rayleigh scatterer. Further, the conversion from intensity to surface pressure involves the absolute planetary surface brightness and atmospheric composition. Finally, the observations themselves are not easy to make and involve some error even with the best of equipment and observers. The total error, excepting the composition effect and non-Rayleigh component effect, could be at least ±50% according to Chamberlain and Hunten.

The composition effect enters in the conversion of derived atmospheric scattering intensity to number of molecules or pressure. A pure CO_2 atmosphere has half as many molecules and about 75% of the surface pressure of an N_2 atmosphere with the same scattering intensity.

If there is a non-Rayleigh component to any atmosphere, its effect depends upon the size and type of particles involved. If they are very small, a few wavelengths of light or less such as typical haze or fog-type particles, the gas pressure will be overestimated by either polarimetric or photometric techniques which assume pure Rayleigh scattering for the atmosphere. Large particles such as ice crystals would add a component of negative polarization at small phase angles which would cause an underestimate of surface pressure. Such effects could be quite gross, causing errors of several hundred percent. In fact a considerable amount of submicron material simply invalidates the whole approach, and photometry has shown that there is at least some non-Rayleigh component.[8]

The photometric approach usually contains its own assumptions such as ignoring illumination of the ground by the atmosphere, illumination of the atmosphere by the ground, and absorption. Even if these are allowed for, it is impossible to correct for the non-Rayleigh scattering component known to exist.

Photometry and polarimetry remain valid methods of studying the surface of Mars, and perhaps with accurate knowledge of the atmosphere gained from other methods they may give useful results on the non-Rayleigh component of the Martian atmosphere. However, as stated in the opening paragraph of this section, they are not by themselves capable of giving a useful surface pressure for the planet.

CONCLUSIONS

Since Mars has an optically thin atmosphere composed of gases with observable spectral features, the most accurate method of remotely determining surface pressure is spectroscopic curve-of-growth analysis. Consequently, the best value for atmospheric pressure at the surface of Mars, 9^{+5}_{-2} (p.e.) mb, is derived from spectroscopic measurements. The spectroscopic value is integrated over perhaps 10^5 km^2 of the planet, whereas the pressure measurement from the occultation experiment is referenced to two isolated local levels, probably somewhat above the mean level. The occultation experiment gives a

largest surface pressure value of 8.2 ±1.3 mb, which, if interpreted as most nearly representative of the mean, is in excellent agreement with the spectroscopic result.

Because of the differences in immersion and emersion data from the occultation experiment and the question of local elevation effects, it seems unwise to reduce the probable error or to change the spectroscopic result. The agreement of two quite diverse methods is very reassuring. Data from current spectroscopic work and the additional data expected from the 1969 Mariner mission to Mars should remove many remaining doubts which cause the quoted errors to be relatively large.

CROSS REFERENCES

The specific section number, subject, and page number to which the reader is referred is given below.

Cross Reference	Section and Subject
[1] Local elevations	3.5..... Topographic relief differences (data summary), p. 1; Relative elevation of light and dark areas (discussion), p. 3.
[2] Carbon dioxide	3.4..... Water and carbon dioxide on the surface (discussion), p. 4; Phase diagram for carbon dioxide and water: pressure vs. temperature (figure), p. 9. 5.1..... Observed atmospheric constituents (data summary), p. 1. 5.3..... Lower atmosphere (data summary), p. 1.
[3] CO_2 abundance and strong- and weak-line data	5.1..... Carbon dioxide (discussion), p. 3-5.
[4] Flattening values	2..... Flattening (data summary), p. 3; Dynamical flattening (discussion), p. 4.
[5] Electris and Mare Acidalium	——..... MEC-1 and MEC-2 maps in pocket of binder. 4.2..... Martian place-names and their locations (figure), p. 25.
[6] Ionosphere	5.4..... Physics of the ionosphere (discussion), p. 3, 4.
[7] Photometry and polarimetry	3.2..... Photometric function (discussion), p. 3, 4; Polarization (discussion), p. 4, 5.
[8] Haze and non-Rayleigh component	4.1..... Clouds and hazes (discussion), p. 2-8.

BIBLIOGRAPHY

Cain, D.L., 1967, The implications of a new Mars mass and radius, p.7-9 in Supporting research and advanced development for the period December 1, 1966-January 31, 1967: Pasadena, Calif., Jet Propulsion Laboratory, Spa. Prog. Summ. 37-43, v.IV (unclassified).

Chamberlain, J.W., and Hunten, D.M., 1965, The pressure and CO_2 content of the Martian atmosphere: a critical discussion: Rev. Geophys., v.3, p.299-317.

Connes, J., and Connes, P., 1966, Near-infrared planetary spectra by Fourier spectroscopy, I. Instruments and results: J. Opt. Soc. Am., v.56, p.896-910.

Danielson, R.E., Guastad, J.E., Schwarzschild, M., Weaver, H.G., and Woolf, N.J., 1964, Mars observations from Stratoscope II: Astron. J., v.69, p.344-352.

de Vaucouleurs, G., 1954, Atmospheric pressure, Chapter IV (p.99-127) in Physics of the planet Mars, Part I: London, Faber and Faber.

Dollfus, A., 1966, Contribution au colloque Caltech-JPL sur la Lune et les planetes: Mars, p.288-304 in Proceedings of the Caltech-JPL lunar and planetary conference, September 13-18, 1965: Pasadena, Calif., Jet Propulsion Laboratory, Tech. Memo. 33-266.

Fjeldbo, G., and Eshleman, V.R., 1965, The bistatic radar-occultation method for the study of planetary atmospheres: J. Geophys. Res., v.70, p.3217-3225.

Goody, R.M., 1964, Atmospheric radiation, I. Theoretical basis: London, Oxford U. Press (Clarendon Press).

Grandjean, J., and Goody, R.M., 1955, The concentration of carbon dioxide in the atmosphere of Mars: Astrophys. J., v.121, p.548-552.

Gray, L.D., 1966, Transmission of the atmosphere of Mars in the region of 2μ: Icarus, v.5, p.390-398.

_____, 1967, (Pasadena, Calif., Jet Propulsion Laboratory): private communication.

Kaplan, L.D., 1967, (Pasadena, Calif., Jet Propulsion Laboratory): private communication.

Kaplan, L.D., Münch, G., and Spinrad, H., 1964, An analysis of the spectrum of Mars: Astrophys. J., v.139, p.1-15.

Kliore, A., Cain, D. L., and Levy, G. S., 1967, Radio occultation measurements of the Martian atmosphere over two regions by the Mariner IV space probe, p. 226-239 in Moon and planets: Amsterdam, North-Holland Pub. Co.

Kliore, A., Cain, D. L., Levy, G. S., Eshleman, V. R., Fjeldbo, G., and Drake, F. D., 1965, Occultation experiment: results of the first direct measurement of Mars' atmosphere and ionosphere: Science, v. 149, p. 1243-1248.

Kliore, A., and Tito, D. A., 1967, Radio occultation investigations of the atmosphere of Mars: J. Spacecraft Rockets, v. 4, p. 578-582.

Kondrat'yev, K. Ya., 1965, Radiative heat exchange in the atmosphere: Oxford, London, New York, Pergamon Press.

Kuiper, G. P., 1952, Planetary atmospheres and their origin, Chapter XII (esp. p. 358-361) in The atmospheres of the Earth and planets, Rev. Edition; Kuiper, G. P., Editor: Chicago, U. of Chicago Press.

_____, 1963, Infrared spectra of planets and cool stars, introductory report: Mem. Soc. R. Sci. Liege, 5th ser., v. 9, p. 365-391.

_____, 1964, Infrared spectra of stars and planets, IV. The spectrum of Mars, 1-2.5 microns, and the structure of its atmosphere: Comm. Lunar Planet. Lab., v. 2, n. 31, p. 79-112.

Lyot, B., 1929, Recherches sur la polarisation de la lumiere des planetes et de quelques substances terrestres: Ann. Obs. Meudon, VIII, v. 1, p. 51-62, 147-150.

Menzel, D. H., 1926, The atmosphere of Mars: Astrophys. J., v. 63, p. 48-59.

Moroz, V. I., 1964, The infrared spectrum of Mars (λ1.1 - 4.1μ): Astron. Zh., v. 41, p. 350-361.

Owen, T., 1966, The composition and surface pressure of the Martian atmosphere: results from the 1965 opposition: Astrophys. J., v. 146, p. 257-270.

Owen, T. C., and Kuiper, G. P., 1964, A determination of the composition and surface pressure of the Martian atmosphere: Comm. Lunar Planet. Lab., v. 2, n. 32, p. 113-132.

Sinton, W., 1963, Recent infrared spectra of Mars and Venus: J. Quant. Spect. Rad. Trans., v. 3, p. 551-558.

5.3 LOWER ATMOSPHERE

DATA SUMMARY

Nine models have been calculated for the lower atmosphere of Mars, each model giving atmospheric profiles for 10 different ground air temperatures. All use contemporary interpretations of the Mariner IV flight occultation data plus the best results of Earth-based observations.[1*] The three models listed below are presented here, representing a reasonable range of ground air temperatures (180 through 290°K) for three combinations of surface pressure and composition; other models are available from the author. At this time Model I is recommended. For instructions on use of the models, see Fig. 1.

	Surface pressure	Composition
Model I (Figs. 2 through 4)	10 mb	80% CO_2, 10% Ar, 10% N_2
Model II (Figs. 5 through 7)	10 mb	60% CO_2, 20% Ar, 20% N_2
Model III (Figs. 8 through 10)	15 mb	60% CO_2, 20% Ar, 20% N_2

DISCUSSION

Layers of the Lower Atmosphere

Using terrestrial nomenclature for classifying various regions of the atmosphere, the troposphere is the lowest region, where the source of heating is conduction from the ground and absorption of infrared energy radiated by the ground, and the principal transport of energy is by convection. It is a region where the kinetic temperature therefore decreases at a rate approximating the adiabatic lapse rate.

At some abrupt level in the lower atmosphere, the convective transport of energy virtually ceases. This level at which radiative equilibrium becomes a good first approximation is known as the tropopause. The height of the tropopause is a function of latitude, season, time of day, and solar activity. Above the tropopause the atmosphere is approximately in a state of radiative equilibrium and is called the stratosphere, a region where the temperature gradient can be either positive or negative depending upon the local conditions of the atmosphere (Goody, 1964). The numerical value of the temperature gradient will depend upon latitude, season, time of day, and solar activity.

*See page 21 for list of cross references.

Above the stratosphere but below the thermosphere is a region called the mesosphere, where the temperature in the terrestrial case decreases with increasing height. The amount of information available about the Earth's mesosphere is very limited and has been obtained largely by the observation of meteor trails through the region and from rocket data. The rocket data indicate that very large wind speeds occur with magnitudes as great as 150 m sec^{-1} (Fleagle and Businger, 1963).

Physics of the Lower Atmosphere

The important physical processes which are believed to occur in the lower atmosphere of Mars are based upon the theories of convective and radiative equilibrium plus the results of the Mariner IV occultation experiment and various Earth-based telescopic observations. These processes form the basis of Lower Atmosphere Models I, II, and III presented in Figs. 2 through 10.

Troposphere [2]

Mars is believed to have a normal troposphere, at least during daylight hours, with convection the dominant process for transporting energy. With this assumption, the temperature lapse rate is the dry-adiabatic lapse rate for the given composition of the atmosphere. For a well mixed atmosphere (the result of convection turbulence) the composition will be uniform with height; that is, for the mass density ρ_i of constituent i and the total mass density $\rho = \sum_i \rho_i$, we have ρ_i/ρ = constant. In an atmosphere of constant composition, the dry-adiabatic lapse rate is

$$A = g_o/\langle c_p \rangle \tag{1}$$

where g_o is the acceleration due to gravity and $\langle c_p \rangle$ is the mean value of the specific heat at constant pressure. The height of the tropopause (top of the troposphere) is below 10 km for Models I, II, and III; hence, g_o was treated as a constant (376 cm sec^{-2}). $\langle c_p \rangle$ is given by

$$\langle c_p \rangle = \frac{\sum_i \rho_i (c_p)_i}{\sum_i \rho_i} \tag{2}$$

Specific heat for N_2 or Ar is nearly independent of temperature over the range of temperatures in question, while the value for CO_2 varies approximately as a weak linear function of temperature. Values of c_p for Ar, N_2, and CO_2 were taken from Hilsenrath et al. (1960). Thus, the lapse rate depends both on the composition and the air temperature found in the troposphere.

The kinetic temperature of the troposphere decreases almost linearly with height since A changes only very slowly.

$$T = T_o - Ah \tag{3}$$

where T_o is the ground air temperature and h the height above ground. Assuming hydrostatic equilibrium and the ideal equation of state, the pressure profile for the troposphere is

$$P = P_o\left(\frac{T}{T_o}\right)^{\mu g_o/kA} \tag{4}$$

where P_o is the surface pressure in dyne cm^{-2}, μ is the mean mass per molecule in gm (mean molecular mass/Avogadro's number), and k is the Boltzmann constant. The total number of atoms and molecules in the troposphere is

$$n = \frac{P}{kT} \tag{5}$$

To obtain the partial concentrations $[CO_2]$, $[Ar]$, and $[N_2]$, n is multiplied by the fractional abundance of the constituent; that is

$$[CO_2] = xn \tag{6}$$

$$[Ar] = yn \tag{7}$$

$$[N_2] = zn \tag{8}$$

where $x + y + z = 1$.

Anderson (1965) assumes that the altitude of the tropopause varies linearly with the ground air temperature, and this assumption is adopted here.

$$h_t = a(T_o + b) \tag{9}$$

where h_t is the altitude of the tropopause and a and b are constants to be determined. The constants a and b were fitted to the results of the Mariner IV data and Model I (44% CO_2, 10-mb surface pressure) of Prabhakara and Hogan (1965).

Anderson interpreted the Mariner IV data (immersion) to indicate a very shallow troposphere or none at all. From his interpretation he derived the result that at $T_o = 175°K$ we have $h_t = 0$. To determine the other constant in Eq. (9), Model I of Prabhakara and Hogan was used, and the model gives the result that at $T_o = 230°K$ we have $h_t = 3$ km; hence, $a = 3/55$ and $b = -175$ for $T_o \geq 175°K$. Models will be added later for $T < 175°K$ based upon straight radiative equilibrium calculations.

Stratosphere and Mesosphere

In the Martian stratosphere, radiative transport is believed to be the dominant mechanism of energy transfer. The results from the Mariner IV experiment do not indicate that radiative transport is the only mechanism present in the Martian stratosphere, but at the level of complexity justified by present knowledge of Mars, this is the only process worth consideration here.

The results of the radiative equilibrium calculations of Prabhakara and Hogan (1965) show temperature gradients which are all negative and range in magnitude from 0.9 to 1.2°K km^{-1}. Models I, II, and III (Figs. 2 through 10) have negative temperature gradients above the tropopause, and the range in magnitudes for the gradients is from 0.08 to 1.8°K km^{-1}. The radiative temperature gradients α in °K km^{-1} are calculated from the expression

$$\alpha = \frac{T_o - 175}{62.5} \tag{10}$$

where T_o, as before, is ground air temperature. Equation (10) is derived from Figure 2 of Anderson (1965). The temperature profile from h_t to 50 km is

$$T = T_1 - \alpha(h - h_t) \tag{11}$$

where $T_1 = T(h_t)$, that is, the kinetic temperature at the height of the tropopause. From the equation of hydrostatic equilibrium and the ideal equation of state, the pressure profile from h_t to 50 km is

$$P = P_1\left(\frac{T}{T_1}\right)^{\mu g_1/k\alpha} \tag{12}$$

where $P_1 \equiv P(h_t)$ and g_1 is treated as a constant with the value of 370 cm sec^{-2} in this region of the atmosphere. The total density profile in the stratosphere is given by Eq. (5), and the partial concentrations of $[CO_2]$, [Ar], and $[N_2]$ are given by Eqs. (6), (7), and (8).

The Martian mesosphere, which is thought to be a layer approximately 40 km thick, in this model is a region where the temperature decreases linearly with height to an altitude of 75 km; above 75 km to an altitude of 90 km the temperature has the constant value of 155°K, which is consistent with the data presented by Gierasch and Goody (1967), and Prabhakara and Hogan (1965). The mesospheric temperature profile used in Models I, II, and III is

$$T = \begin{cases} T_2 - \beta(h - 50) \text{ for } 50 \text{ km} < h < 75 \text{ km} \\ T_3 = 155°\text{K for } 75 \text{ km} \le h \le 90 \text{ km} \end{cases} \tag{13}$$

where $T_2 = 175°K$ and $\beta = 0.8°K\ km^{-1}$. The value of T_2 is fitted to the results of Anderson (1965) at an altitude of 50 km, and the value of the temperature gradient β is chosen to represent a mean value in the 50- to 75-km region. From the equation of hydrostatic equilibrium and the ideal equation of state, the pressure profile in the mesosphere is

$$P = \begin{cases} P_2\left(\frac{T}{T_2}\right)^{\mu g_2/k\beta} \text{ for } 50 \text{ km} < h < 75 \text{ km} \\ P_3 \exp\left[-\frac{\mu g_3}{kT_3}(h - 75)\right] \text{ for } 75 \text{ km} \le h \le 90 \text{ km} \end{cases} \tag{14}$$

where $P_2 \equiv P(h = 50 \text{ km})$ and g_2 is treated as a constant with the value of 362 cm sec^{-2} in the region of 50 to 75 km. P_3 is the pressure at an altitude of 75 km, and g_3 is treated as a constant with a value of 358 cm sec^{-2} in this part of the atmosphere. The total number density n is calculated from Eq. (5). The partial concentrations of the atoms and molecules are determined from Eqs. (6), (7), and (8).

Contemporary Models of the Lower Atmosphere

Types of Models

Interpretation of the data from observational and theoretical studies has produced three distinct types of models for the lower atmosphere of Mars (Fig. 11). These can be classified by the dominant process which transports the energy as convective, radiative, or convective-radiative. The "correct" choice among them is not clear; hence, we have used a combination of the convective and radiative models to produce a series of new models which are classified convective-radiative to represent the "best" approximation to the lower atmosphere of Mars.

Convective. A model which can be classified as convective for the lower Martian atmosphere has been presented by Neubauer (1966). He gives a detailed calculation for the development of thermal convection and then explores the possibilities of the influence of this process in producing "dust-devils" on Mars. In his treatment, thermal convection in the lower atmosphere of Mars is approximated by Brunt's equation

$$\frac{\partial T}{\partial t} = \frac{\partial}{\partial Z}\left[K\left(\frac{\partial T}{\partial Z} + \Gamma\right)\right] \tag{15}$$

where T is the temperature, t is the time, Z is the altitude, K is the coefficient of turbulent heat transfer, and Γ is the adiabatic lapse rate. K depends on the time of day, the Richardson number, the season, solar activity, the latitude, and altitude. Neubauer assumes K to be a function of Z only and assumes the values of K for the Earth's atmosphere to be applicable to the Martian atmosphere. To extrapolate K from the Earth's atmosphere to the Martian atmosphere without considering the seasonal, latitudinal, and diurnal variations of K for the terrestrial case is a dubious exercise. The main result of Neubauer's work is a demonstration that dust-devil formation can occur more easily on Mars than on Earth.[3]

A by-product of Neubauer's study is the diurnal variation of the surface temperature of Mars for southern hemisphere summer solstice at midlatitudes.[4] Figure 3 of Neubauer shows the diurnal variation of two temperature profiles, one for the mean surface and one for 50 cm above the mean surface of Mars. Two results are readily apparent: (1) the diurnal temperature wave becomes damped very rapidly with altitude, and (2) the diurnal temperature waves for the ground and for 50 cm above the ground are in phase with each other. The first observation is disputed by the results of other authors (Leovy, 1966; Goody and Belton, 1967). The validity of the second observation needs to be established with more certainty.

Radiative. A model which can be classified as radiative is presented by Gierasch and Goody (1967). They calculate a "simple" solution to the equation describing the state of radiative equilibrium in the Martian atmosphere. From their solution Gierasch and Goody discuss and evaluate the relative importances of doppler broadening, the effect of water vapor in the Martian atmosphere, solar heating, vibrational relaxation of CO_2, and the development of a convective troposphere. They do not present a complete model for the lower atmosphere of Mars, only the temperature profile up to an altitude of 60 km. The temperature profile was calculated for a pure CO_2 atmosphere with a surface pressure of 4.9 mb and a surface gravity of 372 cm sec^{-2}. A complete model (temperature, pressure, and number density profiles) can be calculated by using their temperature profile together with the equation of hydrostatic equilibrium and the ideal equation of state.

Convective-Radiative. The models of Prabhakara and Hogan (1965) and Leovy (1966) can be classified as convective-radiative models. Prabhakara and Hogan present a detailed calculation of the thermal structure for the atmosphere of Mars based on the absorption of solar photons in the ultraviolet and visible regions of the spectrum by O_2 and O_3 and the absorption of infrared radiation by CO_2.[5] Prabhakara and Hogan use an iterative procedure to calculate the atmospheric parameters of their model. When the surface pressure, surface air temperature, and atmospheric composition are specified, a first guess for the vertical temperature distribution will yield a pressure and number density distribution through the use of the equation of hydrostatic equilibrium and the ideal equation of state. From the vertical variation of the atmospheric constituents, the opacity can be determined for any level of the atmosphere. With the use of the radiative transfer equation plus the atmospheric parameters just determined, a new temperature profile is generated. With this new temperature distribution, they calculate new pressure and number density distributions and then a new opacity. Then another temperature profile is determined with the

use of the radiative transfer equation. This procedure is repeated until a temperature distribution is obtained which satisfies a convergence criterion of Prabhakara and Hogan, specifically, that at any level in the atmosphere the temperature does not change more than 0.1°K in two successive iterations.

The models of Prabhakara and Hogan (1965) predate the results of Mariner IV and the recent Earth-based spectroscopic studies; hence, the models do not contain the most recent initial atmospheric parameters and should be used with caution when they are employed to establish the boundary conditions for upper atmospheric profiles.[6]

The model of Leovy (1966) was developed as a necessary preliminary to a numerical study which attempts to simulate the atmospheric circulation on Mars. Leovy has gone into great detail to produce a model that will represent the diurnal, seasonal, and latitudinal variation of ground and atmospheric temperatures for an atmosphere with a surface pressure of 5 mb and composed entirely of CO_2.

The convective-radiative model of Leovy is derived for a two-layer atmosphere; that is, the upper layer contains half the mass of the troposphere and the mass of the stratosphere, and the lower layer contains the other half of the mass of the troposphere. The two-layer approximation used by Leovy for the lower atmosphere of Mars is not adequate to describe the vertical variation of the atmospheric parameters. Leovy's profiles for the atmospheric parameters instead show the diurnal, latitudinal, and seasonal variations. From his profiles for the temperature at an altitude of 2.89 km, Fig. 1 was derived by extrapolation to the ground.

The atmospheric temperature near the Martian surface is given by

$$T_o \equiv T(h=0) = T_3 + Ah_o = T_3 + 10.1 \tag{16}$$

where T_3 is the temperature at the reference altitude of 2.89 km, A is the temperature lapse rate (3.5°K km^{-1}), and h_o = 2.89 km. To obtain the ground air temperatures for a given time of day, extrapolations of Leovy's results roughly imply

$$T_o\,(\text{sunrise}) = T_o\,(\text{noon}) - \Delta T_o \tag{17}$$

$$T_o\,(\text{sunset}) = T_o\,(\text{noon}) - 1/3\ \Delta T_o \tag{18}$$

$$T_o\,(\text{midnight}) = T_o\,(\text{sunrise}) + 1/3\ \Delta T_o \tag{19}$$

where ΔT_o is the diurnal variation of the ground air temperature and the factor 1/3 is derived from Figures 3 and 6 of Leovy (1966). Use of Eqs. (16) through (19) plus Figures 4 and 5 from Leovy allows calculation of the variation of the ground air temperature with latitude and season as was done in Fig. 1.[7]

Lower Atmosphere Models I, II, and III (Figs. 2 through 10)

These models are based on the general theory given on pages 2 through 5 and, in part, on the types of contemporary models discussed on pages 5 through 7. The models all use interpretations of data from the Mariner IV occultation experiment and the best results of Earth-based observations. The assumptions made in deriving Lower Atmosphere Models I, II, and III are listed below; model parameters all have been adjusted to match the calculated and observational data of Mars given in items 1) through 4).

1) Near the base of the thermosphere the kinetic temperature matches the calculated temperature of 155°K derived by Prabhakara and Hogan (1965) based upon radiative equilibrium calculations.

2) The temperature profile is assumed linear with temperature gradients which are consistent with the radiative equilibrium calculations of Prabhakara and Hogan (1965) and Anderson (1965).

3) The altitude of the Martian tropopause, which is a function of the ground air temperature, is derived from the ingress data of Mariner IV and radiative equilibrium calculations.

4) The thermodynamic parameters (specifically pressure and density) for the lower atmosphere of Mars are derived from the equation of hydrostatic equilibrium.

5) The lower atmosphere of Mars is assumed to be in a state of hydrostatic equilibrium above the tropopause.

6) Gas in the lower atmosphere of Mars is assumed to obey the ideal equation of state.

7) Aerosol concentration of the atmosphere is assumed negligible.

8) Convective transport is assumed to be the dominant mechanism for energy transport in the troposphere and negligible above; radiative transport is assumed to dominate in the stratosphere.

9) The effect of circulation has not been included in the atmospheric models.

10) Latitudinal, seasonal, and diurnal variations of the atmospheric parameters are included as significant effects in the description for the lower Martian atmosphere (see Fig. 1).[7]

11) Storm activity is assumed negligible.

12) Solar activity has not been included in the models.

13) Formation of dry ice (condensed CO_2) is assumed negligible.

14) The phenomenon of the "blue haze" has been ignored.[8]

CONCLUSIONS

Lower Atmosphere Model I (Figs. 2 through 4), with surface pressure of 10 mb and composition of 80% CO_2, 10% Ar, and 10% N_2, is recommended at this time. Figure 1 gives detailed instructions for use of this model.

Contemporary models of the lower atmosphere of Mars which are presented in Fig. 11 are all post-Mariner IV, the model of Prabhakara and Hogan (1965) thereby being excluded. From Fig. 11 we see that there is general consistency among the various atmospheric parameters assumed for the theories. The atmospheric composition assumed is primarily CO_2 with trace amounts of N_2 and Ar. Ohring et al. (1967) prefer an atmospheric composition for the lower Martian atmosphere of 74% CO_2 and 26% N_2. The surface pressure used in these models was 5 mb except for Ohring et al. (1967), who preferred 7 mb. Values of the mean ground air temperatures are difficult quantities to establish with any reasonable certainty. The values used in these models are believed to represent the most reasonable estimates to date. The altitude of the base of the mesosphere is a highly uncertain quantity; two estimates are given in Fig. 11.

Latitude	T_o Ground air temperature, °K				T_o Ground air temperature, °K			
	Noon	Sunset	Midnight	Sunrise	Noon	Sunset	Midnight	Sunrise
	Summer				Winter			
+90	235	235	235	235	143	143	143	143
+70	260	247	235	220	143	143	143	143
+50	265	249	233	217	177	170	162	155
+30	265	248	232	215	225	212	198	185
+10	260	243	227	210	245	230	215	200
-10	245	230	215	200	260	243	227	210
-30	225	212	198	185	265	248	232	215
-50	177	170	162	155	265	249	233	217
-70	143	143	143	143	260	247	235	220
-90	143	143	143	143	235	235	235	235
	Fall				Spring			
+90	143	143	143	143	143	143	143	143
+70	190	181	171	162	208	197	187	176
+50	235	221	206	193	235	220	205	190
+30	250	234	219	203	250	234	217	201
+10	257	241	224	208	260	243	226	209
-10	260	243	226	209	257	241	224	208
-30	250	234	217	201	250	234	219	203
-50	235	220	205	190	235	221	206	193
-70	208	197	187	176	190	181	171	162
-90	143	143	143	143	143	143	143	143

Note: The ground air temperatures are derived neglecting atmospheric circulation and should be used with caution.

Fig. 1. Table of ground air temperatures for Mars referred to northern seasons. Data are the results of calculations from Leovy (1966) and Neubauer (1966). Leovy presents the calculated thermal data in graphic form, from which the table is derived.

To use Lower Atmosphere Models I, II, and III (Figs. 2 through 10), first refer to Fig. 1 and read the appropriate ground air temperature for the pertinent season, latitude, and time of day. Then select the profile with the most nearly correct value for ground air temperature from among the 10 profiles given for each model.

Data for Models I, II, and III are reproduced essentially in the original computer printout format. The "E" or exponent notation following each number in the figures indicates the power of ten by which the number must be multiplied; e.g., 0.100E 06 = 0.100×10^6. A positive exponent is denoted by a blank after the E rather than by a plus sign. All exponents are positive with the single exception of those associated with zero altitude. Zero altitude is always followed on the printout by a large negative exponent, a characteristic of the computer.

H Height above mean surface, cm	Atmospheric parameters			Atmospheric parameters		
	T Kinetic temperature, °K	P Total pressure, dyne cm^{-2}	N Total concentration, cm^{-3}	T Kinetic temperature, °K	P Total pressure, dyne cm^{-2}	N Total concentration, cm^{-3}
	Ground air temperature T_0: 180°K			Ground air temperature T_0: 200°K		
0.000E-38	0.180000E 03	0.100000E 05	0.402442E 18	0.200000E 03	0.100000E 05	0.362198E 18
0.100E 06	0.178511E 03	0.900326E 04	0.365351E 18	0.194887E 03	0.908307E 04	0.337619E 18
0.200E 06	0.178431E 03	0.810835E 04	0.329183E 18	0.192773E 03	0.824143E 04	0.309694E 18
0.300E 06	0.178351E 03	0.730205E 04	0.296582E 18	0.192373E 03	0.747936E 04	0.281642E 18
0.400E 06	0.178271E 03	0.657562E 04	0.267197E 18	0.191973E 03	0.678639E 04	0.256080E 18
0.500E 06	0.178191E 03	0.592118E 04	0.240712E 18	0.191573E 03	0.615637E 04	0.232792E 18
0.600E 06	0.178111E 03	0.533161E 04	0.216842E 18	0.191173E 03	0.558371E 04	0.211579E 18
0.700E 06	0.178031E 03	0.480053E 04	0.195330E 18	0.190773E 03	0.506327E 04	0.192261E 18
0.800E 06	0.177951E 03	0.432214E 04	0.175944E 18	0.190373E 03	0.459041E 04	0.174672E 18
0.900E 06	0.177871E 03	0.389125E 04	0.158474E 18	0.189973E 03	0.416084E 04	0.158660E 18
0.100E 07	0.177791E 03	0.350314E 04	0.142733E 18	0.189573E 03	0.377070E 04	0.144086E 18
0.150E 07	0.177391E 03	0.207011E 04	0.845352E 17	0.187573E 03	0.229753E 04	0.887292E 17
0.200E 07	0.176991E 03	0.122184E 04	0.500079E 17	0.185573E 03	0.139249E 04	0.543569E 17
0.250E 07	0.176591E 03	0.720306E 03	0.295477E 17	0.183573E 03	0.839399E 03	0.331235E 17
0.300E 07	0.176191E 03	0.424129E 03	0.174377E 17	0.181573E 03	0.503195E 03	0.200753E 17
0.350E 07	0.175791E 03	0.249435E 03	0.102787E 17	0.179573E 03	0.299946E 03	0.120998E 17
0.400E 07	0.175391E 03	0.146518E 03	0.605145E 16	0.177573E 03	0.177759E 03	0.725156E 16
0.450E 07	0.174991E 03	0.859603E 02	0.355842E 16	0.175573E 03	0.104724E 03	0.432083E 16
0.500E 07	0.174591E 03	0.503704E 02	0.208991E 16	0.173573E 03	0.613241E 02	0.255933E 16
0.550E 07	0.171000E 03	0.296967E 02	0.125802E 16	0.171000E 03	0.361547E 02	0.153160E 16
0.600E 07	0.167000E 03	0.172906E 02	0.750015E 15	0.167000E 03	0.210507E 02	0.913117E 15
0.650E 07	0.163000E 03	0.993613E 01	0.441576E 15	0.163000E 03	0.120969E 02	0.537604E 15
0.700E 07	0.159000E 03	0.563178E 01	0.256581E 15	0.159000E 03	0.685650E 01	0.312379E 15
0.750E 07	0.155000E 03	0.314624E 01	0.147040E 15	0.155000E 03	0.383044E 01	0.179016E 15
0.800E 07	0.155000E 03	0.175598E 01	0.820661E 14	0.155000E 03	0.213784E 01	0.999125E 14
0.850E 07	0.155000E 03	0.980045E 00	0.458027E 14	0.155000E 03	0.119317E 01	0.557631E 14
0.900E 07	0.155000E 03	0.546982E 00	0.255634E 14	0.155000E 03	0.665932E 00	0.311225E 14
	Ground air temperature T_0: 190°K			Ground air temperature T_0: 210°K		
0.000E-38	0.190000E 03	0.100000E 05	0.381261E 18	0.210000E 03	0.100000E 05	0.344951E 18
0.100E 06	0.185720E 03	0.903950E 04	0.352584E 18	0.204950E 03	0.912541E 04	0.322538E 18
0.200E 06	0.185480E 03	0.817378E 04	0.319230E 18	0.200309E 03	0.830953E 04	0.300506E 18
0.300E 06	0.185240E 03	0.739002E 04	0.288993E 18	0.199749E 03	0.756849E 04	0.274474E 18
0.400E 06	0.185000E 03	0.668053E 04	0.261587E 18	0.199189E 03	0.689172E 04	0.250634E 18
0.500E 06	0.184760E 03	0.603837E 04	0.236749E 18	0.198629E 03	0.627382E 04	0.228806E 18
0.600E 06	0.184520E 03	0.545721E 04	0.214242E 18	0.198069E 03	0.570980E 04	0.208825E 18
0.700E 06	0.184280E 03	0.493134E 04	0.193849E 18	0.197509E 03	0.519510E 04	0.190539E 18
0.800E 06	0.184040E 03	0.445556E 04	0.175375E 18	0.196949E 03	0.472553E 04	0.173810E 18
0.900E 06	0.183800E 03	0.402515E 04	0.158640E 18	0.196389E 03	0.429725E 04	0.158508E 18
0.100E 07	0.183560E 03	0.363583E 04	0.143484E 18	0.195829E 03	0.390672E 04	0.144515E 18
0.150E 07	0.182360E 03	0.218194E 04	0.866742E 17	0.193029E 03	0.241618E 04	0.906742E 17
0.200E 07	0.181160E 03	0.130502E 04	0.521833E 17	0.190229E 03	0.148387E 04	0.565064E 17
0.250E 07	0.179960E 03	0.777872E 03	0.313119E 17	0.187429E 03	0.904743E 03	0.349676E 17
0.300E 07	0.178760E 03	0.462057E 03	0.187242E 17	0.184629E 03	0.547544E 03	0.214831E 17
0.350E 07	0.177560E 03	0.273502E 03	0.111581E 17	0.181829E 03	0.328836E 03	0.131007E 17
0.400E 07	0.176360E 03	0.161317E 03	0.662608E 16	0.179029E 03	0.195931E 03	0.792790E 16
0.450E 07	0.175160E 03	0.948056E 02	0.392081E 16	0.176229E 03	0.115793E 03	0.475974E 16
0.500E 07	0.173960E 03	0.555138E 02	0.231169E 16	0.173429E 03	0.678585E 02	0.283439E 16
0.550E 07	0.171000E 03	0.327292E 02	0.138648E 16	0.171000E 03	0.400072E 02	0.169480E 16
0.600E 07	0.167000E 03	0.190562E 02	0.826602E 15	0.167000E 03	0.232938E 02	0.101041E 16
0.650E 07	0.163000E 03	0.109507E 02	0.486667E 15	0.163000E 03	0.133859E 02	0.594888E 15
0.700E 07	0.159000E 03	0.620686E 01	0.282782E 15	0.159000E 03	0.758709E 01	0.345664E 15
0.750E 07	0.155000E 03	0.346751E 01	0.162055E 15	0.155000E 03	0.423859E 01	0.198091E 15
0.800E 07	0.155000E 03	0.193529E 01	0.904461E 14	0.155000E 03	0.236564E 01	0.110559E 15
0.850E 07	0.155000E 03	0.108012E 01	0.504797E 14	0.155000E 03	0.132031E 01	0.617049E 14
0.900E 07	0.155000E 03	0.602837E 00	0.281737E 14	0.155000E 03	0.736890E 00	0.344387E 14

Fig. 2. Lower Atmosphere Model I for ground air temperatures 180, 190, 200, and 210°K. Surface pressure 10 mb (0.10×10^5 dyne cm^{-2}); atmospheric abundance 80% CO_2, 10% Ar, 10% N_2 by volume; mean molecular mass of atmospheric constituents 0.697119×10^{-22} gm.

H Height above mean surface, cm	Atmospheric parameters			Atmospheric parameters		
	T Kinetic temperature, °K	P Total pressure, dyne cm^{-2}	N Total concentration, cm^{-3}	T Kinetic temperature, °K	P Total pressure, dyne cm^{-2}	N Total concentration, cm^{-3}
	Ground air temperature T_0: 220°K			Ground air temperature T_0: 240°K		
0.000E-38	0.220000E 03	0.100000E 05	0.329271E 18	0.240000E 03	0.100000E 05	0.301832E 18
0.100E 06	0.215012E 03	0.916401E 04	0.308744E 18	0.235131E 03	0.923182E 04	0.284415E 18
0.200E 06	0.210024E 03	0.838072E 04	0.289060E 18	0.230263E 03	0.850841E 04	0.267671E 18
0.300E 06	0.207364E 03	0.765619E 04	0.267458E 18	0.225394E 03	0.782803E 04	0.251586E 18
0.400E 06	0.206644E 03	0.699540E 04	0.245225E 18	0.222266E 03	0.719450E 04	0.234479E 18
0.500E 06	0.205924E 03	0.638962E 04	0.224773E 18	0.221226E 03	0.661312E 04	0.216544E 18
0.600E 06	0.205204E 03	0.583445E 04	0.205963E 18	0.220186E 03	0.607630E 04	0.199906E 18
0.700E 06	0.204484E 03	0.532582E 04	0.188670E 18	0.219146E 03	0.558082E 04	0.184477E 18
0.800E 06	0.203764E 03	0.485996E 04	0.172775E 18	0.218106E 03	0.512368E 04	0.170173E 18
0.900E 06	0.203044E 03	0.443342E 04	0.158170E 18	0.217066E 03	0.470205E 04	0.156918E 18
0.100E 07	0.202324E 03	0.404299E 04	0.144754E 18	0.216026E 03	0.431335E 04	0.144639E 18
0.150E 07	0.198724E 03	0.253724E 04	0.924884E 17	0.210826E 03	0.278420E 04	0.956650E 17
0.200E 07	0.195124E 03	0.157878E 04	0.586120E 17	0.205626E 03	0.177762E 04	0.626235E 17
0.250E 07	0.191524E 03	0.973742E 03	0.368296E 17	0.200426E 03	0.112198E 04	0.405516E 17
0.300E 07	0.187924E 03	0.595092E 03	0.229392E 17	0.195226E 03	0.699644E 03	0.259607E 17
0.350E 07	0.184324E 03	0.360236E 03	0.141573E 17	0.190026E 03	0.430757E 03	0.164209E 17
0.400E 07	0.180724E 03	0.215919E 03	0.865467E 16	0.184826E 03	0.261663E 03	0.102555E 17
0.450E 07	0.177124E 03	0.128092E 03	0.523865E 16	0.179626E 03	0.156702E 03	0.631948E 16
0.500E 07	0.173524E 03	0.751786E 02	0.313842E 16	0.174426E 03	0.924407E 02	0.383910E 16
0.550E 07	0.171000E 03	0.443229E 02	0.187762E 16	0.171000E 03	0.545001E 02	0.230875E 16
0.600E 07	0.167000E 03	0.258065E 02	0.111941E 16	0.167000E 03	0.317321E 02	0.137644E 16
0.650E 07	0.163000E 03	0.148298E 02	0.659060E 15	0.163000E 03	0.182350E 02	0.810390E 15
0.700E 07	0.159000E 03	0.840554E 01	0.382952E 15	0.159000E 03	0.103356E 02	0.470883E 15
0.750E 07	0.155000E 03	0.469582E 01	0.219460E 15	0.155000E 03	0.577405E 01	0.269851E 15
0.800E 07	0.155000E 03	0.262083E 01	0.122485E 15	0.155000E 03	0.322261E 01	0.150609E 15
0.850E 07	0.155000E 03	0.146273E 01	0.683613E 14	0.155000E 03	0.179860E 01	0.840580E 14
0.900E 07	0.155000E 03	0.816381E 00	0.381537E 14	0.155000E 03	0.100383E 01	0.469144E 14
	Ground air temperature T_0: 230°K			Ground air temperature T_0: 250°K		
0.000E-38	0.230000E 03	0.100000E 05	0.314955E 18	0.250000E 03	0.100000E 05	0.289758E 18
0.100E 06	0.225072E 03	0.919935E 04	0.296081E 18	0.245189E 03	0.926176E 04	0.273633E 18
0.200E 06	0.220145E 03	0.844719E 04	0.277958E 18	0.240378E 03	0.856499E 04	0.258112E 18
0.300E 06	0.215217E 03	0.774156E 04	0.260572E 18	0.235567E 03	0.790813E 04	0.243185E 18
0.400E 06	0.214337E 03	0.709654E 04	0.239842E 18	0.230756E 03	0.728963E 04	0.228839E 18
0.500E 06	0.213457E 03	0.650294E 04	0.220686E 18	0.229227E 03	0.671967E 04	0.212353E 18
0.600E 06	0.212577E 03	0.595683E 04	0.202990E 18	0.228027E 03	0.619235E 04	0.196718E 18
0.700E 06	0.211697E 03	0.545461E 04	0.186649E 18	0.226827E 03	0.570394E 04	0.182161E 18
0.800E 06	0.210817E 03	0.499289E 04	0.171563E 18	0.225627E 03	0.525177E 04	0.168613E 18
0.900E 06	0.209937E 03	0.456857E 04	0.157640E 18	0.224427E 03	0.483331E 04	0.156007E 18
0.100E 07	0.209057E 03	0.417875E 04	0.144796E 18	0.223227E 03	0.444622E 04	0.144284E 18
0.150E 07	0.204657E 03	0.266010E 04	0.941558E 17	0.217227E 03	0.290901E 04	0.970081E 17
0.200E 07	0.200257E 03	0.167682E 04	0.606561E 17	0.211227E 03	0.188079E 04	0.645010E 17
0.250E 07	0.195857E 03	0.104622E 04	0.386954E 17	0.205227E 03	0.120082E 04	0.423855E 17
0.300E 07	0.191457E 03	0.645808E 03	0.244347E 17	0.199227E 03	0.756537E 03	0.275079E 17
0.350E 07	0.187057E 03	0.394196E 03	0.152656E 17	0.193227E 03	0.469945E 03	0.176179E 17
0.400E 07	0.182657E 03	0.237803E 03	0.943099E 16	0.187227E 03	0.287569E 03	0.111263E 17
0.450E 07	0.178257E 03	0.141701E 03	0.575838E 16	0.181227E 03	0.173176E 03	0.692214E 16
0.500E 07	0.173857E 03	0.833499E 02	0.347287E 16	0.175227E 03	0.102522E 03	0.423831E 16
0.550E 07	0.171000E 03	0.491404E 02	0.208170E 16	0.171000E 03	0.604437E 02	0.256054E 16
0.600E 07	0.167000E 03	0.286115E 02	0.124108E 16	0.167000E 03	0.351927E 02	0.152656E 16
0.650E 07	0.163000E 03	0.164417E 02	0.730694E 15	0.163000E 03	0.202237E 02	0.898770E 15
0.700E 07	0.159000E 03	0.931914E 01	0.424575E 15	0.159000E 03	0.114627E 02	0.522237E 15
0.750E 07	0.155000E 03	0.520621E 01	0.243314E 15	0.155000E 03	0.640376E 01	0.299281E 15
0.800E 07	0.155000E 03	0.290569E 01	0.135798E 15	0.155000E 03	0.357406E 01	0.167035E 15
0.850E 07	0.155000E 03	0.162172E 01	0.757915E 14	0.155000E 03	0.199475E 01	0.932252E 14
0.900E 07	0.155000E 03	0.905114E 00	0.423007E 14	0.155000E 03	0.111331E 01	0.520308E 14

Fig. 3. Lower Atmosphere Model I for ground air temperatures 220, 230, 240, and 250°K. Surface pressure 10 mb (0.10×10^5 dyne cm^{-2}); atmospheric abundance 80% CO_2, 10% Ar, 10% N_2 by volume; mean molecular mass of atmospheric constituents 0.697119×10^{-22} gm.

H Height above mean surface, cm	Atmospheric parameters			Atmospheric parameters		
	T Kinetic temperature, °K	P Total pressure, dyne cm^{-2}	N Total concentration, cm^{-3}	T Kinetic temperature, °K	P Total pressure, dyne cm^{-2}	N Total concentration, cm^{-3}
	Ground air temperature T_0: 270°K			Ground air temperature T_0: 290°K		
0.000E-38	0.270000E 03	0.100000E 05	0.268295E 18	0.290000E 03	0.100000E 05	0.249792E 18
0.100E 06	0.265300E 03	0.931514E 04	0.254348E 18	0.285406E 03	0.936132E 04	0.237602E 18
0.200E 06	0.260600E 03	0.866619E 04	0.240896E 18	0.280812E 03	0.875405E 04	0.225824E 18
0.300E 06	0.255900E 03	0.805186E 04	0.227930E 18	0.276218E 03	0.817712E 04	0.214449E 18
0.400E 06	0.251200E 03	0.747089E 04	0.215441E 18	0.271624E 03	0.762949E 04	0.203471E 18
0.500E 06	0.246500E 03	0.692203E 04	0.203420E 18	0.267030E 03	0.711012E 04	0.192882E 18
0.600E 06	0.244402E 03	0.641275E 04	0.190071E 18	0.262436E 03	0.661800E 04	0.182675E 18
0.700E 06	0.242882E 03	0.593934E 04	0.177141E 18	0.259845E 03	0.615862E 04	0.171690E 18
0.800E 06	0.241362E 03	0.549824E 04	0.165018E 18	0.258005E 03	0.572985E 04	0.160876E 18
0.900E 06	0.239842E 03	0.508741E 04	0.153656E 18	0.256165E 03	0.532818E 04	0.150673E 18
0.100E 07	0.238322E 03	0.470496E 04	0.143011E 18	0.254325E 03	0.495208E 04	0.141050E 18
0.150E 07	0.230722E 03	0.315891E 04	0.991802E 17	0.245125E 03	0.340642E 04	0.100667E 18
0.200E 07	0.223122E 03	0.209277E 04	0.679448E 17	0.235925E 03	0.230989E 04	0.709240E 17
0.250E 07	0.215522E 03	0.136681E 04	0.459404E 17	0.226725E 03	0.154232E 04	0.492777E 17
0.300E 07	0.207922E 03	0.879132E 03	0.306289E 17	0.217525E 03	0.101272E 04	0.337252E 17
0.350E 07	0.200322E 03	0.556239E 03	0.201145E 17	0.208325E 03	0.652991E 03	0.227061E 17
0.400E 07	0.192722E 03	0.345764E 03	0.129965E 17	0.199125E 03	0.412778E 03	0.150164E 17
0.450E 07	0.185122E 03	0.210857E 03	0.825101E 16	0.189925E 03	0.255330E 03	0.973859E 16
0.500E 07	0.177522E 03	0.125948E 03	0.513945E 16	0.180725E 03	0.154215E 03	0.618137E 16
0.550E 07	0.171000E 03	0.742549E 02	0.314561E 16	0.171000E 03	0.909203E 02	0.385160E 16
0.600E 07	0.167000E 03	0.432342E 02	0.187537E 16	0.167000E 03	0.529374E 02	0.229627E 16
0.650E 07	0.163000E 03	0.248447E 02	0.110414E 16	0.163000E 03	0.304207E 02	0.135194E 16
0.700E 07	0.159000E 03	0.140819E 02	0.641567E 15	0.159000E 03	0.172424E 02	0.785556E 15
0.750E 07	0.155000E 03	0.786699E 01	0.367666E 15	0.155000E 03	0.963262E 01	0.450183E 15
0.800E 07	0.155000E 03	0.439072E 01	0.205201E 15	0.155000E 03	0.537615E 01	0.251256E 15
0.850E 07	0.155000E 03	0.245055E 01	0.114527E 15	0.155000E 03	0.300053E 01	0.140231E 15
0.900E 07	0.155000E 03	0.136770E 01	0.639197E 14	0.155000E 03	0.167466E 01	0.782654E 14

Fig. 4. Lower Atmosphere Model I for ground air temperatures 270 and 290°K. Surface pressure 10 mb (0.10×10^5 dyne cm^{-2}); atmospheric abundance 80% CO_2, 10% Ar, 10% N_2 by volume; mean molecular mass of atmospheric constituents 0.697119×10^{-22} gm.

H Height above mean surface, cm	Atmospheric parameters			Atmospheric parameters		
	T Kinetic temperature, °K	P Total pressure, dyne cm^{-2}	N Total concentration, cm^{-3}	T Kinetic temperature, °K	P Total pressure, dyne cm^{-2}	N Total concentration, cm^{-3}
	Ground air temperature T_0: 180°K			Ground air temperature T_0: 200°K		
0.000E-38	0.180000E 03	0.100000E 05	0.402442E 18	0.200000E 03	0.100000E 05	0.362198E 18
0.100E 06	0.178519E 03	0.904843E 04	0.367169E 18	0.194885E 03	0.912476E 04	0.339171E 18
0.200E 06	0.178439E 03	0.818978E 04	0.332475E 18	0.192771E 03	0.831767E 04	0.312563E 18
0.300E 06	0.178359E 03	0.741230E 04	0.301048E 18	0.192371E 03	0.758351E 04	0.285567E 18
0.400E 06	0.178279E 03	0.670832E 04	0.272578E 18	0.191971E 03	0.691281E 04	0.260853E 18
0.500E 06	0.178199E 03	0.607092E 04	0.246789E 18	0.191571E 03	0.630022E 04	0.238234E 18
0.600E 06	0.178119E 03	0.549385E 04	0.223431E 18	0.191171E 03	0.574080E 04	0.217534E 18
0.700E 06	0.178039E 03	0.497140E 04	0.202274E 18	0.190771E 03	0.523003E 04	0.198595E 18
0.800E 06	0.177959E 03	0.449844E 04	0.183113E 18	0.190371E 03	0.476377E 04	0.181271E 18
0.900E 06	0.177879E 03	0.407029E 04	0.165759E 18	0.189971E 03	0.433823E 04	0.165426E 18
0.100E 07	0.177799E 03	0.368272E 04	0.150043E 18	0.189571E 03	0.394992E 04	0.150936E 18
0.150E 07	0.177399E 03	0.223149E 04	0.911213E 17	0.187571E 03	0.246417E 04	0.951662E 17
0.200E 07	0.176999E 03	0.135060E 04	0.552757E 17	0.185571E 03	0.152953E 04	0.597069E 17
0.250E 07	0.176599E 03	0.816524E 03	0.334933E 17	0.183571E 03	0.944494E 03	0.372711E 17
0.300E 07	0.176199E 03	0.493074E 03	0.202715E 17	0.181571E 03	0.580159E 03	0.231461E 17
0.350E 07	0.175799E 03	0.297413E 03	0.122552E 17	0.179571E 03	0.354447E 03	0.142986E 17
0.400E 07	0.175399E 03	0.179187E 03	0.740043E 16	0.177571E 03	0.215357E 03	0.878543E 16
0.450E 07	0.174999E 03	0.107833E 03	0.446368E 16	0.175571E 03	0.130111E 03	0.536832E 16
0.500E 07	0.174599E 03	0.648174E 02	0.268922E 16	0.173571E 03	0.781560E 02	0.326184E 16
0.550E 07	0.171000E 03	0.391880E 02	0.166009E 16	0.171000E 03	0.472524E 02	0.200172E 16
0.600E 07	0.167000E 03	0.234121E 02	0.101555E 16	0.167000E 03	0.282301E 02	0.122454E 16
0.650E 07	0.163000E 03	0.138135E 02	0.613894E 15	0.163000E 03	0.166562E 02	0.740226E 15
0.700E 07	0.159000E 03	0.804407E 01	0.366484E 15	0.159000E 03	0.969944E 01	0.441902E 15
0.750E 07	0.155000E 03	0.462023E 01	0.215927E 15	0.155000E 03	0.557101E 01	0.260363E 15
0.800E 07	0.155000E 03	0.265126E 01	0.123907E 15	0.155000E 03	0.319685E 01	0.149406E 15
0.850E 07	0.155000E 03	0.152139E 01	0.711024E 14	0.155000E 03	0.183447E 01	0.857345E 14
0.900E 07	0.155000E 03	0.873028E 00	0.408012E 14	0.155000E 03	0.105269E 01	0.491976E 14
	Ground air temperature T_0: 190°K			Ground air temperature T_0: 210°K		
0.000E-38	0.190000E 03	0.100000E 05	0.381261E 18	0.210000E 03	0.100000E 05	0.344951E 18
0.100E 06	0.185730E 03	0.908310E 04	0.354266E 18	0.204935E 03	0.916524E 04	0.323969E 18
0.200E 06	0.185490E 03	0.825272E 04	0.322295E 18	0.200280E 03	0.838302E 04	0.303207E 18
0.300E 06	0.185250E 03	0.749733E 04	0.293174E 18	0.199720E 03	0.766937E 04	0.278173E 18
0.400E 06	0.185010E 03	0.681023E 04	0.266651E 18	0.199160E 03	0.701472E 04	0.255143E 18
0.500E 06	0.184770E 03	0.618533E 04	0.242498E 18	0.198600E 03	0.641433E 04	0.233964E 18
0.600E 06	0.184530E 03	0.561707E 04	0.220506E 18	0.198040E 03	0.586385E 04	0.214490E 18
0.700E 06	0.184290E 03	0.510037E 04	0.200483E 18	0.197480E 03	0.535925E 04	0.196588E 18
0.800E 06	0.184050E 03	0.463062E 04	0.182255E 18	0.196920E 03	0.489683E 04	0.180136E 18
0.900E 06	0.183810E 03	0.420361E 04	0.165665E 18	0.196360E 03	0.447315E 04	0.165020E 18
0.100E 07	0.183570E 03	0.381548E 04	0.150565E 18	0.195800E 03	0.408507E 04	0.151134E 18
0.150E 07	0.182370E 03	0.234618E 04	0.931933E 17	0.193000E 03	0.258479E 04	0.970163E 17
0.200E 07	0.181170E 03	0.143806E 04	0.575001E 17	0.190200E 03	0.162460E 04	0.618746E 17
0.250E 07	0.179970E 03	0.878581E 03	0.353638E 17	0.187400E 03	0.101409E 04	0.391997E 17
0.300E 07	0.178770E 03	0.535001E 03	0.216789E 17	0.184600E 03	0.628528E 03	0.246643E 17
0.350E 07	0.177570E 03	0.324695E 03	0.132460E 17	0.181800E 03	0.386721E 03	0.154092E 17
0.400E 07	0.176370E 03	0.196393E 03	0.806639E 16	0.179000E 03	0.236155E 03	0.955698E 16
0.450E 07	0.175170E 03	0.118382E 03	0.489558E 16	0.176200E 03	0.143093E 03	0.588288E 16
0.500E 07	0.173970E 03	0.711108E 02	0.296100E 16	0.173400E 03	0.860115E 02	0.359322E 16
0.550E 07	0.171000E 03	0.429929E 02	0.182128E 16	0.171000E 03	0.520017E 02	0.220291E 16
0.600E 07	0.167000E 03	0.256853E 02	0.111415E 16	0.167000E 03	0.310674E 02	0.134761E 16
0.650E 07	0.163000E 03	0.151548E 02	0.673500E 15	0.163000E 03	0.183303E 02	0.814626E 15
0.700E 07	0.159000E 03	0.882511E 01	0.402068E 15	0.159000E 03	0.106743E 02	0.486317E 15
0.750E 07	0.155000E 03	0.506883E 01	0.236893E 15	0.155000E 03	0.613095E 01	0.286532E 15
0.800E 07	0.155000E 03	0.290868E 01	0.135938E 15	0.155000E 03	0.351817E 01	0.164422E 15
0.850E 07	0.155000E 03	0.166911E 01	0.780062E 14	0.155000E 03	0.201885E 01	0.943516E 14
0.900E 07	0.155000E 03	0.957795E 00	0.447628E 14	0.155000E 03	0.115849E 01	0.541424E 14

Fig. 5. Lower Atmosphere Model II for ground air temperatures 180, 190, 200, and 210°K. Surface pressure 10 mb (0.10×10^5 dyne cm^{-2}); atmospheric abundance 60% CO_2, 20% Ar, 20% N_2 by volume; mean molecular mass of atmospheric constituents 0.663921×10^{-22} gm.

H Height above mean surface, cm	Atmospheric parameters			Atmospheric parameters		
	T Kinetic temperature, °K	P Total pressure, dyne cm^{-2}	N Total concentration, cm^{-3}	T Kinetic temperature, °K	P Total pressure, dyne cm^{-2}	N Total concentration, cm^{-3}
	Ground air temperature T_o: 220°K			Ground air temperature T_o: 240°K		
0.000E-38	0.220000E 03	0.100000E 05	0.329271E 18	0.240000E 03	0.100000E 05	0.301832E 18
0.100E 06	0.214984E 03	0.920214E 04	0.310069E 18	0.235080E 03	0.926695E 04	0.285560E 18
0.200E 06	0.209969E 03	0.845134E 04	0.291573E 18	0.230160E 03	0.857382E 04	0.269849E 18
0.300E 06	0.207296E 03	0.775381E 04	0.270957E 18	0.225240E 03	0.791922E 04	0.254691E 18
0.400E 06	0.206576E 03	0.711490E 04	0.249497E 18	0.222083E 03	0.730716E 04	0.238347E 18
0.500E 06	0.205856E 03	0.652669E 04	0.229670E 18	0.221043E 03	0.674323E 04	0.220987E 18
0.600E 06	0.205136E 03	0.598529E 04	0.211358E 18	0.220003E 03	0.622047E 04	0.204819E 18
0.700E 06	0.204416E 03	0.548713E 04	0.194449E 18	0.218963E 03	0.573604E 04	0.189766E 18
0.800E 06	0.203696E 03	0.502889E 04	0.178840E 18	0.217923E 03	0.528730E 04	0.175755E 18
0.900E 06	0.202976E 03	0.460750E 04	0.164436E 18	0.216883E 03	0.487176E 04	0.162718E 18
0.100E 07	0.202256E 03	0.422010E 04	0.151146E 18	0.215843E 03	0.448711E 04	0.150593E 18
0.150E 07	0.198656E 03	0.270740E 04	0.987249E 17	0.210643E 03	0.295632E 04	0.101667E 18
0.200E 07	0.195056E 03	0.172289E 04	0.639842E 17	0.205443E 03	0.192755E 04	0.679659E 17
0.250E 07	0.191456E 03	0.108719E 04	0.411349E 17	0.200243E 03	0.124308E 04	0.449694E 17
0.300E 07	0.187856E 03	0.680072E 03	0.262244E 17	0.195043E 03	0.792462E 03	0.294323E 17
0.350E 07	0.184256E 03	0.421564E 03	0.165736E 17	0.189843E 03	0.499085E 03	0.190439E 17
0.400E 07	0.180656E 03	0.258866E 03	0.103800E 17	0.184643E 03	0.310308E 03	0.121741E 17
0.450E 07	0.177056E 03	0.157406E 03	0.644002E 16	0.179443E 03	0.190333E 03	0.768360E 16
0.500E 07	0.173456E 03	0.947395E 02	0.395656E 16	0.174243E 03	0.115079E 03	0.478427E 16
0.550E 07	0.171000E 03	0.572786E 02	0.242645E 16	0.171000E 03	0.695754E 02	0.294738E 16
0.600E 07	0.167000E 03	0.342200E 02	0.148436E 16	0.167000E 03	0.415666E 02	0.180303E 16
0.650E 07	0.163000E 03	0.201904E 02	0.897291E 15	0.163000E 03	0.245250E 02	0.108993E 16
0.700E 07	0.159000E 03	0.117575E 02	0.535666E 15	0.159000E 03	0.142817E 02	0.650666E 15
0.750E 07	0.155000E 03	0.675309E 01	0.315607E 15	0.155000E 03	0.820289E 01	0.383364E 15
0.800E 07	0.155000E 03	0.387517E 01	0.181107E 15	0.155000E 03	0.470712E 01	0.219988E 15
0.850E 07	0.155000E 03	0.222372E 01	0.103926E 15	0.155000E 03	0.270112E 01	0.126237E 15
0.900E 07	0.155000E 03	0.127605E 01	0.596365E 14	0.155000E 03	0.155000E 01	0.724396E 14
	Ground air temperature T_o: 230°K			Ground air temperature T_o: 250°K		
0.000E-38	0.230000E 03	0.100000E 05	0.314955E 18	0.250000E 03	0.100000E 05	0.289758E 18
0.100E 06	0.225033E 03	0.923592E 04	0.297311E 18	0.245126E 03	0.929556E 04	0.274702E 18
0.200E 06	0.220065E 03	0.851510E 04	0.280294E 18	0.240252E 03	0.862808E 04	0.260149E 18
0.300E 06	0.215098E 03	0.783598E 04	0.263897E 18	0.235379E 03	0.799631E 04	0.246093E 18
0.400E 06	0.214218E 03	0.721258E 04	0.243900E 18	0.230505E 03	0.739901E 04	0.232525E 18
0.500E 06	0.213338E 03	0.663652E 04	0.225345E 18	0.228971E 03	0.684640E 04	0.216600E 18
0.600E 06	0.212458E 03	0.610436E 04	0.208134E 18	0.227771E 03	0.633318E 04	0.201419E 18
0.700E 06	0.211578E 03	0.561292E 04	0.192174E 18	0.226571E 03	0.585602E 04	0.187230E 18
0.800E 06	0.210698E 03	0.515925E 04	0.177379E 18	0.225371E 03	0.541256E 04	0.173973E 18
0.900E 06	0.209818E 03	0.474057E 04	0.163668E 18	0.224171E 03	0.500057E 04	0.161591E 18
0.100E 07	0.208938E 03	0.435432E 04	0.150966E 18	0.222971E 03	0.461799E 04	0.150031E 18
0.150E 07	0.204538E 03	0.283142E 04	0.100278E 18	0.216971E 03	0.308161E 04	0.102885E 18
0.200E 07	0.200138E 03	0.182400E 04	0.660194E 17	0.210971E 03	0.203318E 04	0.698118E 17
0.250E 07	0.195738E 03	0.116358E 04	0.430625E 17	0.204971E 03	0.132545E 04	0.468432E 17
0.300E 07	0.191338E 03	0.734739E 03	0.278169E 17	0.198971E 03	0.853157E 03	0.310610E 17
0.350E 07	0.186938E 03	0.459011E 03	0.177870E 17	0.192971E 03	0.541796E 03	0.203386E 17
0.400E 07	0.182538E 03	0.283561E 03	0.112530E 17	0.186971E 03	0.339168E 03	0.131406E 17
0.450E 07	0.178138E 03	0.173127E 03	0.704020E 16	0.180971E 03	0.209101E 03	0.836998E 16
0.500E 07	0.173738E 03	0.104406E 03	0.435318E 16	0.174971E 03	0.126828E 03	0.525082E 16
0.550E 07	0.171000E 03	0.631227E 02	0.267403E 16	0.171000E 03	0.766792E 02	0.324831E 16
0.600E 07	0.167000E 03	0.377115E 02	0.163581E 16	0.167000E 03	0.458106E 02	0.198713E 16
0.650E 07	0.163000E 03	0.222504E 02	0.988841E 15	0.163000E 03	0.270290E 02	0.120121E 16
0.700E 07	0.159000E 03	0.129571E 02	0.590321E 15	0.159000E 03	0.157399E 02	0.717101E 15
0.750E 07	0.155000E 03	0.744211E 01	0.347809E 15	0.155000E 03	0.904042E 01	0.422506E 15
0.800E 07	0.155000E 03	0.427056E 01	0.199586E 15	0.155000E 03	0.518772E 01	0.242450E 15
0.850E 07	0.155000E 03	0.245060E 01	0.114530E 15	0.155000E 03	0.297691E 01	0.139126E 15
0.900E 07	0.155000E 03	0.140625E 01	0.657213E 14	0.155000E 03	0.170826E 01	0.798359E 14

Fig. 6. Lower Atmosphere Model II for ground air temperatures 220, 230, 240, and 250°K. Surface pressure 10 mb (0.10×10^5 dyne cm^{-2}); atmospheric abundance 60% CO_2, 20% Ar, 20% N_2 by volume; mean molecular mass of atmospheric constituents 0.663921×10^{-22} gm.

H Height above mean surface, cm	Atmospheric parameters			Atmospheric parameters		
	T Kinetic temperature, °K	P Total pressure, dyne cm^{-2}	N Total concentration, cm^{-3}	T Kinetic temperature, °K	P Total pressure, dyne cm^{-2}	N Total concentration, cm^{-3}
	Ground air temperature T_0: 270°K			Ground air temperature T_0: 290°K		
0.000E-38	0.270000E 03	0.100000E 05	0.268295E 18	0.290000E 03	0.100000E 05	0.249792E 18
0.100E 06	0.265216E 03	0.934657E 04	0.255286E 18	0.285303E 03	0.939068E 04	0.238433E 18
0.200E 06	0.260433E 03	0.872509E 04	0.242689E 18	0.280607E 03	0.880929E 04	0.227415E 18
0.300E 06	0.255649E 03	0.813456E 04	0.230497E 18	0.275910E 03	0.825499E 04	0.216733E 18
0.400E 06	0.250866E 03	0.757396E 04	0.218705E 18	0.271213E 03	0.772694E 04	0.206382E 18
0.500E 06	0.246082E 03	0.704231E 04	0.207306E 18	0.266517E 03	0.722432E 04	0.196358E 18
0.600E 06	0.243969E 03	0.654712E 04	0.194398E 18	0.261820E 03	0.674632E 04	0.186655E 18
0.700E 06	0.242449E 03	0.608519E 04	0.181815E 18	0.250201E 03	0.629851E 04	0.176026E 18
0.800E 06	0.240929E 03	0.565325E 04	0.169975E 18	0.257361E 03	0.587917E 04	0.165481E 18
0.900E 06	0.239409E 03	0.524953E 04	0.158839E 18	0.255521E 03	0.548504E 04	0.155499E 18
0.100E 07	0.237889E 03	0.487233E 04	0.148368E 18	0.253681E 03	0.511476E 04	0.146054E 18
0.150E 07	0.230289E 03	0.333160E 04	0.104799E 18	0.244481E 03	0.357827E 04	0.106024E 18
0.200E 07	0.222689E 03	0.224920E 04	0.731653E 17	0.235281E 03	0.246927E 04	0.760254E 17
0.250E 07	0.215089E 03	0.149788E 04	0.504470E 17	0.226081E 03	0.167895E 04	0.537961E 17
0.300E 07	0.207489E 03	0.983048E 03	0.343207E 17	0.216881E 03	0.112343E 04	0.375234E 17
0.350E 07	0.199889E 03	0.635106E 03	0.230162E 17	0.207681E 03	0.738739E 03	0.257674E 17
0.400E 07	0.192289E 03	0.403425E 03	0.151980E 17	0.198481E 03	0.476634E 03	0.173957E 17
0.450E 07	0.184689E 03	0.251612E 03	0.986885E 16	0.189281E 03	0.301193E 03	0.115269E 17
0.500E 07	0.177089E 03	0.153845E 03	0.629313E 16	0.180081E 03	0.186025E 03	0.748305E 16
0.550E 07	0.171000E 03	0.930179E 02	0.394024E 16	0.171000E 03	0.112469E 03	0.476444E 16
0.600E 07	0.167000E 03	0.555688E 02	0.241041E 16	0.167000E 03	0.671923E 02	0.291460E 16
0.650E 07	0.163000E 03	0.327865E 02	0.145708E 16	0.163000E 03	0.396446E 02	0.176186E 16
0.700E 07	0.159000E 03	0.190927E 02	0.869852E 15	0.159000E 03	0.230863E 02	0.105180E 16
0.750E 07	0.155000E 03	0.109661E 02	0.512505E 15	0.155000E 03	0.132600E 02	0.619707E 15
0.800E 07	0.155000E 03	0.629277E 01	0.294094E 15	0.155000E 03	0.760905E 01	0.355611E 15
0.850E 07	0.155000E 03	0.361103E 01	0.168762E 15	0.155000E 03	0.436635E 01	0.204063E 15
0.900E 07	0.155000E 03	0.207214E 01	0.968419E 14	0.155000E 03	0.250557E 01	0.117099E 15

Fig. 7. Lower Atmosphere Model II for ground air temperatures 270 and 290°K. Surface pressure 10 mb (0.10×10^5 dyne cm^{-2}); atmospheric abundance 60% CO_2, 20% Ar, 20% N_2 by volume; mean molecular mass of atmospheric constituents 0.663921×10^{-22} gm.

H Height above mean surface, cm	Atmospheric parameters			Atmospheric parameters		
	T Kinetic temperature, °K	P Total pressure, dyne cm^{-2}	N Total concentration, cm^{-3}	T Kinetic temperature, °K	P Total pressure, dyne cm^{-2}	N Total concentration, cm^{-3}
	Ground air temperature T_o: 180°K			Ground air temperature T_o: 200°K		
0.000E-38	0.180000E 03	0.150000E 05	0.603664E 18	0.200000E 03	0.150000E 05	0.543297E 18
0.100E 06	0.178519E 03	0.135726E 05	0.550753E 18	0.194885E 03	0.136871E 05	0.508757E 18
0.200E 06	0.178439E 03	0.122847E 05	0.498713E 18	0.192771E 03	0.124765E 05	0.468844E 18
0.300E 06	0.178359E 03	0.111185E 05	0.451571E 18	0.192371E 03	0.113753E 05	0.428350E 18
0.400E 06	0.178279E 03	0.100625E 05	0.408867E 18	0.191971E 03	0.103692E 05	0.391280E 18
0.500E 06	0.178199E 03	0.910638E 04	0.370184E 18	0.191571E 03	0.945033E 04	0.357350E 18
0.600E 06	0.178119E 03	0.824078E 04	0.335147E 18	0.191171E 03	0.861119E 04	0.326301E 18
0.700E 06	0.178039E 03	0.745711E 04	0.303412E 18	0.190771E 03	0.784504E 04	0.297893E 18
0.800E 06	0.177959E 03	0.674766E 04	0.274669E 18	0.190371E 03	0.714566E 04	0.271906E 18
0.900E 06	0.177879E 03	0.610544E 04	0.248639E 18	0.189971E 03	0.650735E 04	0.248138E 18
0.100E 07	0.177799E 03	0.552408E 04	0.225065E 18	0.189571E 03	0.592489E 04	0.226405E 18
0.150E 07	0.177399E 03	0.334723E 04	0.136682E 18	0.187571E 03	0.369626E 04	0.142749E 18
0.200E 07	0.176999E 03	0.202591E 04	0.829135E 17	0.185571E 03	0.229429E 04	0.895603E 17
0.250E 07	0.176599E 03	0.122479E 04	0.502399E 17	0.183571E 03	0.141674E 04	0.559066E 17
0.300E 07	0.176199E 03	0.739612E 03	0.304073E 17	0.181571E 03	0.870239E 03	0.347192E 17
0.350E 07	0.175799E 03	0.446119E 03	0.183828E 17	0.179571E 03	0.531670E 03	0.214478E 17
0.400E 07	0.175399E 03	0.268781E 03	0.111006E 17	0.177571E 03	0.323035E 03	0.131782E 17
0.450E 07	0.174999E 03	0.161750E 03	0.669553E 16	0.175571E 03	0.195166E 03	0.805248E 16
0.500E 07	0.174599E 03	0.972261E 02	0.403383E 16	0.173571E 03	0.117234E 03	0.489276E 16
0.550E 07	0.171000E 03	0.587819E 02	0.249014E 16	0.171000E 03	0.708786E 02	0.300258E 16
0.600E 07	0.167000E 03	0.351182E 02	0.152332E 16	0.167000E 03	0.423451E 02	0.183680E 16
0.650E 07	0.163000E 03	0.207203E 02	0.920841E 15	0.163000E 03	0.249843E 02	0.111034E 16
0.700E 07	0.159000E 03	0.120661E 02	0.549726E 15	0.159000E 03	0.145492E 02	0.662853E 15
0.750E 07	0.155000E 03	0.693034E 01	0.323891E 15	0.155000E 03	0.835652E 01	0.390544E 15
0.800E 07	0.155000E 03	0.397688E 01	0.185861E 15	0.155000E 03	0.479528E 01	0.224109E 15
0.850E 07	0.155000E 03	0.228208E 01	0.106654E 15	0.155000E 03	0.275171E 01	0.128602E 15
0.900E 07	0.155000E 03	0.130954E 01	0.612018E 14	0.155000E 03	0.157903E 01	0.737964E 14
	Ground air temperature T_o: 190°K			Ground air temperature T_o: 210°K		
0.000E-38	0.190000E 03	0.150000E 05	0.571892E 18	0.210000E 03	0.150000E 05	0.517426E 18
0.100E 06	0.185730E 03	0.136247E 05	0.531399E 18	0.204935E 03	0.137479E 05	0.485953E 18
0.200E 06	0.185490E 03	0.123791E 05	0.483443E 18	0.200280E 03	0.125745E 05	0.454811E 18
0.300E 06	0.185250E 03	0.112460E 05	0.439761E 18	0.199720E 03	0.115041E 05	0.417259E 18
0.400E 06	0.185010E 03	0.102153E 05	0.399977E 18	0.199160E 03	0.105221E 05	0.382715E 18
0.500E 06	0.184770E 03	0.927799E 04	0.363747E 18	0.198600E 03	0.962150E 04	0.350946E 18
0.600E 06	0.184530E 03	0.842560E 04	0.330758E 18	0.198040E 03	0.879578E 04	0.321735E 18
0.700E 06	0.184290E 03	0.765055E 04	0.300724E 18	0.197480E 03	0.803888E 04	0.294882E 18
0.800E 06	0.184050E 03	0.694593E 04	0.273383E 18	0.196920E 03	0.734524E 04	0.270204E 18
0.900E 06	0.183810E 03	0.630541E 04	0.248497E 18	0.196360E 03	0.670972E 04	0.247530E 18
0.100E 07	0.183570E 03	0.572323E 04	0.225848E 18	0.195800E 03	0.612761E 04	0.226702E 18
0.150E 07	0.182370E 03	0.351927E 04	0.139790E 18	0.193000E 03	0.387719E 04	0.145524E 18
0.200E 07	0.181170E 03	0.215709E 04	0.862501E 17	0.190200E 03	0.243690E 04	0.928119E 17
0.250E 07	0.179970E 03	0.131787E 04	0.530457E 17	0.187400E 03	0.152113E 04	0.587996E 17
0.300E 07	0.178770E 03	0.802501E 03	0.325183E 17	0.184600E 03	0.942793E 03	0.369965E 17
0.350E 07	0.177570E 03	0.487043E 03	0.198689E 17	0.181800E 03	0.580082E 03	0.231138E 17
0.400E 07	0.176370E 03	0.294590E 03	0.120996E 17	0.179000E 03	0.354233E 03	0.143355E 17
0.450E 07	0.175170E 03	0.177573E 03	0.734336E 16	0.176200E 03	0.214640E 03	0.882432E 16
0.500E 07	0.173970E 03	0.106666E 03	0.444150E 16	0.173400E 03	0.129017E 03	0.538983E 16
0.550E 07	0.171000E 03	0.644894E 02	0.273192E 16	0.171000E 03	0.780025E 02	0.330437E 16
0.600E 07	0.167000E 03	0.385280E 02	0.167123E 16	0.167000E 03	0.466012E 02	0.202142E 16
0.650E 07	0.163000E 03	0.227322E 02	0.101025E 16	0.163000E 03	0.274955E 02	0.122194E 16
0.700E 07	0.159000E 03	0.132377E 02	0.603102E 15	0.159000E 03	0.160115E 02	0.729476E 15
0.750E 07	0.155000E 03	0.760324E 01	0.355339E 15	0.155000E 03	0.919643E 01	0.429797E 15
0.800E 07	0.155000E 03	0.436302E 01	0.203907E 15	0.155000E 03	0.527725E 01	0.246634E 15
0.850E 07	0.155000E 03	0.250366E 01	0.117009E 15	0.155000E 03	0.302828E 01	0.141527E 15
0.900E 07	0.155000E 03	0.143669E 01	0.671442E 14	0.155000E 03	0.173774E 01	0.812136E 14

Fig. 8. Lower Atmosphere Model III for ground air temperatures 180, 190, 200, and 210°K. Surface pressure 15 mb (0.15×10^5 dyne cm^{-2}); atmospheric abundance 60% CO_2, 20% Ar, 20% N_2 by volume; mean molecular mass of atmospheric constituents 0.663921×10^{-22} gm.

H Height above mean surface, cm	Atmospheric parameters			Atmospheric parameters		
	T Kinetic temperature, °K	P Total pressure, dyne cm^{-2}	N Total concentration, cm^{-3}	T Kinetic temperature, °K	P Total pressure, dyne cm^{-2}	N Total concentration, cm^{-3}
	Ground air temperature T_0: 220°K			Ground air temperature T_0: 240°K		
0.000E-38	0.220000E 03	0.150000E 05	0.493907E 18	0.240000E 03	0.150000E 05	0.452748E 18
0.100E 06	0.214984E 03	0.138032E 05	0.465103E 18	0.235080E 03	0.139004E 05	0.428340E 18
0.200E 06	0.209969E 03	0.126770E 05	0.437359E 18	0.230160E 03	0.128607E 05	0.404774E 18
0.300E 06	0.207296E 03	0.116307E 05	0.406435E 18	0.225240E 03	0.118788E 05	0.382037E 18
0.400E 06	0.206576E 03	0.106724E 05	0.374245E 18	0.222083E 03	0.109607E 05	0.357520E 18
0.500E 06	0.205856E 03	0.979003E 04	0.344506E 18	0.221043E 03	0.101149E 05	0.331481E 18
0.600E 06	0.205136E 03	0.897794E 04	0.317037E 18	0.220003E 03	0.933071E 04	0.307229E 18
0.700E 06	0.204416E 03	0.823070E 04	0.291674E 18	0.218963E 03	0.860406E 04	0.284648E 18
0.800E 06	0.203696E 03	0.754334E 04	0.268261E 18	0.217923E 03	0.793094E 04	0.263632E 18
0.900E 06	0.202976E 03	0.691125E 04	0.246654E 18	0.216883E 03	0.730764E 04	0.244077E 18
0.100E 07	0.202256E 03	0.633016E 04	0.226720E 18	0.215843E 03	0.673067E 04	0.225890E 18
0.150E 07	0.198656E 03	0.406110E 04	0.148087E 18	0.210643E 03	0.443448E 04	0.152501E 18
0.200E 07	0.195056E 03	0.258433E 04	0.959763E 17	0.205443E 03	0.289133E 04	0.101949E 18
0.250E 07	0.191456E 03	0.163078E 04	0.617023E 17	0.200243E 03	0.186462E 04	0.674541E 17
0.300E 07	0.187856E 03	0.102011E 04	0.393366E 17	0.195043E 03	0.118869E 04	0.441484E 17
0.350E 07	0.184256E 03	0.632346E 03	0.248605E 17	0.189843E 03	0.748627E 03	0.285658E 17
0.400E 07	0.180656E 03	0.388298E 03	0.155700E 17	0.184643E 03	0.465462E 03	0.182611E 17
0.450E 07	0.177056E 03	0.236109E 03	0.966003E 16	0.179443E 03	0.285500E 03	0.115254E 17
0.500E 07	0.173456E 03	0.142109E 03	0.593484E 16	0.174243E 03	0.172618E 03	0.717640E 16
0.550E 07	0.171000E 03	0.859178E 02	0.363968E 16	0.171000E 03	0.104363E 03	0.442107E 16
0.600E 07	0.167000E 03	0.513300E 02	0.222654E 16	0.167000E 03	0.623498E 02	0.270455E 16
0.650E 07	0.163000E 03	0.302856E 02	0.134594E 16	0.163000E 03	0.367874E 02	0.163489E 16
0.700E 07	0.159000E 03	0.176363E 02	0.803500E 15	0.159000E 03	0.214225E 02	0.975999E 15
0.750E 07	0.155000E 03	0.101296E 02	0.473411E 15	0.155000E 03	0.123043E 02	0.575046E 15
0.800E 07	0.155000E 03	0.581276E 01	0.271661E 15	0.155000E 03	0.706068E 01	0.329982E 15
0.850E 07	0.155000E 03	0.333558E 01	0.155889E 15	0.155000E 03	0.405168E 01	0.189356E 15
0.900E 07	0.155000E 03	0.191408E 01	0.894548E 14	0.155000E 03	0.232500E 01	0.108659E 15
	Ground air temperature T_0: 230°K			Ground air temperature T_0: 250°K		
0.000E-38	0.230000E 03	0.150000E 05	0.472432E 18	0.250000E 03	0.150000E 05	0.434638E 18
0.100E 06	0.225033E 03	0.138539E 05	0.445966E 18	0.245126E 03	0.139433E 05	0.412053E 18
0.200E 06	0.220065E 03	0.127726E 05	0.420442E 18	0.240252E 03	0.129421E 05	0.390224E 18
0.300E 06	0.215098E 03	0.117540E 05	0.395845E 18	0.235379E 03	0.119945E 05	0.369139E 18
0.400E 06	0.214218E 03	0.108189E 05	0.365850E 18	0.230505E 03	0.110985E 05	0.348787E 18
0.500E 06	0.213338E 03	0.995477E 04	0.338018E 18	0.228971E 03	0.102696E 05	0.324900E 18
0.600E 06	0.212458E 03	0.915654E 04	0.312201E 18	0.227771E 03	0.949977E 04	0.302128E 18
0.700E 06	0.211578E 03	0.841939E 04	0.288262E 18	0.226571E 03	0.878403E 04	0.280844E 18
0.800E 06	0.210698E 03	0.773887E 04	0.266069E 18	0.225371E 03	0.811883E 04	0.260959E 18
0.900E 06	0.209818E 03	0.711085E 04	0.245502E 18	0.224171E 03	0.750086E 04	0.242386E 18
0.100E 07	0.208938E 03	0.653148E 04	0.226449E 18	0.222971E 03	0.692698E 04	0.225046E 18
0.150E 07	0.204538E 03	0.424713E 04	0.150418E 18	0.216971E 03	0.462241E 04	0.154327E 18
0.200E 07	0.200138E 03	0.273600E 04	0.990291E 17	0.210971E 03	0.304977E 04	0.104718E 18
0.250E 07	0.195738E 03	0.174538E 04	0.645938E 17	0.204971E 03	0.198817E 04	0.702648E 17
0.300E 07	0.191338E 03	0.110211E 04	0.417253E 17	0.198971E 03	0.127974E 04	0.465915E 17
0.350E 07	0.186938E 03	0.688516E 03	0.266805E 17	0.192971E 03	0.812695E 03	0.305079E 17
0.400E 07	0.182538E 03	0.425341E 03	0.168796E 17	0.186971E 03	0.508751E 03	0.197110E 17
0.450E 07	0.178138E 03	0.259691E 03	0.105603E 17	0.180971E 03	0.313652E 03	0.125550E 17
0.500E 07	0.173738E 03	0.156609E 03	0.652977E 16	0.174971E 03	0.190243E 03	0.787623E 16
0.550E 07	0.171000E 03	0.946841E 02	0.401104E 16	0.171000E 03	0.115019E 03	0.487247E 16
0.600E 07	0.167000E 03	0.565672E 02	0.245372E 16	0.167000E 03	0.687159E 02	0.298069E 16
0.650E 07	0.163000E 03	0.333756E 02	0.148326E 16	0.163000E 03	0.405435E 02	0.180181E 16
0.700E 07	0.159000E 03	0.194357E 02	0.885481E 15	0.159000E 03	0.236098E 02	0.107565E 16
0.750E 07	0.155000E 03	0.111632E 02	0.521713E 15	0.155000E 03	0.135606E 02	0.633759E 15
0.800E 07	0.155000E 03	0.640584E 01	0.299378E 15	0.155000E 03	0.778159E 01	0.363674E 15
0.850E 07	0.155000E 03	0.367591E 01	0.171794E 15	0.155000E 03	0.446536E 01	0.208690E 15
0.900E 07	0.155000E 03	0.210937E 01	0.985819E 14	0.155000E 03	0.256239E 01	0.119754E 15

Fig. 9. Lower Atmosphere Model III for ground air temperatures 220, 230, 240, and 250°K. Surface pressure 15 mb (0.15×10^5 dyne cm^{-2}); atmospheric abundance 60% CO_2, 20% Ar, 20% N_2 by volume; mean molecular mass of atmospheric constituents 0.663921×10^{-22} gm.

H Height above mean surface, cm	Atmospheric parameters			Atmospheric parameters		
	T Kinetic temperature, °K	P Total pressure, dyne cm^{-2}	N Total concentration, cm^{-3}	T Kinetic temperature, °K	P Total pressure, dyne cm^{-2}	N Total concentration, cm^{-3}
	Ground air temperature T_0: 270°K			Ground air temperature T_0: 290°K		
0.000E-38	0.270000E 03	0.150000E 05	0.402442E 18	0.290000E 03	0.150000E 05	0.374688E 18
0.100E 06	0.265216E 03	0.140198E 05	0.382930E 18	0.285303E 03	0.140860E 05	0.357650E 18
0.200E 06	0.260433E 03	0.130876E 05	0.364034E 18	0.280607E 03	0.132139E 05	0.341123E 18
0.300E 06	0.255649E 03	0.122018E 05	0.345746E 18	0.275910E 03	0.123825E 05	0.325100E 18
0.400E 06	0.250866E 03	0.113609E 05	0.328057E 18	0.271213E 03	0.115904E 05	0.309573E 18
0.500E 06	0.246082E 03	0.105635E 05	0.310958E 18	0.266517E 03	0.108365E 05	0.294537E 18
0.600E 06	0.243969E 03	0.982068E 04	0.291597E 18	0.261820E 03	0.101195E 05	0.279983E 18
0.700E 06	0.242449E 03	0.912779E 04	0.272723E 18	0.259201E 03	0.944776E 04	0.264039E 18
0.800E 06	0.240929E 03	0.847988E 04	0.254963E 18	0.257361E 03	0.881875E 04	0.248222E 18
0.900E 06	0.239409E 03	0.787429E 04	0.238258E 18	0.255521E 03	0.822755E 04	0.233249E 18
0.100E 07	0.237889E 03	0.730850E 04	0.222551E 18	0.253681E 03	0.767214E 04	0.219081E 18
0.150E 07	0.230289E 03	0.499739E 04	0.157198E 18	0.244481E 03	0.536741E 04	0.159036E 18
0.200E 07	0.222689E 03	0.337379E 04	0.109748E 18	0.235281E 03	0.370391E 04	0.114038E 18
0.250E 07	0.215089E 03	0.224682E 04	0.756705E 17	0.226081E 03	0.251843E 04	0.806941E 17
0.300E 07	0.207489E 03	0.147457E 04	0.514811E 17	0.216881E 03	0.168515E 04	0.562850E 17
0.350E 07	0.199889E 03	0.952660E 03	0.345243E 17	0.207681E 03	0.110811E 04	0.386511E 17
0.400E 07	0.192289E 03	0.605138E 03	0.227969E 17	0.198481E 03	0.714951E 03	0.260935E 17
0.450E 07	0.184689E 03	0.377418E 03	0.148033E 17	0.189281E 03	0.451789E 03	0.172904E 17
0.500E 07	0.177089E 03	0.230767E 03	0.943970E 16	0.180081E 03	0.279037E 03	0.112246E 17
0.550E 07	0.171000E 03	0.139519E 03	0.591037E 16	0.171000E 03	0.168703E 03	0.714666E 16
0.600E 07	0.167000E 03	0.833532E 02	0.361562E 16	0.167000E 03	0.100788E 03	0.437190E 16
0.650E 07	0.163000E 03	0.491798E 02	0.218562E 16	0.163000E 03	0.594669E 02	0.264280E 16
0.700E 07	0.159000E 03	0.286390E 02	0.130478E 16	0.159000E 03	0.346295E 02	0.157770E 16
0.750E 07	0.155000E 03	0.164492E 02	0.768758E 15	0.155000E 03	0.198899E 02	0.929561E 15
0.800E 07	0.155000E 03	0.943916E 01	0.441142E 15	0.155000E 03	0.114136E 02	0.533416E 15
0.850E 07	0.155000E 03	0.541654E 01	0.253143E 15	0.155000E 03	0.654953E 01	0.306094E 15
0.900E 07	0.155000E 03	0.310821E 01	0.145263E 15	0.155000E 03	0.375836E 01	1.175648E 15

Fig. 10. Lower Atmosphere Model III for ground air temperatures 270 and 290°K. Surface pressure 15 mb (0.15×10^5 dyne cm^{-2}); atmospheric abundance 60% CO_2, 20% Ar, 20% N_2 by volume; mean molecular mass of atmospheric constituents 0.663921×10^{-22} gm.

Author	Class of model	T_o Ground air temperature, °K	Main constituents of lower atmosphere	P_o Surface pressure, mb	T_{meso} Temperature at mesosphere base, °K	h_{meso} Altitude of mesosphere base, km	g/c_p Adiabatic temperature gradient, °K/km
Neubauer, 1966	Convective	~250	CO_2, N_2	-	-	-	-
Anderson, 1965	Convective-radiative	175-325	CO_2, Ar	5.55	-	-	4.7-5.7
Leovy, 1966	Convective-radiative	225	CO_2	5	-	-	3.5
Ohring et al., 1967	Convective-radiative	148-260	CO_2, N_2	5-14	145-165	~25	4.35
Gierasch and Goody, 1967	Radiative	150-280	CO_2	4.9	155	50	5

Fig. 11. Table of contemporary models for lower atmosphere of Mars.

CROSS REFERENCES

The specific section number, subject, and page number to which the reader is referred is given below.

Cross Reference	Section and Subject
[1] Mariner IV data and Earth-based observations	5.1.....Observed atmospheric constituents (data summary), p.1. 5.2.....Surface pressure (data summary), p.1.
[2] Troposphere	3.5.....Wind action (discussion), p.12.
[3] Dust-devil formation	4.1.....Yellow clouds (discussion), p.5-7.
[4] Surface temperature	3.1.....Surface temperatures (data summary), p.1, and brightness temperature characteristics (data summary), p.2; Martian surface temperature (figure), p.8.
[5] Absorption of solar photons and infrared radiation	6.....Absorption in the Martian atmosphere (discussion), p.6.
[6] Prabhakara and Hogan's 1965 model in relation to establishing boundary conditions for upper atmospheric profiles	5.4.....Upper Atmosphere F_1-Model (discussion), p.10.
[7] Diurnal, seasonal, and latitudinal variation of atmospheric parameters	3.1.....Surface thermal properties (discussion), p.3. 4.2.....Seasonal activity, entire section.
[8] The blue haze	4.1.....The violet layer (data summary), p.1; The violet layer, blue clouds, and blue clearing (discussion), p.2-5.

BIBLIOGRAPHY

Anderson, A.D., 1965, A model for the lower atmosphere of Mars based on Mariner IV occultation data: Palo Alto, Calif., Lockheed Palo Alto Research Lab., Tech.Memo.6-75-65-62.

Fleagle, R.G., and Businger, J.A., 1963, An introduction to atmospheric physics (esp. p.70): New York, Academic Press.

Gierasch, P., and Goody, R.M., 1967, An approximate calculation of radiative heating and radiative equilibrium in the Martian atmosphere: Cambridge, Mass., Harvard U., Preprint.

Goody, R.M., 1964, Atmospheric radiation, I. Theoretical basis (esp. p.329): London, Oxford U.Press (Clarendon Press).

Goody, R.M., and Belton, M.J., 1967, Radiative relaxation times for Mars: a discussion of Martian atmospheric dynamics: Planet.Space Sci., v.15, p.247-256.

Hilsenrath, J., Hoge, H.J., Beckett, C.W., Masi, J.F., Benedict, W.C., Nuttall, R.L., Fano, L., Touloukian, Y.S., and Woolley, H.W., 1960, Tables of thermodynamic and transport properties of air, carbon dioxide, carbon monoxide, hydrogen, nitrogen, oxygen, and steam: New York, Pergamon Press.

Leovy, C., 1966, Radiative-convective equilibrium calculations for a two-layer Mars atmosphere: Santa Monica, Calif., RAND Corp., Memo.RM-5017-NASA.

Neubauer, F.M., 1966, Thermal convection in the Martian atmosphere: J.Geophys.Res., v.71, p.2419-2426.

Ohring, G., House, F., Sherman, C., and Tang, W., 1967, Study of the Martian atmospheric environmental requirements for spacecraft and entry vehicles: Bedford, Mass., GCA Corp., TR-67-12-G.

Prabhakara, C., and Hogan, J.S., Jr., 1965, Ozone and carbon dioxide heating in the Martian atmosphere: J.Atmos.Sci., v.22, p.97-109.

5.4 UPPER ATMOSPHERE

DATA SUMMARY

Interpretation of the data from the Mariner IV occultation experiment has led to development of three distinct types of models for the upper atmosphere of Mars: a preliminary E-Model, an F_1-Model at maximum solar flux (Figs. 1 through 5), and an F_2-Model at minimum solar flux (Figs. 6 through 8).[1*] In addition to occultation data, each of the models uses the best results of Earth-based observations, which are presented elsewhere in this document.[2]

The E-, F_1-, and F_2-Models are distinguished by the type of Earth-analog ionospheric layer which the ionized layer detected in the Martian atmosphere is thought to represent; they thus differ primarily in the structure of the ionosphere as derived from the physical and chemical processes thought to occur there. The "correct" choice among the models is not clear. The basic point of disagreement is proper identification of the concentration peak of the electron density profile measured at an altitude of approximately 120 km above Electris at the time of immersion of Mariner IV's S-band transmission on July 15, 1965.

DISCUSSION

Layers of the Upper Atmosphere

Using terrestrial nomenclature for classifying various regions of the atmosphere, the thermosphere is the highest region of the atmosphere where collisional interactions are still important, a region where kinetic temperature increases from its lowest value to a constant (which is quite high in the terrestrial case). The thermosphere differs from lower atmospheric levels because ionization and dissociation occur and diffusion becomes more important than mixing. The ionization region, or ionosphere, and dissociation region lie largely in the thermosphere. Both are produced primarily by interactions (photoionization and photodissociation) of extreme ultraviolet solar photons with atmospheric gases.

At some level in every atmosphere, called the critical level, the horizontal mean free path of neutral particles becomes equal to the density scale height. This critical level marks the base of the exosphere. In the exosphere, particles move along ballistic trajectories to a first approximation. If a magnetic field is present, it will fill a volume known as the magnetosphere, which generally extends beyond the exosphere and which must be considered in terms of its effects on charged-particle trajectories. The exosphere or magnetosphere is the region whose conditions determine the probability of escape of an atmospheric constituent.[3]

*See page 20 for list of cross references.

A planet without a permanent magnetic field may have a weak field convected into it by the solar wind. This, it is thought, would add to the formation of a collisionless bow shock in the solar wind ahead of and extending around the planet. Solar wind flow in the zone behind the shock offers a further factor affecting the exosphere. Attempts to account for this feature in relation to the Martian atmosphere are still in early stages and are not included in the atmospheric models presented in this section. (For additional reading about upper atmospheres, see Craig, 1965, and Fleagle and Businger, 1963).

Physics of the Upper Atmosphere

The important photochemical and physical processes which are believed to occur in the upper atmosphere of Mars are based upon the theories of photochemical and diffusive equilibrium in a quasi-stationary (approximately steady-state) atmosphere. These processes form the basis of the models presented in this section. The only available direct measurements of the properties of and processes occurring in the upper Martian atmosphere were provided by the 1965 Mariner IV occultation experiment.

Photodissociation Region

The photodissociative solar flux at a given height depends upon how much attenuation of the flux has taken place above the given level. The primary constituent that is photodissociated on Mars is CO_2. The significant reactions occurring are

$$CO_2 + h\nu \rightarrow CO + O \tag{1}$$

$$CO + O \rightarrow CO_2 + h\nu \tag{2}$$

$$O + O + M \rightarrow O_2 + M \tag{3}$$

$$O + O \rightarrow O_2 + h\nu \tag{4}$$

$$O_2 + h\nu \rightarrow O + O \tag{5}$$

$$O + CO + M \rightarrow CO_2 + M \tag{6}$$

where M is any third body in the three-body process, and $h\nu$ is the energy of the incident photon.

Absorption of the solar spectrum between 1800 and 2400 Å by CO_2 and O_2 is negligible (Norton, 1964). Rayleigh (molecular) scattering of extreme ultraviolet solar photons with wavelengths lying between 1800 and 2400 Å is quite small. The optical depth for Rayleigh scattering at $\lambda 2100$ at the surface of Mars for a pure CO_2 atmosphere is less than 0.5 and decreases as the height increases because there are fewer and fewer molecules to scatter the radiation (Coulson and Lotman, 1962). This radiation is therefore able to penetrate to a lower level, where it is available to be absorbed by ozone, if any ozone exists. There will be some modification in detail if nitrogen exists in significant quantities.

When atomic oxygen is released from photodissociation of CO_2, it is available for the oxidation of CO. The atomic oxygen may react with molecular oxygen through a third body to produce ozone.[4] Ozone could then disappear by absorption of the extreme ultraviolet solar radiation. In fact, there is good evidence that there is little ozone present and that a great deal of ultraviolet radiation penetrates to the Martian surface.[1]

To establish the major chemical processes important in the photodissociation region, the reaction rates of Eqs. (1) through (6) must be known. Two reactions produce CO_2, one by two-body association (Eq. 2) and the other by three-body association (Eq. 6). At the densities and temperatures of the Martian atmosphere, two-body association dominates (Smith and Beutler, 1967). Both two-body (Eq. 4) and three-body (Eq. 3) association of O_2 must be considered, as the rates are comparable (Smith and Beutler, 1967).

At 90 and 100 km the concentrations of CO, O_2, and O in the F_1-Model are given (Fig. 1) by photochemical equilibrium calculations based upon the reactions given by Eqs. (1) through (6). These were modified between 100 and 110 km by estimating the effect of the transport terms in the continuity equation (diffusion) to improve the values of the concentrations. From 110 km up to the critical level (the base of the exosphere) at about 500 km, the various atmospheric species are thought to be in diffusive equilibrium as given by

$$[x] = [x]_{110\ \mathrm{km}} \frac{T_{110\ \mathrm{km}}}{T} \exp\left[-\frac{m}{k}\int_{110\ \mathrm{km}}^{h} \frac{g}{T}\, dh\right] \tag{7}$$

where $[x]_{110\ \mathrm{km}}$ and $T_{110\ \mathrm{km}}$ are the concentration of any photodissociation product and the temperature, respectively, at a height of 110 km, m is the mean molecular mass, k is the Boltzmann constant, and g is the acceleration due to gravity.

Equation (7) is based upon the assumptions of hydrostatic equilibrium and the ideal equation of state and hence represents a diffusive distribution. Its applicability to the upper atmosphere of Mars to describe the concentration of various constituents as a function of altitude is valid even above the critical level, provided the deviation from hydrostatic equilibrium is small. Chamberlain (1963), in his monograph on the physics of planetary exospheres, tabulates the departure from hydrostatic equilibrium in terms of generally applicable atmospheric parameters. In the F_1-Model of Smith and Beutler the critical level occurs at approximately 500 km based upon the mean free path between oxygen-oxygen collisions. Yet Chamberlain's work shows Eq. (7) to be applicable to an altitude of nearly 30,000 km if magnetospheric phenomena are ignored.

Ionosphere

One method of formation of an ionospheric layer, the classic Chapman layer, can be understood as follows. At large heights the density of any gas is very low and the corresponding rate of formation of electron-ion pairs is low.

At small heights the ultraviolet solar flux capable of ionizing a particular gas may be reduced by its passage through the atmosphere; hence, the rate at this height can also be low. At intermediate heights the formation rate of electron-ion pairs will reach a maximum since the product of density and ionizing flux reaches a maximum.

There are other ways to form a layer. In general, however, ionization of various species occurs throughout a thermosphere, with rather broad maxima being as likely as distinct layers. The Mariner IV occultation data indicated the presence of an ionized layer in the Martian atmosphere at an altitude of approximately 120 km (ingress).

Ionization Processes. The production rate of electrons and ions is in competition with the loss rate. The primary reactions for the production of electrons are

$$X + h\nu \rightarrow X^+ + e \tag{8}$$

and

$$XY + h\nu \rightarrow XY^+ + e \tag{9}$$

where X is the atom and X^+ the corresponding ion, XY is the molecule and XY^+ the corresponding ion. Production of ions is more complex than that of electrons as a result of the various chemical processes that can occur. Figure 9 gives the reactions that may occur significantly in the ionosphere of Mars for a pure CO_2 lower atmosphere and shows that the primary constituents of the Martian ionosphere are CO^+, CO_2^+, O^+, O_2^+, and electrons. Smith and Beutler (1967) derive the following equations for the concentrations of these constituents based upon chemical equilibrium:

$$[CO^+] = \frac{q_3[CO]}{k_1[O] + (k_3 + k_5)[O_2] + k_8[CO_2] + \alpha_3[e]} \tag{10}$$

$$[CO_2^+] = \frac{q_4[CO_2] + k_8[CO^+]}{(k_2 + k_7)[O] + k_6[O_2] + \alpha_4[e]} \tag{11}$$

$$[O^+] = \frac{q_1[O] + (k_1[CO^+] + k_2[CO_2^+])[O] + k_3[CO^+][O_2]}{k_4[O_2] + k_9[CO_2] + \alpha_1[e]} \tag{12}$$

$$[O_2^+] = \frac{q_2[O_2] + (k_4[O^+] + k_5[CO^+] + k_8[CO_2^+])[O_2] + k_7[CO_2^+][O]}{\alpha_2[e]} \tag{13}$$

Charge neutrality requires that

$$[e] = [CO^+] + [CO_2^+] + [O^+] + [O_2^+] \tag{14}$$

The q's, α's, and k's in Eqs. (10) through (13) are rate coefficients for the various chemical processes appearing on the right side of Fig. 9.

The rate for photoionization q is not given explicitly in Fig. 9 but can be determined from Fig. 10. Values of the photoionization rate at a given altitude can be estimated by multiplying the extreme ultraviolet solar flux $J_o(\lambda)$ at the top of the Martian atmosphere by the cross section for photoabsorption $\sigma(\lambda)$ and by $e^{-\tau(\lambda)}$, where $\tau(\lambda)$ is the optical depth (at that altitude) at wavelength λ, to allow for absorption in higher atmospheric layers. The product $J_o(\lambda)\sigma(\lambda)e^{-\tau(\lambda)}$ is then integrated over λ for each constituent of the atmosphere.

To discuss the rate coefficients α and k it is necessary to simultaneously discuss the various chemical processes that can remove electrons and ions. The simplest process for loss of electrons and ions is the inverse of Eqs. (8) and (9), namely, radiative recombination.

$$X^+ + e \rightarrow X + h\nu \tag{15}$$

$$XY^+ + e \rightarrow XY + h\nu \tag{16}$$

A typical radiative recombination process which appears in Fig. 9 is

$$O^+ + e \rightarrow O + h\nu \tag{17}$$

with a rate coefficient $\alpha_1 = 2 \times 10^{-12}$ cm^3 sec^{-1}.

Nonradiative processes can remove electrons and ions much faster. If a molecular ion XY^+ recombines with an electron, the energy of recombination can dissociate the molecule into two atoms X and Y and will proceed with a far greater rate constant than processes involving photon emission.

$$XY^+ + e \rightarrow X + Y \tag{18}$$

Dissociative recombination is limited to the lower parts of the upper atmosphere because under diffusive equilibrium these molecules will tend to be concentrated lower in the atmosphere than lighter constituents such as atomic oxygen.

The ionization balance of atomic species must take account of charge transfer, that is,

$$X^+ + YZ \rightarrow YZ^+ + X \tag{19}$$

and ion-atom (or molecule) exchange

$$X^+ + YZ \rightarrow XY^+ + Z \tag{20}$$

which with Eq. (18) offer a vehicle for efficient removal of X^+ ions and electrons. A typical charge transfer reaction appearing in Fig. 9 is

$$O^+ + O_2 \rightarrow O_2^+ + O \tag{21}$$

with a rate coefficient $k_4 = 3.5 \times 10^{-11}$ cm^3 sec^{-1}

In addition to the processes thus far mentioned, electron attachment can become important in the lower parts of the ionosphere.

$$X + e + M \rightarrow X^- + M \tag{22}$$

where M is any third body. The negatively charged ion can combine with a positively charged ion to produce two neutral particles.

$$X^- + Y^+ \rightarrow X + Y \tag{23}$$

The total recombination rate coefficient, which includes radiative and dissociative recombination, must take account of dielectronic recombination. Dielectronic recombination represents the capture of an electron by an ion in a process which results in excitation of the resulting neutral into an upper quantum state. In the process the captured electron gives up some of its extra energy to one of the bound electrons. The result of dielectronic recombination is thus an atom or molecule with a doubly-excited state which then normally decays by ordinary photon emission.

Thermal Processes. The vertical temperature distribution and vertical temperature gradient of the Martian ionosphere is calculated from a detailed energy balance. The Martian ionosphere obtains its energy from the Sun and is expected to be in quasi-stationary equilibrium with the local UV photon flux at any given time of day.[1]

A certain fraction of the solar radiant energy is reflected or absorbed directly by atmospheric gases or by clouds,[5] and the remainder is absorbed or

reflected by the Martian surface.[6] Of the energy absorbed by the Martian surface a large fraction is then reradiated in the infrared, where it can be absorbed by gases in the lower atmosphere. This energy trapping in the lower atmosphere constitutes a greenhouse effect which results in an increase of the surface temperature[7] above the temperature for a corresponding atmosphere that is optically thin (transparent) at all wavelengths.

The extreme ultraviolet solar photons that are absorbed by the Martian atmospheric gases supply the energy required to maintain the thermosphere. The rate of thermal energy input into the thermosphere for each constituent is

$$E_j(h) = \int \epsilon_j(\lambda)\, \sigma_j(\lambda)\, N_j\, J_o(\lambda)\, e^{-\tau(\lambda)}\, d\lambda \tag{24}$$

where N_j represents the number density of constituent j and $\epsilon_j(\lambda)$ represents the efficiency for conversion of ultraviolet solar radiation to heat via photochemical processes by the j-th constituent; the other quantities have been defined previously. The total rate of heat input is the sum of E_j for all constituents; hence,

$$E(h) = \sum_j E_j(h) \tag{25}$$

The thermosphere of Mars is cooled by the rotational, vibrational, and electronic radiation of CO, CO_2, and O, respectively. The total rate of energy loss at each level of the thermosphere from the infrared radiation is

$$R(h) = \sum_j R_j(h) \tag{26}$$

where R_j represents the infrared radiative term for each constituent j. The only other mechanism considered significant in heat loss is thermal conduction. The thermal conductive flux is $AT^{1/2}\, dT/dh$ where $(AT^{1/2})$ is a weighted mean coefficient of thermal conductivity for CO_2, O_2, CO, and O.

The energy balance equation can now be written

$$\rho c_V \frac{\partial T}{\partial t} = \frac{\partial}{\partial h}\left(-AT^{1/2}\frac{\partial T}{\partial h}\right) + E(h) - R(h) \tag{27}$$

where ρ is total mass density of the gas, c_V is specific heat at constant volume, and $\partial T/\partial t$ is time rate of change of the kinetic temperature. Equation (27) is solved for quasi-stationary equilibrium ($\partial T/\partial t \simeq 0$); hence,

$$AT^{1/2}\frac{dT}{dh} = \int_h^\infty (E - R)\, dh \tag{28}$$

Equation (28) determines the temperature gradient for the upper atmosphere of Mars. The temperature profile is then found by numerical integration using a previously derived lower atmosphere as the lower set of boundary conditions. Since E(h), through $e^{-\tau(\lambda)}$, depends on the integrated atmosphere above h, an iterative procedure is necessary.

Contemporary Models of the Upper Atmosphere

Contemporary models of the upper Martian atmosphere are based on the general theory beginning on page 2 and ending above. They all use interpretations of data from the Mariner IV occultation experiment and the best results of Earth-based observations. The models are classified by approximate analogy to terrestrial ionospheric nomenclature as E-, F_1-, or F_2-(region) Models. Ionospheric regions or layers are differentiated by the wavelength of the radiation producing the region, by the principal ionic constituent, and by the dominant loss mechanism of ions and electrons.

The E-region of the Earth's atmosphere is produced primarily by x-rays from about 10 to about 100 Å assisted by some ultraviolet radiation from 800 to 1026 Å — particularly by emission lines such as Lyman β at 1025 Å (Craig, 1965). The most important ion produced is O_2^+, and the loss mechanism is primarily dissociative recombination. This region is a fair approximation to the classic Chapman layer described briefly on page 3, a layer in which the peak electron density is approximately coincident with the peak of the electron production.

The terrestrial F-region is produced by extreme ultraviolet radiation in the wavelength range from 200 to 800 Å with some contribution from longer wavelengths. The principal ion present is O^+ (Craig, 1965). The loss mechanism is ion-atom interchange up to a high level, where radiative recombination becomes dominant. This is a height-dependent process which results in the peak electron density being at a much higher altitude than the peak of production, a so-called Bradbury layer. Actually, the F-region contains two peaks: a lower layer called the F_1-layer near the production maximum, and the Bradbury layer peak called the F_2-peak (Craig, 1965).

Preliminary E-Model

In their preliminary paper, Chamberlain and McElroy (1966) interpret the ionization layer above Electris to be an E-region. They assume a composition of only 44% CO_2, the remainder being N_2. Their model relies heavily on the speculative assumption that mixing provides homogeneous composition of constituent gases throughout the entire upper atmosphere. They assume that the rate of photodissociation is so small that CO_2 will be only partially photodissociated, even at great heights, primarily because the rapid formation of O_2 (from O resulting from the CO_2 dissociation) shields the CO_2. They further assume a very large rate coefficient for dissociative recombination of CO_2^+ to prevent formation of an F_1-region above the E-region (since of course none was observed). A new determination of this coefficient by Weller and Biondi (1967) makes it difficult to accept such an assumption.

These assumptions can result in an ionosphere dominated by O_2^+ (or perhaps NO^+)[8] in a Chapman layer created primarily by x-rays.[1] With appropriate rate coefficients the layer is of the strength and at the height measured by

Mariner IV. Chamberlain and McElroy's assumptions seem questionable according to proponents of other models; in addition, they do not present the observed ionospheric scale height. However, Chamberlain and McElroy are working on much more detailed calculations, and a final E-Model will be added to this section when the results become available from these authors.

F_1-Model (Figs. 1 through 5)

This model is based upon the work of Smith and Beutler (1967), who have interpreted the ionization layer observed over Electris to be an F_1-region. It presents the largest reasonable values possible for density and kinetic temperatures above 90 km, without going to an E-type model, and utilizes maximum ultraviolet solar flux and the best available rate coefficients for photochemical and diffusive processes. (The model has been used to illustrate the discussion on pages 2 through 8.) More extreme models are possible if there are errors in current theories and/or constants.

The calculated neutral number densities and temperatures versus altitude for the F_1-Model are tabulated in Fig. 1. Figure 2 contains profiles of electron density and densities of the most abundant molecular and atomic ion species; the CO_2^+ abundance is very small and therefore is not shown. Figures 3 and 4 respectively give profiles of temperature versus altitude and of neutral density versus altitude. Figure 5 shows the rate of photoionization of neutral atoms and molecules above an altitude of 90 km. Since production of electron-ion pairs by photoabsorption completely dominates other formation mechanisms, the figure thus represents total ion production rate, which in turn is based upon the rate of photoabsorption of extreme ultraviolet solar photons at sunspot maximum (Fig. 10).

The F_1-Model results in three ionization peaks characterized by F-type charge transfer loss processes. In the lower layers of the upper atmosphere the most abundant molecular ion is O_2^+. Peak concentration of O_2^+ is 37,000 particles cm^{-3} at an altitude of 160 km. The dominant ion in the upper, or F_2-type, layer is O^+, which reaches a concentration of 8.8×10^5 particles cm^{-3} at an altitude of 420 km. In fact, O^+ is the most abundant atomic ion anywhere in the upper atmosphere of Mars.

The results of the Mariner IV occultation experiment as presented by Kliore et al. (1967) indicate that only one of these layers, the lowest, was detected; peak electron concentration (ingress) was $9.0 \pm 1.0 \times 10^4$ electrons cm^{-3} at an altitude of 123 ± 3 km. Smith and Beutler (1966) suggest that with low solar activity and at large solar zenith angle, as encountered by Mariner IV, the large upper peak (of the F_2-type) at 420 km will disappear. They further imply that the two lower peaks at 120 and 160 km will coalesce under these conditions into a single thin but rather dense O_2^+ peak of the F_1-type, creating the peak observed by Mariner IV. In a brief paper that presents no detailed results, Donahue (1966) also interprets the ionization layer over Electris to be an F_1-region and comments that an F_2-layer can be suppressed if loss of O^+ via the reaction

$$O^+ + CO_2 \rightarrow CO + O_2^+ \tag{29}$$

indeed has a rate coefficient of 1.2×10^{-9} cm^3 sec^{-1}

At an altitude of 90 km, which is roughly the lower boundary of the thermosphere in the Smith and Beutler F_1-Model, the kinetic temperature, total gas pressure, and concentration of CO_2 are taken from lower atmosphere Model I of Prabhakara and Hogan (1965).[9] The concentration of CO_2 for Model I of Prabhakara and Hogan is changed from 44% to 100%. The assumptions used to generate the F_1-Model of Smith and Beutler (1967) are listed below.

1) CO_2 is assumed to be the only significant constituent of the lower atmosphere. This is consistent with the results of Mariner IV data.

2) The atmosphere is assumed to be in a quasi-stationary equilibrium.

3) Advection, the horizontal transport of convective cells of matter, is considered negligible. Inclusion of horizontal transport would reduce the effectiveness of diffusion.

4) The solar extreme ultraviolet spectrum used to represent the dissociating and ionizing agent for the upper atmosphere is based on data from maximum solar activity (Fig. 10). If the spectrum were based on data from minimum solar activity, the flux contained in Fig. 10 would be smaller by a factor of approximately two (Ohring, 1967).

5) Mixing and eddy diffusion are assumed present in the lower atmosphere and represent the primary mechanism for the transport of photodissociation products to this region. With this assumption Smith and Beutler use the results of Prabhakara and Hogan (1965) to obtain the concentration of CO_2 and temperature at the base of the photodissociation region.

6) The primary mechanisms that establish the adopted temperature profile for the upper atmosphere of Mars are assumed to be heating due to absorption of the extreme ultraviolet solar radiation and subsequent cooling by radiation in the infrared and thermal conduction.

7) Both chemical and diffusive equilibrium are used to establish the particle concentration in the upper atmosphere.

8) The equation of state for the upper atmosphere and ionosphere of Mars is assumed ideal.

9) Gravity through the upper atmosphere is assumed to vary inversely with the square of the areocentric distance $(R_o + h)$.

10) Accretion or escape of CO_2 to the interplanetary medium is assumed negligible. This implies no net flux or transport of CO_2 other than the removal by photodissociation.

11) The magnetic field of Mars is assumed negligible. A magnetic field does not affect neutral constituents of an atmosphere. If the neutral constituents are in diffusive equilibrium, they will maintain this equilibrium with the injection of a magnetic field. On the other

hand, the molecular and atomic ions will be affected by lines of force and ultimately will be able to diffuse only along the magnetic lines of force. A magnetic field would lead to the probable development of weak radiation belts high in the upper atmosphere.[3]

12) Collisional dissociation and ionization by the solar wind is assumed negligible. During maximum solar activity the solar wind and extreme ultraviolet radiation will have comparable energy fluxes.

13) Aerosol concentration is considered negligible.

14) The model is derived for the subsolar region of the atmosphere.

15) Latitudinal and seasonal variations in the atmosphere are neglected.

16) Charge neutrality is assumed; hence, no residual electric fields exist.

F_2-Model (Figs. 6 through 8)

This model is based upon the work of Fjeldbo, Fjeldbo, and Eshleman (1966b), who have interpreted the ionization layer above Electris to be an F_2-region. It should be considered a limiting lower density model with the lowest reasonable exospheric temperature; it uses minimum extreme ultraviolet solar flux and the best available photochemical and diffusive constants. A more extreme model is conceivable only if there are errors in the current theories and/or constants.

The calculated neutral and electronic number densities and temperatures versus altitude for the F_2-Model are tabulated in Fig. 6. Figure 7 gives the calculated concentrations of [O], [CO], [CO_2], and [e] for the upper atmosphere, the base of which starts at roughly 90 km—the altitude for minimum temperature. Above this altitude [O] becomes the dominant constituent. Figure 8 gives the temperature profile above an altitude of 90 km. Above 135 km the temperature becomes isothermal at a value of 80°K.

The F_2-Model relies heavily on the assumption that loss of O^+, which Fjeldbo et al. assume to be the principal constituent of the ionosphere, is governed by Eq. (29) with a rate coefficient of 10^{-9} cm^3 sec^{-1}. The model does not include additional nonradiative processes such as those found in Fig. 9.

At an altitude of 120 km the electron concentration and kinetic temperature of the F_2-Model agree with the results from the Mariner IV occultation experiment (ingress), which also indicated that at the surface of Mars (Electris) the pressure was 4.9 to 5.2 mb, air temperature was 175 to 180°K, and concentration of CO_2 was 1.9 to 2.1 x 10^{17} particles cm^{-3} (Kliore et al., 1967). The model parameters are adjusted to match these data. Egress data over Mare Acidalium indicated a surface pressure of 7.6 to 8.2 mb and a temperature of 235 to 240°K, but this information was not yet available when Fjeldbo et al. produced their model. Since this is presented as a limiting model, the lack of egress data is immaterial.[10]

The assumptions used to generate the F_2-Model of Fjeldbo, Fjeldbo, and Eshleman (1966b) are as follows:

1) The lower atmosphere is assumed to be pure CO_2.

2) The photochemistry assumed to be significant in the upper atmosphere is photodissociation of CO_2 and O_2 by the extreme ultraviolet solar radiation.

3) Three-body association is assumed to be the dominant mechanism for formation of O_2 and CO_2.

4) Molecular diffusion is assumed to be the dominant physical process that establishes the concentration of constituents.

5) "Hard" corpuscular radiation is assumed to be a negligible ionizing agent.

6) The temperature profile represents an empirical fit to the data of the Mariner IV occultation experiment. No energy balance was assumed.

7) It is assumed that formation of dry ice (condensed CO_2) can occur near the base of the exosphere.

8) Aerosol concentration is assumed negligible.

9) The model is derived for local conditions over the occulting regions on Mars.

10) Latitudinal and seasonal variations in the atmosphere are neglected.

11) The magnetic field of Mars is assumed negligible.

12) The equation of state for the upper atmosphere is assumed ideal.

13) Gravity through the upper atmosphere is assumed to vary inversely with the square of the areocentric distance.

14) Charge neutrality is assumed; hence, no residual electric fields exist.

Johnson (1965) has also interpreted the ionization layer above Electris as an F_2-region. The model of Johnson is an empirical model which uses the plasma scale height observed by Mariner IV and assumes that O^+ is the dominant ion in the upper atmosphere in order to derive an exospheric temperature of 85°K. The temperature distribution is not obtained from a detailed energy balance but is assumed to follow the vapor pressure curve for dry ice in the phase equilibrium diagram.[11] This highly speculative assumption is not based upon calculated or observed results but represents the result of plausibility arguments. Fjeldbo et al. (1966a) compare all post-Mariner IV models in a good review of the subject.

CONCLUSIONS

Lacking detailed information, contemporary models tend to rely heavily on terrestrial analogy even though the differences in atmospheric composition between planets make such analogies of dubious value. For example, an F_1 ionization layer in the terrestrial atmosphere will generally appear more frequently near midday and in summer than near sunset or sunrise or in winter (Yonezawa, 1966). The reason for this is that the level at which the peak in the electron production profile occurs in the terrestrial atmosphere is a function of the solar zenith angle. Table VII of Yonezawa demonstrates that the altitude at which the peak in the electron production profile occurs increases as the solar zenith angle increases. If the altitude of the electron production peak lies below the altitude of the boundary that separates radiative and nonradiative removal processes, then an F_1-region will appear. If the above conditions are not satisfied, then an F_1-region will not form. The immersion data from Mariner IV occurred in winter with a solar zenith angle of 67° above Electris (Kliore et al., 1967).[12] Therefore, it would seem inappropriate to call the ionization layer observed over Electris an F_1-layer even though it has some of the properties of such a layer.

All the models use photochemical and diffusive rate coefficients which are not well determined. The result of using various values for the rate coefficients that exist is to produce models that contain a great deal of uncertainty. With an inappropriate identification of the ionization layer that was observed by Mariner IV, and the ignoring of predicted layers not observed by the probe, plus the use of different rate coefficients, plus some "hand-waving," many models can be produced that will reproduce the Mariner IV data. Figure 11 outlines the models that are based on the results of Mariner IV. From the figure it is seen that there are great differences in atmospheric parameters among the various models. The E- and F_1-Models show a high exospheric temperature while the F_2-Models show a low exospheric temperature. The effort to build a model that correctly describes the Mariner IV occultation experiment has created more questions than answers about the structure of the upper atmosphere of Mars.

h Height above mean surface,[a] km	T Kinetic temperature of atmospheric constituents, °K	Concentration,[b] cm^{-3}				H(O) Density scale height for atomic oxygen, km
		$[CO_2]$	[CO]	$[O_2]$	[O]	
90	155	1.89^{13}	1.16^{12}	3.64^{11}	4.32^{11}	-
100	137	5.92^{12}	1.82^{12}	1.34^{11}	1.55^{12}	-
110	132	1.47^{12}	1.31^{12}	2.22^{10}	1.26^{12}	-
120	135	3.70^{11}	5.28^{11}	3.58^{9}	7.45^{11}	20.1
130	149	9.10^{10}	2.08^{11}	5.00^{8}	4.20^{11}	22.3
140	166	2.04^{10}	8.97^{10}	9.3^{7}	2.48^{11}	24.9
160	200	2.88^{9}	2.08^{10}	2.4^{6}	9.93^{10}	30.4
200	327	1.13^{8}	2.22^{9}	1.6^{3}	2.24^{10}	50.9
240	415	1.37^{7}	5.31^{8}	-	8.94^{9}	66.0
280	462	2.57^{6}	1.77^{8}	-	4.55^{9}	75.1
320	488	6.10^{5}	6.84^{7}	-	2.57^{9}	81.1
400	508	4.38^{4}	1.26^{7}	-	9.67^{8}	88.1
480	514	3.70^{3}	2.63^{6}	-	3.92^{8}	92.8
560	516	3.63^{2}	6.00^{5}	-	1.68^{8}	97.2
640	520	-	-	-	9.25^{7}	102.1
720	520	-	-	-	5.22^{7}	106.1
800	520	-	-	-	3.00^{7}	110.4
900	520	-	-	-	1.58^{7}	115.6
1000	520	-	-	-	8.42^{6}	121.3

[a] Smith and Beutler (1967) <560 km; Monash >560 km including H(O) and [O] calculated from Eq. (7), page 3.

[b] The superscript in concentration values is the power of ten to which the value must be raised. For example, $1.89^{13} = 1.89 \times 10^{13}$.

Fig. 1. Upper Atmosphere F_1-Model: table of calculated neutral number densities and temperatures vs. altitude. $H(O) = kT/\mu g = 5.20 \times 10^1\ T/g$, where $g = g_o/(1 + h/R_o)^2$. T is in °K, g in cm sec^{-2}. $g_o = 375$ cm sec^{-2}, and $R_o = 3380$ km.

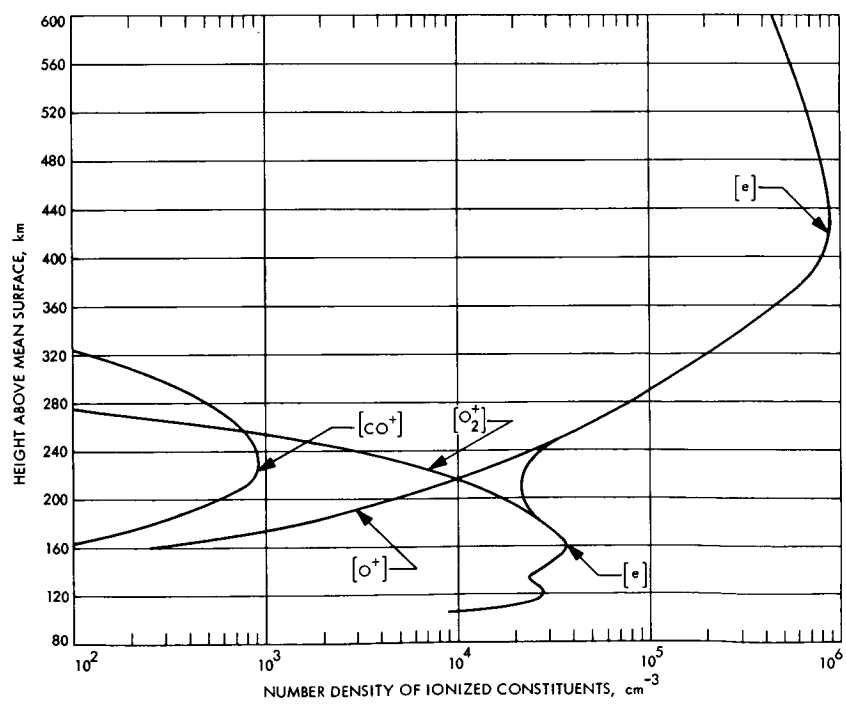

Fig. 2. Upper Atmosphere F_1-Model: ion and electron density vs. altitude. Note that below 200 km, the curve for electron concentration coincides with the O_2^+ concentration curve. Above 240 km, the curve for electron concentration coincides with the O^+ concentration curve.

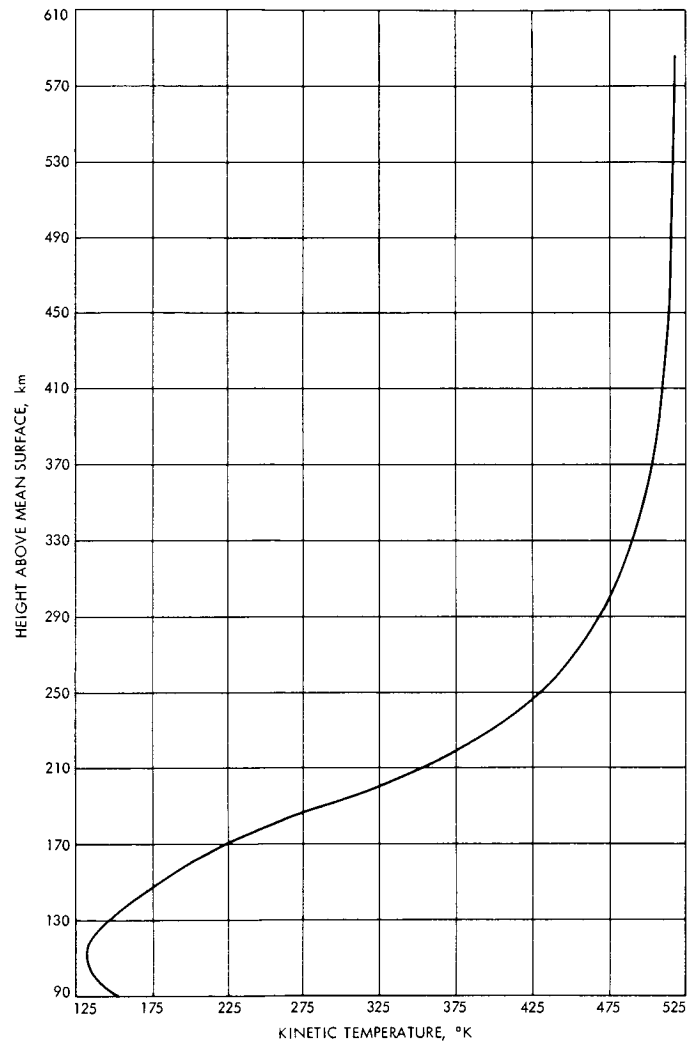

Fig. 3. Upper Atmosphere F_1-Model: temperature vs. altitude. This figure is a graph of the second column (Temperature) of Fig. 1; the same precautions that exist for Fig. 1 therefore apply.

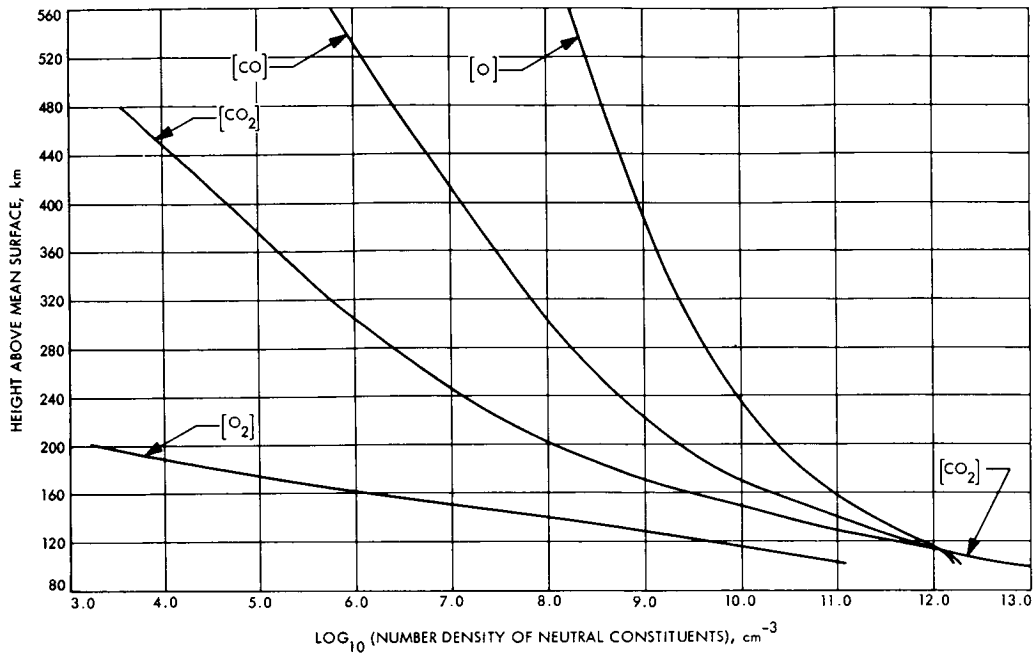

Fig. 4. Upper Atmosphere F_1-Model: neutral density vs. altitude. This figure is a graph of the third through sixth columns (Concentration) of Fig. 1; the same precautions that exist for Fig. 1 therefore apply.

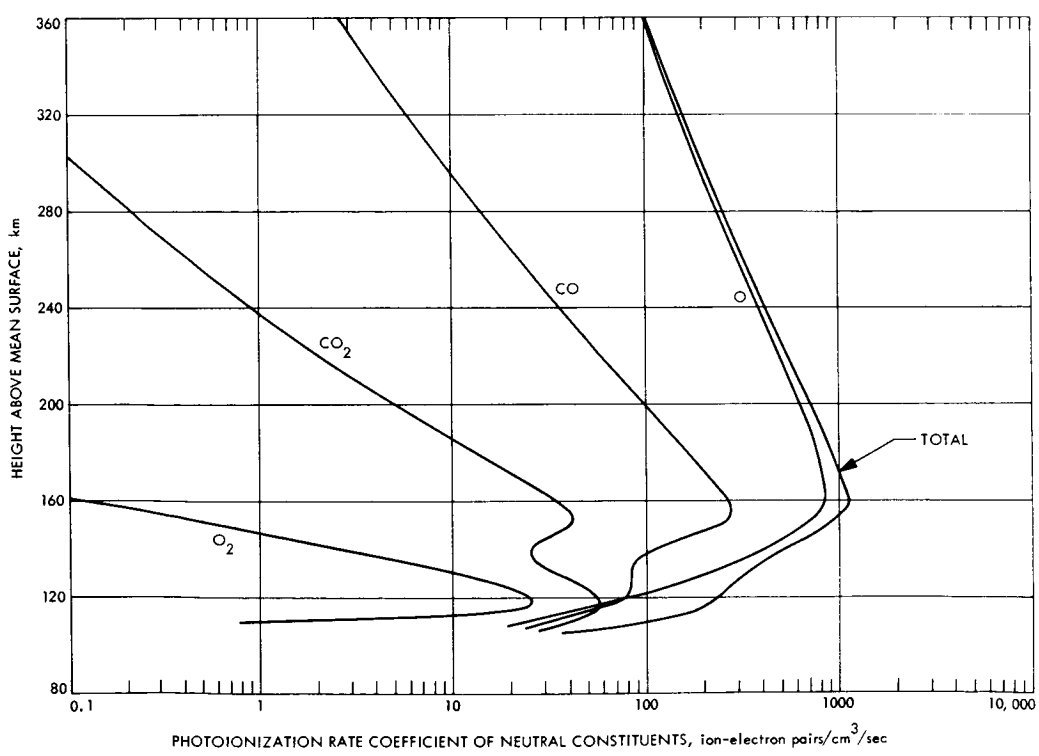

Fig. 5. Upper Atmosphere F_1-Model: profiles of photoionization rate of neutral constituents.

h Height above mean surface, km	T Kinetic temperature of atmospheric constituents, °K	Concentration,[a] cm^{-3}				H(O) Density scale height for atomic oxygen, km
		[CO_2]	[O]	[CO]	[e]	
90	50	7.95^{10}	5.01^{10}	1.58^{10}	-	7.31
100	51	1.26^{9}	1.26^{10}	1.78^{9}	2.00^{4}	7.49
110	60	5.63^{7}	3.16^{9}	1.78^{8}	3.16^{4}	8.87
120	70	3.16^{6}	1.00^{9}	2.00^{7}	8.90^{4}	10.4
130	78	2.00^{5}	3.54^{8}	3.54^{6}	6.60^{4}	11.7
140	80	-	1.41^{8}	1.00^{6}	4.78^{4}	12.0
150	80	-	7.08^{7}	-	3.32^{4}	12.1
160	80	-	3.54^{7}	-	2.34^{4}	12.2
170	80	-	1.86^{7}	-	1.58^{4}	12.2
180	80	-	1.00^{7}	-	1.00^{4}	12.3
190	80	-	5.63^{6}	-	-	12.4
200	80	-	3.54^{6}	-	-	12.4

[a]The superscript in concentration values is the power of ten to which the value must be raised. For example, $7.95^{10} = 7.95 \times 10^{10}$.

Fig. 6. Upper Atmosphere F_2-Model: table of calculated neutral and electronic number densities and temperature vs. altitude. $H(O) = kT/\mu g = 5.20 \times 10^1\ T/g$, where $g = g_o/(1 + h/R_o)^2$. T is in °K, g in cm sec^{-2}. $g_o = 375$ cm sec^{-2}, and $R_o = 3380$ km.

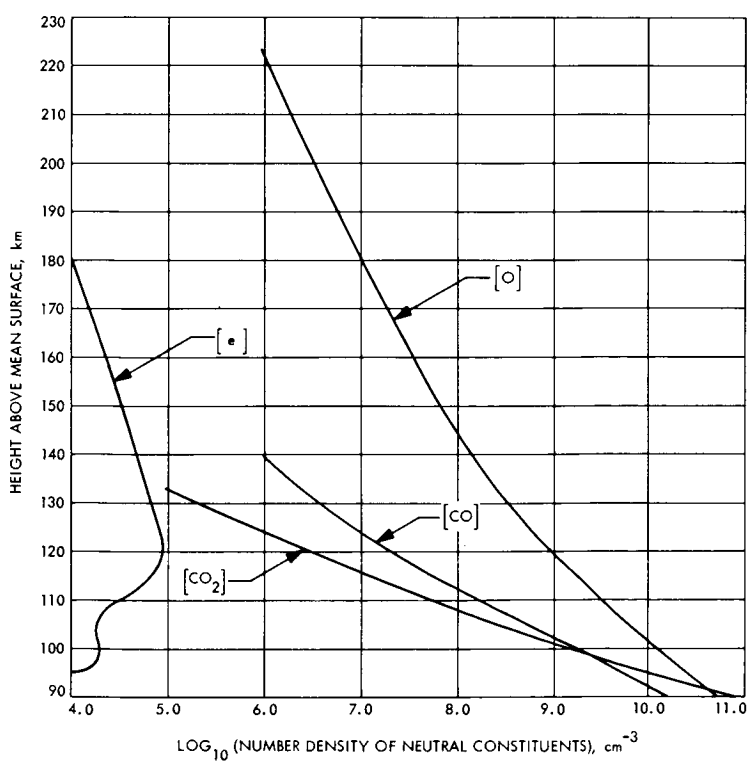

Fig. 7. Upper Atmosphere F_2-Model: number density of electronic and neutral constituents vs. altitude.

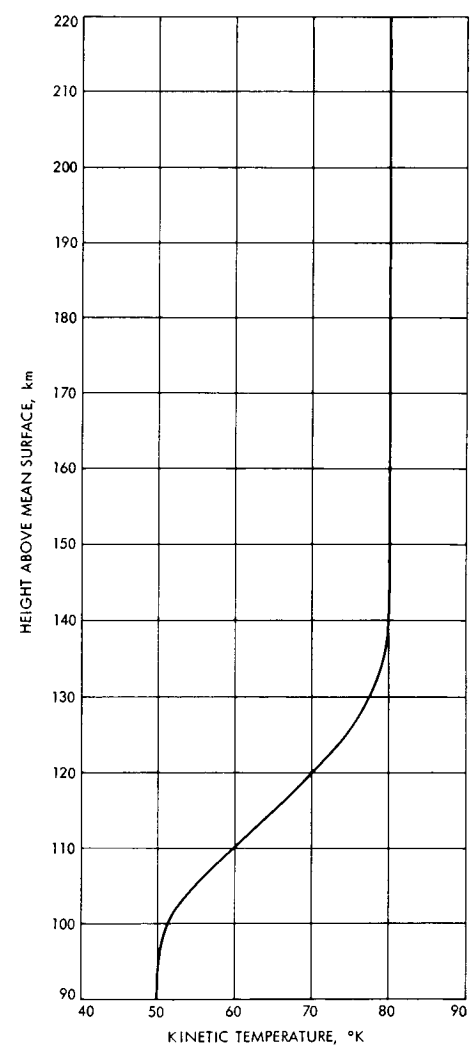

Fig. 8. Upper Atmosphere F_2-Model: temperature vs. altitude.

Reaction	Rate coefficient
$O + h\nu \rightarrow O^+ + e$	q_1 sec^{-1}
$CO^+ + O \rightarrow O^+ + CO + 0.38$ e.v.	$k_1 = 2 \times 10^{-12}$ cm^3 sec^{-1}
$CO_2^+ + O \rightarrow O^+ + CO_2 + 0.16$ e.v.	$k_2 = 2 \times 10^{-12}$ cm^3 sec^{-1}
$CO^+ + O_2 \rightarrow O^+ + CO_2 + 0.73$ e.v.	$k_3 = 1 \times 10^{-12}$ cm^3 sec^{-1}
$O^+ + e \rightarrow O + h\nu$	$\alpha_1 = 2 \times 10^{-12}$ cm^3 sec^{-1}
$O^+ + O_2 \rightarrow O_2^+ + O + 1.58$ e.v.	$k_4 = 3.5 \times 10^{-11}$ cm^3 sec^{-1}
$O_2 + h\nu \rightarrow O_2^+ + e$	q_2 sec^{-1}
$CO^+ + O_2 \rightarrow O_2^+ + CO + 1.93$ e.v.	$k_5 = 2 \times 10^{-10}$ cm^3 sec^{-1}
$CO_2^+ + O_2 \rightarrow O_2^+ + CO_2 + 1.71$ e.v.	$k_6 = 1 \times 10^{-10}$ cm^3 sec^{-1}
$CO_2^+ + O \rightarrow O_2^+ + CO + 1.36$ e.v.	$k_7 = 5 \times 10^{-11}$ cm^3 sec^{-1}
$O_2^+ + e \rightarrow O + O + 6.92$ e.v.	$\alpha_2 = 2 \times 10^{-7}$ cm^3 sec^{-1}
$CO + h\nu \rightarrow CO^+ + e$	q_3 sec^{-1}
$CO^+ + CO_2 \rightarrow CO_2^+ + CO + 0.22$ e.v.	$k_8 = 1.1 \times 10^{-9}$ cm^3 sec^{-1}
$CO^+ + e \rightarrow C + O + 2.85$ e.v.	$\alpha_3 = 1 \times 10^{-7}$ cm^3 sec^{-1}
$CO_2 + h\nu \rightarrow CO_2^+ + e$	q_4 sec^{-1}
$O^+ + CO_2 \rightarrow O_2^+ + CO + 1.20$ e.v.	$k_9 = 1.2 \times 10^{-9}$ cm^3 sec^{-1}
$CO_2^+ + e \rightarrow CO + O + 8.23$ e.v.	$\alpha_4 = 3 \times 10^{-7}$ cm^3 sec^{-1}

Fig. 9. Table of significant reactions in the Martian ionosphere for a pure CO_2 lower atmosphere. (Smith and Beutler, 1967)

Wavelength region, Å	Incident solar flux density, cm^{-2} sec^{-1}		σ Absorption cross section, cm^2			
	J_0 Photons	S_0 Ergs	(O_2)	(CO_2)	(O)	(CO)
1800-1700	974×10^9	10.95	0.25×10^{-18}	0.0064×10^{-18}	-	-
1700-1600	358	4.28	2.0	0.0741	-	-
1600-1300	193	2.51	8.0	0.0432	-	-
1300-1100	164	2.74	0.5	1.88	-	-
1100-1030	6.44	0.131	0.5	17.5	-	-
1030-912	5.33	0.0942	5.15	5.15	-	-
912-885	2.48	0.0434	7.28	7.28	2.69×10^{-18}	-
885-712	1.77	0.0543	10.17	12.90	3.05	12.90×10^{-18}
712-200	5.88	0.382	17.00	12.34	8.80	12.34
200-130	1.06	0.123	6.61	5.71	3.30	5.71
130-90	0.276	0.0531	1.67	1.60	0.87	1.60
90-44	0.649	1.85	0.84	0.65	0.42	0.66

Fig. 10. Table of incident solar flux densities at Mars and absorption cross sections for selected wavelength regions. (Smith and Beutler, 1967)

Author	Class of model	T_{ex} Exospheric temperature, °K	Main constituents of upper atmosphere	Concentration per cm^3 at 100-km altitude			P_o Assumed surface pressure, mbar	h_{ex} Height of exosphere above surface, km
				$[CO_2]$	$[O]$	$[CO]$		
Chamberlain and McElroy, 1966	E-region	~400	NO^+ or O_2^+	2×10^{13}	-	2×10^{12}	10	~300
Johnson, 1965	F_2-region	85	O^+	3×10^{10}	1×10^{10}	3×10^{9}	~4	100
Smith and Beutler, 1966	F_1-region	420	O^+	5×10^{11}	2×10^{11}	3×10^{11}	7	~600
Donahue, 1966	F_1-region	400	O_2^+	2×10^{12}	3×10^{10}	3×10^{10}	7	250
Fjeldbo, Fjeldbo, and Eshleman, 1966b	F_2-region	80	O^+	2×10^{9}	2×10^{10}	2×10^{9}	5	~140
Gross, McGovern, and Rasool, 1966	?	550	O^+	-	-	-	8	~300
Smith and Beutler, 1967	F_1-region	520	O^+	5.92×10^{12}	1.55×10^{12}	1.82×10^{12}	10	560

Fig. 11. Table of models for upper atmosphere of Mars based on Mariner IV results.

CROSS REFERENCES

The specific section number, subject, and page number to which the reader is referred is given below.

Cross Reference	Section and Subject
[1] Solar flux, ultraviolet radiation, x-radiation	6.....Solar electromagnetic radiation (discussion), p.5,6.
[2] Mariner IV data and Earth-based observations	5.1.....Observed atmospheric constituents (data summary), p.1. 5.2.....Occultation experiment results (discussion), p.3; Occultation (discussion), p.8,9.
[3] Exosphere or magnetosphere	6.....Magnetic fields, solar wind, and energetic particles (discussion), p.7-9.
[4] Atomic oxygen, molecular oxygen, and ozone	5.1.....Assumed atmospheric constituents (discussion), p.7,8.
[5] Clouds	4.1.....Clouds and hazes, entire section.
[6] Surface reflectivity	3.2.....Spectral reflectivity and distribution (data summary), p.2; Albedo, magnitude, and color (discussion), p.4.
[7] Surface temperature and the greenhouse effect	3.1.....Surface thermal properties, entire section.
[8] NO^+ in the ionosphere	5.1.....Oxides of nitrogen (discussion), p.9.
[9] Upper Atmosphere F_1-Model—temperature, gas pressure, and CO_2 concentration at 90-km altitude	5.3.....Prabhakara and Hogan's 1965 convective-radiative models of the lower atmosphere (discussion), p.6,7.
[10] Surface pressure and ground air temperature	5.2.....Surface pressure (data summary), p.1. 5.3.....Ground air temperatures (figure), p.10.
[11] Phase equilibrium diagram	3.4.....Phase diagram for carbon dioxide and water: pressure vs. temperature (figure), p.9.
[12] Martian seasons at the time of Mariner IV Mars flyby	1.....Calendar of Earth-Mars equivalent dates for 1964 and 1965 (figure), p.17. 4.2.....Seasonal activity map for northern summer and southern winter (figure), p.23; Martian place-names and locations (figure), p.25.

BIBLIOGRAPHY

Chamberlain, J. W., 1963, Planetary coronae and atmospheric evaporation: Planet. Space Sci., v. 11, p. 901-960.

Chamberlain, J. W., and McElroy, M. B., 1966, Martian atmosphere: the Mariner occultation experiment: Science, v. 152, p. 21-25.

Coulson, K. L., and Lotman, M., 1962, Molecular optical thickness of the atmospheres of Mars and Venus: Philadelphia, Penn., General Electric Co., Space Sci. Rep. R62 SD 71.

Craig, R. A., 1965, The upper atmosphere—meteorology and physics: New York, Academic Press.

Donahue, T. M., 1966, Upper atmosphere and ionosphere of Mars: Science, v. 152, p. 763-764.

Fjeldbo, G., Fjeldbo, W. C., and Eshleman, V. R., 1966a, Atmosphere of Mars: Mariner IV models compared: Science, v. 153, p. 1518-1523.

_____, 1966b, Models for the atmosphere of Mars on the Mariner 4 occultation experiment: J. Geophys. Res., v. 71, p. 2307-2316.

Fleagle, R. G., and Businger, J. A., 1963, An introduction to atmospheric physics: New York, Academic Press.

Gross, S. H., McGovern, W. E., and Rasool, S. I., 1966, Mars: upper atmosphere: Science, v. 151, p. 1216-1221.

Johnson, F. S., 1965, Atmosphere of Mars: Science, v. 150, p. 1445-1448.

Kliore, A. J., Cain, D. L., and Levy, G. S., 1967, Radio occultation measurements of the Martian atmosphere over two regions by the Mariner IV space probe, p. 226-239 in Moon and planets: Amsterdam, North-Holland Pub. Co.

Norton, R. B., 1964, A theoretical study of the Martian and Cytherian ionospheres: Washington, D. C., National Aeronautics and Space Administration, NASA Tech. Note TND-2333.

Ohring, G., 1967, Study of the Martian atmospheric environmental requirements for spacecraft and re-entry vehicles (esp. p. 21): Bedford, Mass., GCA Corp., Spec. Rep. 67-147.

Prabhakara, C., and Hogan, J. S., Jr., 1965, Ozone and carbon dioxide heating in the Martian atmosphere: J. Atmos. Sci., v. 22, p. 97-109.

Smith, N., and Beutler, A. E., 1966, A model Martian atmosphere and ionosphere: Ann Arbor, Mich., U. of Mich. Radio Astronomy Observatory, Rep. 66-3.

Smith, N., and Beutler, A. E., 1967, A model Martian atmosphere and ionosphere: Ann Arbor, Mich., U. of Mich. Space Physics Research Laboratory, Preprint.

Weller, C. S., and Biondi, M. A., 1967, Measurements of dissociative recombination of CO_2^+ ions with electrons: Phys. Rev. Lett., v. 19, p. 59-61.

Yonezawa, T., 1966, Theory of formation of the ionosphere: Space Sci. Rev., v. 5, p. 3-56.

SECTION 6 CONTENTS

6. CIS-MARTIAN MEDIUM, RADIATION: MAGNETIC AND RADIATION ENVIRONMENT OF MARS

Data Summary 3
- Solar Constant 3
- Solar Interplanetary Magnetic Field 3
- Magnetic Fields at Mars 3
- Solar Wind 4
- Energetic Particles 4

Discussion 5
- Solar Electromagnetic Radiation 5
  - The Solar Constant 5
  - Solar Spectral Distribution 5
  - Extreme Ultraviolet Radiation 5
  - X-Rays 6
  - Radio Waves 6
  - Absorption in the Martian Atmosphere 6
- Magnetic Fields 7
  - Solar Interplanetary Magnetic Field 7
  - Martian Magnetosphere and Magnetic Moment 7
  - Surface Magnetic Fields 8
- Solar Wind 8
  - Description 8
  - Effects on the Martian Atmosphere 8
- Energetic Particles 8
  - Solar Flare Protons 8
  - Cosmic Radiation 9
  - Interaction with the Martian Atmosphere 9

Cross References 19

Bibliography 20

Figures
1. Solar spectrum at Mars above the atmosphere 10
2. Table of solar spectral irradiance for the quiet Sun outside of any atmosphere at the mean distances of Earth and Mars 11
3. Table of solar wind proton (H^+) data for Earth and derived estimates for Mars 12
4. Table of solar wind alpha-particle (α) data for Earth and derived estimates for Mars 12
5. Table of solar wind electron (e^-) data for Earth and derived estimates for Mars 13
6. Estimates and upper limits of time histories of energetic protons produced by solar flares 14

6. (cont'd)

7. Estimate and upper limit of time-integrated flux of protons produced by a single solar flare vs. proton energy 15
8. Time-integrated flux of protons produced by solar flares vs. proton energy, for periods in 1959 and 1960 15
9. Probability of an integrated six-month flux (of protons with E > 5 Mev) greater than N produced by solar flares 16
10. Probability of an integrated six-month flux (of protons with E > 10 Mev) greater than N produced by solar flares 17
11. Cosmic-ray-induced charged-particle flux at the surface vs. atmospheric mass for Mars and Earth 18

6. CIS-MARTIAN MEDIUM, RADIATION: MAGNETIC AND RADIATION ENVIRONMENT OF MARS

DATA SUMMARY (Data sources are given in the Discussion.)

Solar Constant

The Sun emits electromagnetic radiation at all wavelengths from radio waves to x-rays. The mean solar constant is the integrated solar spectral irradiance. Spectral distribution is given in Figs. 1 and 2.

Preferred value at mean distance of Mars (based upon a value of 1.952 ±0.02 cal cm^{-2} min^{-1} at Earth)	0.841 cal cm^{-2} min^{-1} (586 W m^{-2})
Range of values at Mars:	
At aphelion[1]*	0.703 cal cm^{-2} min^{-1} (490 W m^{-2})
At perihelion	1.023 cal cm^{-2} min^{-1} (713 W m^{-2})

Solar Interplanetary Magnetic Field

Strength at 1.5 A.U., the mean distance of Mars from the Sun (1 A.U. = 1.495984 x 10^8 km):	Strength is dependent upon solar activity and may fluctuate 1 to 2 orders of magnitude.
Average	2γ ($1\gamma = 10^{-5}$ gauss)
Range	0 to 25γ

Magnetic Fields at Mars

The following upper limit values are based on the apparent absence of a Martian shock wave or magnetosphere along the Mariner IV trajectory. The magnetic moment of the Earth = M_E = 8.05 ±0.02 x 10^{25} gauss cm^3.

Martian magnetic moment, upper limit	3×10^{-4} M_E
Surface magnetic field at equator, upper limit	100γ
Piled-up interplanetary field at subsolar point (if internal moment is zero)	$\sim 35\gamma$

*See page 19 for list of cross references.

Solar Wind (properties at 1.5 A. U.)

Flow velocity:

Average:	
Quiet Sun	320 km sec^{-1}
Active Sun (Mariner II data)	500 km sec^{-1}
Range	200 to 860 km sec^{-1}

Density:

Average	5 cm^{-3}
Range	0.5 to 100 cm^{-3}

Temperature:

Average:	
Protons, quiet Sun	$T_p = 4 \times 10^4 °K$
Protons, active Sun (Mariner II data)	$T_p = 1.5 \times 10^5 °K$
Alpha particles	$\sim 4\ T_p$, typically
Range:	
Protons (T_p)	6×10^3 to $8 \times 10^5 °K$
Electrons (T_e)	$\leq 7 \times 10^4$ to $\geq 2 \times 10^5 °K$
T_e/T_p	1 to 10

Composition, average	96% protons, 4% alpha particles
n_α/n_p, range	0 to 20%

Energetic Particles

Energetic particles consist of protons and other particles accelerated in solar flares (typical energy 10^8 ev) and galactic cosmic ray ions (typical energy 10^9 ev).

DISCUSSION

More extended discussions of most of the material in this section are given in the Handbook of Geophysics and Space Environments (1965).

Solar Electromagnetic Radiation

The Solar Constant

By definition the solar constant is the total electromagnetic irradiation per unit area normal to a solar radius vector, at a distance of one astronomical unit from the Sun and outside the Earth's atmosphere. It is a direct measure of solar power output. Laue and Drummond (1968) have just published a new solar constant value of high precision which includes direct measurements made from an X-15 aircraft at an altitude of about 82 km, 1.952 ±0.02 cal cm^{-2} min^{-1} (1361 W m^{-2}). Values given on page 3 for the solar irradiance at Mars are scaled to the appropriate distance from the Sun from this new figure.

Solar Spectral Distribution [2]

The distribution with wavelength of the Sun's power can be roughly approximated in visible light by that of a 5900°K blackbody as shown in Fig. 1, although the Sun's effective temperature (the temperature of a blackbody having the same total power output as the Sun) is only about 5760°K. The flux in various wavelength intervals is given in Fig. 2. The sum of the indicated values is 1391 W m^{-2}. Laue and Drummond's (1968) work indicates that values for wavelengths less than 6070 Å should be reduced by about 7%. This will result in a sum agreeing with their new value for the solar constant. Extreme ultraviolet, x-ray, and radio radiations from the Sun are strong functions of the solar cycle and of sporadic solar events. Such radiation constitutes an insignificant fraction of the total power output of the Sun, but the very short wavelengths do have a large effect on ionospheric structure and atmospheric escape. Variations in these extreme wavelengths are discussed in the following paragraphs.

Extreme Ultraviolet Radiation [3]

Extreme ultraviolet normally encompasses that part of the electromagnetic spectrum from 100 Å up to about 1800 Å, where quartz begins to transmit and ordinary photographic emulsions become usable. Above 1800 Å there is strong and constant continuum radiation from the Sun. At wavelengths shorter than 1600 Å most solar power is in discrete emission lines. No absorption lines are observed below about 1700 Å. The entire extreme ultraviolet is dominated by the resonance line of atomic hydrogen (Lyman-α) at 1216 Å, which emits 5.1×10^{-3} W m^{-2} in the central 1 Å of the line, more than all other lines combined (Handbook of Geophysics and Space Environments, 1965). Under quiet Sun conditions near sunspot minimum the total flux from 165 Å to 1027 Å is about 2.8×10^{-3} W m^{-2}; that from 1027 Å to 1325 Å is 5.7×10^{-3} W m^{-2}; and that from 1325 Å to 1775 Å is 32×10^{-3} W m^{-2}, most of it continuum radiation in the longest 200 Å (Hinteregger et al., 1965). Good values of extreme ultraviolet flux near sunspot maximum will soon become available as the new maximum arrives.

X-Rays [4]

Although a more precise definition could be given in terms of the origin of the photon, the region of the spectrum between 0.1 Å and 100 Å is normally thought of as the x-ray region. Total emission of the quiet Sun below 60 Å varies between 1.3×10^{-4} W m^{-2} at sunspot minimum and 1.0×10^{-3} W m^{-2} at sunspot maximum (Handbook of Geophysics and Space Environments, 1965). X-ray emission 70 times the intensity of the quiet background has been measured from active regions. Gregory and Kreplin (1967) have measured changes of up to 50% in less than one minute in the 1- to 8-Å region. Total emission between 40 Å and 100 Å varies between 1.0×10^{-4} W m^{-2} at sunspot minimum and 1.0×10^{-3} W m^{-2} at sunspot maximum for the quiet Sun (Brandt and Hodge, 1964). A more complete table of x-ray fluxes for the quiet Sun is given in the Handbook of Geophysics and Space Environments (1965).

Radio Waves

At millimeter wavelengths the Sun radiates about like a 6000°K blackbody. For wavelengths longer than one centimeter the quiet Sun has a brightness temperature between 10^4 and 10^6°K, while the disturbed Sun may exhibit brightness temperatures as high as 10^{10}°K (Handbook of Geophysics and Space Environments, 1965). The total power involved at these wavelengths is minute, however, amounting to about 10^{-19} W m^{-2} Hz^{-1} at 1 cm (Handbook of Geophysics and Space Environments, 1965). The detailed radio behavior of the Sun is quite complex, but it is of far more importance in understanding the Sun than in any effect upon the planets.

Absorption in the Martian Atmosphere [5]

Evans (1965) suggests that, based upon a rocket spectrometer experiment, there is little, if any, absorption in the Martian atmosphere from ~2000 Å to 3000 Å. Rayleigh scattering will diffuse incoming and outgoing radiation but will prevent little of it from reaching the surface. Öpik (1960) has suggested that the violet haze is a layer of carbon particles absorbing in the violet and blue regions of the spectrum, but this explanation is not generally accepted. The best hypothesis today is that the violet haze is a very tenuous scattering layer of submicron-size particles, possibly of CO_2 or H_2O.

The best current hypothesis is that there is little true absorption in the Martian atmosphere in visible light. The absorption of a few microns of water vapor is minute. Only the occasional white clouds could be significant absorbers. In the infrared carbon dioxide is the most significant absorber. In the ultraviolet, violet, and blue there is Rayleigh scattering and perhaps a small amount of particulate scattering. In the visible there is significant scattering at times caused by 2- to 50-μ dust particles and by the white clouds. To a first approximation the solar flux above the Martian atmosphere also is the flux at the Martian surface. It is hoped that departures from this approximation can be evaluated at some future time.

Magnetic Fields

Solar Interplanetary Magnetic Field

The solar interplanetary magnetic field from 0.5 A.U. to at least 1.75 A.U. from the Sun is that carried by the solar wind plasma (q.v.). The gross field pattern observed is recurrent with a 27.3-day period equal to the solar rotation period. At 1 A.U. the field preferentially parallels the plane of the ecliptic and follows a spiral angle toward or away from the Sun. Structure tends to be organized into distinct sectors having distinct polarity toward or away from the Sun. During 1962-1964 there were commonly four sectors, as illustrated on the right. The pattern then broke up, and since 1964 the number and sizes of the sectors seem to have been changing with time on a scale less than 27 days (Neugebauer, 1968).

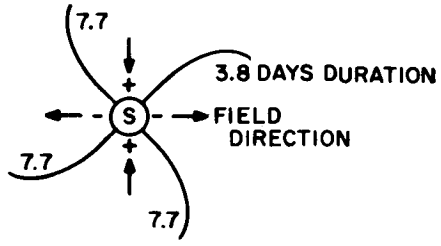

The average field strength at the orbit of Mars is expected to be about 2 γ, but the instantaneous value may range up to 25 γ. The larger field values—and abrupt changes in direction—are associated with hydromagnetic shock waves passing through the solar wind plasma.

Martian Magnetosphere and Magnetic Moment

A planet's magnetic field is expected to be bounded on the sunward side by currents flowing in the solar wind plasma (q.v.). The field is thus confined to a roughly tear-drop-shaped cavity known as the magnetosphere. The boundary of the magnetosphere (magnetopause) is a surface along which, roughly speaking, the planetary magnetic field pressure ($B^2/8\pi$) is balanced by the effective pressure of the solar wind directed flow. "Radiation belts" of energetic electrons and protons are expected to be contained within the magnetosphere.

The magnetosphere forms an obstacle to the solar wind flow. Because this flow is "supersonic," a shock wave (bow shock) is expected to be formed in the flow ahead of the magnetosphere and to be readily detectable as a surface of discontinuity in plasma and field parameters.

The Mariner IV instruments gave no indication of any effects associated with a Martian magnetosphere, its radiation belts (Van Allen et al., 1965), or its associated bow shock (Smith et al., 1965). This fact, interpreted in terms or appropriately scaled terrestrial magnetospheric parameters, was used to set a limit on the possible sunward projection of the bow shock (at 0.6 R_M above the surface) and thus to set an upper limit on the Martian magnetic moment.[6]

Even if it has little or no intrinsic magnetic field, Mars may be expected to have a bow shock standing about 1/3 planetary radius sunward of the planet's surface. The effective "magnetosphere" is set up by induced currents in the Martian ionosphere that "pile up" interplanetary fields carried by the solar wind flow.[7] Venus has been found to possess such a bow shock (Bridge et al., 1967).

Surface Magnetic Fields

The Mariner IV data would permit an intrinsic surface (dipole) field as large as 100 γ and a magnetosphere extending to about 0.5 R_M above the surface on the sunward side (Smith et al., 1965). A diurnal field variation produced by currents at the magnetopause would evidently be observable at the surface.

For an intrinsic field less than about 35 γ the ionospheric currents would replace the magnetopause with an "ionopause" (Bridge et al., 1967) and time-varying fringing fields of the compressed interplanetary fields of about 35 γ would be expected on the surface near the sub-solar point, dropping away to or below interplanetary values past the terminator.

Solar Wind

Description

The solar wind, a high-temperature, rarefied plasma emitted continuously by the Sun, flows outward at a supersonic rate. It carries irregular amounts of magnetic flux and interacts with the Earth's magnetic field to produce the boundary of the magnetosphere. Solar wind temperature and mean flow velocity do not vary with distance; the density shows an r^{-2} dependence. Comparisons of solar wind proton,[8] alpha-particle, and electron data for Earth and Mars are given in Figs. 3, 4, and 5, respectively.

Effects on the Martian Atmosphere

From a theoretical consideration of the solar wind bombardment on planetary atmospheres, Gunn (1968) has concluded that ~85% of the incident flux is reflected from the convected-field bow shock and roughly half of the remaining kinetic energy is absorbed in the atmosphere. His calculated accretion rate for hydrogen is 1.4×10^6 hydrogen atoms cm^{-2} sec^{-1}. The atmospheric removal time for collision-induced loss of upper atmosphere atoms is $\sim 2 \times 10^8$ years for Mars. The solar wind bombardment loss for oxygen is $\sim 2.7 \times 10^7$ cm^{-2} sec^{-1}. Thus, the loss time is short relative to the planet's age, and Gunn concludes that there must be "some mechanism of continuous production to retain the atmosphere Mars now possesses."[9]

Energetic Particles

Solar Flare Protons

Time histories of the energetic protons produced by solar flares are shown in Fig. 6. The solar flare energy spectra are shown in Figs. 7 and 8; probabilities of an integrated 6-month flux greater than a given value for protons with E > 5 and > 10 Mev are shown in Figs. 9 and 10, respectively. Solar flare behavior varies with the phase of the 11-year sunspot cycle; thus, the "solar maximum" behavior of 1959-1960 should be approximately repeated in 1970-1971. Haines (1967) concludes that the greatest natural radiation source on the Martian surface is from solar flare particles.

For a fuller discussion, see the Handbook of Geophysics and Space Environments (1965).

Cosmic Radiation

The term cosmic radiation is now customarily used to denote high-energy particles originating outside the solar system, although solar protons are sometimes referred to as solar cosmic radiation.

Protons constitute 80% of cosmic rays, while alpha particles make up about 19%. Most energies are in the general range from 1×10^9 to 3×10^9 ev, but the spectrum is broad and some energies as high as 10^{18} ev have been recorded.

Interplanetary magnetic fields are strong enough to bend the trajectories of cosmic rays into arcs with radii of curvature small compared with solar system dimensions. The cosmic rays thus are believed to diffuse into the solar system through the fields of varying orientations. The general negative radial gradient of the field strength acts to repel the particles from the center of the solar system. These effects are expected to result in a radial increase in average cosmic ray intensity of some few percent per astronomical unit. This gradient and thus the total flux at Mars are expected to vary with the phase of the solar activity cycle as a result of this magnetic field dependence.

Interaction with the Martian Atmosphere

Collisions of these high-energy particles with nuclei of atmospheric atoms (e.g., of oxygen, nitrogen, and carbon) produce fast secondary particles, chiefly neutrons, protons, and electrons. The atmosphere of a planet thus absorbs the incident particles but can multiply the net particle flux.

Figure 11 shows charged-particle flux at the surface versus atmospheric mass for Mars and Earth. The thin atmosphere on Mars increases the flux of charged particles expected at the surface in comparison with that in space. With a 7-mb surface pressure on Mars,[10] the flux on the surface increases by 90%. Haines (1967) concludes that the fast neutron flux arising from cosmic ray collisions with atmospheric atoms cannot possibly exceed 50 cm^{-2} sec^{-1}. This flux is probably insufficient to produce a measurable radiation field by neutron activation of the surface (causing emission of electrons and γ-rays in resultant beta-decay processes).

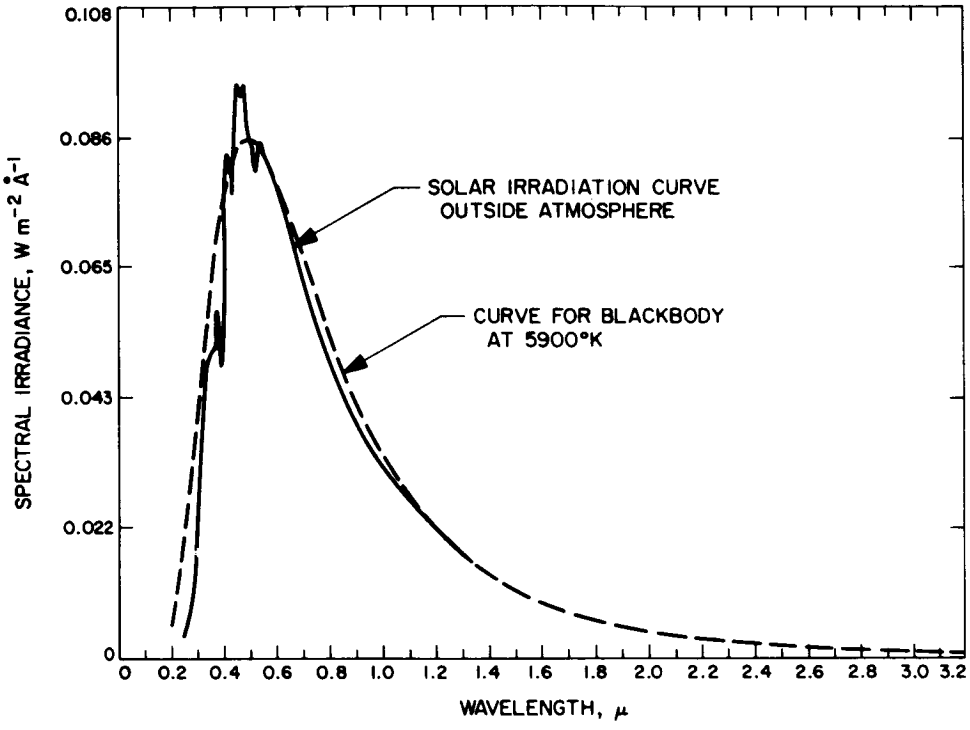

Fig. 1. Solar spectrum at Mars above the atmosphere. Spectral distribution curve is based on scaling the measured spectrum at Earth. The amplitude for wavelengths shorter than 6070 Å should be reduced 7% to give an integral which agrees with the 1968 value of the solar constant. (after Handbook of Geophysics and Space Environments, 1965)

Wavelength interval	Flux in wavelength interval, $W\ m^{-2}\ \Delta\lambda^{-1}$		Percent of total flux
	Earth	Mars	
(Å)			
1-8	$<10^{-9}$ [a]	$<0.4 \times 10^{-9}$	$<10^{-11}$ [a]
8-31	10^{-7} [b]	0.4×10^{-7}	7×10^{-9} [b]
31-165	0.70×10^{-3} [c]	0.3×10^{-3}	4.9×10^{-5} [c]
165-303	1.18×10^{-3}	5.08×10^{-4}	8.3×10^{-5}
304	0.25×10^{-3}	1.08×10^{-4}	1.8×10^{-5}
305-460	3.15×10^{-3}	1.36×10^{-3}	2.2×10^{-4}
460-1215	1.74×10^{-3}	7.49×10^{-4}	1.2×10^{-4}
1216	4.40×10^{-3}	1.90×10^{-3}	3.1×10^{-4}
1216-1800	3.30×10^{-2}	1.42×10^{-2}	2.3×10^{-3}
1800-2250	0.9	0.39	6.5×10^{-2}
(μ)			
0.225-0.3	17	7.3	1.3
0.3-0.4	110	47	7.9
0.4-0.5	200	86	14.4
0.5-0.6	193	83.1	13.9
0.6-0.7	162	69.8	11.7
0.7-0.8	128	55.1	9.2
0.8-0.9	101	43.5	7.2
0.9-1.0	81	35	5.8
1.0-1.1	66	28	4.8
1.1-1.2	55	24	4.0
1.2-1.3	45	19	3.2
1.3-1.5	66	28	4.7
1.5-2.0	84	36	6.1
2.0-3.0	54	23	3.9
3.0-11.0	27	12	1.9
11.0-30.0	0.7	0.3	0.05
1 cm-30 m	10^{-11} [d]	0.4×10^{-11}	$<10^{-13}$ [d]

[a] Increases 10^3 and 10^5 for disturbed Sun and for Class 3 flare, respectively.

[b] Increases by factor of at least 50 for disturbed Sun.

[c] Increases by factor of 7 for disturbed Sun.

[d] Increases by factor of 10^3 for disturbed Sun.

Fig. 2. Table of solar spectral irradiance for the quiet Sun outside of any atmosphere at the mean distances of Earth and Mars. (The mean distance of Mars is 1.5237 A.U.) The table sums to 1391 W m^{-2}, about 2% higher than the latest and best value for the solar constant. Flux for wavelengths less than 6070 Å should be reduced by about 7% to give an integral which agrees with the 1968 value for the solar constant. (after Handbook of Geophysics and Space Environments, 1965)

Solar wind proton data for	v Velocity, km sec^{-1}	n Density, cm^{-3}	T Temperature, °K	nv Directional flux	$\approx nmv^2/2$ Energy density, ergs cm^{-3}	$\approx mv^2/2$ Energy per particle, ev
Earth						
Minimum	200	1	$\leq 1 \times 10^4$	2×10^7	3×10^{-10}	200
Average	500	6	1×10^5	3×10^8	1.3×10^{-8}	1300
Maximum	$\geq 800^a$	$\geq 50^a$	1×10^6	4×10^{9a}	1.3×10^{-7a}	3200^a
Mars						
Minimum at aphelion	200	~0.4	$\leq 1 \times 10^4$	0.7×10^7	1×10^{-10}	200
Average at aphelion	500	~2	1×10^5	1×10^8	5×10^{-9}	1300
Average at perihelion	500	~3	1×10^5	1.6×10^8	7×10^{-9}	1300
Maximum at perihelion	$\geq 800^a$	$\sim 26^a$	1×10^6	2×10^{9a}	7×10^{-8}	3200^a

[a]Uncertain

Fig. 3. Table of solar wind proton (H^+) data for Earth and derived estimates for Mars. (from data of Neugebauer, 1968)

Solar wind alpha-particle data for	v Velocity, km sec^{-1}	n Density, cm^{-3}	T Temperature, °K	nv Directional flux	$\approx nmv^2/2$ Energy density, ergs cm^{-3}	$\approx mv^2/2$ Energy per particle, ev
Earth						
Minimum	200	0	2×10^{4a}	0	0	800
Average	500	0.3^a	6×10^{5a}	1.5×10^{7a}	1×10^{-9a}	5×10^{3a}
Maximum	$\geq 800^a$	$\geq 5^b$	4×10^{6b}	4×10^{8b}	5×10^{-8b}	1×10^{4b}
Mars						
Minimum at aphelion	200	0	2×10^4	0	0	8×10^2
Average at aphelion	500	0.1	6×10^5	5×10^6	4×10^{-10}	5×10^3
Average at perihelion	500	1.5×10^{-1}	6×10^5	8×10^6	5×10^{-10}	5×10^3
Maximum at perihelion	≥ 800	2.6	4×10^6	2×10^8	2.6×10^{-8}	1×10^4

[a]Uncertain
[b]Very uncertain

Fig. 4. Table of solar wind alpha-particle (α) data for Earth and derived estimates for Mars. (from data of Neugebauer, 1968)

Solar wind electron data for	v Velocity,[a] km sec^{-1}	n Density, cm^{-3}	T Temperature, °K	$n\bar{v}_{th}/4$ Omnidirectional flux,[b] cm^{-2} sec^{-1}	≈3/2 nkT Energy density, ergs cm^{-3}	≈kT Energy per particle, ev
Earth						
Minimum	200	1	3×10^4[c]	2×10^7[c]	5×10^{-12}[c]	6[c]
Average	500	6	2×10^5[d]	8×10^8[d]	2×10^{-10}[d]	2×10^1[d]
Maximum	800	50	10^6[c]	1.4×10^9[c]	1×10^{-8}[c]	1×10^2[c]
Mars						
Minimum at aphelion	200	4×10^{-1}	3×10^4	7×10^6	2×10^{-12}	6
Average at aphelion	500	2	2×10^5	1.4×10^7	7×10^{-11}	2×10^1
Average at perihelion	500	3	2×10^5	4×10^8	1×10^{-10}	2×10^1
Maximum at perihelion	800	26	10^6	7×10^{10}	5×10^{-9}	1×10^2

[a] Directed away from Sun
[b] $\bar{v}_{th} = \sqrt{2kT}/m$
[c] Very uncertain
[d] Uncertain

Fig. 5. Table of solar wind electron (e^-) data for Earth and derived estimates for Mars. (from data of Neugebauer, 1968)

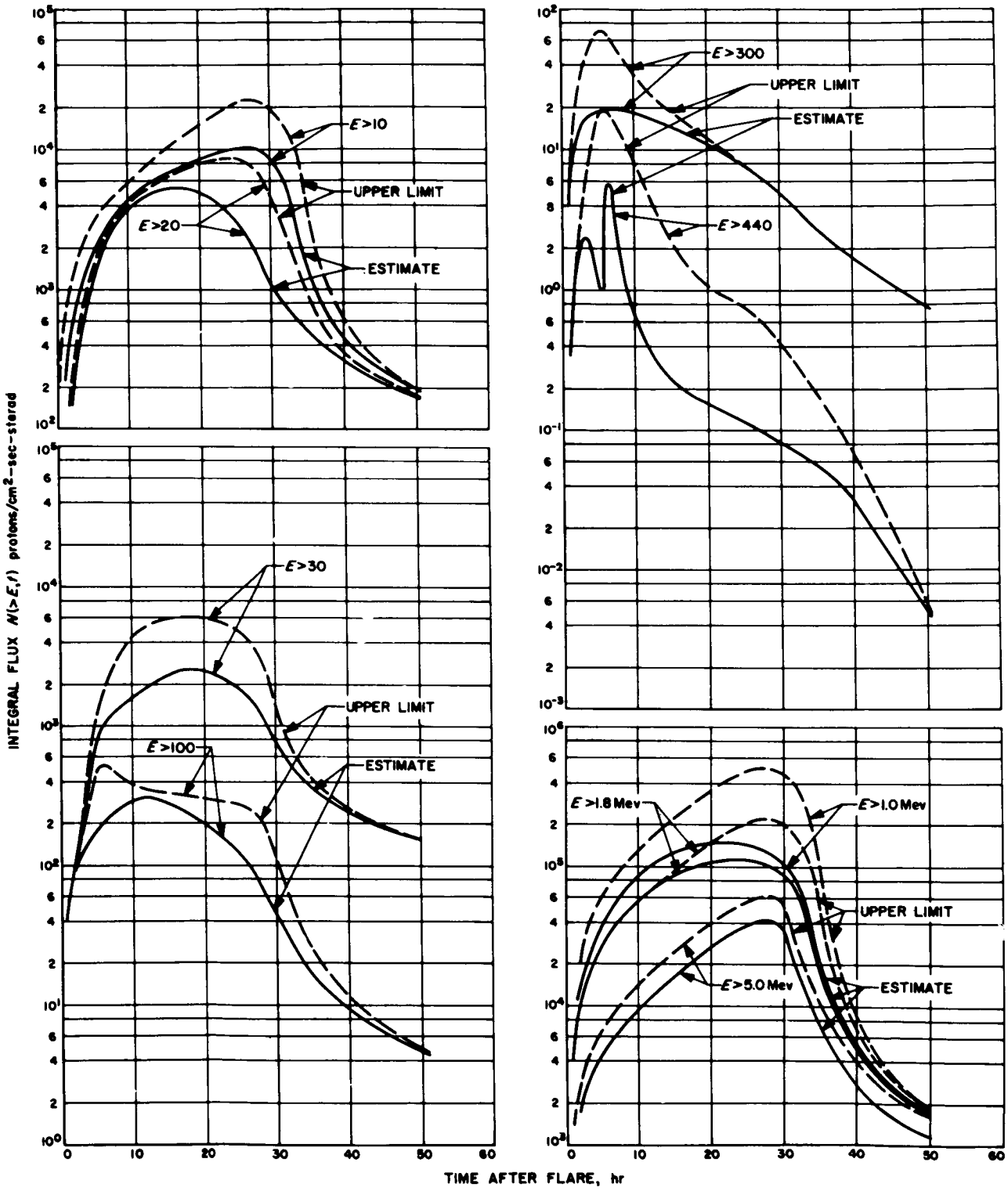

Fig. 6. Estimates and upper limits of time histories of energetic protons produced by solar flares. E > X (X takes discrete values from 1.0 to 440 Mev). (Mariner Mars 1969 Spacecraft System Environmental Estimates, 1967)

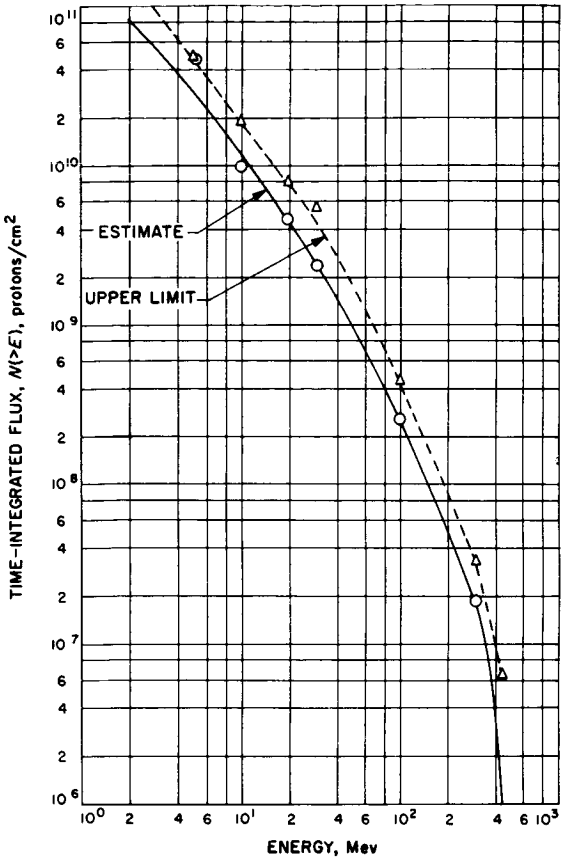

Fig. 7. Estimate and upper limit of time-integrated flux of protons produced by a single solar flare vs. proton energy. (Mariner Mars 1969 Spacecraft System Environmental Estimates, 1967)

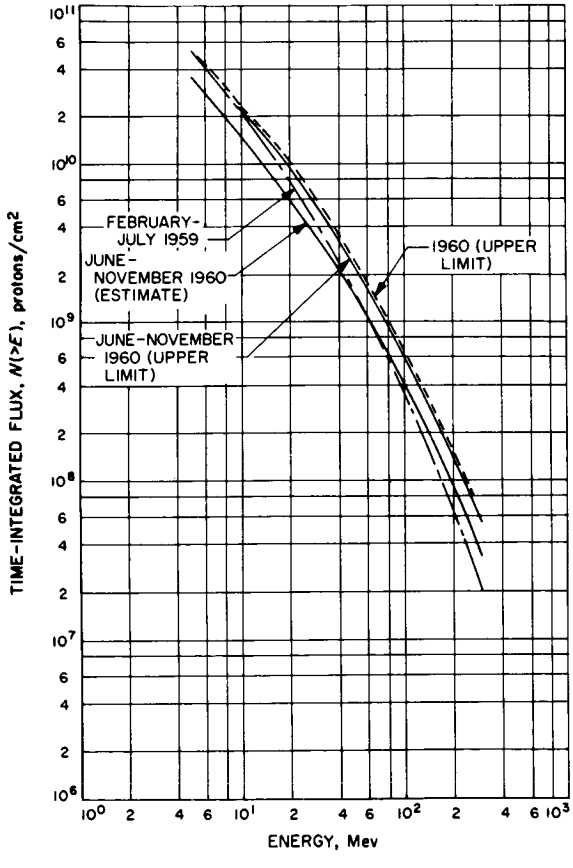

Fig. 8. Time-integrated flux of protons produced by solar flares vs. proton energy, for periods in 1959 and 1960. Energy spectra represent maximum exposure flux expected for a six-month and a yearly period. (Mariner Mars 1969 Spacecraft System Environmental Estimates, 1967)

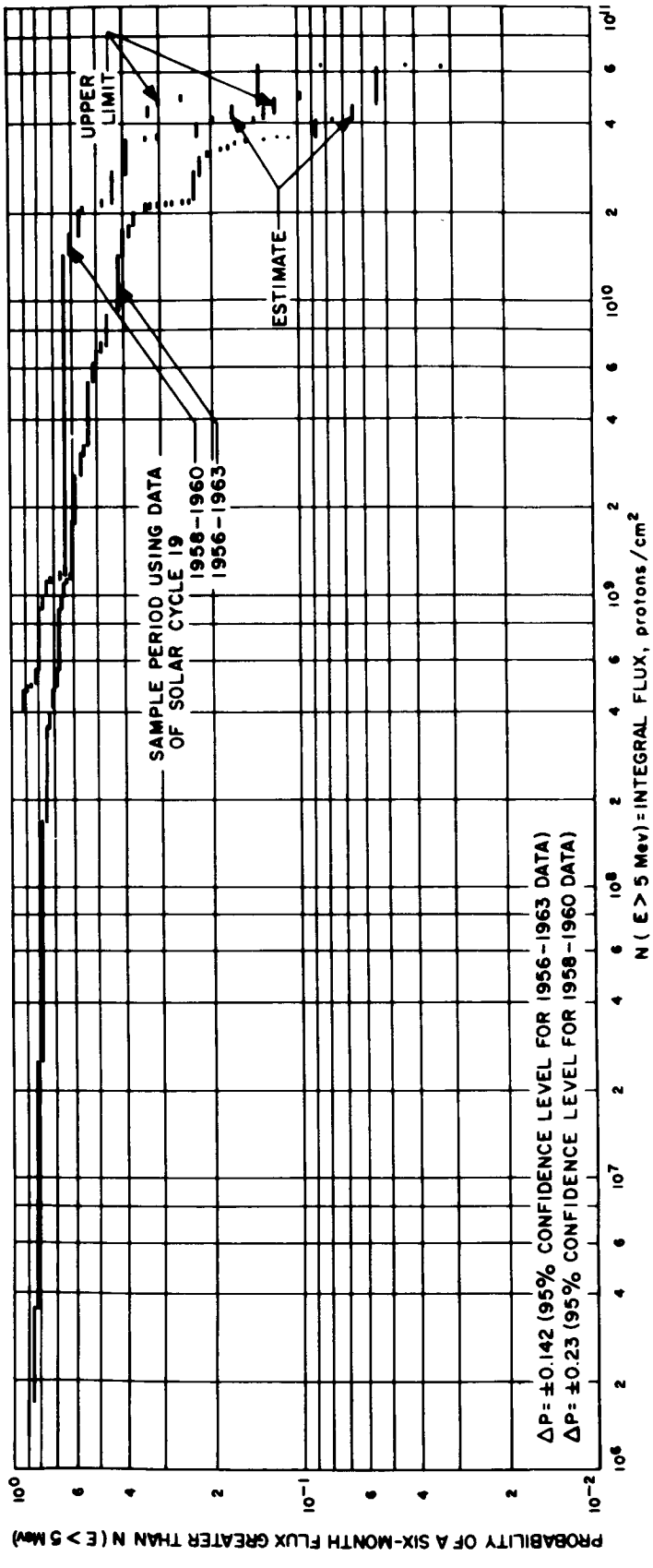

Fig. 9. Probability of an integrated six-month flux (of protons with E > 5 Mev) greater than N produced by solar flares. Based on near-Earth data for solar cycle 19. (Mariner Mars 1969 Spacecraft System Environmental Estimates, 1967)

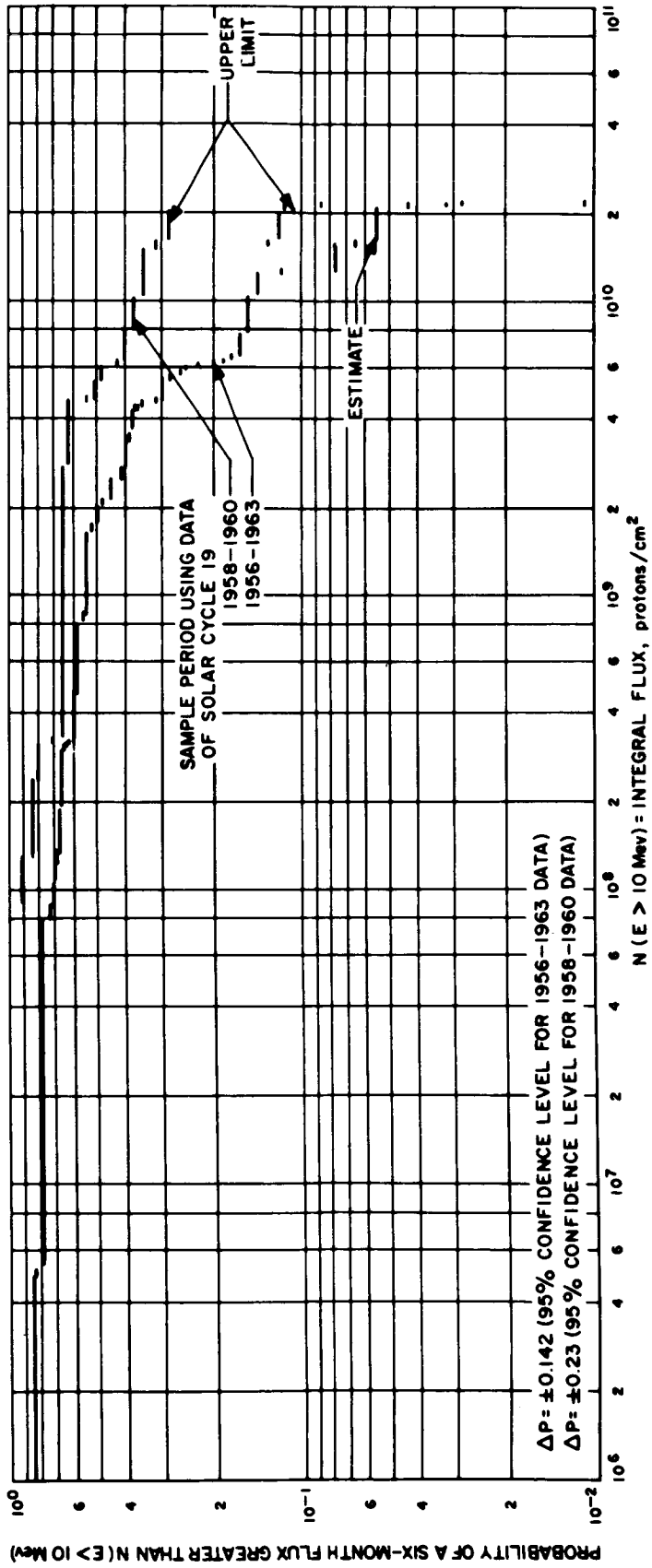

Fig. 10. Probability of an integrated six-month flux (of protons with E > 10 Mev) greater than N produced by solar flares. Based on near-Earth data for solar cycle 19. (Mariner Mars 1969 Spacecraft System Environmental Estimates, 1967)

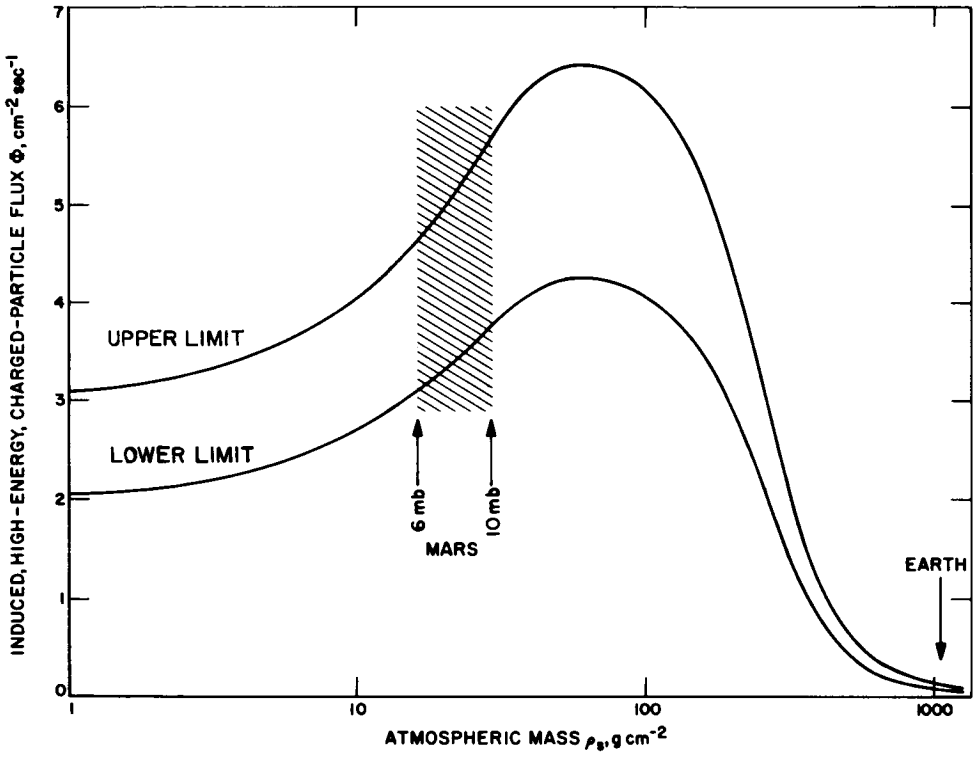

Fig. 11. Cosmic-ray-induced charged-particle flux at the surface vs. atmospheric mass for Mars and Earth. (Haines, 1967)

CROSS REFERENCES

The specific section number, subject, and page number to which the reader is referred is given below.

Cross Reference	Section and Subject
[1] Distance of Mars from the Sun	1.....Orbital values (data summary), p.3.
[2] Solar spectral distribution	3.1.....Surface thermal properties (discussion), p.3. 3.2.....Surface spectral reflectivity and distribution (data summary), p.2.
[3] Extreme ultraviolet radiation	5.4.....Upper Atmosphere F_1-Model using maximum solar flux (discussion), p.9-11; Upper Atmosphere F_2-Model using minimum solar flux (discussion), p.11,12; Incident solar flux densities (figure), p.18.
[4] X-rays	5.4.....Upper Atmosphere Preliminary E-Model (discussion), p.8,9.
[5] Absorption in the Martian atmosphere	4.1.....The violet layer, blue clouds, and blue clearing (discussion), p.2-5; White clouds (discussion), p.5. 5.1.....Observed atmospheric constituents (data summary), p.1; Ozone in the atmosphere (discussion), p.8. 5.3.....Lower atmosphere convective-radiative models (discussion), p.6. 5.4.....Photodissociation region (discussion), p.2,3.
[6] Martian magnetic moment	2.....Lyttleton's interior model (discussion), p.7; Urey's interior model (discussion), p.8.
[7] Martian "magnetosphere" and ionosphere	5.4.....Layers of the upper atmosphere (discussion), p.1,2; Ionosphere (discussion), p.3-8.
[8] Solar wind protons	3.4.....Surface bearing strength and sintering (discussion), p.6.
[9] Solar wind and the atmosphere	5.4.....Physics of the upper atmosphere (discussion), p.2,3.
[10] Surface pressure	5.2.....Surface pressure (data summary), p.1. 5.3.....Lower atmosphere models (data summary), p.1.

BIBLIOGRAPHY

Brandt, J.C., and Hodge, P., 1964, Solar system astrophysics: New York, McGraw Hill Book Co.

Bridge, H.S., Lazarus, A.J., Snyder, C.W., Smith, E.J., Davis, L., Jr., Coleman, P.J., Jr., and Jones, D.E., 1967, Mariner V: plasma and magnetic fields observed near Venus: Science, v.158, p.1669-1673.

Evans, D.C., 1965, Ultraviolet reflectivity of Mars: Science, v.149, p.969-972.

Gregory, B.N., and Kreplin, R.W., 1967, Observations of solar x-ray activity below 20 angstroms: J.Geophys.Res., v.72, p.4815-4820.

Gunn, J.E., 1968, (Princeton, N.J., Princeton U.): private communication.

Haines, E.L., 1967, Estimate of the natural radiation on the surface of Mars: presented to Voyager Space Power Systems Panel at Mount Laboratory, Miamisburg, O., January 11, 1967.

Handbook of geophysics and space environments, 1965; Valley, S.L., Editor: New York, McGraw-Hill Book Co.

Hinteregger, H.E., Hall, L.A., and Schmidtke, G., 1965, Solar XUV radiation and neutral particle distribution in July 1963 thermosphere, p.1175-1190 in Space research V: Amsterdam, North Holland Pub.Co.

Laue, E.G., and Drummond, A.J., 1968, Solar constant: first direct measurements: Science, v.161, p.888-891.

Mariner Mars 1969 spacecraft system environmental estimates, 1967; Hyde, J.R., Editor: Pasadena, Calif., Jet Propulsion Laboratory, Doc.605-18 (PD-92).

Neugebauer, M., 1967, 1968, (Pasadena, Calif., Jet Propulsion Laboratory): private communication.

Öpik, E.J., 1960, The atmosphere and haze of Mars: J.Geophys.Res., v.65, p.3057-3063.

Smith, E.J., Davis, L., Jr., Coleman, P.J., Jr., and Jones, D.E., 1965, Magnetic field measurements near Mars: Science, v.149, p.1241-1242.

Van Allen, J.A., Frank, L.A., Krimigas, S.M., and Hills, H.K., 1965, Absence of Martian radiation belts and implications thereof: Science, v.149, p.1228-1233.

DOCUMENT CONTROL LIST

This initial release of the Mars Scientific Model consists of 272 numbered pages and 14 unnumbered pages dated as shown below, and of 23 blank pages, also listed below. These 309 pages together with the 18 dividers and the two maps (MEC-1 and MEC-2 in the pocket on the inside-front cover) form the total content of the document as published July 15, 1968.

Title page (i) 7-15-68
Copyright page (ii) 7-15-68
Frontispiece (iii) . . . . . (7-15-68)
(iv) . . . . . blank
v thru viii 7-15-68

SECTION 1

1 7-15-68
(2) . . . . . blank
3 thru 5 4-1-67
6 8-14-67
7 thru 11 4-1-67
12 7-1-68
13 thru 26 4-1-67
27 7-15-68
28 7-1-68

SECTION 2

1 7-15-68
(2) . . . . . blank
3 thru 5 11-1-67
6 thru 9 4-1-67
10 thru 13 7-15-68
(14) . . . . . blank

SECTION 3

1 thru 5 7-15-68
(6) . . . . . blank

3.1

1 thru 8 7-1-68
9 7-15-68
10 7-1-68

3.2

1 thru 7 4-1-67
(8) . . . . . blank
9 thru 11 4-1-67
12 7-15-68
13 4-1-67
(14) . . . . . blank

3.3

1 thru 13 7-1-68
14 7-15-68
15 and 16 7-1-68

3.4

1 thru 9 7-15-68
10 and 11 7-1-67
12 thru 18 7-15-68

3.5

1 thru 13 7-1-68
14 4-1-67
15 7-1-68
16 thru 18 4-1-67
19 thru 25 7-1-68
26 and 27 5-5-67
28 4-1-67
29 7-1-68
(30) . . . . . blank
31 and 32 7-15-68
33 thru 35 7-1-68
(36) . . . . . blank

SECTION 4

1 thru 3 7-15-68
(4) . . . . . blank

4.1

1 thru 16 7-15-68

4.2

1 thru 6 7-15-68
(7) . . . . . blank
8 thru 10 7-15-68
11 4-1-67
(12) . . . . . blank
13 4-1-67
(14) . . . . . blank
15 4-1-67
(16) . . . . . blank
17 4-1-67
(18) . . . . . blank
19 (+2 overlays and 1 color map) 4-1-67
(20) . . . . . blank
21 (+3 overlays and 1 color map) 4-1-67
(22) . . . . . blank
23 (+2 overlays and 1 color map) 4-1-67
(24) . . . . . blank
25 (+1 overlay) 4-1-67
(26) . . . . . blank
27 and 28 7-15-68

SECTION 5

1 thru 3 7-15-68
(4) . . . . . blank
5 4-1-67
(6) . . . . . blank

5.1

1 8-28-67
2 4-1-67
3 thru 5 8-28-67
6 thru 9 4-1-67
10 7-15-68
11 thru 13 8-30-67
(14) . . . . . blank

5.2

1 thru 3 8-30-67
4 thru 9 4-1-67
10 and 11 8-30-67
12 7-15-68
13 and 14 8-30-67

5.3

1 9-11-67
2 thru 4 8-18-67
5 thru 20 9-11-67
21 7-15-68
22 9-11-67

5.4

1 thru 18 7-3-67
19 4-1-67
20 7-15-68
21 and 22 7-3-67

SECTION 6

1 thru 20 7-15-68

APPENDIX

1 7-15-68
(2) . . . . . blank